BALKAN ASTRONOMICAL MEETING
BAM 2004
June 2004, Rozhen, Bulgaria

**Under the patronage of
the first Bulgarian cosmonaut
GEORGY IVANOV**

Together with the Institute of Astronomy

Editors:
Prof. Kiril Panov
Dr. Lachezar Filipov
Dr. Valeri Golev

Technical Editors:
Valeri Vasev
Maria Dimitrova

C O N T E N T S

Aerospace research

Galaxies

Stellar Physics

Dear colleagues and guests,

It is my pleasure to welcome you all here in the Rozhen National Astronomical Observatory, to the Balkan Astronomical Meeting!

I can see here our colleagues and friends from Romania, Serbia and MN, Macedonia, Greece, Russia, Hungary, the Czech Rep., Poland, and Bulgaria. Altogether, about 90 participants will attend this Meeting. It is also my pleasure to welcome here the first Bulgarian cosmonaut, Mr. Georgi Ivanov! Mr. G. Ivanov is a sponsor of our Meeting and I would like to thank him very much!

This Meeting is organized by the Institute of Astronomy, Bulgarian Academy of Sciences, by the Institute of Space Research, BAS, and by the Department of Astronomy of the "St. Kliment Ohridski" University of Sofia.

The Meeting is dedicated to the 25th anniversary of the first light received with the 2-m telescope, to the 25th anniversary of the space flight of the first Bulgarian cosmonaut, Mr. Georgi Ivanov, and to the 110th anniversary of the first Bulgarian astronomical observatory in Sofia, which belongs to the Sofia University.

I wish you all a successful meeting and I am sure, it will provide the basis for a better collaboration in future between our countries in the field of Astronomy!

Dr. Kiril Panov,
director,
Institute of Astronomy, BAS

Dear colleagues and friends,

I am glad to welcome you all in the National Astronomical Observatory Rozhen. Astronomy is probably the oldest science. Ever since the dawn of civilization, mankind has been trying to understand the world we live in. today, the Astronomy is a very important part of Physics and many new ideas and developments in Physics have come from Astronomy. This is not surprising, if we consider the limits of physical experiments, carried out in our laboratories. On the other hand, processes in the Universe can take place under extreem conditions, like temperatures, densities, pressure, gravitational fields, electro-magnetic fields etc. No doubt, the Astrophysics is now an invaluable source of new ideas and knowledge.

During the last years there is a good tradition in organizing meetings of astronomers from Balkan and neighbouring countries. Several astronomy meetings have already taken place in Romania, Serbia and MN and in Belogradchik. I am very glad that this good tradition now continues in the on-going scientific cooperation in the South-Eastern Europe, which is, in my view, the best way to integrate the science of our countries with the European science.

The National Astronomical Observatory Rozhen is operational since 1981. It is, until now, the biggest astronomical observatory in the SEE. With its main 2m telescope, NAO Rozhen is also biggest research department of the Bulgarian Academy of Sciences. Despite financial difficulties, which are common for all of the countries in the transition to market economy, the Bulgarian Academy of Sciences has put a lot of resources to maintain the Observatory and to keep it on the up-to-date level. During the past 23 years of operation, research in NAO Rozhen provided outstanding results, published in hundreds of publications in all renowned astronomical journals.

Most of these publications are achieved in collaboration with astronomers from different European countries. We should point out the large scale of international collaboration in NAO Rozhen, including all countries from our region, all countries from Eastern Europe, Germany, Finland, Norway, France, Italy, UK and many others.

The Bulgarian Academy of Sciences is determined to continue to support the international collaboration in the NAO Rozhen. A recent joint project has been

started in collaboration between Bulgaria, Romania, Serbia and MN and Turkey. As I understand, this joint project was approved by UNESCO - ROSTE and will get a support: delivery of a new high performance CCD camera for NAO Rozhen. The BAS will support this project and we hope the collaboration will go on for the benefit of all of us.

I am sure this astronomical meeting will bring up new ideas, new projects and new friendships.

I wish you a successful meeting and successful continuation of your research, after the meeting.

<div align="center">
akademician N. Sabotinov
Vice-President of Bulgarian Academy of Sciences
</div>

THE ROZHEN NATIONAL ASTRONOMICAL OBSERVATORY: OBSERVATIONAL FACILITIES, RESEARCH ACTIVITIES AND POSSIBILITIES FOR COLLABORATION BETWEEN COUNTRIES FROM SOUTH-EASTERN EUROPE

Kiril Panov

Institute of Astronomy, Bulgarian Academy of Sciences,

The Rozhen National Astronomical Observatory belongs to the Institute of Astronomy. It is the biggest research facility of the Bulgarian Academy of Sciences and also the biggest observatory for optical observations in the SEE. The Rozhen NAO is situated on peak Rozhen in the Rhodopy mountains, some 25 km from the town of Smolyan. (longitude = -01h 38m 58s, latitude = +41° 41′ 48″ , altitude = 1750 m). It was built in the late 70-ties and officially inaugurated in 1981. The main instrument is a 2 m Ritchey-Chretien-Coude telescope, built by Carl Zeiss Jena, Germany (Fig 1). In the Ritchey focus the field is   1° x   1°   (F/8), with 12.9 arcsec/mm. Observations can be carried out either directly with a CCD and filter block, or else with a double channel focal reducer (1). Two highly sensitive CCD cameras are used: the Photometrics AT200 system (SITe chip, 1024 x 1024 , pixel = 24 μm) and the newly introduced VersArray 1300B from Princetone Instruments (1340 x 1300, pixel = 20 μm). The VersArray   CCD has been sponsored by UNESCO-ROSTE, in the framework of a joint regional project including Bulgaria, Romania, Serbia and MN and Turkey. This joint project deals with studies of variable stars and the small bodies of the Solar system. In the Coude-focus (F/36), there are 3 different cameras for dispersions of 4 Å/mm, 9 A/mm and 18 Å/mm. There is a set of gratings with the mostly used one of 630 lines/mm.
With 2 px resolution, at 5000 Å and 4 Å/mm the spectral resolution would be R= 27 000 (Fig 2).

The 60 cm telescope is dedicated to photoelectric photometry. It is a Cassegrain (F/12.5)   telescope, equipped with an UBV, single channel, photon counting, computer controlled photometer (Fig 3).

The 50/70 cm Schmidt-telescope (5° x 5° field) is presently equipped with a SBIG ST8 CCD (1500 x 1000, pixel = 9 μm, CCD field is: 27.5 x 18 arcmin) . The Schmidt telescope is shown on Fig 4.
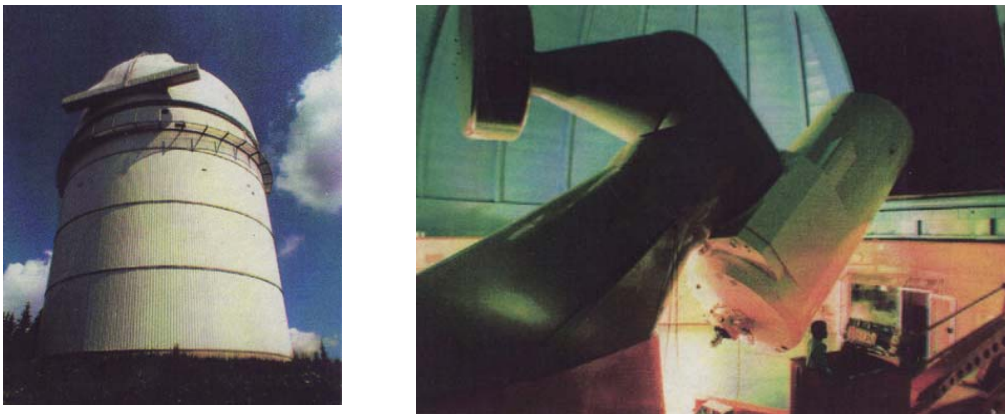
Fig. 1 The dome of the 2-m   Fig. 1 View of the 2-m telescope
telescope.

Fig. 2. The Coude spectrograph of the 2-m telescope

The last observing facility in Rozhen NAO is a 15 cm solar coronograph, presently under construction in the Institute of Astronomy. The solar coronograph will be operational by 2005.

In the Rozhen NAO, studies are carried out of different programs, in connection to the institutes scientific departments: Sun, Solar system, Nonstationary stars, Chemically peculiar stars, Stellar atmospheres and envelopes, stellar clusters and Galaxies. The Rozhen NAO is also a major facility for international collaboration. During the 23 years of operation, a

great number of project were carried out with international collaboration involved: all countries from Eastern Europe, all neighbouring countries, Germany, Finland, Norway, Russia,UK, Italy, France etc.

The observing conditions in Rozhen NAO are similar to places in the Mediterranean region. There are about 150 observing nights per year (110 for photometry), distributed over two main seasons: 60 % of the clear nights in the summer and autumn and 40 % in winter and spring. The mean seeing is about 2 arcsec. The sky brightness is about 22.2 mag in B per square arcsec. Some observing results are shown below, to illustrate the possibilities of the Rozhen NAO.

Fig. 3. The dome of the 60-cm telescope.
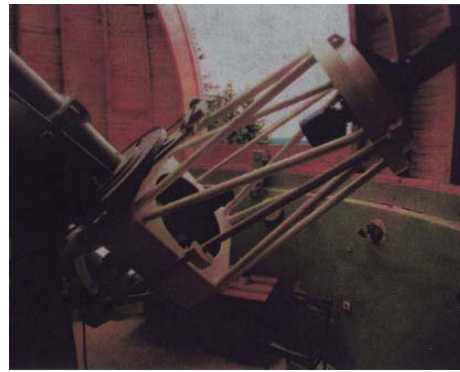
Fig. 3. The 60-cm photometric telescope.
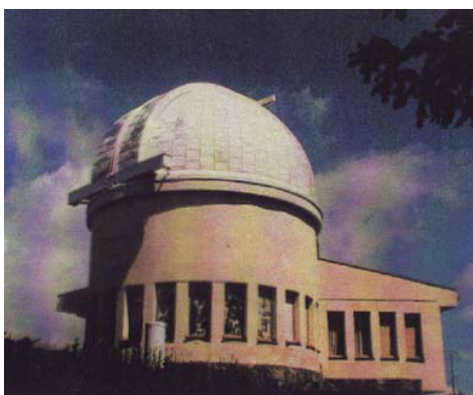
Fig.4. The dome of the Schmidt telescope.
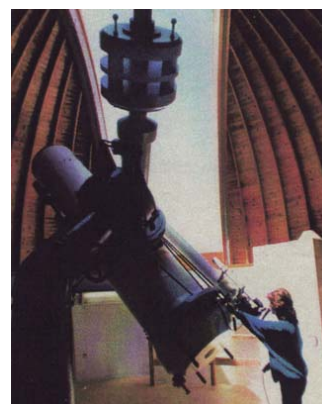
Fig.4. The 50/70 cm Schmidt telescope.

Observation of the Halley comet in 1986, Jan 14, is shown on Fig 5 (courtesy of V. Skodrov and V. Ivanova). The Halley comet was first spotted in Rozhen NAO on Nov 25 , 1984, which is also first observation from Europe.

Observations of the flare star EV Lac and the spotted star BY Dra are shown in Fig 6. Stellar flares are being registered in U filter , with time resolution of 1 s or even 0.1 sec. Spot modulation of brightness can be obtained for amplitudes of several hundreds of mag, with errors being typically 0.003 - 0.005 mag , for bright stars (2).

Fig 7 shows the Wolf-Rayet star WR 140 in 1991 – 2001 (3). For the first time, a photometric dip was registered in Rozhen NAO, around the phase of periastron in that system. The dip is a result of an "eclipse", due to carbon dust building by the colliding stellar winds of the two components. The photometric system on the 60 cm telescope was stable for more than 10 years, making possible such long term observing program.

Fig 8 shows the light curves in UBVRI of the SN 2002ap in M74, observed with all three telescopes in Rozhen (4).

Bulgarian astronomers are open for collaboration and we acknowledge very much the support of UNESCO-ROSTE, which is an important contribution to our regional projects.

References

1. Jockers, K., Credner, T., et al, 2000, KFNTS, 3, 13.
2. Goranova, Yu.,Panov, K., 2001, Balkan Meeting of Young Astronomers, Proceed. P. 136.
3. Panov, K.P., Dimitrov, D., 2001, IBVS 5177.
4. Borisov, G., Dimitrov, D., et al., 2002, IBVS 5264.

Fig. 5. Comet Halley on January 14 1986. The photography is taken with Schmidt telescope of NAO Rozhen by V. Shkodrov and V. Ivanova.
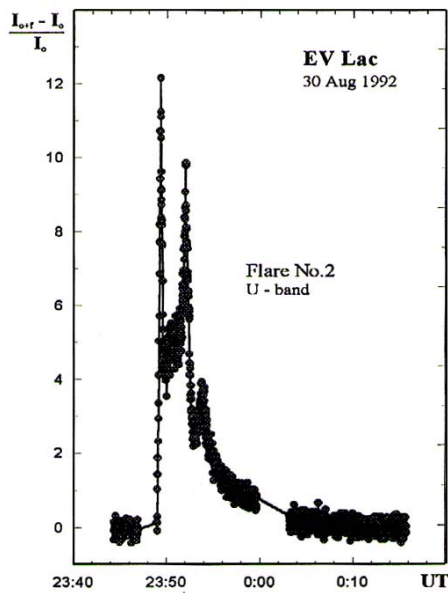
Fig. 6. Flare on EV Lac in U band.   Spot light curves of the star
60 cm telescope Rozhen NAO   BY Dra. 60 cm telescope NAO.
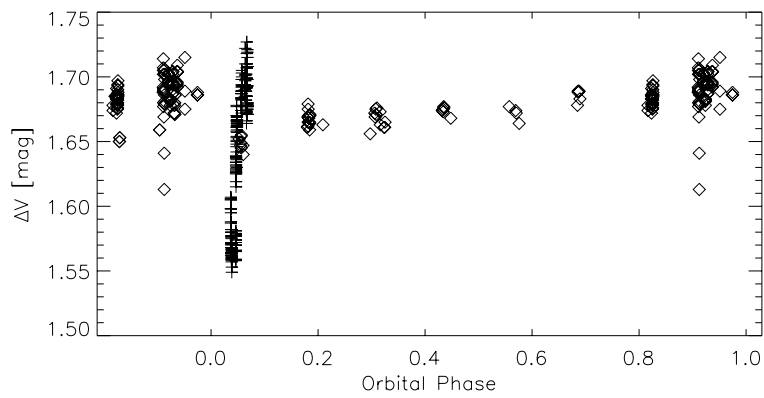
Fig. 7. WR 140 light curve in filter V for 1991 – 2001. 60 cm telescope NAO
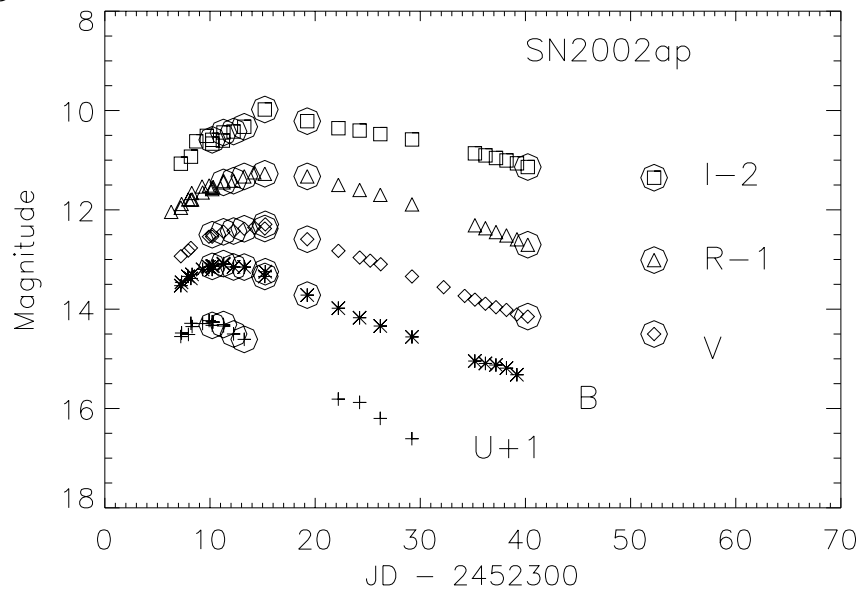
Fig. 8. Light curves in UBVRI of SN 2002ap in M74. 2-m telescope, 50/70 cm Schmidt telescope and 60 cm telescope of Rozhen NAO, with additional data from the literature.

14

RETURN AND PROFITABILITY OF SPACE PROGRAMS. INFORMATION - THE MAIN PRODUCT OF FLIGHTS IN SPACE

Irena Nikolova

Space Research Institute

Abstract

The basic branch providing global information, as a product on the market, is astronautics and in particular aero and space flights. Nowadays economic categories like profitability, return, and self-financing are added to space information. The activity in the space information service market niche is an opportunity for realization of high economic efficiency and profitability.

The present report aims at examining the possibilities for return and profitability of space programs. Specialists in economics from different countries strive for defining the economic effect of implementing space technologies in the technical branches on earth. Still the priorities here belong to government and insufficient market organization and orientation is apparent. Attracting private investors and searching for new mechanisms of financing are the factors for increasing economic efficiency and return of capital invested in the mentioned sphere.

Return of utilized means is an economically justified goal, a motive for a bigger enlargement of efforts and directions for implementing the achievements of astronautics in the branches of economy on earth.

Market economy is an economic system of forms and methods of organization and management of public production, in which economic solutions have been taken by economically independent producers and consumers who meet on the market and through it coordinate their own actions, which are subjected to the demand and supply laws.

Market economy imposes essential alterations in the realization approach of economic activity, in the goals and tasks of each economic section.

The achievement of goals referred to economic stability and development of economic unit requires good comprehension of economic conditions and the economic law requirements, revealing their impact through the market and the market mechanisms.

Research target on the part of marketing is the type, special features and characteristics of a product offered on market. Diverse economic activities give various products. Under the modern conditions special interest is displayed in the unique product – the "information".

The basic branch providing global information, as a product on the market, is astronautics and in particular aero and space flights. Nowadays economic categories like profitability, return and self-financing are added to space information.

Space equipment very distinctly manifests its unique, compared to other analogous resources, possibilities to spread information to any place on Earth. Some aspects of human activity like transport, navigation, intercommunications and communications, meteorology and others are impossible to exist without the information provided by satellites. It is hard to imagine any of the world large-scale industrial centers without access to space information channels. The activity in the space information service market niche is an opportunity for realization of high economic efficiency and profitability. Because of the specific and complex character of this activity there exists a slight unclearness regarding the price of such kind of product, control over the financial resources and the market orientation. Still the priorities here belong to government and insufficient market organization and orientation is apparent. Attracting private investors and searching for new mechanisms of financing are the factors for increasing economic efficiency and return of capital invested in the mentioned sphere. Specialists in economics from different countries strive for defining the economic effect of implementing space technologies in the technical branches on the earth.

Return of utilized means is an economically justified goal, a motive for a bigger enlargement of efforts and directions for implementing the achievements of astronautics in the branches of economy on earth. The actual tendencies, settled in the modern political way of thinking in the international relations, are the tendencies with high level of cooperation and integration. The countries mutual work originates from the common interest, direct and indirect benefits of the national and international programs, ecological and social risk.

The contemporary space systems and their practical application have international and to some extent global character. As a consequence of this the space program expenses could turn out to be extremely high compared to the benefits for a separate country and fully economically justified for a group of countries. In this sense it is necessary to find out an estimation approach for the economic efficiency of space activity. Particular attention must be paid to the questions of international investigation cooperation and especially the question of space exploration.

The nature of space activities, the scale of their public significance and the specific nature of economic profitability lead to crucial steps

undertaken for reorientation of the national programs in order to gain efficiency growth by participating in international space programs.

The statistical data, characterizing the development of the world astronautics during the last decades, enable us to pay attention to economic indicators closely referred to profitability.

The document analysis made by international organizations and the work of experts from different countries over the economic problems of astronautics give a possibility to form three groups of criteria with stimulating effect on aeronautics concerning the choice of the most effective ways and resources for a definite country regarding the transfer of space achievements in the scope of economics.

The first group of criteria has approximately general character. The funds provided for space programs are compared with the total economic utility, including financial, political, military, prestigous logical benefits, which are evaluated in actual financial values. For example, according to the reports of the Middle West Institute in USA, the positive effect on the american economy of the project "Apolon" is 1:7, i.e. 25 billion dollars investments made and total benefits of 175 billion dollars. On this principle is based the assessment of the economic activity of the investments in aeronautics which principle has been presented by the american congressman D. Fuke in 1982 and it says that every dollar invested in a space program returns new 14 dollars.

The second group includes concrete and universal criteria according to the possibilities of their usage for project assessment in separate countries and international organizations. These criteria are distributed in space systems to resolve practical tasks (connected with meteorology, navigation, remote study of natural resources, environment protection, etc.) and are defined by the principal of comparing the expenses for development, production and exploitation of space systems to the relevant expenses of "not space systems", performing similar functions. This group includes assessment of the benefits for economics, households and the population from definite regions as a result of the space systems exploitation.

The third group of criteria for the economic efficiency and profitability of aeronautics is not directly connected with the space systems development and exploitation. But it includes very important heterogeneous indicators, stimulating the effect of space activities over scientific and technical progress. These criteria describe the scale and profitability of the choice and application of space programs innovations in other economic branches and in the field of services.

The statistics shows that the expenses for space programs are considerable in different countries. The reinstatement of the resources used is economically justified task and a motive for a larger extension of the efforts and directions for utilization of aeronautics achievements in economical branches on the Earth.

Fig.1, 2 Expenses for space researches

Expenses for space researches
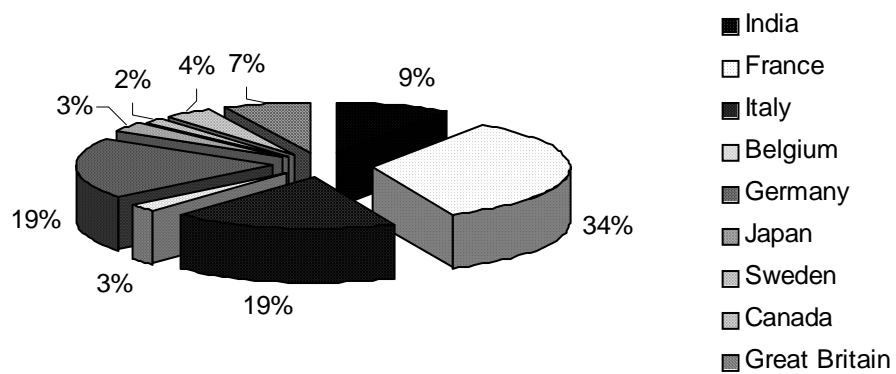
Expenses for space researches
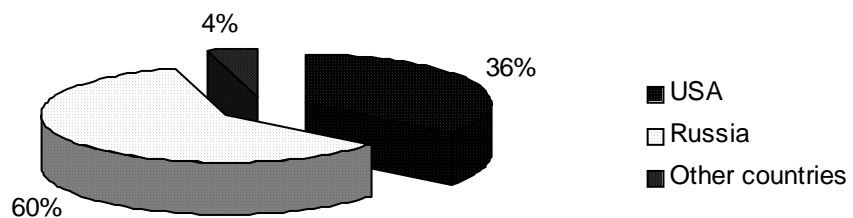
Space forecast

The different space researches and the real utilization of the Universe in all countries are accomplished in accordance with short- and long-term programs. These programs cover planned activities in details for the near future, forecasts of results expected and necessary resources. Space prognoses for the coming years worldwide are as follows:

2005-2020 – international system of new generation for intercommunications and telecommunications;

- foresight of elemental calamities;

2010-2015 – semi-industrial production of unique materials in Space;

2010-2025 г. – release of dangerous industrial wastes in space;

2015-2035 – pilot operated stations on the Moon, as well as a possible stage for preparation of pilot operated expedition to Mars;

2015-2040 – pilot operated expeditions to Mars and other planets;

2015-2040– release of radioactive wastes from nuclear power engineering at special places in the Space (initially with volume of 800 tones per year and later in complete volume of over 1200 tones per year);

2005-2025 – utilization of 200 kilowatt and 1 megawatt power in space solar energetics

2020-2050 г. – system for global military security.

National Aeronautics and Space Administration

The National Aeronautics and Space Administration (NASA) conducts research in four areas: 1) Space Science inquires into the origins, evolution, and nature of life and our universe; 2) Earth Science seeks to understand the forces affecting our planet's environment; 3) Biological and Physical Research uses the space environment to gain insight into how the laws of nature work; and 4) Aeronautics Technology develops new technologies to improve the nation's air transportation system.

NASA is a science and technology agency pursuing research in fields as diverse as astronomy and astrophysics, global climate change, human physiology, and aeronautical engineering. Because the agency conducts so many types of research, it must prioritize its resources to accomplish its most important research goals.

NASA's New Mission
- To understand and protect our home planet
- To explore the universe and search for life
- To inspire the next generation of explorers

Table 1 National Aeronautics and Space Administration
(In millions of dollars)

Spending	2002 Actual	Estimate	
		2003	2004
Discretionary Budget Authority:			
Science, Aeronautics and Exploration (non-add)	*(6,542)*	*(6,975)*	*(7,661)*
Space Science	2,902	3,414	4,007
Earth Science	1,592	1,628	1,552
Biological and Physical Research	824	842	973
Aeronautics	997	947	959
Education Programs	227	144	170
Space Flight Capabilities (non-add)	*(8,326)*	*(8,000)*	*(7,782)*
Space Flight	6,773	6,131	6,110
Crosscutting Technology	1,553	1,869	1,672
Inspector General	24	25	26
Total, Discretionary budget authority	14,892	15,000	15,469

Reference

1. http://www.nasa.gov/missions/highlights/index.html
2. http://spacelink.nasa.gov/NASA.Projects/.index.html
3. http://www.atmosp.physics.utoronto.ca/people/ben/pages/mission_costs_and_reliability.htm
4. http://www.whitehouse.gov/news/usbudget/budget-fy2004/nasa.html
5. Todor Tagarev, ed., *Transparency in Defence Policy, Military Budgeting and Procurement* (Sofia: George C. Marshall – Bulgaria and Geneva Centre for the Democratic Control of Forces, 2002). – 200 pp.
6. Amiling, D. F., *Investments. Analysis and Management.* Prentice Hall, 1989

ANALYSIS OF REMOTE SENSING METHODS FOR FOREST ECOMONITORING IN DIFFERENT SEASONS

Rumen Nedkov, Albena Pavlova

Space Research Institute – BAS

Abstract
Contemporary space technologies enable wide application of remote sensing methods for impartial investigation and control of environment conditions. An important point especially is a research of processes dynamic in ecosystems in local, regional and global scale.
Various aerospace methods allow data receiving in different temporal modes. These data are information source for the actual state of the investigated object in different seasons. Annual information is important in the case of complex monitoring with main aim to study phenological variations of particular land cover type. This assumes exploitation of different methods and aerospace data for one and the same time period (climatic season). Unseasonable factors, which give influence over individual elements of ecosystems, suppose casual character upon their progress for short time period. All this requires a profound analysis of the advantages and disadvantages of different remote and aerospace methods, which must be utilize for an optimal eco-monitoring in various climatic seasons.
In the proposed paper is made comparative analysis of aerospace methods and used data enclosed to monitoring of forest vegetation.

Key wards: remote sensing methods, eco-monitoring, temporal diapason

1. Seasonal Changes in vegetation associated to the pigment alteration and water content in respect of radiant energy

Seasonal changes in the forest occur naturally and are usually easily detected. Seasonal changes in vegetation are a consequence from the rotation of the earth around the sun and its own axis. The earth is slightly tilted at approximately 23.5°. This tilt is what's responsible for the temperature variation and change of length of days from season to season in temperate regions. It is hot in the summer time because the rays of the sun are more direct and summer days are long because more time is spent in sunlight due to the tilt of the earth. On the other hand, winter days are short and cold because the rays are less direct and there is less sunlight each day. These seasonal changes affect every organism living on earth.

1.1. Climatic conditions

Plants are of interest when studying seasonal changes because most leaves change color and fall off the trees. The primary factor in this spectacular phenomenon is termed "photoperiod" or in other words, the amount of sunlight a specific region receives over the course of the year. Some areas receive a sufficient amount of sunlight all year and some do not receive enough sunlight in the winter. It is essential for the food making process that occurs in plants known as "photosynthesis" The leaves have pigments in them that absorb light. The main one is chlorophyll which is responsible for the green color in leaves because it absorbs the blue and red light waves and reflects green wavelengths. When the fall season arrives, the amount of sunlight and temperature both decrease. This causes the chlorophyll absorption of light to become low. Approximately two weeks before the leaves undergo a change in color, a hardened cell layer forms at the bottom of the leaf due to the lack of photosynthesis. This hardened layer blocks off important nutrients such as magnesium and phosphorus and moisture from flowing to the leaf. This process inhibits the production of chlorophyll. The remaining chlorophyll starts to break down as the nutrients are absorbed into the trunk and roots. When enough chlorophyll has broken down, the green color starts to disappear and the yellow color starts to emerge. The yellow color is actually present year round but is never showed due to the high amounts of chlorophyll. The yellow color of the leaf is actually due to a pigment known as carotenoid. The red color that appears in leaves is due to the sugars becoming trapped in the leaves. The red color becomes more resonant when there is an increase in sunny days but cool nights. The pigments are known as anthocyanins which protect the leaves from frost. Photosynthesis is not the only factor in plants affected by a change in season; water content of woody tissues of trees also undergoes seasonal fluctuations. The wood of young trees undergoes an annual cycle of water content, varying from 100% of dry weight in the carry spring to as little as 60% in the late summer. The temperate coniferous forests receive most of their precipitation during the fall, winter, and spring, and are subject to summer drought. Seasonal drought usually lasts between July and October. In particularly dry summers, carbon is often allocated for deep root growth. Roots involved principally in water uptake are not active in the surface layers, but occur only in the deeper soil layers where moisture is persistent during summer periods. So when precipitation is infrequent in the summer, the lack of an active upper root layer prevents significant water uptake from that upper soil layer. Deciduous trees usually dominate temperate forests, where the growing season is moist and at least 4 months

long. These forests generally receive more winter precipitation than temperate grasslands. Winters in deciduous forests last from 3 to 4 months, and although snowfall may be heavy, winters in these forests are relatively mild.

1.2. Anthropogenic influence

The seasonal changes describe above are typical for climatic factors and processes.

The vegetation is quite sensitive to anthropogenic impacts. Anthropogenic changes are likely to alter growth patterns of plant species which will result in changed patterns of forest succession. Forest fires made by human carelessness, indiscriminate slaughter, pollution from tourism, and effects on water supply are the some of the anthropogenic influence, which can alter the forest structure and canopy. Forest damages are concerned with variables as defoliation, discoloration, growth reduction.

Human impact on the forest results in change of chlorophyll content, photosynthetic activity and leaves structure, which can reduce the time of natural changes in forest canopy. That's why the study of forest phenology and forest parameters, which are related to forest canopy are of great importance in assessing seasonal changes.

1.3. Parameters in forest cover

The physiological activity of a forest stand is influenced by the vitality and health status of the trees. Most forest parameters are related to each other. A large group of parameters is connected to tree size and canopy structure (age, stem volume, crown cover, forest density, tree height, biomass), and another group of parameters is related to the chemical composition of trees and leaves/needles (chlorophyll concentration, water content, pigment concentrations, health condition, defoliation, mineral content, chemical stress). Also soil type, climatic conditions and landscape structure are related to the forest type and forest parameters. In most cases remote sensing instruments do not measure the desired forest parameter directly and parameter retrieval algorithms rely on adequate correlation between the measurable physical properties and the desired forest parameter. The relations between parameters are mostly specific to local species.
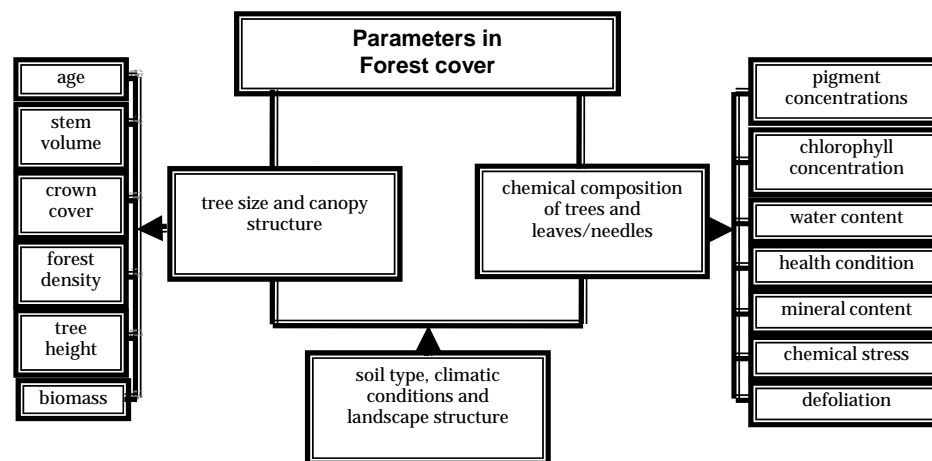
Fig.1 Parameters in forest cover

The forest parameters are can be divided into two main types: categorical variables and continuous variables. Categorical variables can be obtained through a classification process, in which each pixel is attributed to one of a set of categories or classes. Estimators of continuous parameters are established by identifying a function that describes the relationship between the observed pixel values and the desired forest parameter.

Parameter estimation and classification can be performed directly on the observed data, but in many cases it is advantageous to compute certain features from the original image data, and then effectuate the parameter estimation on the feature vectors. The features may e.g. describe the texture of a set of neighboring pixels. Finding an estimator of a continuous forest parameter typically consists of establishing a relationship between the image data and measurements of this forest parameter. This may include physical models or statistical models. Statistical modeling relies on estimation of the relationship between the image data and the parameter using a combination of training data and prior knowledge regarding the type of relationship. The prior knowledge mentioned here is generally based on knowledge about physical processes. A frequently used class of methods is regression analysis. There is a large family of well-established models for multivariate data in the class of generalized linear models in literature.

Land cover change forms a complex and interactive system at different spatial and temporal scales.

2. Analysis of aerospace methods for monitoring of forest vegetation.

Remote sensing is a way to obtain information on forest biomass and stand conditions over large areas in a timely and cost-effective manner. Remote sensing utilizes aerial photographs, satellite images, laser altimetry, and radar.

Visible and infrared sensors just measure the amount of sunlight reflected off of a surface. They use the optical properties of the components of the forest canopy, which are important to the understanding of how plants interact with their environment and how this information may be used to determine vegetation characteristics by means of remote sensing. Unlike solar illumination which, coming from a distant source, sends its signal as continuous parallel rays of light (photons) onto a sensed surface, radar sends a discontinuous (intermittent) series of photon pulses from a point source that then spreads out as an angular beam. Laser altimetry, or lidar (light detection and ranging), is an alternative remote sensing technology that promises to both increase the accuracy of biophysical measurements and extend spatial analysis into the third (z) dimension. Lasers for terrestrial applications generally have wavelengths in the range of 900–1064 nanometers, where vegetation reflectance is high. Lidar sensors directly measure the three-dimensional distribution of plant canopies as well as subcanopy topography, thus providing high-resolution topographic maps and highly accurate estimates of vegetation height, cover, and canopy structure. In addition, lidar has been shown to accurately estimate LAI and aboveground biomass even in those high-biomass ecosystems where passive optical and active radar sensors typically fail to do so [1].

Table 1 Tasks for forest monitoring and the demands for Remote Sensing systems

Main goals	Season and period for observations	Effective time for image processing	Spatial resolution, m	Scale of the output maps	Spectral resolution
Investigation of forest damages from pests and diseases	summer one month	5 days	1-2 5-10	1:10000- 1:5000	0,470; 0,555; 0,659; 865; 1,240; 1,640 2,130 μm (0,5-0,6; 0,6-0,7; 0,8-0,9 μm)
forest damages on account of natural factors (winds, land slides)	summer-autumn two month	10 days	5-10 (20-30)	1:10 000 1:25 000	0,5-0,6; 0,6-0,7; 0,8-0,9 μm
technogenic	spring	1 month	20-30	1:25000	0,470; 0,555; 0,659;

contamination in forest	**summer autumn single image**				**0,865; 1,240; 1,640 and 2,130 μm**
rehabilitation of coppices and burnt forest	**Summer single image**	**1 month**	**1-2 (5-10) 20-30**	**1:10000-1:25000**	**0,5-0,6; 0,6-0,7; 0,8-0,9 μm**
Assessment of the forest phonological condition	**spring autumn**	**1 day**	**150-1000**	**1: 200000**	**0,5-0,6; 0,6-0,7; 0,8-0,9 μm**
Assessment of forest eco-diversity	**Summer single image**	**1 month**	**10-20**	**1: 25000**	**0,5-0,6; 0,6-0,7; 0,7-0,8; 0,8-0,9 μm**
Assessment of the forest phytomass	**Summer single image**	**1 month**	**20-30 (1-5)**	**1: 25000**	**0,5-0,6; 0,6-0,7; 0,7-0,8; 0,8-0,9 μm radar X, S, L range**
effect from forest fire, anthropogenic activity and the processes connected with the carbon accumulation	**Summer single image**	**1 month**	**20-30 (1-5)**	**1: 25000**	**0,5-0,6; 0,6-0,7; 0,7-0,8; 0,8-0,9 μm radar X, S, L range**
Definition the degree of wetness of burning materials	**Spring summer autumn 12-24 hour**	**1 hour**	**5-10**	**1: 5000 1: 10000**	**0,7-1,2; 1,5-2,5; 3-5; 8-14 μm radiometer 0,8-3; 10-50 cm**
Large scale thematic mapping of forest	**Summer single image**	**1 month**	**10-20**	**1:50000**	**0,5-0,6; 0,6-0,7; 0,8-0,9 μm**

Conclusion

The possibility of remote sensing of objects on the earth's surface by space methods is based on objective, existing relations between the characteristics (parameters) of the environment and the radiation (reflected and natural) field of the earth's surfaces. Some parameters are directly measurable. Optical and infrared multichannel instruments will react to the forest structure and spectral properties (determined by chemical composition) of trees and leaves (health condition, content of chlorophyll). All optical methods, including aerial photography and satellite imagery, are essentially observations of leaf area development because that is the forest component that most strongly reflects or absorbs visible and near-infrared radiation. Laser altimeters, scanning lidars and ranging scatterometers

(radars) measure the tree height directly. Also the crown cover extent can be measured in most cases with these instruments. The backscattering coefficient measured by SAR instruments depends on ground and canopy water content and distribution. At the P-band a major contribution to the backscattering coefficient comes from the double reflection from tree trunks, which contain water. Therefore, a P-band SAR will provide information on the forest density and stem volume. At L- and C-band branch- and leaf-related reflection and scattering become more pronounced. Laser and radar methods are able to give much more detailed images, but are generally more expensive and aren't as extensive yet.

References

1.   Michael A. Lefsky Warren B. Cohen, and co., Lidar Remote Sensing for Ecosystem Studies, *BioScience:* Vol. 52, No. 1, pp. 19–30
2.   http://www-eosdis.ornl.gov/SNF/guides/leaf_optical_tms.html
3.   Сухих В. И., Функциональная структура космического сегмента мониторинга лесов Росси, Изследование земли из Космоса, 2001, №3, с. 61-67
4.   Лукашевич Е.Л., Карпухина О.А., и др. Информационное обеспечение решения задач экологического мониторинга космеческой видеоинформацией – соществувющие и потенциальные возможности, Госцентър „Природа"

GROUND CONTROL EXPERIMENT TO STUDY THE IMPACT OF MICROGRAVITY-SPECIFIC WATER AND OXYGEN DISTRIBUTION IN SUBSTRATE MEDIUM ON PLANTS[*]

Iliana Ilieva, Plamen Kostov, Tania Ivanova, Svetlana Sapunova

Space Research Institute - Bulgarian Academy of Sciences,

Abstract
The plant growth experiments conducted in space in the recent 10 years showed that microgravity-specific environmental factors may alter plant growth. Microgravity changes the behavior of fluids and gases and the constructed plant growth facilities often utilized technical constraints than plant physiological requirements. The combination of these factors led to plant stress and poor growth.
A ground control experiment studding the impact of altered water and oxygen distribution in substrate medium is presented in this article. Plant root and shoot responses and adaptations to low oxygen content into the root zone are described.

INTRODUCTION

Plant root system physiology is dependent upon water, nutrients and oxygen availability. A great deal of research has been directed towards the development of plant nutrient delivery systems for spaceflight application that utilize the requirements for appropriate water and nutrients delivery, but little attention has been paid to the oxygen content in the root zone during the design process. The lack of nutrients and water delay plant growth and development, but the lack of oxygen might affect the overall biochemical and physiological status of the plant.

Oxygen content in the root zone depends on the size of the substrate particles. As the size of the particles decreases substrates can hold more water by capillary forces and thus the volume of air per bulk volume decreases. The diffusion of gases in water is 10 000 fold less than in free air. The displacement of air by water may further increase because water does not drain in microgravity. [1]

The above-mentioned characteristics of water and oxygen distribution in substrate medium and the difficulties to maintain both adequate water content for liquid flux and adequate air-filled porosity for gas flux lead to a

---

lower level of oxygen in the root medium in microgravity than on earth. Plants grown in different space plant growth facilities showed signs of oxygen depletion stress [2,3].

The objective of this experiment was to study on earth plant physiological responses during growth in saturated substrate medium – process that occurs in microgravity and to qualify plant stress by nondestructive methods - measurement of plant heights and leaf color image processing.

MATERIALS AND METHODS
Hardware
The experiment was conducted in the laboratory prototype of the flown on the MIR Orbital Station SVET Space Greenhouse (SVET SG). SVET SG consists of Plant Growth Chamber (PGC) of an open type that contains Light Unit (LU) and mounted like a drawer Root Module (RM). The LU provides 400 $\mu mol.m^{-2}.s^{-1}$ PAR at the top of the canopy. The RM has 0,1 m^2 growing area and is divided into two 5,2 L Vegetation Vessels (VV1,2) each with two flowerbeds. Both VVs have independent moisture control maintained by a moisture sensor placed at 3 cm depth below the surface. The two VVs were filled with 1,0-1,5 mm particle sized substrate Balkanine.

Plant culture and cultivation procedures
Pea (*Pisum sativum L.* cv "Ran-1") was cultivated for 56 days. Plants were sown at 2,5 cm depth. Initially, all plants were grown at one and the same conditions - 16/8 hours light/dark period, substrate moisture 1/3 from saturation, air temperature varying between 23-25°C and upward air flow (from the laboratory through the PGC and out of it) at 0,2 m/s speed. On the 17th day of plant development, i.e. during the active vegetative plant growth – water-logging stress was applied in VV1 (test) by rising the moisture threshold for 1 week and slowly submerging the substrate. At the same time, the Light Period (LP) was daily increased with 1-hour step to 23 hour light / 1 hour dark in order to eliminate plants stress compensation mechanism during the dark period. Plants in VV2 (controls) continued to grow at the same substrate moisture as before and the new LP as for VV1. During the stress treatment the air temperature varies between 16-23°C for the test and control plants.

Plant responses to the maintained substrate moisture in both VVs were detected by measuring plant height and leaf color image processing obtained

from a photo camera. Plant heights were measured on the 4, 7, 10, 13, 17, 21, 25, 29, 56 day of development and photo images were made during this period.

RESULTS AND DISCUSSION

Seeds started to germinate 4 days after planting. Plants developed normally for 11 days when yellow-brown-red spots were noticed on the lower leaves. The affected leaves than withered and dropped. As "Fig. 1" shows the air temperature in the laboratory was higher than the required optimum for pea growth at the beginning of the experiment. The interaction between high air temperatures, low relative air humidity and dry air with 0,2 m/s speed in the PGC was the main reason for the observed phenomenon.
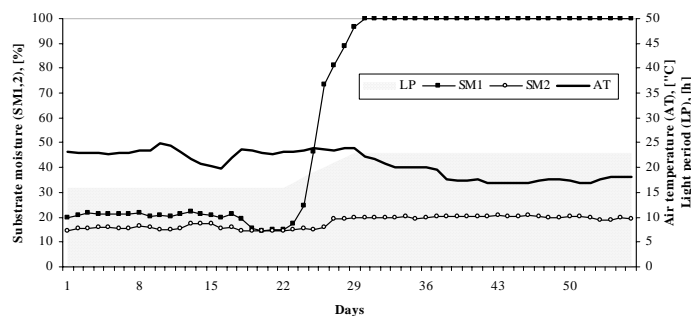
Fig. 1. Environmental parameters maintained in SVET SG

During the water-logging stress test plants showed typical responses to oxygen depletion stress. Plants stopped to develop in height "Table 1" and chlorosis was observed on the 10th day after treatment. A few new leaves developed but they were small and stunted. The leaf wither and sencense continued during the treatment and plants died before reaching maturity.

Extra elongation of the vegetative growth and delay in the reproductive phase was observed in the control plants. Flowers were obtained on the 39-day of plant development and fruits on the 41-day, and the plant yield was low. Two reasons might contribute for these results – 1) plants lost 2/3 of their leaves before reaching reproductive phase due to unexpected leaf sencense. 2) Post-experimental analysis of the RM reviled that due to insufficient water conductive properties of substrate Balkanine a water-logging zone had also formed in VV2 at nearly one half of the substrate volume. For this reason root systems of the control plants were situated in layer of 4,5 cm in depth. The analysis of the root systems reviled well-

developed main and secondary roots. The root systems of the test plants were shallow without main root and with many secondary roots growing upwards in the substrate and out of it.

Table 1. Plant heights measured during the experiment

Days after emergence	Cultivation period	Height in VV1		Heights in VV2	
		Line 1	Line 2	Line 1	Line 2
4	Shoot emergence and initial development	1,2	0,8	0,9	1,0
7		2,8	2,2	2,3	2,7
10	Active vegetative growth	4,8	5,2	4,8	5,7
13		8,3	8,0	8,2	9,2
17	Start of step-by-step moisture increase in VV1	12,3	12,7	13,7	14,5
21		16,2	17,2	18,8	20,2
25	Start of water-logging stress in VV1	20,7	22,7	26,7	27,6
29	Water-logging stress in VV1	25,2	26,3	29,2	29,3
56	End of water-logging stress in VV1	28,8	29,8	50,5	49,9

During the water-logging stress air temperature in the laboratory started slowly to decrease reaching 16-18°C "Fig.1". New shoot growth from the dead stems of the test plants was observed on the 39th day of plant development. Low temperature stimulated reproductive development of the control plants and only in a few days flowering and fruiting phase was reached. The decrease of temperature showed to be an anti-stress factor and could decrease the impact of water-logging stress.

REFERENCES
1. B i n g h a m, G.E., S.B. J o n e s, I.G. P o d o l s k y, B.S. Y e n d l e r, Porous substrate water relations observed during the Greenhouse-2 flight experiment, SAE Technical Paper Series, 961547, 1996, 1-11.
2. P o r t e r f i e l d, D.M., D.J. B a r t a, D.W. M i n g, R.C. M o r r o w, M.E. M u s g r a v e, ASTROCULTURE[TM] root metabolism and cytochemical analysis, Advances in Space Research, 26, 2000, 315-318.
3. S t o u t, S. C., D. M. P o r t e r f i e l d, L. G. B r i a r t y, A. K u a n g, M.E. M u s g r a v e, Evidence of root zone hypoxia in *Brassica rapa l.* grown in microgravity, International Journal of Plant Science, 162, 2001, 249-255.

VOLT-AMPERE CHARACTERISTICS OF A CYLINDRICAL PROBE IN THE IONOSPHERE PLASMA IRREGULARITIES REGIONS*

G.L.Gdalevich(1), N.Bankov(2), St.Chapkunov(2), L.Todorieva(2), R.Shkevov(2)

(1) – IKI RAN, (2) – IKI BAN

Abstract

Cylindrical Langmuir probes are widely used for measurements of ionosphere plasma density and temperature. But a great deal of experimental data for such probe measurements fulfilled abroad "ICBulgaria-1300" satellite showed that Langmuir probe Volt-Ampere (V-A) characteristics with extraordinary forms were frequently observed. In this report it is shown that thanks to uneven distributions of plasma parameters inside irregularities, the Langmuir probe's V-A characteristics whose execution time period happened to be close to those time intervals which were necessary for the satellite to pass through such irregularities, are subjected to some characteristic distortions. Also possible ways to originate these irregular structures will be discussed and it will be shown that sources for these structures can be situated in the magnetosphere or in the ionosphere.

Introduction:

The cylindrical Langmuir probes have been widely employed on rockets and satellites because of there manufacturing simplicity and possibility to measure electron density and temperature when magnetic field exists. The theory of moving cylindrical probe have been developed by taking into account the influence of the metal, used to cover the probe's surface, the influence of the end effects, as well as the influence of the magnetic field over the results. The conclusion is that the material for probe's manufacturing influences negligibly the accuracy of the measurements. The existence of the end effect and magnetic field, sometimes, under certain conditions, leads to situation that V-A characteristics of the cylindrical probe behave close to those of the spherical probe with the same diameter [1-9]. There is no complete theory about the behavior of the probe in a magnetic field, but the experimental

data show that, when the cylindrical probe radius is considerably bigger then the electron giroradius, the magnetic field doesn't affect the measurements of the electron density and temperature. Up to now in scientific publications V-A characteristics of an unusual type were not shown. In this work unusual V-A characteristics will be considered, there appearance and the connection with the plasma irregularities will be discussed.

Measurements results:

Measurements are discussed that took place on board of the satellite "Intercosmos-Bulgaria-1300", launched on 07.08.1981. The data from cylindrical Langmuir probe, which collector is a metal cylinder, manufactured from stainless steel with a length of 11.5cm and diameter of 1mm, are used. The collector's sweep voltage period is 1 sec. The results from a three-electrode ion spherical probe with a floating potential on the outer cover are used to determine the density of the positive ions. Data from the electric field measurements, analyzer of low energy protons and electrons and three-component magnetometer are used.

On fig.1a the satellite orbit at 21.11.1981 in geographic coordinates and in invariant length-local time coordinates is shown. It could be seen that the satellite flew through subauroral and auroral regions, and entered the polar cup in the morning-night time as well. On fig.1b results of the electric and magnetic field measurements are presented. It could be noted that the Z component of the magnetic field has the largest value. On fig.2 some V-A characteristics of the cylindrical probe are shown. It is seen, that in the electron retardation region, where potentials applied to the probe are negative relative to the plasma, the characteristics have the usual form for such probe. In the electron saturation region (positive probe potentials relative the plasma) the characteristics have unusual form that the authors haven't seen in the literature yet. On fig.3 a values for ion density, measured by three-electrode ion probe, and electron currents with energy 1keV are shown. At that time, the satellite cross the auroral region, between the auroral and polar picks of ionization. On the plot of the ion density some large and comparatively small irregularities, with periods about 0.5-1 sec., could be seen.

Results discussions:

In the general case, the theory about the behavior of the probes when magnetic field exists, is not developed. However, in the plasma of the gaseous discharge with values of the magnetic field, such that the cyclotron radius of the electron is smaller then usual probe dimensions and smaller then the Debye radius, following the proposal of Bom, the ion part of the probe characteristic is used. The following considerations are taken into account. If the cyclotron radius of the electron is larger then the Debye radius, the particles movements in the coaxial sheath of charged particles surrounding the probe, can be considered as if the magnetic field is absent. It is supposed, that in the presence of magnetic field, the cyclotron radius should be considered rather then the path length of the free particles.

The works of Spivak and Reixrudel show that for a cylindrical probe, which radius is considerably smaller then the electron's cyclotron radius, the magnetic field doesn't affects the measurements of the electron temperature and density [4].

Smith mentions in Technical Manuel of COSPAR that the magnetic field doesn't influence the measurements of the electron temperature, if the electrons cyclotron radius is larger then the probe radius and Debye radius [2]. In this case the magnitude of the probe electron current decreases. Dote and Amemiya have established that, if the axis of the cylindrical probe are parallel to the magnetic field lines, on the retarding region of the electrons the volt-ampere characteristic remains exponential when applied voltage values are close to the values of the plasma potential [3].

As was mentioned above, in the results description, we assume that in the electron retarding region the characteristic remains exponential for voltages, applied to the collector, corresponding to the plasma potential relatively the satellite airframe.

The distortion of the V-A characteristic begins in the regions where the voltages correspond to the electrons saturation. In this region begins the influence of the plasma irregularities, if the part of the period of the linear change of voltage, applied to the probe (and corresponding to the electron acceleration), is near the time interval during which the satellite pass through the irregularities. Note that, in the region of small density values, Debye radius

is near the cyclotron radius and the magnetic field begins to influence the form of the probe characteristic.

More over the satellite flows through a region of magnetic field lines, for which the main component of the magnetic field is almost vertical. So it is possible that the electric field, created by the probe, penetrates the sheath surrounding the probe, thus creating drift of the plasma in the crossed E,B field:

$$Vd \approx \frac{E}{B}$$

In this way the distortions of the V-A characteristics could be observed for small densities in the regions of inhomogeneous structures of the ionosphere and in the regions, where the main component of the magnetic field is almost vertical.

Here some remarks about the origin of the inhomogeneous plasma structures should be made. Their appearance in the aurora region should be connected, before all, with the precipitation of flows of electrons, whose energy excesses the ionization potential of the ionosphere. Consequently, in ionization regions the plasma is electrically unstable. That can be the reason for the occurrence of the irregularities.

Conclusion:

Small electron density values $\approx 10^3 cm^3$ in the inhomogeneous plasma leads to comparable Debye radius and cyclotron one. That is the reason of the penetration of the probe electric field beyond the sheath surrounding the probe. At the same time the main component of the magnetic field is vertical. This generates a drift movement of the electrons and the ions in the plasma, so the electrons don't reach the probe surface. These effects explain the unusual form of the volt-ampere characteristic of the cylindrical probe.

References
1.   W.R. Hoegy, L.F.Wharton , Current to making cylindrical electrostatic probe, J. Appl. Phys., v. 44, n 12, pp 5365 – 5576, 1973
2.   L.J. Smith, Technical Manuel on Electron Density and Temperature Measurements in Ionosphere in Cospar Information Bulletin, n 17, 1964, pp 37-65
3.   T. Dote, H. Amemiya, Negative Characteristic of a Cylindrical Probe in a Magnetic Field, J. Phys. Sc., Japan, v. 19, n. 8, pp 1915-1924, 1964

4. G.V. Spivak, E.M. Reixrudel, To the common theory on the probe, placed in a gaseous discharge, JETF, v. 6, vyp. 8, pp 816-844, 1938

5. L.H. Brace, G.R. Carignan, J.A. Fidlay, Experimental Evolution of Ionosphere Electron Temperature Measurement by Cylindrical Electrostatic Probes, Space Research XI, pp 1072-1115, Akademic Verlag, Berlin, 1971

6. Chen, F.F., Plasma Diagnostic Technical (edited by R.H.Huddleston and S.L.Leonard) Akademic Verlag, New Jork, 1965

7. G.L.Gdalevich, Methodic Probes of Measurements Ionosphere, Сборник Ионосферных исследований, МГГ, М, Наука, №18, с. 95, 1969

8. D.Johanning, W.Seifert, A.Best , Analitical density correction for cylindrical Langmuir probes showing end effects, Plasma Physics and Controlled Fusion, Vol. 27, No 2, pp 159-179, 1985.

9. G.L.Gdalevich, N.I. Izhovkina, V.D.Ozerov, Sources of Plasma Through in Midlattitude and Subauroral Topside Ionosphere, Cosmic Research, v. 41, n 3, pp 230-234, 2003

10. Arshinkov S.I., Bochev A.B., Abadzhiev N.S., Shkolnikova S.I., First results of magnetic field measurements on board Intercosmos-Bulgaria-1300 satellite, Kosmi. Issled., in Russian, 1983, v. 21, N 5, pp 710-717

11. Stanev G., Petrunova M., Teodosiev D., Kutiev I., Serafimov K., Chapkynov s., Chmyrev V., Isaev N., Puschaev P., Pimenov I., Belichenko S., An instrument for DC electric field measurements aboard Intercosmos-Bulgaria-1300 satellite, Adv. Space Res., 1983, v. 2 N 1, pp 43-47

12. Ivanov I., T.Dachev, Y. Matviichuk, D. Kresheva, M. Telzov, Energetic particle spectrometr with adaptive recording system, presented at XXIV COSPAR Meeting, Comm. On Space Programms and Res., Ottawa, Canada, May 16 to June 2, 1982
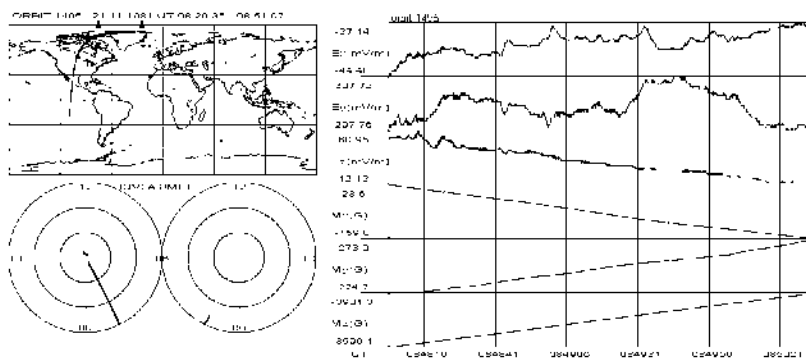
Fig.1
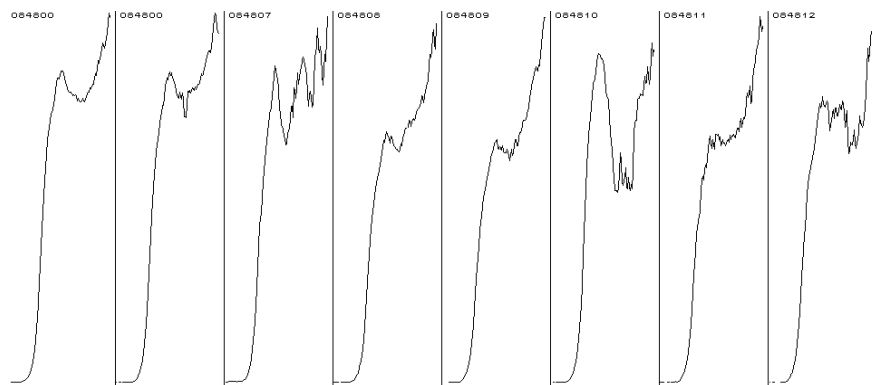
Fig.2
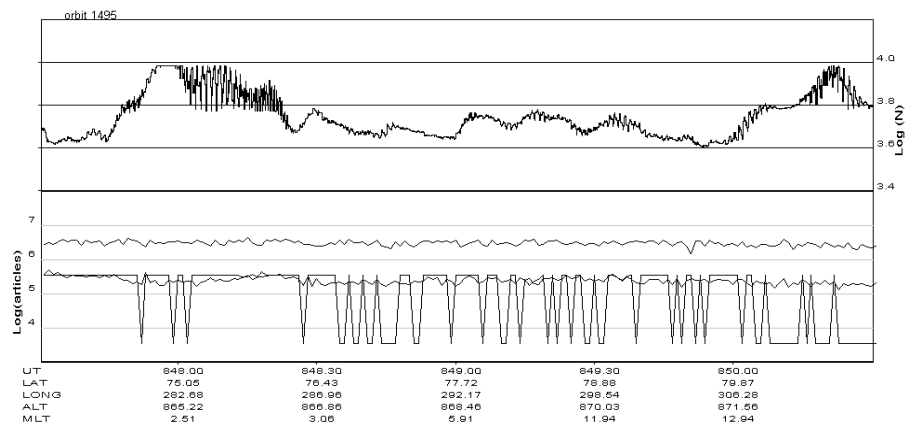
Fig.3

CROP SPECTRAL REFLECTANCE WITH REFERENCE TO GROWING CONDITIONS

Rumiana Kancheva,   Denitsa Borisova
Solar-Terrestrial Influences Lab.-BAS E-mail: rumik@abv.bg, dsbn@abv.bg

Abstract

Ecological problems relevant to anthropogenic impacts on the environment, and first of all on the biosphere, are of global importance and draw the attention of various scientists. They impose the necessity of efficient means for assessing the effects of anthropogenic factors on vegetation land covers, for instance. In agriculture the possibility for early phytodiagnostics and timely identification of abnormal crop state is of particular importance. Remote sensing techniques have proved abilities in this respect. The goal of the paper is to illustrate the implementation of spectral reflectance data for crop monitoring during plant growth. Vegetation reflectance spectra are used as an informational feature about crop development under different conditions which are represented here by nitrogen fertilization and heavy metal contamination.

The anthropogenic impact on the environment, and first of all on the biosphere, impose the necessity of efficient means for vegetation monitoring. In agriculture, for instance, crop state assessment and detection of stress situations is of particular importance. This paper shows the potential of crop spectral reflectance as an informational feature about plant growing conditions.

The different radiation behaviour of land covers lies at the root of spectrometric studies. The visible and near infrared (0.4 - 0.9 μm) measurements have proved abilities for crop monitoring [1,2]. The reason is that this wavelength range reveals significant sensitivity to plant biophysical properties. The information is carried by the specific distribution of the reflected radiation which depends on such plant parameters as biomass amount, leaf area, vegetation cover ratio, chlorophyll content, etc. They are growth parameters associated with crop phenological and physiological development and closely related to the growing conditions.

Some results are presented here from experiments with spring barley and peas treatments grown under different nutrient and contamination conditions. Ground-based reflectance measurements have been performed with multichannel radiometers [3-5] and regression analyses of the

experimental spectrometric and biometric data have been carried out. The spectral variables used in the regression models are combinations of the measured reflectance factors at wavelengths in the green (G=0.55 μm), red (R=0.67 μm) and near infrared (NIR=0.8 μm) bands.

In Fig.1 the established statistical relationships between barley spectral index R/(G+R+NIR) at ear-forming stage, plots canopy cover (vegetation relative portion) and nickel pollution of the soil are shown.

Another example of the effect of the growing conditions on plant bioparameters and thus on crop reflectance properties is Fig.2 where peas spectral index (NIR-R)/(NIR+R) is shown as a function of the vegetation biomass (a) and the Cd contamination (b). Fig.2c presents the heavy metal induced stress on biomass production. The biomass values are given as percentage out of the control (unpolluted) treatment. Good correspondence is observed between the measured values and the spectral model estimates of the biometrical feature and the stress factor (Fig.2d, Fig.2e and Fig.2f).

a)

b)

c)
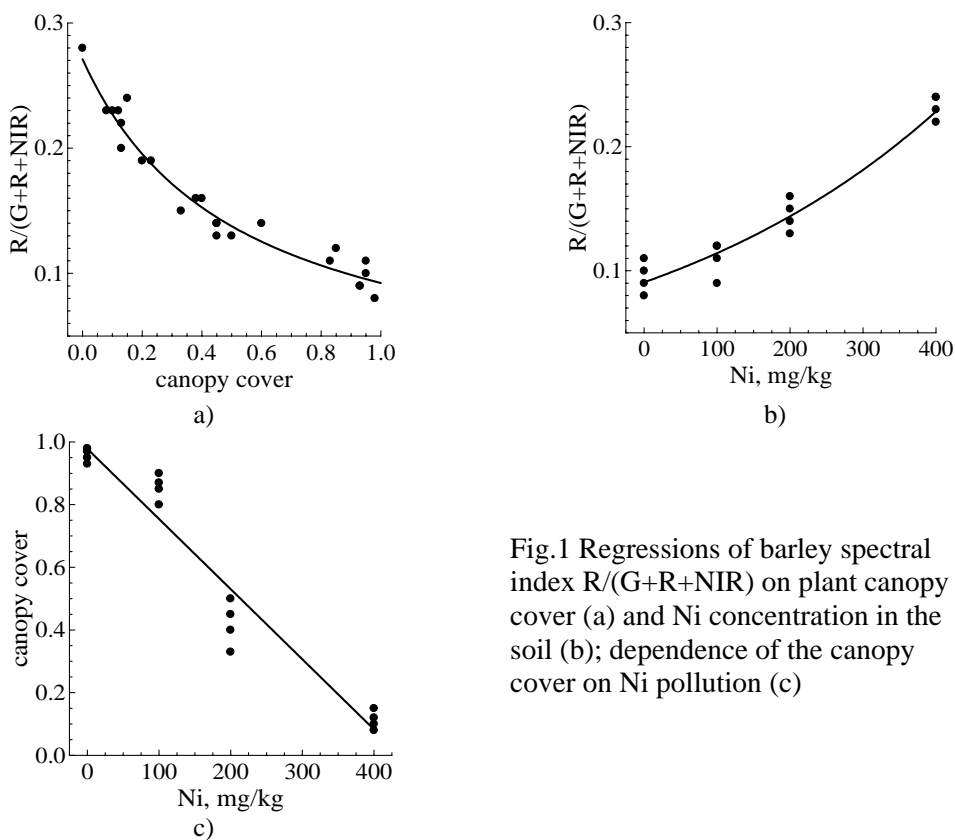
Fig.1 Regressions of barley spectral index R/(G+R+NIR) on plant canopy cover (a) and Ni concentration in the soil (b); dependence of the canopy cover on Ni pollution (c)

40

In all the cases high correlations (with coefficients of determination $r^2 > 0.9$) proved to exist. The results show that growing conditions cause statistically significant variations of plant reflectance properties. The established empirical dependences do not only illustrate the informational potential of spectral data but attach to it quantitative expression. Derived at different phenological stages they provide for crop state monitoring and detection of stress situations as well as for the evaluation of the inhibiting effect of unfavourable factors on the growth process. The knowledge of plant bioparameters and their stress-induced values is essential because of the direct contribution these parameters to potential yield. Multispectral data can be successfully used as inputs in regression models for crop agrodiagnostics and assessment of the growing conditions.

Of significant interest is plant reflectance behaviour during the whole phenological period. Temporal spectral data are indicative of variations in plant development caused by the growing conditions. Such studies provide for periodical monitoring and evaluation of crop status.
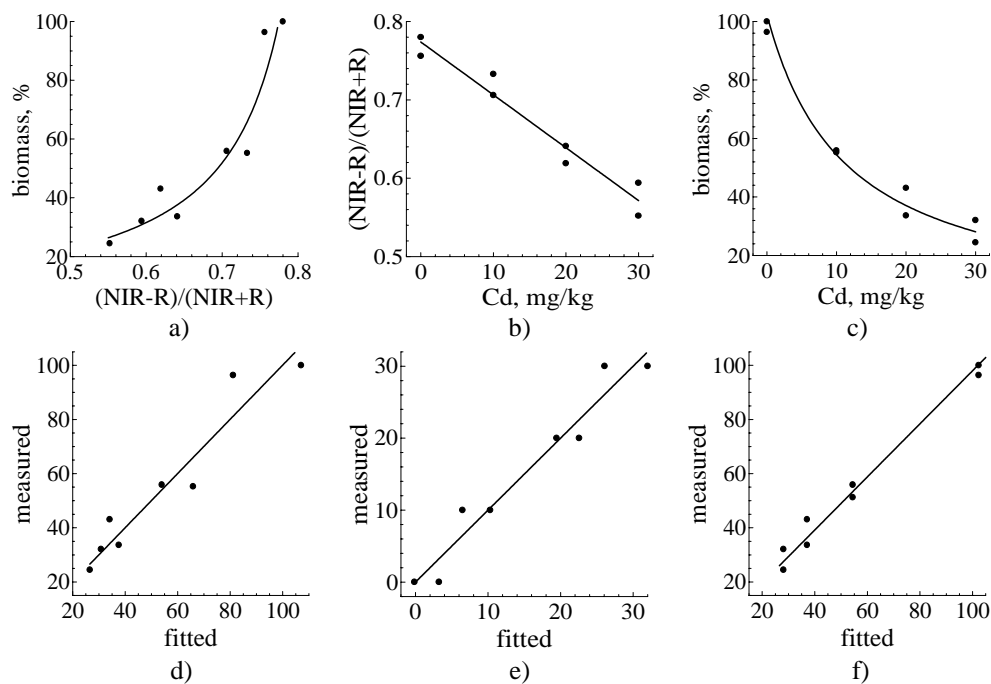
Fig.2 Relationships between peas plots spectral index (NIR-R)/(NIR+R), biomass (relative to the control treatment) and Cd contamination (a,b,c); correspondence between the actual and fitted (model) values of the bioparameter (d,f) and the stress factor (e)

In Fig.3 the spectral index (NIR-R)/(NIR+R) temporal profiles of barley

grown under different nutrient supply are presented. Fig.3a shows the effect of the fertilizer (NH_4NO_3) amount. Nutrient deficit is an unfavourable condition clearly manifested and detected by plant reflectance features. That is why nutrition suffering croplands can be depicted using multispectral data. It is interesting to mention that differences in crop reflectance are observed also in relation to fertilizer type. This is illustrated by Fig.3b where the nitrogen concentration in the soil is the same (800 mg/kg) for all treatments but the spectral profiles differ due to the nitrogen compound applied.
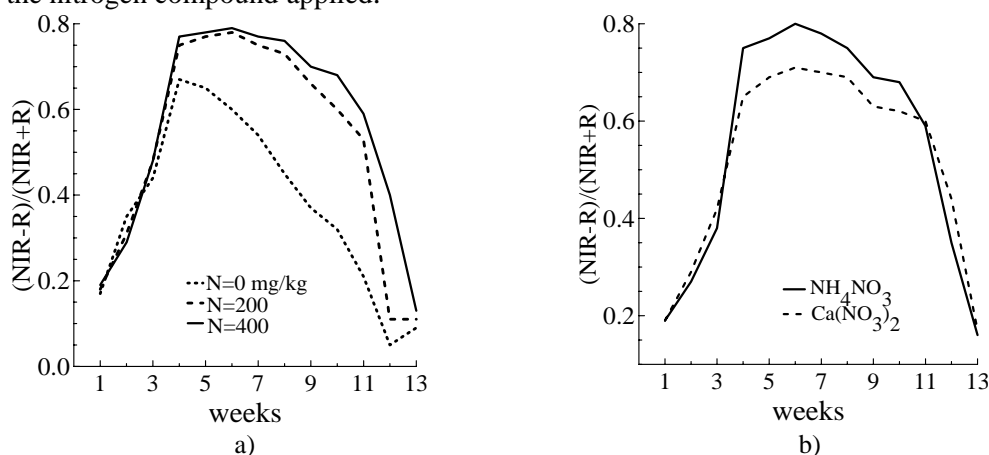
Fig.3 Temporal behaviour of barley spectral index (NIR-R)/(NIR+R) depending on the nitrogen fertilizer amount (a) and compound (b)

As seen, the dependence of plant spectral reflectance on the growing conditions is observed throughout the whole vegetation period. Since spectral-temporal data carry information about the current and previous plant status and show development trends, forecasting of the processes and the growing conditions impact is possible.

Summarizing the results of the experimental studies, a conclusion is drawn that reflectance temporal behaviour and regression models relating spectral features to plant bioparameters can be used for quantitative assessment of plant state and growing conditions.

Reference

1. K a n c h e v a R., A. K r u m o v, V. B o y c h e v a. Crop agroecological..., Proceed. 'International Space Year' Conf., Munich,1992, 873-979.

2. 2. K a n c h e v a R., A. K r u m o v, V. B o y c h e v a, V. I l i e v a. Remote sensing..., Compt. Rend. Acad. bulg. Sci., Sofia, 45(7), 1992, 49-52.

3. 3. М и ш е в Д. Дистанционни изследвания…, БАН, София, 1981, 206.

4. 4. И л и е в И. Многоканални спектрометрични..., Дисертация, София, 2000, 200.

5. 5. И л и е в И. Спектрометрична система..., III Симпозиум СИАС'92, Варна, 1992.

SPECTROSCOPY OF LUNAR AND TERRESTRIAL BASALTS

Denitsa Borisova, Rumiana Kancheva

Solar-Terrestrial Influences Lab.-BAS E-mail: dsbn@abv.bg, rumik@abv.bg

Abstaract

Reflectance spectroscopy is a rapidly growing science that could be used to derive significant information about mineralogy. Absorption bands in telescopic spectral reflectance of the moon and other solar system objects are potential for obtaining mineralogical and chemical information. Real land and solar bodies' covers are mixtures of materials and the theory of mixed spectral classes is an efficient method to study various rocks and minerals. Laboratory spectral measurements of basalt samples have been performed in the visible, near infrared and thermal infrared bands with multi-channel radiometers. Basalts are mixed classes of their rock-forming minerals and the data obtained have been used to illustrate the application of spectral mixture analysis for mineralogical and chemical differentiation.

Since the earliest days of spectroscopic remote sensing [1] of the lunar surface electronic transition bands exhibited by lunar soils and rocks in the visible and near-infrared regions of the spectrum are used to determine mineralogical composition [2]. Much less is known about the spectral behaviour of lunar rocks in the thermal infrared.

The interpretation of reflectance spectra of unknown materials requires an understanding of how the reflectance of different components combines into a single curve. An efficient method for spectrometric data processing is the mixed classes' theory [3]. The real land cover is a mixture of materials at just about any scale we view it. Rocks are mixture of their rock-forming minerals. Of particular interest are iron-containing rock-forming minerals because they are widespread.

Description of measured basalt samples:

1) Terrestrial samples are light grey porphyritic rocks with green olivine phenocrysts; dark grey slightly vesicular rocks consisting of black and light green phenocrysts; vesicular rocks with small phenocrysts.

2) Lunar samples are mare regolith.

In this investigation laboratory spectral measurements of the basalt samples is performed in the visible, near infrared and thermal infrared (TIR) bands with multi-channel radiometers – SPM-1 [4,5] and IR-1 [6].

Figure 1 and Figure 2 present reflectance spectra of lunar and terrestrial basalts in different spectral ranges.
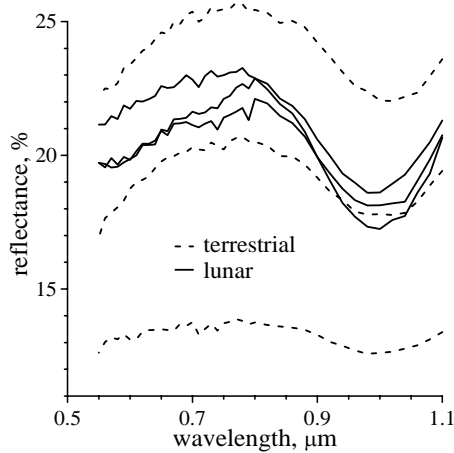
Fig. 1. Reflectance spectra of basalts (measured with SPM-1)
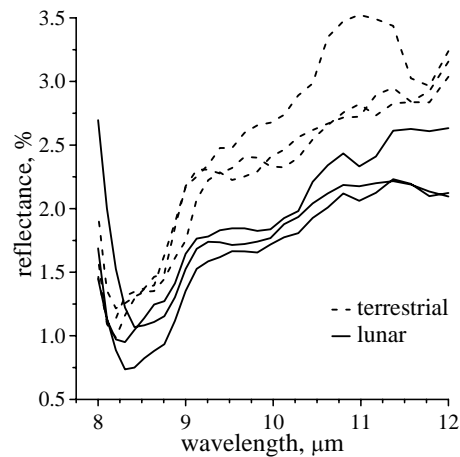
Fig. 2. Reflectance spectra of basalts (measured with IR-1)

The typical for the iron reflectance minimum at about 1 µm is observed in the spectral behaviour of all curves (Figure 1). The absorption at 1.0 µm varies depending on the iron content and is more pronounced for the lunar samples because of the higher iron content compared to the terrestrial basalts. In the TIR range (Figure 2) the lunar samples reflectance is lower than the reflectance of the terrestrial ones. Besides, the reflectance curves inclination of the terrestrial samples is steeper. This is used in the further spectral data analysis for rock mineral assessment.
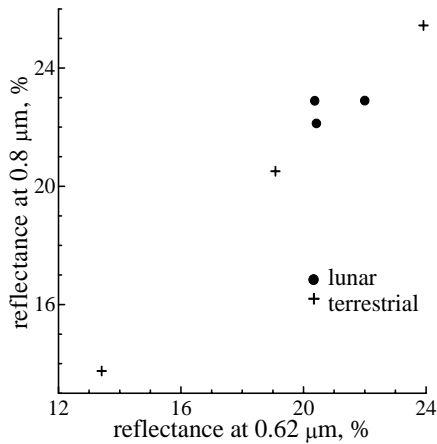
Fig. 3. NIR (0.8 μm) vs. Red (0.62 μm)
reflectance of basalts
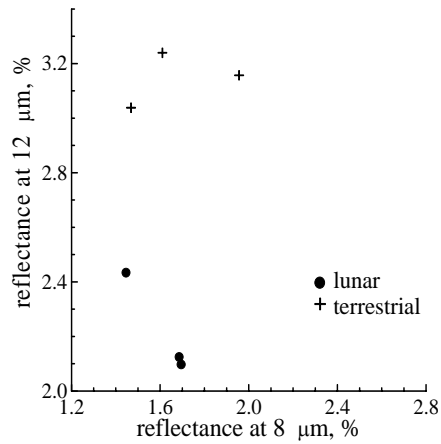
Fig. 4. TIR (12 μm vs. 8 μm)
reflectance of basalts

The plot of NIR = 0.8 μm versus Red = 0.62 μm reflectance is presented in Figure 3. It is seen that terrestrial and lunar basalts lie on a well-defined rock line analogously to the soil baseline [7]. However, although closely grouped lunar basalts cannot be reliably distinguished from the terrestrial in this wavelength range (see also Fig.1). In Figure 4 TIR (12 μm versus 8 μm) reflectance of the basalts is shown. In this case the lunar and terrestrial samples form clearly separated unoverlaping clusters.
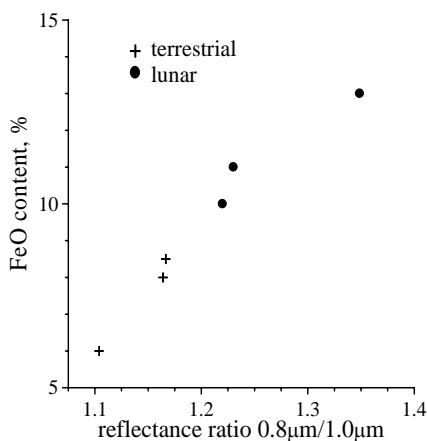
Fig. 5. Relationship between the iron
content (as FeO) and basalts
reflectance ratio 0.8 μm/1.0 μm
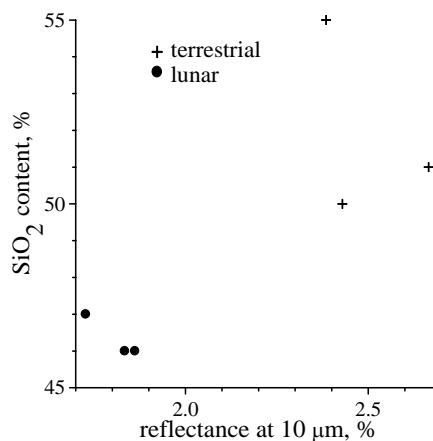
Fig. 6. Relationship between the
quartz content and basalts
reflectance at 10 μm.

Figure 5 presents the relationship between the iron content as FeO and the reflectance ratio 0.8 μm/1.0 μm. The lunar and terrestrial samples have almost the same mineral composition but different FeO content. As a result they form two clusters in Fig.5. This dependence can be used for detection of various iron-containing minerals and distinguishing between rocks of different origin.

The same refers to the relationship between basalts quartz content and spectral reflectance at 10 μm displayed in Figure 6. The fundamental Si-O stretching vibration bands of silicates are greatly diminished in intensity for lunar samples.

Detailed spectral data analysis including the theory of mixed classes and other methods (ratio indices, continuum removal) to isolate specific reflection and absorption features could certainly improve the success of distinguishing rocks and minerals.

Reference

1. Spiridonov H., A. Krumov, K. Katzkov, S. Yovchev. Measurement results and…, Space Research in Bulgaria, Sofia, 1983, 4, 59-69. 2. Adams, J. Visible and near-infrared…, J.Geophys.Res., 1974, 79, 4829-4836. 3. Mishev D. Spectral characteristics of…, Publ. House of the Bulg. Acad. of Sci., Sofia, 1986, 150. 4. Илиев И. Многоканални спектрометрични ..., Дисертация, София, 2000, 200. 5. Mischev D., I. Iliev. System for measuring…, Compt. Rend. Acad. Bulg. Sci., Sofia, 1992, 45 (12), 41-43. 5. Ferdinandov E., V. Tsanev. Mathematical modelling of…, Infrared Phys., 1993, 34(5), 457-466. Elvidge C., R. Lyon,. Influence of rock-soil…, Rem. Sen. Env., 1985, 17, 265-279.

NON-LINEAR APPROACH IN MULTISPECTRAL DATA CLASSIFICATION

Hristo Nikolov

Solar-Terrestrial Influences Lab.-BAS

Introduction

During the past 20 years, statistical classification methods, such as the minimum distance and the maximum likelihood classifiers, have been widely used. However, these methods have their restrictions, related particularly to the distribution assumptions and limitations in the input data types. In the past decade, the non-linear approaches, theoretically a more sophisticated and robust methods of image classification has been introduced and employed in remote sensing applications. Although these methods have been used in a wide range of scientific disciplines for a variety of applications since the early 1980s, their use in remote sensing area is relatively new, dating only from the early 1990s. Studies have shown that non-linear methods are more robust than conventional statistical methods in terms of producing classification results with higher accuracies and requiring fewer training samples. One of the most important of their characteristics is perhaps the non-parametric nature of the model, assuming no a priori knowledge, particularly of the frequency distribution of the data. Because of their adaptability and their ability to produce high-quality results, the use of non-linear methods has increased the in the remote sensing field research. Often comparison is made with model which applies maximum likelihood classification and this will be the approach stated hereafter.

Method and Data

In this study only classification methods based on supervised learning will be considered. The non-linear methods used to achieve the results are:

- *NN method* - the most common neural network model is the multilayer perceptron (MLP) - type networks that work in a feed-forward direction where information progresses from an input layer to an output layer in the learning phase. Such networks contain an extra layer or layers termed the hidden layer(s) to overcome the problems of the perceptron. Due to the involvement of one or more extra layers

and the use of nonlinear rather than linear transfer functions (in this research sigmoidal function), the MLP can approximate and map any kind of problem. Bostock (1994) emphasizes that the major reason for the popularity of MLP models is that whilst some problems are more efficiently modeled by other more specialized networks, such as radial basis function networks or binary tree structures, the multilayer perceptron trained by backpropagation learning algorithm, is a good general learning tool for a wide range of applications. A typical neural network consists of one input layer, one or two hidden layers and one output layer. Training a feed-forward neural network using the backpropagation algorithm involves setting several initial parameters including network structure, learning rate, momentum term and activation function. According to Hand (1997), 'a network with two hidden layers allows convex regions to be combined, producing no convex, even disconnected regions i.e. two hidden layers are enough for any task while retaining good generalization.

- *SVM method* – Support Vector Machines (SVM) have been recently introduced in the statistical learning theory domain for regression and classification problems, and applied to the classification of multispectral images. The technique consists in finding the optimal separation surface between classes thanks to the identification of the most representative training samples of the side of the class called support vectors. If the training data set is not linearly separable, a kernel method (linear, polynomial kernels) is used to simulate a non-linear projection of the data in a higher dimension space, where the classes are linearly separable. Actually, the projection can be simulated using a kernel method. Besides, unless statistical estimations, a small number of training samples is enough to find the support vectors. This classifier proposes a very interesting property for multispectral image processing- it does not suffer from the Hughes phenomenon and it may perform class separation even with means very closed to each other with a small number of training samples (Gualtieri'99). In this investigation a multiple class separation is performed by so called one against one approach - *M(M-1)/2*

classifiers are applied on each on each pair of classes, the most often computed label is kept for each vector.

- ***Bayes classifier*** (BC)– this method rely on the local distribution functions $p(x_i/pa_i; \Theta_i; Sh)$ are essentially classification/regression models. Therefore, if we are doing supervised learning where the explanatory (input) variables cause the outcome (target) variable and data is complete, then the Bayesian-network and classification approaches are identical. A Bayesian network is a graphical model for probabilistic relationships among a set of variables. One of its most prominent properties is the fact that Bayesian networks can readily handle incomplete data sets (Chickering'96). Bayesian methods in conjunction with Bayesian networks and other types of models offers an efficient and principled approach for avoiding the over fitting of data. When dealing with incomplete data sets Monte-Carlo methods yield accurate results, but they are often intractable in large sample size. Another approximation that is more efficient than Monte-Carlo methods and often accurate for relatively large samples is the Gaussian approximation, which we used in this study.

The effectiveness of the above methods was tested with data from laboratory experiments (contracts with MES МУНЗ 1201/03 and Б1306/03) and satellite data from ETM instrument of Landsat7. Both data sets were divided in training and validation sets with total number of samples 130 and 2200 respectively.

Results and Discussion

The results for training and classification are shown in tables below. Maximum likelihood (ML) statistic method is used for reference for the ones introduced above.

Training data for classification (number of multispectral pixels- samples)

Type of land cover	Laboratory	Satellite
Vegetation	45	275
Rocks	35	600
Water	50	580
Urban	-	745

Accuracy over the validation set after training for both data sets (percent)

Type of land cover	ML		NN		SVM		BC	
	Lab	*Sat*	*Lab*	*Sat*	*Lab*	*Sat*	*Lab*	*Sat*
Vegetation	58.7	56.3	63.2	65.8	68.4	70.6	71.2	73.6
Rocks	60.8	58.6	70.3	75.8	82.3	79.4	84.3	82.6
Water	75.8	78.4	76.9	80.1	82.5	81.5	85.6	90.3
Urban	-	82.3	-	86.4	-	92.6	-	94.2

Conclusions

As it can be seen the Bayes classifier offers better performance for all the data and especially for incomplete training data since it is closer to the optimal classification. On the other hand the other methods discussed should not be underestimated and considered as a competitive equivalent. The non-linear methods for classification stated here, are seen as an introduction of larger feature space (i.e. 10 or more features) that could be used by conventional statistical methods.

References:
1. Bateson, A. and Curtiss, B. A method for manual endmember selection and spectral unmixing. Remote Sensing of Environment, 55, 229-243., 1996;
2. Gualtieri J. A. and R. F. Cromp, "Support vector machines for hyperspectral remote sensing classification" in Proceedings of the SPIE, vol. 3584, 1999, pp. 221–232.;
3. Hand D. J., Construction and Assessment of Classification Rules. New York: John Wiley & Sons, 1997.
4. Heckerman David, A Tutorial on Learning with Bayesian Networks, Microsoft Research Advanced Technology Division, 1996;
5. Chickering, D. and Heckerman, D., Efficient approximations for the marginal likelihood of incomplete data given a Bayesian network, Technical Report MSR-TR-96-08, Microsoft Research, Redmond, WA

THEMATICALLY ORIENTED MULTICHANNEL SPECTROMETER (TOMS)

Doyno Petkov, George Georgiev, Hristo Nikolov

Solar-Terrestrial Influences Lab.-BAS

Abstract

The goal of the study is describe the key parameters and the process of working out a multichannel spectrometric system in the visible and near infrared bands of the electromagnetic spectrum. This system will be used for remote sensing investigations:

- *recognition of main land covers (soils, natural and agricultural vegetation, water areas)*
- *state assessment and monitoring of the studied objects.*
- *Investigation of the relationships between the reflectance and spectral features of the studied objects; development and validation of spectral-biophysical models for estimation of land cover parameters.*
- *Soil state assessment – type, moisture content, surface texture.*

Description of spectrometric system

The multichannel spectrometric system has been designed to measure the reflected by ground objects solar radiation in the visible and near infrared range of the electromagnetic spectrum on board of a remotely-controlled airborne platform.

The measurements are performed in a basic working regimen - nadir, platform velocity – up to 20 km/h, height – up to 1000 m (optimal 200 m), flight duration - up to 30 min.

Components of the system

- VIS-NIR multichannel spectrometer - optical unit – lenses and fiber; optional color digital still camera -
- control of the on-board system – spectrometer control unit, onboard storage module (flash disk), GPS (for Earth investigations);
- on-board power supply device – litium battery; fitting elements for installation of the system on board of the airborne platform;
- unit for on-board pre-processing of spectrometric data;

- communication unit for data transmission;

The technical specification of the spectrometric system are summarized in table below:

Spectral VIS- NIR range:	$(450 \div 900)$ nm
Number of spectral channels:	128 / 64
Channel location:	even
Spectral resolution:	$(3 \div 10)$ nm
Spatial resolution:	$(1 \div 25)$ m^2
CCD line elements:	2048
Dynamic range: of the system	4×10^4
per scan	2000 : 1
Exposure time:	$(3 \div 60)$ ms
Measurement duration:	$(10 \div 30)$ min

Technical requirements and characteristics of the platform:

Navigational (flight conditions and spectrometric system operational regimen) - composition and relief of the studied territories

Constructional (location and installation of the spectrometric system):

➢ Necessity of a digital camera and requirements for linking the spectrometric data with the regional map;

➢ Requirements for geometric corrections, radiometric calibration, map and time control of the spectrometric data (technical parameters of the GPS interface);

➢ Requirements to the data processing system (hardware, software) - development of data processing and interpretation algorithms (digital filtration, visualization, user interpretation, etc.);

➢ Laboratory investigations with the system.

In the visible (VIS) spectral band $(400 \div 710$ nm) vegetation optical properties depend mainly on plant pigment content and concentration. The reflectance maximum is observed at 550 nm, i.e. in the green region where the absorption of the incident radiation is relatively low. Plant senescence or stress factors inhibiting chlorophyll synthesis or causing chlorophyll destruction decrease the amount of the absorbed solar radiation in the red (670 nm) spectral band where the zone of vegetation minimum reflection is located.

Fig.1The reflected by vegetation solar radiation () has a specific spectral distribution.

Fig2 Spectral reflectance of wheat crops for green plants and plants with different degree of senescence

Fig.3 Spectral reflectance of various soil types

Fig. 4 Spectral reflectance of two soil types with different water content
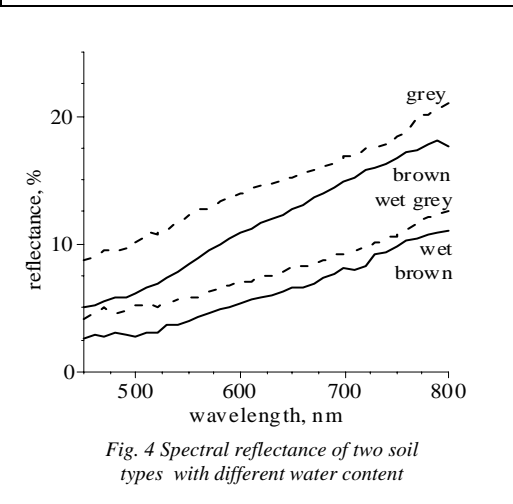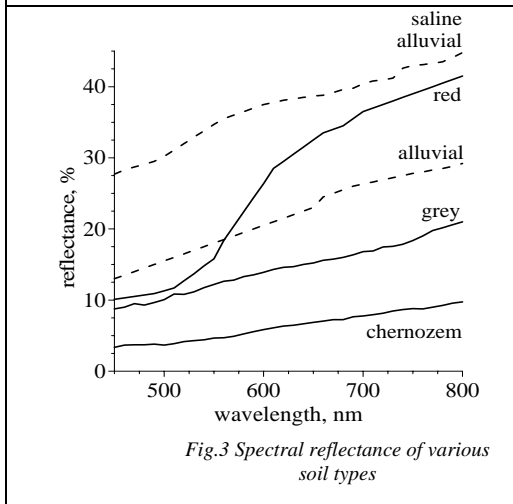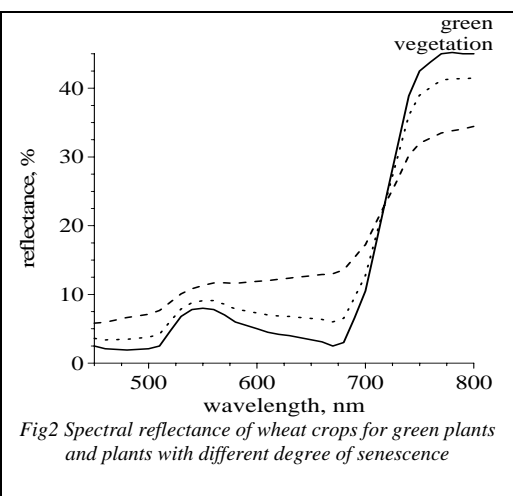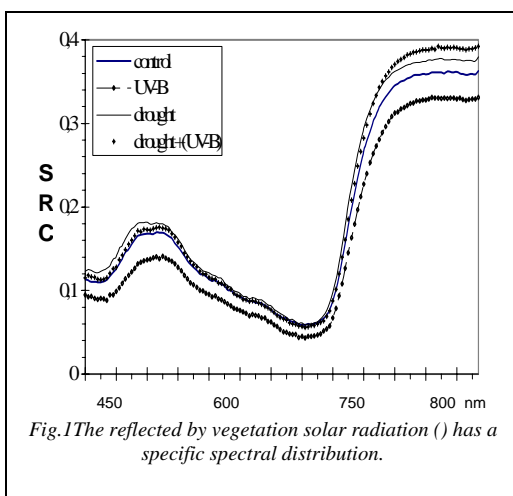
This leads to higher reflectance values in this spectral band (Fig.2). This leads to higher reflectance values in this spectral band (Fig.2).

In the near infrared region (NIR) of the spectrum (710÷1300 nm) the vegetation reflectance ability increases, a steep slope being observed in the wavelength range 700 ÷ 760 nm. Reflectance variation in the NIR band depends on plant structural parameters and can be used for vegetation

classification and state assessment. In Fig.1 the spectral reflectance curves of maize leaves are shown for the case of plant normal (control) and stress growing conditions. In Fig. 2 the reflectance spectra of wheat crops are presented for green plants and plants with different degree of senescence.

Soils have a reflectance increase in the VIS-NIR spectral range. The reflectance behavior is a function of various soil parameters (mineral composition, organic matter content, surface moisture and roughness, etc.).
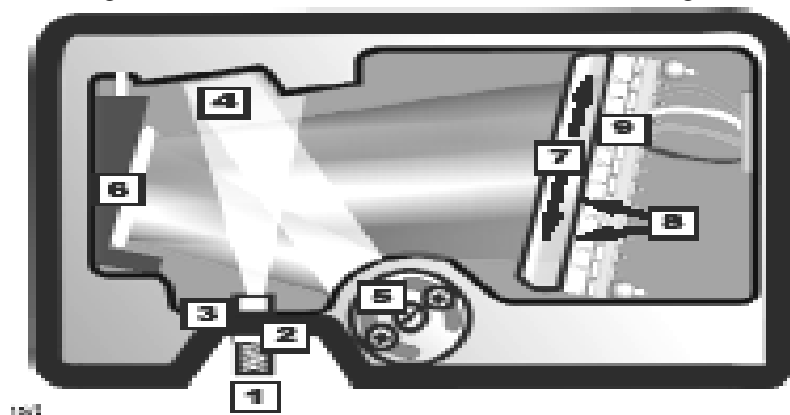
Fig5. Diagram of the optical unit 1. SMA connector; 2. Fixed slit; 3. Absorbance filter; 4. Collimating mirror; 5. Grating; 6. Focusing mirror; 7. Detector collection lens 8. OVLF filter; 9. UV detector.

Conclusion

The idea in designing multichannel a spectrometric system is to provide large number of scientists and specialists with reliable device for measuring different types of natural and anthropogenic origin. As it was shown by the laboratory investigations the results are promising since the spectral accuracy of the spectrometer is comparable with this of similar commercial systems.

ATMOSPHERIC ABSORPTION STRIPS' INFLUENCE ON OPTICAL PYROMETERS' WORK IN THE INFRARED SPECTRAL RANGE

Jivko Zhekov, Garo Mardirossian, Angel Manev*,
Kunyo Palazov*, Ivan Hristov

Space Research Institute – Bulgarian Academy of Sciences
www.space.bas.bg ; e-mail: office@space.bas.bg

* Solar-Terrestrial Influences Central Laboratory –
Bulgarian Academy of Sciences
www.stil.acad.bg; e-mail: palazov@mbox.digsys.bg

Abstract
There is a great interest in investigating the constant decrease of infrared radiation, which influences essentially general reduction in the atmospheric absorption strips. The atmospheric absorption strips are of great importance when solving important problems concerning ecology, defence and especially, space research.

The subject of the paper is detection of atmospheric strips' absorption, their influence on the operation conditions in pyrometers' work, the spectral strips located in the closer infrared spectral range.

The results prove the need to account for atmospheric gas absorption when working with pyrometers, sensitive in the infrared spectral range while observing distant objects of emanation.

There is a great interest in investigating the constant decrease of infrared radiation, which influences essentially general reduction in atmospheric absorption strips. Atmospheric absorption strips are of great importance when solving important problems concerning ecology, defence and especially, space research [1,3,4].

The need of a way to detect the existence of gas absorbing strips, constituting the atmosphere arises in measuring the temperature of distant objects with the help of a pyrometer - receiver of emanation, precise in the infrared optic spectral range. It is known [2] that the main absorbing components in the ground level of the atmosphere are water vapors and carbon gas. The correlation between them and their influence depend greatly on

atmospheric conditions - humidity, temperature, quantity and composition of aerosols. Some strips - for example those in about 2.75 μm, 6.3 μm of H_2O and 2.7 μm, 4.3 μm, 5.2 μm of CO_2 and others decrease greatly their emanation even in normal atmospheric conditions.

The subject on the paper is detection of atmospheric strips' absorption, their influence on the operation conditions in pyrometers' work, the spectral strips located in the closer infrared spectral range.

In pyrometers' operation, a significant variation of ambient mean temperature is tolerated, t_a from + 5 ... + 50 °C and relative humidity from 30 ... 80 %. The average concentration of CU_2 in the atmosphere is accepted in the borders 0,03 ... 0,04 %. The seasonal variations of CO_2 concentration in the ground level of the atmosphere are between 80 ... 90 % per year [5]. CO_2 concentration depends primarily on the place where the measurements are taken, whereas in industrial areas the variations of CO_2 might go beyond the above values. All this could lead to significant differences in received data, compared to real values, even with the use of an absolute black body model.

In order to eliminate the influence of atmospheric permeability, it is necessary to choose spectral intervals, in which there are no atmospheric absorption strips. In a number of cases, to ensure the necessary correlation between signal and noise, one should isolate sufficiently wide spectral intervals, within which atmospheric absorption strips fully or partially exist.

The operating permeability factor, $\tau_g(T)$ [7] is equal to:

$$\tau_g(T) = \frac{\int\limits_{\lambda}^{\lambda+\Delta\lambda} \tau(\lambda, t_a)\xi(\lambda)\varepsilon(\lambda, T)b_0(\lambda, T)d\lambda}{\int\limits_{\lambda}^{\lambda+\Delta\lambda} \xi(\lambda)\varepsilon(\lambda, T)b_0(\lambda, T)d\lambda} \quad , \qquad (1)$$

where: $b_0(\lambda, T)$ - spectral energetic luminance of an absolute black body with wavelength λ and temperature T;

$\xi(\lambda) = \tau_s(\lambda)S_\lambda$ - spectral transmitting function of the pyrometer;

$\tau_s(\lambda)$ - spectral characteristic of the light filter;

S_λ - spectral sensitivity of the emanation receiver;

$\tau(\lambda, t_a)$ - spectral atmospheric permeability factor at atmospheric

temperature t_a;

$\varepsilon(\lambda, T)$ - spectral emanating ability of the investigated object.

It is worth minding that permeability alteration in the atmosphere influences the value of pyrometers' boundary effective wavelengths.

Having in mind the complex spectrum of water vapors and carbon gas's permeability, the object's temperature etc., it could be seen that the precise estimation of temperature alterations, at the time of variations of these values, requires enormous effort. An approximate calculation may be used for preliminary evaluation of the conditions accounting for such influence.

In [6], the average value of absorption $A = 1 - \tau$ in a certain frequency interval is presented. Au is a synonymous function of the effective quantity of water vapors along the path of beam l. The function determines the quantity of water vapors ω, which is measured in centimeters per layer of evaporated water.

$$\omega = ql(P_x + rP_a)^{2k} - \omega P^{2k}, \tag{2}$$

where: q - concentration in centimeters per layer of evaporated water, in kilometers per layer;

P_x - pressure of the absorbing gas;

P_a - atmospheric pressure;

r = 5; k = 0,4 for the place of water vapors' spectrums in the range between 1 ... 8,5 μm.

As shown in [6], the experimental data could be averaged by the formula:

$$A = 1 - \exp\left[-\left(\frac{\omega}{\omega_0}\right)\right], \qquad (0,05 < A < 1) \tag{3}$$

where: ω_0 - value, representing the effective quantity of water vapors, where A = 0,05 and depends on the wavelength.

We calculate the vapors' permeable spectrums of H_2O according to

formula (3) for different values of ω (between 0,001 and 0,1 cm), characteristic of pyrometers' use and normal conditions (t_a = 20 °C). Since our task is to study the pyrometer's work at the ground level of the atmosphere, we could ignore the alteration of the pressure P, which is about 3 %, and in laboratory conditions, even less. The results are shown on Table 1.

Table 1.

Receiver of emanation	ω, cm	T, κ	τ_g
Germanium	0.001	1,200	0.98
	0.100	1,200	0.96
	0.100	1,200	0.83
Non-coolable PbSe	0.001	700	0.92
	0.010	700	0.74
	0.100	700	0.54
Germanium windows	0.001	500	0.93
	0.010	500	0.71
	0.100	500	0.46

Carbon gas absorbs in strips between 2.7 and 4.3 μm. When working with a pyrometer, it is necessary to account for these strips and the area of spectral sensitivity where the strips of Ge (Au), InSb, PbSe, Ge(Hg) and other types of emanation receivers are positioned.

The influence of CO_2 absorption strips could be eliminated, filtering these strips with the help of light filters (for example a cuvette filled with carbon gas). It is not possible to use cuvette with water vapors to determine the absorption strip of water vapors, because the vapors will condense on the cuvette's walls. This must be done with the help of special interferential filters or organic substances, possessing strips of absorption in these areas of the spectrum.

In conclusion it is worth noticing, that the results prove the need to account for atmospheric gas absorption when working with pyrometers, sensitive in the infrared spectral range while observing distant objects of emanation.

References:
1. Гецов, П. Космос, екология, сигурност. Нов български университет,   София, 2002, 211 с.
2. Зуев, В. Распространение видимх и инфракрасньгх воли в атмосфере.   Москва, "Сов. Радио", 1970.
3. Мардиросян, Г. Аерокосмически методи в екологията и изучаването на   околната среда, част I, Академично издателство "Марин Дринов", София, 2003, 208 с.
4. Стоянов, С. Обобщена характеристика на спектрите на погльщане   на атмосферния озон и газове в оптичния диапазон при   изследвания   с наземни и сателитни уреди и апаратури.   Годишник   на   Технически Университет,   Варна,   ISSN-896X,   2001, стр. 916 – 921.
5. Gerritsma, C. I., Haanstra I., Infrared Phys. 2000, 12, p. 467.
6. Noakes, W. Contr. and Instrum. 2001, 4, p. 32.
7. Smit, R. Applied Science Revinv. 1995, 11, p. 342.

MULTICOLOUR SURFACE PHOTOMETRY OF SEYFERT GALAXIES: FIRST RESULTS

Luba S. Slavcheva-Mihova, Georgy T. Petrov, Boyko M. Mihov

Institute of Astronomy, Bulgarian Academy of Sciences,

Introduction

One- or two-dimensional decomposition of surface brightness distribution to its individual components is a technique widely used in studying Seyfert galaxies. Almost all decompositions of Seyfert galaxies light distribution made by different groups are based on the following analytical models for the separate components: single/double Gaussian for the nucleus, de Vaucouleurs law for the bulge and exponential law for the disk (e.g. [1], [2]). However, firstly, it was found that Sersic law is more suitable to model the bulge light distribution ([3]) and, secondly, important components of spiral galaxies light distribution are missed in the decompositions of Seyferts, namely, the bar and the lens ([4]). Using de Vaucouleurs law instead of Sersic one and neglecting the bar and the lens light distributions simplifies the numerical computations but could lead to systematic errors in the model parameters and in the total magnitudes.

In this paper we make an attempt to account for the above two problems. For this purpose we obtained *UBVRcIc* broad-band images of a number of galaxies have already been decomposed by other authors. In addition we observed several galaxies for which no surface brightness distribution decomposition had been done before.

Observations

Observations were performed with the 2-m Ritchey-Chretien telescope of the Rozhen National Astronomical Observatory of Bulgaria equipped with 1024x1024 Photometrics CCD camera (CCD chip SITe SI003AB with $24\mu m$ pixel size that corresponds to 0.309 arcseconds on the sky) and standard Johnson-Cousins filters. Observations were carried out from June 1, 1997 till April, 21, 1999 for a total of 22 nights. A total of 33 galaxies were observed; 21 of them were imaged once, the other 12 - between 2 and 4 times at

different epochs. The CCD camera was used in both full and 2x2 binned mode upon the seeing conditions. Standard fields in the clusters M67, M92 and NGC7790 were observed 2 or 3 times per night. Flat field frames were taken in morning and/or evening twilight. Zero exposure frames were taken regularly during each observing run. The dark current is negligible as the CCD camera is cooled down to –100 degrees of Celsius. *I*c band frames of relatively blank night sky regions were taken for the fringe frame composition by dithering the telescope between the exposures to prevent eventual stars from landing on the same location. We found the fringe pattern did not change for the entire period of observation.

Data reduction

The primary reduction of the data was performed by means of ESO-MIDAS package. The debiased frames were flat fielded and cosmic ray events cleaned. We created a super fringe frame for the whole set of observations, with the help of which the *I*c band images were defringed. All frames of an object were shifted to match the *R*c frame and then coadded to create the final frame.

Extraction of one-dimensional galaxy profiles was performed with ESO-MIDAS context SURFPHOT. The frames were adaptive filtered, the background stars were removed from the galaxy image and the sky background was subtracted before the ellipse fitting. The sky background was determined by fitting a tilted plane to regions of the frame free of objects or CCD chip defects. The ellipse fitting itself was performed following the algorithm presented in [5]. As a result of the ellipse fitting radial profiles of surface brightness, ellipticity and position angle were obtained for each galaxy image in each band. We also computed the fourth order cosine Fourier coefficient profile examining the two-dimensional difference between the image and the corresponding ellipse model (e.g. [5]). Finally, the surface brightness profiles were transformed to the standard Johnson-Cousins photometric system using standard stars in the fields of M67 ([6]), M 92 ([7]) and NGC 7790 ([8]) clusters.

Results

Sample *UBVRcIc* profiles of the surface brightness, colour index, ellipticity, position angle and fourth cosine Fourier coefficient versus the major semi-axis for the galaxy Mrk79 observed on February 16, 1999 (seeing was about 3 arcsec) are presented in Fig. 1.

The galaxy Mrk79 is a barred spiral and from its profiles some useful information could be extracted: bar length of about 20 arcsec; host galaxy *B–V* colour of about 0.8-0.9 mag; bar ellipticity and position angle of about 0.55-0.6 and 51 deg, respectively; disk ellipticity and position angle of about 0.15-0.2 and 150 deg, respectively. The fourth cosine Fourier coefficient is close to zero, so the galaxy isophotes are well represented by ellipses. The run of the ellipticity, position angle and fourth cosine Fourier coefficient profiles is similar in the different bands; the structures in the inner 6 arcsec (or two seeing disks) are not real because of seeing and sampling influence.

We also made two kinds of profile comparisons in order to check the accuracy of our results. Firstly, we compared surface brightness profiles of galaxies observed twice or more in different epochs. The result of such a comparison is presented in Fig. 2 in the case of the galaxy NGC4151 observed on March 10, 1999 (solid line) and on April 19, 1999 (a dashed line). Secondly, our profiles are compared with the ones presented in [9]. In Fig. 2 and in Fig. 3 we present the results of such a comparison in the cases of NGC4151 and Mrk766 (observed on February 15, 1999) galaxies, respectively. In both figures only *V* band profiles are presented.

One can see the good correspondence between our profiles at different epochs and between our profiles and the profiles presented in [9]. The differences in the central part are due to the nuclei variability and the differences in the outer part are due to the sky background determination errors (over- or under- subtraction of the sky level). The region of NGC4151 profile between 40 and 80 arcsec is dominated by spiral arms which have irregular structure: this could lead the ellipse fitting algorithm to find slightly different solutions in this region depending on the seeing, signal to noise ratio and background determination. This could explain the profiles' difference in this region observed in Fig. 2.
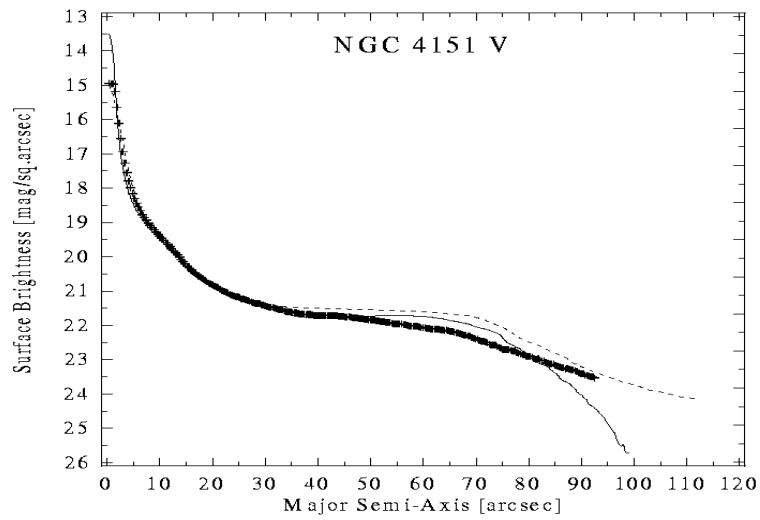
Fig. 2. *V* band profiles comparison in the case of NGC4151 galaxy: a solid line – March 10, 1999 profile, a dashed line – April 19, 1999 profile and crosses – the profile presented by [9].
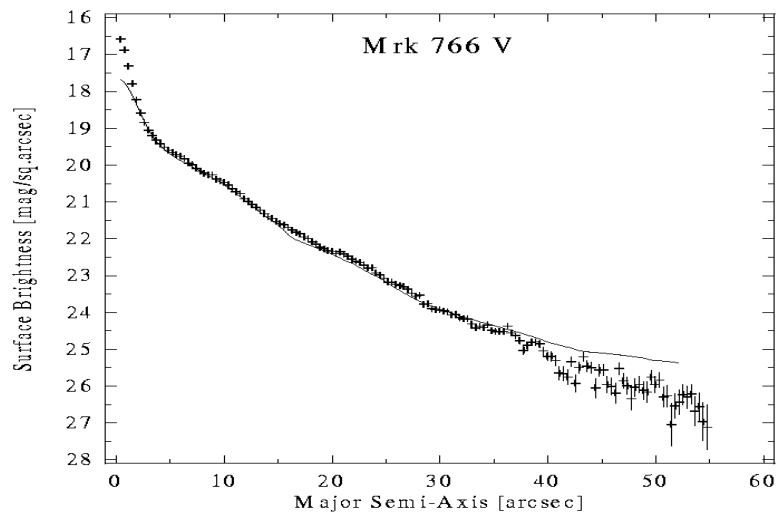
Fig. 3. *V* band profiles comparison in the case of Mrk766 galaxy: a solid line – February 15, 1999 profile and crosses – the profile presented by [9].
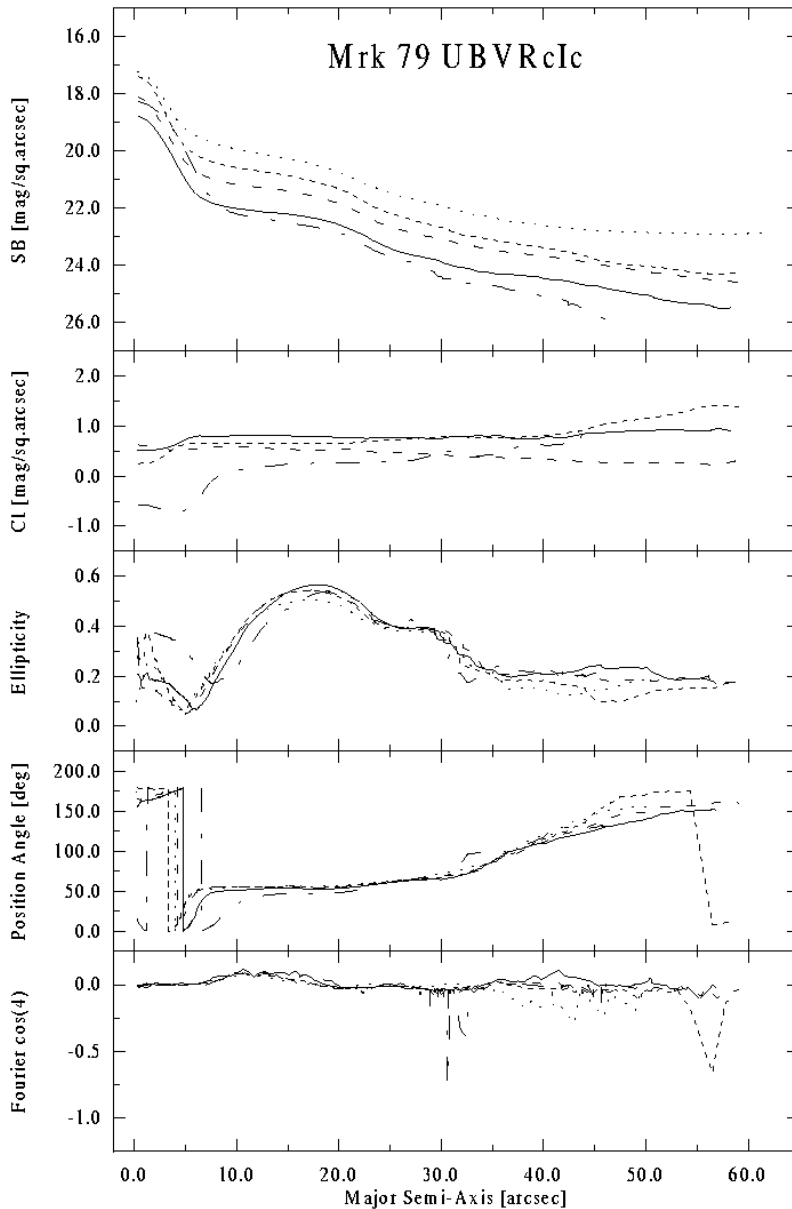
Fig. 1. Profiles of surface brightness, colour index, ellipticity, position angle and fourth cosine Fourier coefficient versus the major semi-axis for the galaxy Mrk79. *U* and *U–B* profiles are represented by a dash-dotted line, *B* and *B–V* – a solid line, *V* and *V–R*c – a long dashed line, *R*c and *R*c–*I*c – a short dashed line and *I*c – a dotted line.

References

1. G r a n a t o G. L., V. Z i t e l l i, F. B o n o l i, L. D a n e s e, C. B o n o l i, F. D e l p i n o. A study of a homogeneous sample of optically selected active galactic nuclei. III. Optical observations, ApJS, 89, 1993, 35-56

2. V i r a n i S. N., M. M. D e R o b e r t i s, M. L. V a n D a l f s e n. A CCD Study of the Environment of Seyfert Galaxies. III. Host Galaxies and the Nearby Environments, AJ, 120, 2000, 1739-1749

3. A n d r e d a k i s Y. C., R. H. S a n d e r s. Exponential bulges in late-type spirals: an improved description of the light distribution, MNRAS, 267, 1994, 283-296

4. K o r m e n d y J. Brightness distributions in compact and normal galaxies. I - Surface photometry of red compact galaxies, ApJ, 214, 1977, 359-382

5. B e n d e r R., C. M o e l l e n h o f f. Morphological analysis of massive early-type galaxies in the Virgo cluster, A&A, 177, 1987, 71-83

6. C h e v a l i e r C., S. A. I l o v a i s k y. Cousins BVRI CCD photometry of stars in the M67 "dipper asterism", A&AS, 90, 1991, 225-229

7. M a j e w s k i S. R., R. G. K r o n, D. C. K o o, M. A. B e r s h a d y. Deep UBVRI photometric calibration of high-latitude fields: SA 57 (1307+30) and Hercules (1720+50), PASP, 104, 1994, 1258-1270

8. P e t r o v G., W. S e g g e w i s s, A. D i e b a l l, B. K o v a c h e v. CCD standards for U and I in the open cluster NGC 7790, A&A, 376, 2001, 745-750

9. H u n t L. K., M. A. M a l k a n, B. R u s h, M. D. B i c a y, B. O. N e l s o n, R. M. S t a n g a, W. W e b b. Morphology of the 12 Micron Seyfert Galaxies. II. Optical and Near-Infrared Image Atlas, ApJS, 125, 1999, 349-362

EXTREMELY RED GALAXIES AT z~1

Nedelia Antonia Popescu, Marian Doru Suran

Astronomical Institute of Romanian Academy
Str.Cuțitul de Argint, 5, RO-75212 Bucharest 28, Romania
E-mail:delia@aira.astro.ro, suran@aira.astro.ro

Abstract.

In this paper we use optical and near infrared photometrical (R, I, J, K) data and morphological data for the galaxies in the fields of 3C 184 (z=0.996), 3C 210 (z=1.169) and RX J0848+4453 (z=1.273), in order to determine the cumulative number of Extremely Red Galaxies (ERGs), the surface density and the fraction of ERGs with respect to the entire galaxies from each studied field. The radial trends of the ERGs, the clustering tendency of galaxies and ERGs are also revealed. The presence of the red sequence in the color-magnitude diagram and the morphology of the galaxies are analyzed.

1. Introduction

Extremely Red Galaxies (ERGs) are characterized by extreme properties such as very red optical to near-infrared (NIR) colors (R-K)>5, (I-K)>4, (J-K)>1.8 and moderately faint NIR magnitudes (K~17.5-20). As the 4000Å break falls between R (or I, J) band and K band, at z ~1 the old passively-evolving galaxies should be characterized by red optical-NIR colors, representing redder colors than most galactic stars and field galaxies.

The red colors of ERGs population are consistent with two classes of galaxies:

a) old passively evolving elliptical galaxies at z~1;

b) high-redshift dusty starburst galaxies, characterized by high star formation rates, or AGN reddened by strong dust extinction.

ERGs represent a mix of dusty star-forming galaxies, edge-on spiral galaxies and early type galaxies, therefore it is necessary to combine the color selected samples of ERGs with morphological information about them.

2. Galaxies and ERGs studied samples

In this paper we present the results of a ***photometrical*** and ***morphological*** study of galaxies and ERGs in the field of 3C 184 (z = 0.996, 35 gal. in a 6.2 arcmin^2 field); 3C 210 (z = 1.169, 57 gal. in a 6.2 arcmin^2 field); RX J0848+4453 (z=1.273, 70 gal. in a 6.2 arcmin^2 field)

using optical and NIR photometrical data and HST/WFPC2 morphological data [1]. The photometrical data are derredened for Galactic extinction. The fields are centred on the brightest cluster galaxy (BCG).

From the morphological point of view the ERGs elliptical galaxies are compact, regularly shaped objects and starburst galaxy present a much more irregular shape (if the starburst is triggered by a merger or if a large amount of irregularly distributed dust is present in the galaxy).

The general color selection criteria for the ERGs are (R-K)>5, (I-K)>4 and (J-K)>1.8.

The HST /WFPC2 morphology of galaxies in:

- *3C 184 field*: 15 E/S0, 7 Sa/Sb, 5 Sc/Sd, 5 Irr/disturbed galaxies and 3 galaxies outside the WFPC2 field;
- *3C 210 field*: 23 E/S0 , 6 Sa/Sb, 6 Sc/Sd, 22 Irr/disturbed galaxies;
- *RX J0848+4453 field*: 14 E/S0, 14 Sa/Sb, 6 Sc/Sd, 18 Irr/disturbed galaxies, 15 galaxies outside the WFPC2 field, 3 stars.

The HST /WFPC2 morphology and the total surface density of ERGs in:

- *3C 184* field: 12 ERGs with 6 E/S0, 1 Sa/Sb, 2 Sc/Sd, 1 Irr/disturbed galaxies, 2 outside the WFPC2 field. ERGs are determined for (J-K)>1.8 color selection criterion and the total surface density is 1.93 gal/arcmin^2.
- *3C 210* field: 24 ERGs with 11 E/S0, 3 Sa/Sb, 1 Sc/Sd, 9 Irr/disturbed galaxies. ERGs are determined for (I-K)>4 and (J-K)>1.8 color selection criteria and the total surface density is 3.87 gal/arcmin^2.
- *RX J0848+4453*: 31 ERGs with of 13 E/S0, 4 Sa/Sb, 2 Sc/Sd, 5 Irr, 1 merger and 6 ERGs outside the WFPC2 field of view (i.e. without morphology). The total surface density is 5 gal/arcmin^2.

In the Table 1 we present the results on the multi color selected ERGs subsamples of 3C 210 and RX J0848+4453 fields. We present in column 2 the cumulative number of ERGs (ERG) and the cumulative number of galaxies from the fields (Gal.) selected at each K limiting magnitude. For each color criteria we determine the cumulative number of ERGs selected at each K limiting magnitude (Nr), the surface density (D), in $objects / arc\min^2$, and the fraction of ERGs with respect to the entire galaxies from the fields (Fr.).

Table 1

		RX J0848+4453								3C 210		
	ERG (Gal.)	R-K>5 I-K>4		R-K>5 J-K>1.8		I-K>4 J-K>1.8		R-K>5 I-K>4 J-K>1.8		Gal.	I-K>4 J-K>1.8	
K<		Nr	D (Fr.)	Nr	D (Fr.)	Nr	D (Fr.)	Nr	D (Fr.)		Nr	D (Fr.)
17										5	2	0.322 0.4
17.5	1 (4)							1	0.161 0.25	9	3	0.483 0.33
18	3 (9)							3	0.483 0.33	12	4	0.645 0.33
18.5	4 (11)							4	0.645 0.363	24	10	1.612 0.417
19	14(24)	1	0.161 0.042			2	0.322 0.083	11	1.774 0.458	31	17	2.741 0.548
19.5	16(31)	2	0.322 0.065	1	0.161 0.032	2	0.322 0.065	11	1.774 0.355	42	19	3.064 0.452
20	25(50)	2	0.322 0.04	2	0.322 0.04	2	0.322 0.04	19	3.065 0.38	57	24	3.87 0.421
20.5	31(70)	3	0.483 0.043	3	0.483 0.043	2	0.322 0.028	23	3.709 0.328			

3. Radial trends of the ERGs number density

The 3C 184, 3C 210 and RX J0848+4453 fields' densities as function of radial projected distance from the brightest field galaxy are analyzed. The galaxy density was calculated in successive annuli of $10^{"}$ wide, centered on the BCGs. Fig. 1 presents radial density profiles of the galaxies (diamonds with solid line) and the ERGs sample (circles with solid line) from the studied fields. The theoretical radial cluster profile, determined with the following formula:

$$\rho(r) = \frac{\rho_0}{\left[1 + (r/R_{core})^2\right]^{0.75}} \ ,$$

where $R_{core} = 20^{"}$ represents the core radius and ρ_0 is the corresponding surface density, is also drown using dashed lines. The radial density profiles reveal a strong concentration of the galaxies in the central region of the fields [2]. **ERGs** are located in the inner region of the fields, close to BCG and with **clustering tendency.**
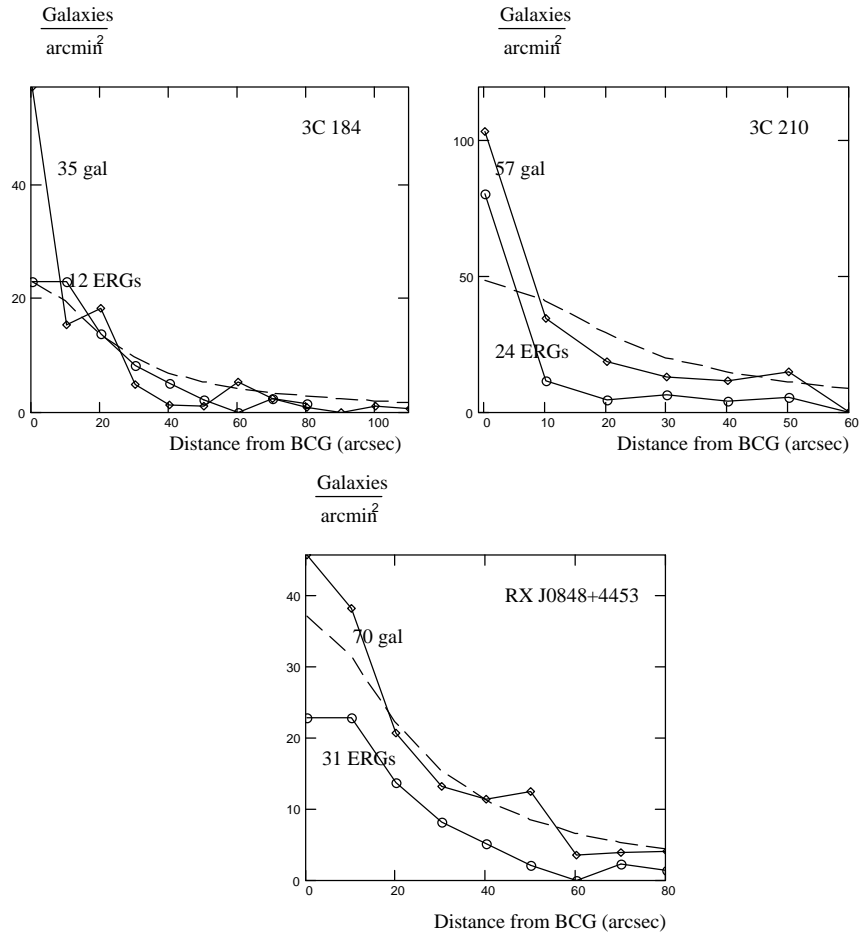
Fig. 1 – Radial density profiles of the galaxies and ERGs

4. (J-K)-K color-magnitude diagram and the morphology of z~1 red sequence galaxies

The (J-K)-K color-magnitude diagrams for the 3C 184 (Fig.2 top), 3C 210 (Fig.2 bottom) and RX J0848+4453 (Fig. 3) fields are presented. The solid lines represent the loci of the color-magnitude relations at the considered redshifts, predicted by the passive evolution models of Kodama et al. [3]. The lower dashed lines represent the adopted cut between red sequence and blue galaxies. Galaxies redder than these lines represent the red sequence galaxies and the majority of these galaxies are **morphologically early-type** (E/S0 and even Sa) - see the figures.
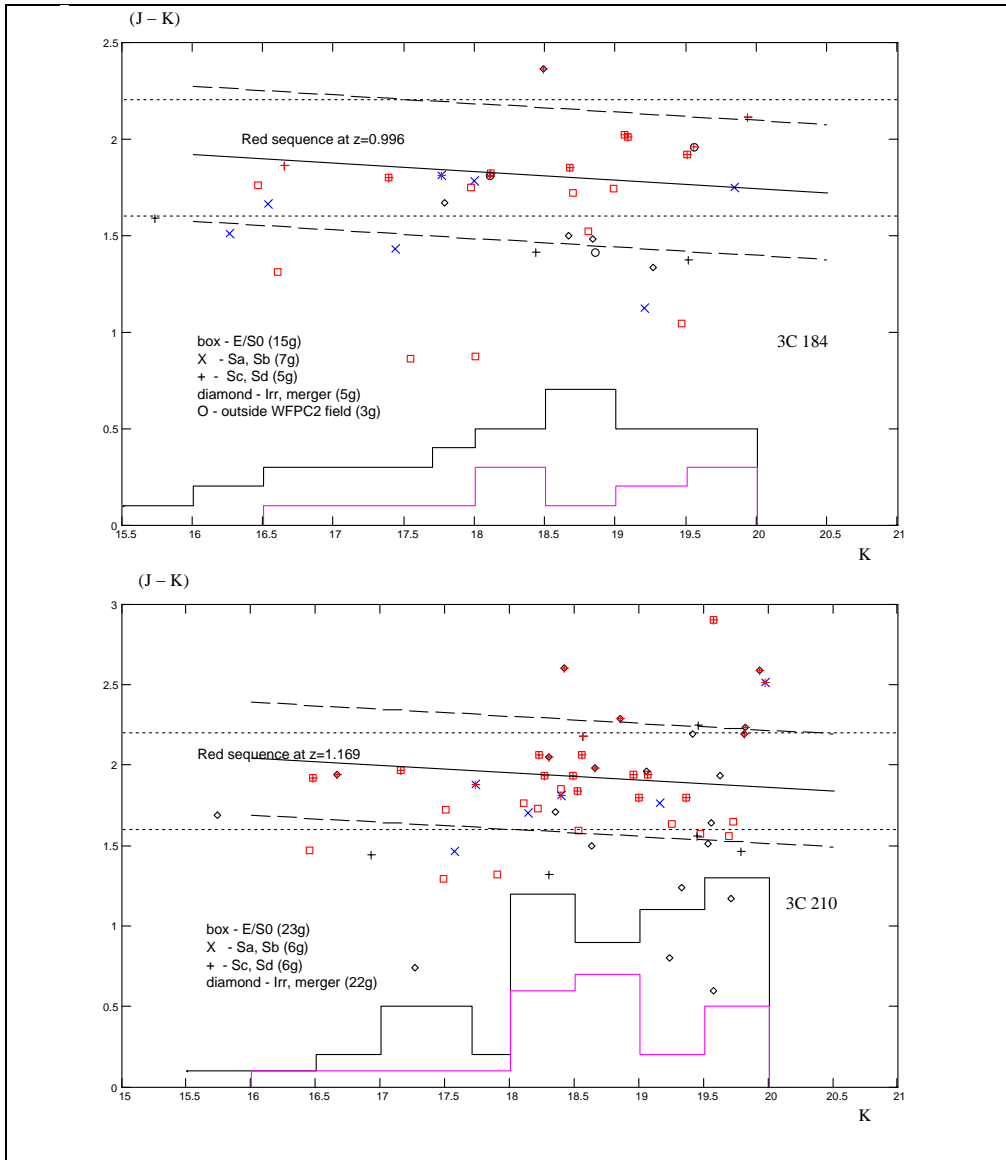
Fig. 2 - (J-K)-K color-magnitude diagrams

The upper horizontal dotted line represents the color cut (J-K) = 2.2 , above the red color-magnitude sequence of the possible cluster members. In this way is avoided the contamination with red background galaxies. Objects bluer than (J-K) = 1 are considered stars or foreground galaxies. The solid (dotted) histogram represents the (number of galaxies)/10 (ERGs/10) function of K magnitude.
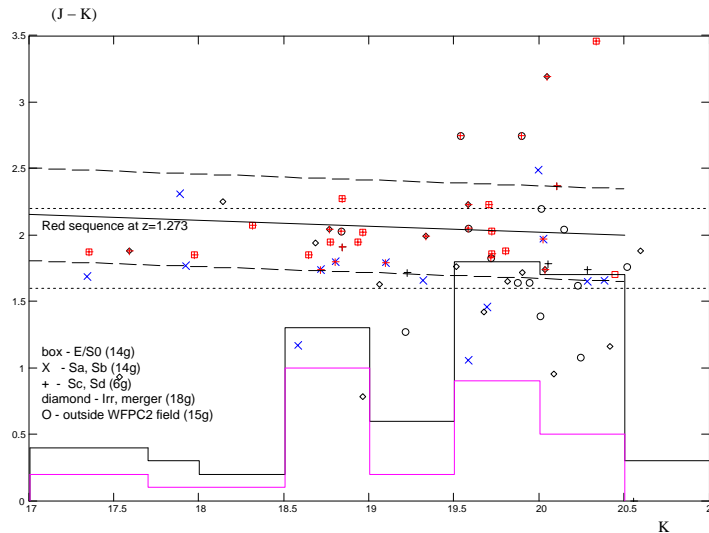
Fig. 3 - (J-K)-K color-magnitude diagram for RX J0848+4453

The 3C 184, 3C 210 and RX J0848+4453 cluster candidates belong to the sequence of red galaxies, near the passive evolution prediction at the considered redshifts, **confirming the presence of massive clusters**. The majority of these galaxies consists of **ERGs** (represented with overlapped cross on the existing symbols).

5. Conclusions

The selection criteria of the passively evolving elliptical galaxies by means of red optical and near-infrared colors contribute to the identification of galaxies clusters at z ~1. We studied the galaxies and ERGs clustering **function of colors and morphology**, specially the clustering properties of (R-K), (I-K) and (J-K) red galaxies. We determined the **presence of an excess of ERGs in the field of 3C 210** and **RX J0848+4453**, representing extremely rich samples of galaxies with extremely red colors.

References

1. Stanford, S.A., Peter R. Eisenhardt, Mark Dickinson, B.P. Holden, Roberto De Propris. Optical and Near-Infrared Photometry of Distant Galaxy Clusters, Astrophys. J. Suppl., 142, 2002, 153.

2. Popescu, N.A., M.D. Suran: Colors and HST morphology of Extremely Red Galaxies at z>1, Rom.Astron. J., 14, 2004, 3.

3. Kodama, T., N. Arimoto, A.J. Barger, A. Aragon-Salamanca: Evolution of the colour-magnitude relation of early-type galaxies in distant clusters, Astron. Astrophys, 334, 1998, .

EXOTIC ESCAPE DYNAMICS
IN HÉNON-HEILES' MODEL

Vasile Mioc[1], Badaoui Elmabsout[2], Magda Stavinschi[1]

[1]*Astronomical Institute of the Romanian Academy, Str. Cutitul de Argint 5,
RO-040559 Bucharest, Romania, E-mails: vmioc@aira.astro.ro,
magda@aira.astro.ro*
[2]*Université Paris VI Pierre et Marie Curie, Laboratoire de Modélisation en
Mécanique, E-mail: bae@ccr.jussieu.fr*

Abstract
We tackle the two-body problem associated to Hénon-Heiles' renowned potential, using the qualitative analysis methods, for the limit situation of escape. The study of the infinity flow reveals many "exotic" features as regards behaviour of escape solutions.

1. INTRODUCTION

Hénon-Heiles' potential [1] was intended to model the motion of a star within a galaxy. It reads $U(q_1, q_2) = Aq_1^2 + Bq_2^2 + Cq_1^2 q_2 + Dq_2^3$, with $(q_1, q_2) \in \mathbf{R}^2$ Cartesian coordinates and $(A, B, C, D) \in (0, +\infty)^2 \times \mathbf{R}^2$.

In this paper we tackle the escape dynamics in the two-body problem associated to this potential, via qualitative analysis. Using McGehee's techniques [2, 3], we construct the *infinity manifold* and depict the flow on it. We find many "exotic" features, which point out the complexity of the escape dynamics in this field.

2. BASIC EQUATIONS AND SYMMETRIES

Consider the relative motion of a unit-mass particle w.r.t. the field source. Its dynamics is associated to the planar Hamiltonian

$$H(\mathbf{q}, \mathbf{p}) = (p_1^2 + p_2^2)/2 - U(\mathbf{q}), \qquad (1)$$

in which $\mathbf{q} = (q_1, q_2) \in \mathbf{R}^2$ and $\mathbf{p}(= \dot{\mathbf{q}}) = (p_1, p_2) \in \mathbf{R}^2$ are the configuration vector and the momentum vector of the particle, respectively.

The system admits the first integral of energy, $H(\mathbf{q}, \mathbf{p}) = h$ (energy constant), but, given the anisotropic structure of the potential, the angular momentum is not conserved.

To tackle the escape dynamics, we pass to polar coordinates (r, θ) and polar components of velocity $(\dot{r}, r\dot{\theta})$. Then we use the McGehee-type transformations [3, 4]

$$\rho = r^{-1}; \quad (x, y) = \rho^{3/2}(\dot{r}, r\dot{\theta}); \quad d\tau = \rho^{-1/2}dt, \tag{2}$$

which make the motion equation corresponding to (1) become

$$
\begin{aligned}
&\rho' = -\rho x, \quad \theta' = y, \\
&x' = -3x^2/2 + y^2 + 2(A\cos^2\theta + B\sin^2\theta)\rho + \\
&\quad + 3(C\cos^2\theta + D\sin^2\theta)\sin\theta, \\
&y' = -5xy/2 + 2(B - A)\rho\sin\theta\cos\theta + \\
&\quad + [3(D - C)\sin^2\theta + C]\cos\theta.
\end{aligned} \tag{3}
$$

The energy integral reads

$$
\begin{aligned}
&(x^2 + y^2)/2 - (A\cos^2\theta + B\sin^2\theta)\rho - \\
&- (C\cos^2\theta + D\sin^2\theta)\sin\theta = h\rho^3.
\end{aligned} \tag{4}
$$

In (3)-(4), $' = d/d\tau$, and we kept, by abuse, the same notation for the new functions of τ.

Equations (3) have four symmetries: $S_i = S_i(\rho, \theta, x, y, \tau)$, $i = \overline{0,3}$:

$$
\begin{aligned}
&S_0 = (\rho, \theta, x, y, \tau) = I \ (identity), \quad S_1 = (\rho, \theta, -x, -y, -\tau), \\
&S_2 = (\rho, \pi - \theta, -x, y, -\tau), \quad S_3 = (\rho, \pi - \theta, x, -y, \tau),
\end{aligned} \tag{5}
$$

which form an Abelian group with idempotent structure, isomorphic to Klein's group. These symmetries are of much help in describing the escape dynamics (see below).

3. INFINITY MANIFOLD AND THE FLOW ON IT

Eqs. (3) are well defined for the boundary $\rho = 0$ (escape), which is invariant to the flow, because $\rho' = 0$ for $\rho = 0$; (4) also extends smoothly to this boundary. In this way, we obtain the *infinity manifold* (pasted on the phase space), provided by (4) with $\rho = 0$:

$$
M_\infty = \left\{ (\rho, \theta, x, y) \mid \rho = 0, \ \theta \in S^1, \atop x^2 + y^2 = 2(C\cos^2\theta + D\sin^2\theta)\sin\theta \right\},
$$

and the corresponding vector field, provided by (3) with $\rho = 0$:

$$\theta' = y, \quad x' = 5y^2/2, \quad y' = -5xy/2 + [3(D - C)\sin^2\theta + C]\cos\theta,$$

We see that the flow on M_∞ is gradientlike w.r.t. x. We also see that M_∞ is never defined on the whole S^1, its shape and domains of existence depending on C and D.

Let us depict the flow on M_∞. It has no physical significance, but – due to the continuity of solutions w.r.t. initial data – it yields valuable information about orbits that neighbour escape. We distinguish the following cases:

(1.1) $C = D > 0$. M_∞ is homeomorphic to a 2D-elipsoid of axis length π along θ for $\theta \in [0, \pi]$, and $M_\infty = \Phi$ else. By (7), the flow on M_∞ has two equilibria: $E^\pm(\theta, x, y) = (\pi/2, \pm\sqrt{2D}, 0)$. E^- is a source, E^+ is a sink, whereas the rest of the flow consist of heteroclinic orbits that move from E^- to E^+ (Fig. 1).

(1.2) $C = D < 0$. The case is identical to (1.1), but $\theta \in [\pi, 2\pi]$ and $E^\pm(\theta, x, y) = (3\pi/2, \pm\sqrt{-2D}, 0)$.

(2.1) $0 < C \neq D > 0$. If $C \leq 3D/2$, we have the same phase portrait as (1.1). If $C > 3D/2$, M_∞ is a "dumb-bell" in $[0, \pi]$ with six equilibria: $E_{1,3}^-$ (sources), $E_{1,3}^+$ (sinks) and $E_2^\pm$ (saddles). Besides them, there are four permanent heteroclinic connections: source-saddle ($E_1^- \to E_2^-, E_3^- \to E_2^-$) and saddle-sink ($E_2^+ \to E_1^+, E_2^+ \to E_3^+$), and eight or four more heteroclinic orbits that form three different phase portraits (see Figs 2–4).

(2.2) $0 > C \neq D < 0$. For $C \geq 3D/2$ and $C < 3D/2$, the flows are identical to those corresponding to the cases (1.1) and (2.1), but shifted by π w.r.t. θ ($\theta \in [\pi, 2\pi]$).

(2.3) $C > 0, D < 0$. M_∞ is homeomorphic to *three* disjoint 2D-ellipsoids, spread on $[0, 2\pi]$ along θ, on which the flow is identical to the case (1.1).

(2.4) $C < 0, D > 0$. From a qualitative standpoint, this case is identical to (2.3), only the position of the ellipsoids along the θ-axis differs.
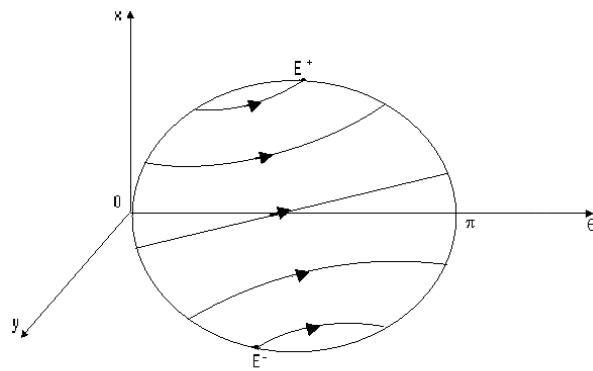
Fig. 1
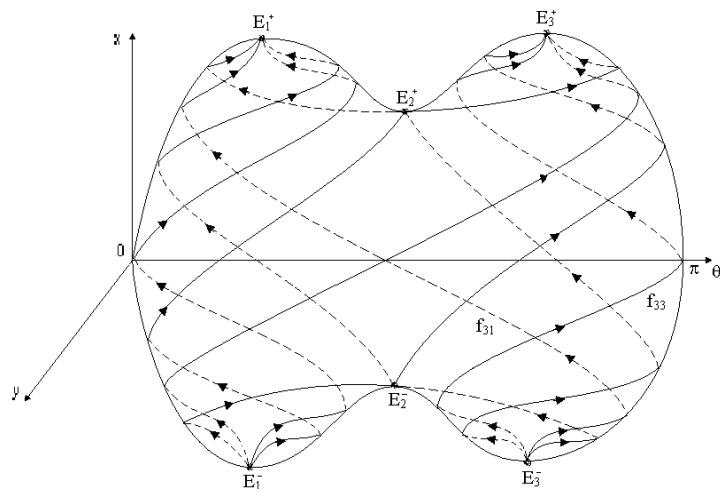
Fig. 2
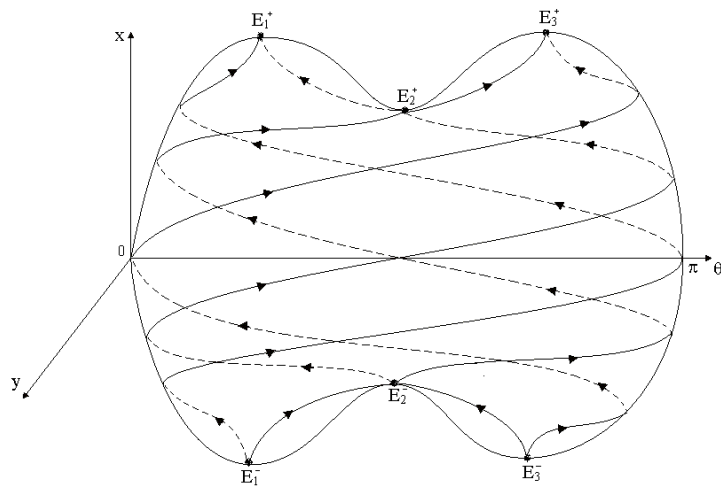
Fig. 3
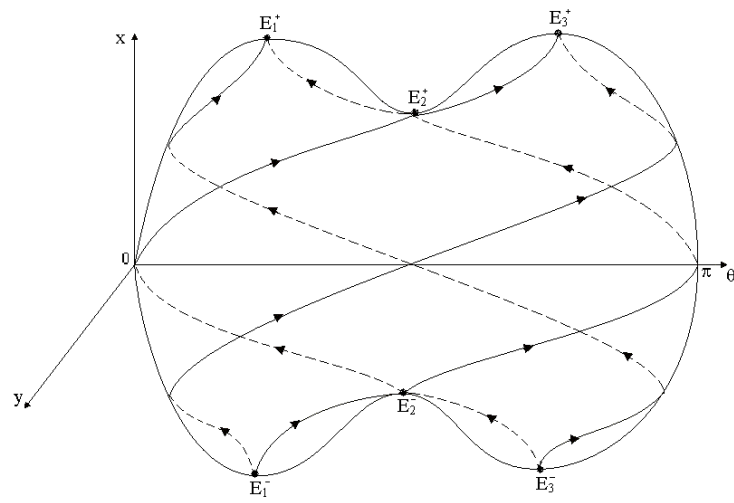
Fig. 4

4. CONCLUSIONS

Without proof, we state the main conclusions:

- Escape solutions are not regularizable.
- Escape solutions are of three different kinds: radial (with zero angular momentum), spiral (with nonzero angular momentum keeping its sign), or oscillatory (with the angular momentum alternating its sign).
- The nonradial escape motion tends asymptotically to rectilinear escape.
- The flow on the infinity manifold obeys three quite different scenarios, which are noncontradictory as regards uniqueness and symmetries. This means that there are hidden bifurcations we are not able to detect yet. However, following [4], we conjecture that saddle-saddle connections (Figs 3 and 4) are much more improbable (from the standpoint of the Lebesgue measure) than the connections illustrated in Fig. 2.

This offers a wide understanding of escape dynamics in Hénon-Heiles' model.

REFERENCES

1. Hénon M., C. Heiles. The applicability of the third integral of motion: some numerical experiments, Astron. J. 69, 1964, 73-79

2. McGehee R.. A stable manifold theorem for degenerate fixed points with applications to celestial mechanics, J. Diff. Eq. 14, 1973, 70-88

3. McGehee R. Triple collision in the collinear three body problem, Invent. Math. 27, 1974, 191-227

4. Devaney R. L. Collision orbits in the anisotropic Kepler problem, Invent. Math. 45, 1978, 221-251

PMS versus Post-MS

Marian Doru Suran

Astronomical Institute of the Romanian Academy
e-mail: suran@aira.astro.ro

Abstract

Close to the main sequence the HR diagram is confusing, as stars of similar global properties but with different stages of evolution occupy the same position. Pulsating stars (both PMS and Post-MS) were discovered in this area. In some cases the young PMS stars are recognized through specific characteristics - for instance the presence of nebulosity or high degree of activity. An alternative is to take advantage of seismological information whenever it is possible. In this case the discrimination between PMS and Post-MS can be made using differences in their oscillatory frequency distributions in the low frequency range.

1. Introduction

In the vicinity of the main sequence, the HR diagram is confusing as stars of similar global properties but different stages of evolution lie at the same position. The outer layers of PMS and Post-MS stars having the same effective temperature and gravity are very similar. For pulsating stars, as these layers drive the pulsation in this range of temperature, it is reasonable to expect that PMS stars in the instability strip are also destabilized by a classical opacity mechanism with a similar range of unstable modes as for the Post-MS stars. This supports the vibrational instability as explanations for few stars which are suspected to be in the PMS stage (HAEBE type stars).

Differences, on the other hand, exists (in the deep interior) between the two stages: whereas PMS are relicts of the gravitational contraction phase, the Post-MS stars develop chemical inhomogenities. What is the imprint of these differences on the observable (near-surface *f*-, *p*- modes) modes of the stars? Is it possible to decide the evolutionary status of the stars using only the asteroseismological data? Some of the answers will be given in this paper.

2. Evolutionary tracks

In the early stages of PMS evolution, rapid dynamical and thermal processes occur which modify the internal structure of the protostar. By the time when a $1.8 M_\odot$ protostar reaches the classical instability strip on its way towards the main sequence, these complex phenomena have long disappeared and the evolution has considerably slowed down. The usual quasi-static approximation then holds and it is assumed here. Rotation is not considered and the star is modeled in the spherically symmetric equilibrium state.

Equilibrium models have been computed with the **CESAM code** (Morel [1])), an evolutionary code with a numerical accuracy of first order in time and third order in space. The evolutionary model is built with ~300 mesh points in mass, but to perform detailed pulsation calculations, the mesh has been extended to 2400 mesh points, using spline interpolation functions. An EFF equation of state (Eggleton et al. [2]) , opacities from Livermore Library (Iglesias & Rogers[3]) completed at low temperature (T<10000K) by Alexander & Ferguson [4], nuclear reaction rates of Caughlan & Fowler ([5]), standard mixing length treatment of convection with solar α=1.67, X=0.71, Y=0.27, Z=0.02, and a standard solar mixture of heavy elements (Grevesse & Noels [6]) are used in our calculations (as sufficient approximations for an $1.8 M_\odot$ star).

Fig. 1 shows the evolutionary track running from the latest PMS stages to the early Post-MS ones for our $1.8 M_\odot$ star. We plot results from two different evolutionary codes – CESAM code (C, already discussed) and Henyey code (B, based on classical 'old' libraries and equation of state) - both implemented on a **Silicon Graphics ALTIX system**.
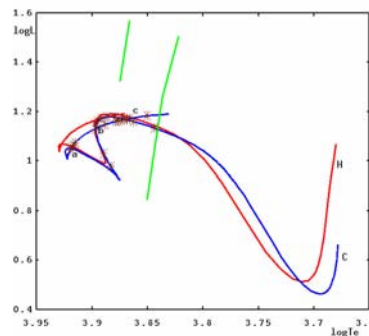
Figure 1. The evolutive tracks of 1.8 $M_\odot$ star in the HR diagram using CEASAM(C) and HENYEY(B) codes. We have labeled the common points (PMS,Post-MS) as a.,b.,c. The edges of the instability strip are also shown.

On the track, three common points of the PMS and Post-MS (labeled as a-, b-, c-) can be found for both C and B models (see Tab. 1).

The comparative physical structures of the $1.8M_\odot$ in the point **c.** (both the PMS and Post-MS evolutive stages) are shown in Fig.2. We choose point **c.** because here the differences between PMS and Post-MS stages are maximal (far stellar evolutive points on each branches). As expected, the outer layers of associated models are very similar (practically the same κ- and Γ_1 profiles). On the other hand, the central regions differ significantly (differences in ε- profile). The PMS model is still contracting and *remains chemically homogeneous.* By contrast, the Post-MS model *has already developed*, in the central region *a μ chemical gradient.* The signature of this chemical gradient (due to hydrogen depletion and the fully mixing in the central core) on the Post-MS stage is clearly seen on the profile of th Brünt Vaissälä frequency, N.

	Log T	Log L	R	Age	X_c	r_{conv}
a.M13	3.919	1.050	1.621	4.8	0.7134	0.186
M16	3.920	1.044	1.608	300.	0.6383	0.204
b.M8	3.897	1.129	1.970	1.25	0.7142	0.221
M19	3.897	1.131	1.978	900.	0.4355	0.191
c.M4	3.872	1.170	2.319	0.7	0.7142	0.068
M23	3.872	1.167	2.312	1160.	0.3132	0.180

Table 1. Common PMS and Post-MS points on the track of an $1.8M_\odot$ star. Ages are in Myr, luminosities and total stellar radius, in solar units, convective radii r_{conv} in unit of the total stellar radii and X_c (the central hydrogen content) in percentage.
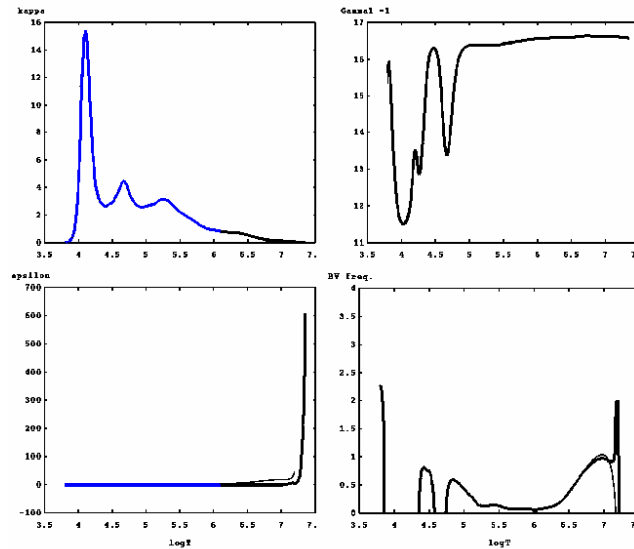
Figure 2. The structure of the stars in the common point c. Thin line-PMS star, thick line– Post-MS star. We have represented (from top left): κ, Γ_1, ε, and Brunt-Vaissala frequency.

3. Nonradial pulsations

The question which we address is: would it be possible to discriminate the evolutive stage using only asteroseismological data (frequency differences), even though the stellar surface parameters for the three points are the same? If YES, which kind of different phenomena can be inferred in the PMS and Post-MS stages.

This problem can be understood more easely comparing the nonradial pulsationary properties (the power spectrum) for the $1.8 M_\odot$ star during the whole stellar evolutionary track (see Fig.3).

For the calculation of the nonradial pulsations we use a **LNAWENANR code** (a linear, non adiabatic, non radial code) implemented also on the **SGI ALTIX platform**. We use an eigenfrequency range $0 \leq \omega_R \leq 16$ (which include *g-, f-, p-* modes, *n ranging from -10 to 10*), a spectrum range $l = 0$-2, with κ-, Γ_1- *and* ε- *pulsation mechanisms inferred,* and in place of ω_I we use the Dziembowski unitary parameter η.
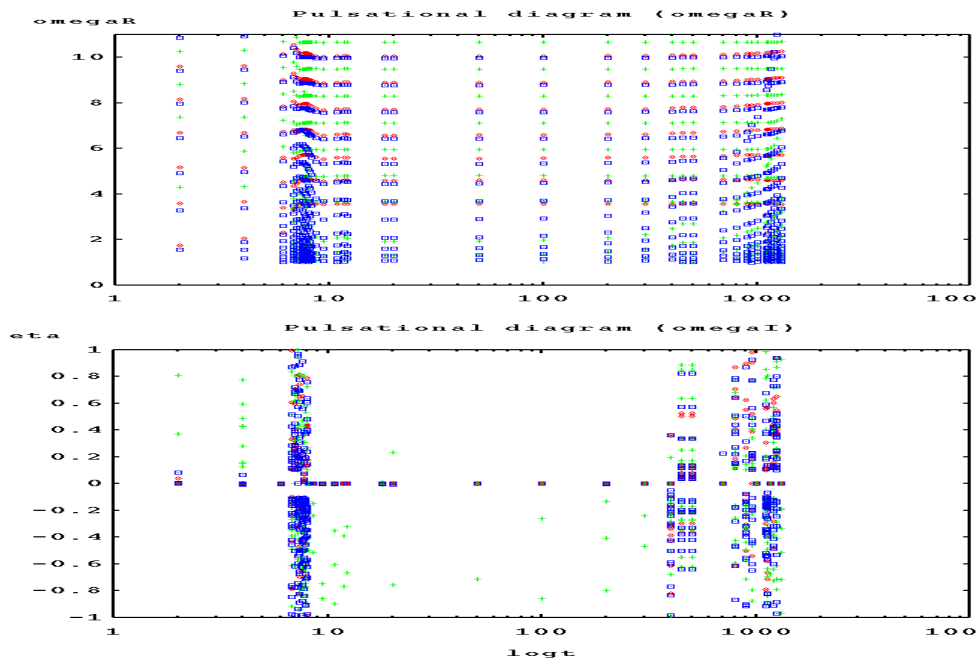
Figure 3. The evolutive power spectrum. Top: ω_R; bottom: ω_I. Time in Myr.

For the calculation of the nonradial pulsations we use a **LNAWENANR code** (a linear, non adiabatic, non radial code) implemented also on the **SGI ALTIX platform**. We use an eigenfrequency range $0 \leq \omega_R \leq 16$ (which include *g-*, *f-*, *p-* modes, *n ranging from -10 to 10*), a spectrum range $l = 0\text{-}2$, with κ-, Γ_1- and ε- *pulsation mechanisms inferred,* and in place of ω_I we use the Dziembowski unitary parameter η.

Our calculations show that in the instability strip (both in the PMS and the Post-MS regions) the main destabilizing pulsatory mechanism remains the κ- mechanism. The ZAMS and post-MS pulsatory region is occupied by well known δ Scuti stars, and the PMS pulsatory region is occupied by HAEBE (Herbig Ae/Be) stars. Our point **c.** and possible **b.** point (depending on the location of the blue limit of the instability strip) lies in this region.

Another instability region is present near ZAMS (including PMS, ZAMS, Post-MS phases), our point **a.** lying to this region. This zone represents a prolongement of the instability region which extends between β-Cephei (destabilizing κ- mechanism, high *g*-modes) to Sun-like pulsators (chaotic surface excitation mechanism, *p*- modes).

In the present paper we restricted only to the instability strip. Two distinct disturbative phenomena can be seen on the [evolutive] power spectrum, one in the PMS region and other in the Post-MS region. If in the latest Post-MS stages the well known *effect of avoid crossing* (mode penetrating) is present, new phenomena are seen in the PMS region: *the bump of modes* and *the occurrence of strange modes*. These phenomena are related both to the complicate interaction of convection and pulsation for the PMS stars. Indeed the transaction from the convection to the radiation and the interaction with pulsation in a PMS star are complicated (and not yet well explained!) phenomena. Finally, the frequency calculations show the existence of strange modes, *i.e.* surface modes trapped in the very superficial outer layers. Whether these modes are excited or are not is probably strongly dependent on the convection-pulsation interaction, which is very approximately taken into account in our paper.

The comparison between the pulsational properties ($l = 2$), for the three common points a-,b-,c-, are presented in Fig.4. The differences between modes are due to the presence of that two disturbing phenomena - bumps of modes in the PMS region and avoid crossing/penetrating modes in the post-MS stages.
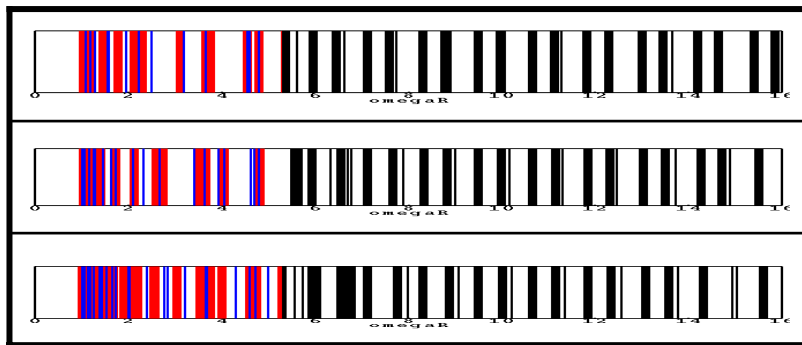
Figure 4. The comparative power spectrum (*l*=2) in points a-, b-, c- (from top to bottom).Thin line – PMS star, thick line – Post-MS star.

4. Conclusions

PMS star of $1.8M_\odot$ crossing the classical instability strip on the way to the ZAMS, are found to be vibrationally unstable (HAEBE stars),

destabilized by the same mechanism as for the δ Scuti stars, indicated as ZAMS or Post-MS stars. The asteroseismological differences between the PMS and Pot-MS stars are due to two different mechanisms which are present during the evolution of the $1.8M_{\odot}$ star.

One is the well known avoid crossing phenomenon for the Post-MS evolution, which gives birth to the penetrating modes. The other, is a new discovered phenomenon (Suran et al. [7]), the bump of pulsating modes for PMS stars which gives birth to different hieratic, strange, modes. These modes are complicated and represent the interaction of convection with the pulsation in the early stages of the stellar evolution.

Our results could be directly applied to the star V351 Ori, a prototype of such a PMS/Post-MS star, which has an estimated mass of $\sim 1.8M_{\odot}$, and lies very close to our point **c.** on the HR diagram

On the other hand, we must find out observationally more PMS/HAEBE and POST-MS/δ Scuti stars sharing the same HR region. The future asteroseismological COROT mission – in which our team intends to participate – could be such a good observational opportunity.

References

1. M o r e l, P. A code for the stellar evolution calculations, A&AS, 124, 1997, 597
2. E g g l e t o n, P.P., F a u l k n e r, J., F l a n n e r y, B.P., An approximate equation of state for stellar material, A&A, 23, 1973, 325
3. I g l e s i a s, C., R o g e r s, F., Up date opacities, ApJ, 464, 1996,943
4. A l e x a n d e r, D.R., F e r g u s o n, J.W., Low-temperature Rosseland opacities, ApJ,437, 1994, 879
5. C a u g h l a n, G.R., F l o w e r, W.A., Thermonuclear reaction rates (V), Atomic Data and Nuclear Data Tables, 40, 1988, 284
6. G r e v e s s e, N., N o e l s, A., A revision of the solar abundance, A&A, 271, 1993, 587
7. S u r a n, M.D., G o u p i l, M.J., B a g l i n, A., L e b r t o n, Y, C a t a l a, C., Comparative seismology of pre- and main sequence stars in the instability strip, A&A, 372, 2001, 233.

DISTANCE MODULUS OF THE DWARF GALAXY IC10

Evgeni Ovcharo, Petko Nedialkov

Department of Astronomy, Sofia University, 5 J. Bourchier Blvd.,

Abstract.

*We used three new metallicity dependent distance indicators based on the **K**-luminosity function of red supergiants in the field of the dwarf galaxy **IC10** to derive the distance modulus and the total extinction along that sightline. The obtained values: $(m-M)_0 = (24.3 \pm 0.3)^m$ and $A_K = (0.46 \pm 0.05)^m$ are in a good agreement with the recent results based on the **TRGB** method.*

The irregular dwarf galaxy **IC10** (**RA(J2000)** $= 00^h\ 20^m\ 23.16^s$; **DEC(J2000)** $= +59° \ 17'\ 34.7''$) is a member of the Local group, laying close to the Galactic equator ($\mathbf{b} = -3.3°$). The high and uncertain value of the foreground extinction combined with the peculiarities of **IC10** itself (a widespread burst of star formation and a significant amount of varying internal extinction) lead to contradictive results when the distance modulus has been considered. The values of the obtained $\mathbf{(m-M)_0}$ fall in the range of $(\mathbf{23.86 \pm 0.12})^{\mathbf{m}}$ as derived in [1] and $(\mathbf{24.95 \pm 0.20})^{\mathbf{m}}$ – in [2].

In this work we used three new distance indicators based on the luminosity function in **K**-passband for red supergiants (**RSGs**) in order to obtain a distance to **IC10**, taking for the first time into account the metallicity effect.

Our study is based on data provided by Two Micron All Sky Survey (**2MASS** - http://ftp.ipac.caltech.edu/pub/2mass/allsky/) as **J&K** magnitudes of ~ **2000** point-like sources (stars) in a target field, centered on **IC10** and covering total area of **360** square arcmin. For the metallicity we adopted values **[O/H]+12 = 8.25** of [3] and **[Fe/H]** $= -0.5$ of [4], corresponding to 0.006 in terms of metallicity **Z**. We also assumed a standard extinction law ($\mathbf{R_V = 3.1}$) along all sightlines toward **RSGs** in **IC10**.

We used theoretical evolutionary tracks for the most massive in the **RSGs** phase on the **CMD M_K** vs. **$(J-K)_0$** with varying metallicity **Z = 0.004, 0.016, 0.028** to obtain an universal liner fit relating the luminosity and the colour (Fig. 1). The adopted linear fit allows selection of the **RSGs** branch on the **CMD**, taking into account the errors of photometry. Its slope was found to be quite steep: **-14.7 ± 1.1** and not very sensitive to the metallicity

Initially, we divided the stars samples in the target field of **IC10** into two sub-samples, covering equal area inside and outside the galaxy, respectively. The next step was to construct the **CMDs** (Fig. 2) for the inner (upper left panel) and the outer field (upper right panel). The **RSGs'** branch is identified via numerical subtraction (applying an algorithm, removing the closest neighbouring points on the **CMD**s for the inner and outer field), resulting in a new **CMD**, shown in lower left panel of Fig. 2. The adopted line for metallicity **Z = 0.006** (corresponding to mean true colour **$(J-K)_0 = 0.85^m$**) is slided along reddening vector in order to fit the cloud of **RSGs**. This allowed us to estimate the mean total (foreground + internal) extinction of the **RSGs**: **$A_K = (0.46 \pm 0.05)^m$**. Finally, we constructed (see, the lower right panel of Fig. 2,) the apparent **K**-luminosity function found to be complete for the first four bins. Thus, we applied a completeness correction for the fifth bin in order to use the distance indicators, calibrated for the brightest 5 half magnitude bins.
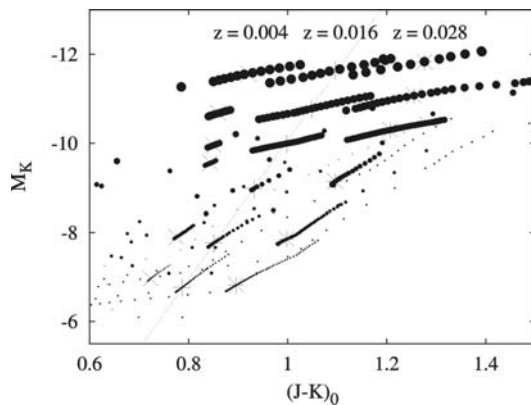
Fig. 1: Theoretical evolutionary tracks for massive stars in **RSGs'** phase on **CMD** diagram **M_K** vs. **$(J-K)_0$**. The size of the symbols is proportional to the

stellar mass in the range 7÷30 Solar masses. The metallicity Z varies between 0.004 and 0.028. Thin dashed line represents the linear fit with a slope of –14.7.

Table 1. Distance modulus of **IC10** galaxy and mean extinction toward it as derived by different authors

Parameter	Value	Reference
(m – M)$_0$ [mag]	24.95 ± 0.20	[2]
	23.86 ± 0.12	[1]
	24.10 ± 0.19	[7]
	24.59 ± 0.30	[6]
	24.57± 0.21	[9]
	24.90 ± 0.10	[3]
	24.30 ± 0.30	this work
A$_K$ [mag]	0.35 (total)	[1]
	0.52	[8]
	0.40 (total)	[7]
	0.27 (total)	[3]
	0.30	[10]
	0.46 (total)	this work

We used the selected **RSGs**, ordered by increasing apparent **K**-magnitude, and the constructed **K**-luminosity function, to determine three parameters, namely **K(0.12)** − the apparent magnitude of a real **RSG** with a consecutive number N, defined as $N/N_{tot} = 0.12$, where N_{tot} is the total number of **RSGs** in the first five half magnitude bins, **K(12%)** and **K(21%)** - apparent magnitudes, corresponding to the value of the linear fit "**log(N) – K**" defined as $N/N_{tot} = 12\%$ and **21%**. The values of **K(0.12)**, **K(12%)** and **K(21%)** are related to the distance indicators $M_K(0.12)$, $M_K(12\%)$ and $M_K(21\%)$, calibrated by [5] as a function of metallicity and easily obtained via substitution with the adopted values of **[O/H]+12** and **[Fe/H]**. Finally, the distance modulus is estimated are via the equation: $(m – M)_0 = K - A_K - M_K$.

The obtained values are $(23.84 \pm 0.26)^m$, $(24.18 \pm 0.29)^m$ and $(24.44 \pm 0.29)^m$, respectively. They are consistent at 2σ level, but only the last two are really luminosity function based on. Their mean $(24.3 \pm 0.3)^m$, together with other results, is given in Tab. 1.

Their own **IR**-photometry was used by [1] to select **RSGs** and to derive a distance modulus of $(23.86 \pm 0.12)^m$. However, they did not take into account the difference of **0.4** in metallicity between **IC10** and **IC1613**. Our result is in best agreement with $(m-M)_0$ of [7]: $(24.10 \pm 0.19)^m$,

Fig. 2: Infrared **CMDs** and luminosity function in the field of **IC10** galaxy: upper panels - **CMD** for the inner field (left) and outer field (right); lower left panel – the difference "inner field **CMD** -outer field **CMD**"; lower right panel – the apparent **K**-luminosity function of **RSGs**.
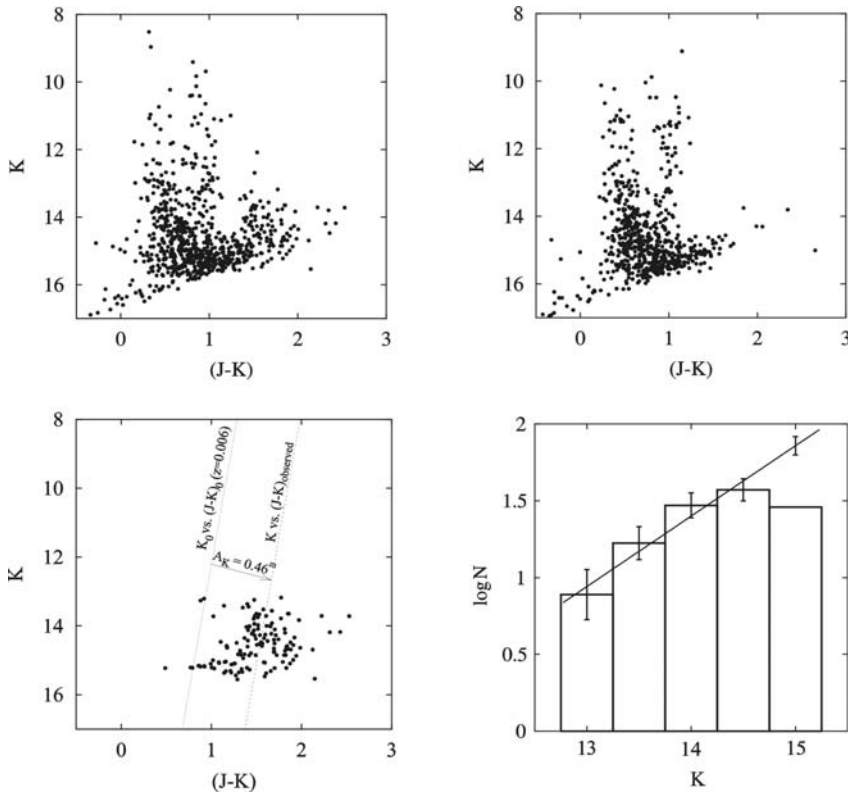
which is somehow expected, because all distance indicators are based on distances, calibrated by the Tip of the Red Giant Branch (**TRGB**) method.

Acknowledgments

References

[1] B o r i s s o v a J., L; G e o r g i e v, M. R o s a d o, R. K u r t e v, A. B u l l e j o s, M. V a l d e z - G u t i e r r e z, Infrared photometry of the Local Group dwarf irregular galaxy IC10, A&A, 363, 2000, 130 - 140

[2] H u n t e r D., The Stellar Population and Star Clusters in the Unusual Local Group Galaxy IC10, ApJ, 559, 2001, 225 - 242

[3] M a s s e y P., T. A r m a n d r o f f, The Massive Star Content, Reddening, and Distance of the Nearby Irregular Galaxy IC10, AJ, 109, 1995, 2470 - 2479

[4] O e s t r e i c h e r M., T h. S c h m i d t - K a l e r, Red supergiants in the LMC - II. Spectrophotometry and model atmospheres, MNRAS, 299, 1998, 625 - 636

[5] O v c h a r o v E., P. N e d i a l k o v, New distance indicators based on the IR luminosity function of red supergiants, Meetings in Physics, 5, 2004, (in press)

[6] S a h a A., J. H o e s s e l, J K r i s t, E. D a n i e l s o n, Variable Stars in the Dwarf Galaxy IC10, AJ, 111, 1996, 197 - 207

[7] S a k a i S., B. M a d o r e, W. F r e e d m a n, Cepheid and Tip of the Red Giant Branch Distances to the Dwarf Irregular Galaxy IC10, ApJ, 511, 1999, 671 - 679

[8] S c h l e g e l D., D. F i n k b e i n e r, M. D a v i s, Maps of Dust Infrared Emission for Use in Estimation of Reddening and Cosmic Microwave Background Radiation Foregrounds, ApJ, 500, 1998, 525 - 553

[9] W i l s o n C., D. W e l c h, I. R e i d, A. S a h a, J. H o e s s e l, The Distance To IC10 From Near - Infrared Observations of Cepheids, AJ, 111, 1996, 1106 - 1109

[10] H y p e r L e d a, http://www-obs.univ-lyon1.fr/hypercat

THE GRAVITY DARKENING EFFECT: FROM VON ZEIPEL UP TO DATE

Rovithis-Livaniou H.

Section of Astrophysics, Astronomy & Mechanics, Dept. of Physics, Athens University, Panepistimiopolis, Zografos 157 84, Athens, Greece.
e-mail: elivan@cc.uoa.gr

Abstract

The gravity darkening effect and the theoretical methods developed so far – starting from von Zeipel, who theoretically predicted it– are briefly referred. The various approaches made by several investigators to get the gravity darkening exponents of close binaries, from the analysis of their observational data, are also referred and discussed. Special attention is given to the latest obtained results.

1. Introduction

The existence of the gravity darkening effect over the surfaces of stars in radiative and hydrostatic equilibrium, distorted by axial rotation, was theoretically predicted as early as 1924 [1]. While a few years later it was extended to tidally distorted configurations [2].

On the other hand, the photometric consequences of this effect on the light changes of close eclipsing binaries for centrally condensed stars in total or partial radiation were studied [3,4]. Moreover, the laws of gravity darkening for the black body case -appropriate for any particular effective wavelength- were formulated [5].

Besides the forgoing mentioned very early approaches to the subject, the effect of gravity darkening has attracted the interest of many investigators. So, it was theoretically studied for stars with convective envelopes, too [6]; and recently it became the subject of extended examination [7,8,9,10].

Moreover, attempts were made to get gravity darkening values via observational data analysis, using various techniques. These were mainly applied to close binary stars, where the effect was expected to be stronger because of their components' distortion.

Thus, in this brief review, the most important of the theoretical as well as the observational attempts to study the gravity darkening effect will be referred and discussed.

2. Theoretical Approaches

More than a century ago, in 1924, von Zeipel [1] concluded that: "*the emergent flux, F, of the total radiation at any point over the surface of a rotationally or tidally distorted star in radiative equilibrium varies proportionally to the local gravity g*". That is: $F \prec g$ or $F \prec g^\tau$, where the exponent τ is known as the *gravity-darkening coefficient*. And if the energy transfer in the sub-surface layers of a star is purely radiative, it was found that τ is equal to unity ($\tau=1$).

Many years later, a different value for τ was given. Actually, fitting together convective envelopes having different surface gravities at a depth where the temperature gradient becomes adiabatic, it was found that $\tau=0.32$ [6].

And since between the emergent flux and the temperature there exist the relation:

$F \sim (T_{eff})^4$, it is obviously: $T_{eff} \prec g^{\tau/4}$ or: $T_{eff} \prec g^\beta$

where β -known as the *gravity darkening exponent*- is equal to $\tau/4$.

The relations: $F \prec g^\tau$ or $T_{eff} \prec g^\beta$ are also referred and known as the gravity darkening law, and:

a) $\beta=0.25$, when the energy transfer is purely radiative, (von Zeipel's law), while

b) $\beta= 0.08$, for stars with convective envelopes (Lucy's law).

Later, from more detail studies, it was pointed out that the von Zeipel gravity-darkening law is strictly only true [11]. That is, if: 1) the rotation law is conservative, i.e. the centrifugal force is derivable from a potential and 2) the radiative flux is approximated by the diffusion equation $F = -\frac{4\pi}{3}\frac{1}{k\rho}\nabla B$ used in stellar interiors. All symbols used in the previous equation have their usual meaning: k & ρ stand for opacity and density, respectively; while, B is the integrated Planck function; that is: $B = \frac{1}{\pi}\sigma T^4$.

Then, ρ, T, and the pressure P are all functions of the total potential Ψ (gravitational plus centrifugal), and: $F = -\frac{4\pi}{3}\frac{1}{k\rho}\frac{dB}{d\Psi}\nabla\Psi = -f(\Psi)g$, where $g = \nabla\Psi$ is the effective gravity.

If the transfer equation is used, but meridional circulation is neglected, a perturbation treatment shows that the emergent flux F satisfies the relation: $|F| \propto g^{1/2}$ for all conservative rotation laws. The inclusion of circulation, however,

seems to restore von Zeipel's law, $\lvert F \rvert \prec g$. For non-conservative rotation laws, $\lvert F \rvert$ is no longer a simple power of g, even assuming the diffusion equation.

Similarly, for magnetic stars, it was concluded that the important factor determining β might be **the ratio of magnetic energy to rotational energy** rather than the absolute value of either [12]. And for most of the models studied, a good approximation for the gravity darkening would be: $\lvert F \rvert \propto \lvert g \rvert^{1.1}$. However, there is some evidence that slowly rotating, strongly magnetic stars could have a much stronger dependence of $\lvert F \rvert$ on $\lvert g \rvert$, comparable to that found by others [11], for some non-magnetic rotating models [13]. Generally we could say that for most of the models studied, there is only a small departure from von Zeipel relation. However, for stars with a large ratio of magnetic to rotational energy the variation of emergent flux with gravity could be quite strong, (which could be relevant for a few **Ap** stars).

On the other hand, for stars with convective envelopes, it was found that assuming a simple opacity law, and *if the entropy is constant* in an envelope, the values of β are compatible with the earlier derived [14]. While, a modified form of Lucy's gravity darkening law was obtained and it was shown that, for the secondary components of **W UMa** type contact binaries, the gravity-darkening coefficient was $\tau \approx 0.32$, in agreement with Lucy's predictions [15]. In particular, the gravity darkening exponent β was calculated for a broad spectrum of masses and mass ratios, and was found that for the secondary component in **W UMa** type stars $\beta \sim 0.08$. This means that β **does not change significantly** with the mass-ratio **q** and the mass m_s of the secondary component. Similarly, for the secondary main sequence component in *cataclysmic variables* the gravity-darkening exponent does not change with mass. Actually: for $M_2 \leq 0.7 M_\odot$, $\beta \approx 0.05$, while for $M_2 \geq M_\odot$, $\beta \approx 0.08$ [15].

In the mean time, it had been pointed out that for a contact binary in hydrostatic equilibrium having a common convective envelope, *the convective flux depends on the effective temperature only and not on its gradient*. In other words: *there is no relation between T_{eff} and effective gravity* [16]. So $\beta = 0$, but this approach, applied to the reflection effect, predicts *zero albedo*, which disagrees with observations.

This was the situation till 1980 or even 1990. But, the gravity darkening effect has attracted the interest of many investigators, as already mentioned. So, recently (1994), the very high values of β obtained for some semi-detached

binary systems [17] were interpreted as an enthalpy transport linked with the mass exchange process [18]. And just a few years ago (1997-1999), the gravity darkening (or brightening, as is also referred by some investigators) in non-illuminated convective gray and non-gray atmospheres for different T_{eff}, in the range: $3700 < T_{eff} < 7000$ was studied [7,8]. It was then found that β depends on T_{eff}, being rather insensitive to variations of mixing length parameter, of the stellar mass and to the use of gray or non-gray atmospheres. These results, confirmed Lucy's [6] value $\beta=0.08$, for $T_{eff} \approx 6500$ K.

The latest studies on the subject have been presented by Claret -1998 & 2000- in two papers [9,10]. In the first, the gravity-darkening exponent was presented as a function of mass and age, based on the triangles strategy [19], and the adopted stellar models [20] had a representative chemical composition of X=0.70 & Z=0.02. The conclusion was that: The old values of the gravity darkening exponent *β=0.25 and β=0.08* for radiative and convective envelopes, respectively are superseded by new results according to which a *smooth transition* is achieved between the *two extreme energy transport mechanisms*. In other words: *The two processes of energy transport can exist even simultaneously in a determined stellar envelope.*

In the second paper [10], it was pointed out that the light we observe from the components of a binary system depends not only on the geometrical configuration but also on how the specific intensities are distributed along the stellar disk. Often, such components are distorted by rotation and tides, and the flux distribution is not uniform over their surfaces. Thus: *The gravity-darkening phenomenon is related not only with atmospheric parameters but also with the internal stellar structure and with details of the rotating law.* Moreover, the influence of changing the input physics on the gravity-darkening exponents was investigated, and found that they depend slightly on the chemical composition mainly in the zone of the radiative/convective phase transition. For deep convective envelopes, it is found no significant differences in *β's* computed for different mixing-length parameter.

Finally, the gravity distribution on the outer equipotential surface of contact binaries has been presented in three dimensions [21]. In particular, the *iso-g* curves were computed and plotted on the outer surface *Cs* of contact configurations for various combinations of the filling factor (*f*), and the mass ratio (*q*). While, applications were later made to specific systems [22,23].

3. Observational Treatments

Gravity-darkening coefficients -as second order parameters- is very difficult to be determined directly from the observations. However, several approaches were made -by various investigators, using different methods- to derive such parameters. The results of these efforts considering either one particular star, or more, were published in one or in a series of papers. And it is worthwhile to refer a few details concerning some of the derived results, since in some cases they are not consistent with the theoretical findings.

So, for contact binaries:

- From the analysis of **26** late type *W UMa*-type binaries, the gravity-darkening coefficient, $(\tau=4\beta)$, was found to be greater than unity [24]. In particular it was in the range **(1.1-7.1)** with a typical value around *2*.
- A similar result was found for the contact binary ***RZ Com***[25] for which τ seemed to be from **1.1** to **1.5**, instead of **0.32** appropriate for stars with convective envelopes.
- In general, values of τ or β greater than the theoretical ones have been reported for contact systems of *W UMa-type*. To be more specific: it was found to be so for ***TX Cnc*** [26], for ***AK Her*** [27], and for **16** other analyzed systems [28].
- The gravity darkening exponent β was found to be equal to zero for **4** *late-type* contact binaries, and under certain conditions [29].

Concerning the semi-detached systems, very different results have obtained by the various investigators. Thus:

- Very high values of τ have been reported for the secondary components of *Algol-type* binaries [30]. To be more specific: The analyzed sample contained stars with convective and radiative components. A high dependence of the surface brightness with the gravity was found. The derived τ values were in the range **2.3 to 9.4**, which is in disagreement with the classical theoretical values.
- High values of τ were also derived for the primary components of *reverse Algols* [17]. Although in general they were found to be less than for *Algols*.
- Rather normal gravity darkening values, and in very good agreement with theory, derived from the analysis of some semi-detached systems [31,32].

4. Summary - Discussion

Since the pioneer work of von Zeipel and the gravity darkening law he found for stars in radiative equilibrium: $F \prec g^{\tau}$ or $T_{eff} \prec g^{\beta}$, a lot has been added to our knowledge. So, while von Zeipel had considered rotationally distorted stars, the study was extended to tidally distorted configurations [2]. In general it was found that $\tau=1$ or $\beta=0.25$ for stars in radiative equilibrium. Moreover, the conditions under which this law is valid and how it varies especially for magnetic stars were examined, too [11,12].

Then, stars with convective envelopes were studied [6], and a different value for the gravity darkening coefficient (or the exponent) was theoretically derived: $\tau=0.32$ or $\beta=0.08$.
And recently it was suggested that both energy transfer mechanisms could be simultaneously in action; so, all intermediate values of τ or β should be expected [9,10].

Besides, the gravity distribution over the surfaces of contact systems has been presented in 3-D graphs [21], and applied to particular binaries [22,23].

As concerns the efforts to get gravity darkening exponents from the analysis of observational data, most of the firstly analyzed systems were contact binaries of *W UMa*-type. Apart from them, the best objects for which theoretical gravity darkening could be tested by observations were the distorted components of semi-detached systems. So, the light curves of such systems were analyzed using different methods and techniques.
One of the original and best such attempts was that in which systems of all kinds with both radiative and convective envelopes were included. The obtained mean values of τ were **0.91** and **0.31**, respectively [33], in quite good agreement with the theory. The same is true in some other cases, too. But, as was already referred, the obtained results from such analyses were not always in close accordance to the theoretical predictions. Why is this so? Does it have a special meaning?

Regarding contact binaries:
From a quantitative analysis, made in 1968, it was concluded that either the gravity darkening is considerably larger than that predicted by the theory, or the only effective way of reconciling the theory with the observations would be to assume that the mean fractional
radii of the two components are appreciably larger than those appropriate for contact models in which the two stars just fill the largest closed Roche equipotentials capable to contain their mass [24].

In general, values of τ or β greater than the theoretical ones have been reported for contact systems of **W UMa-type**. And this does not concerns only the systems **TX Cnc**, **AK Her**, or some others previously referred [26,27,28]. A similar situation has reported for some other cases, too [34,35]; but the obtained gravity values although greater than for purely convective envelopes are consistent, at least for some cases, with the latest theoretical findings [9,10]. On the other hand, it was found that curiously there is no evidence of anomalous large gravity darkening values in early type close binary systems, and it was suggested that there might exist some non-linear peculiar effect to contact systems with common convective envelopes [36].

Moreover, only for **4** contact systems, namely **W UMa** (itself), **XY Leo**, **TX Cnc** and **AH Vir**, the gravity darkening exponent β was found to be very small, almost zero [29]. This is in accordance to the only one theoretical work that differs from all others [16]. But if this is so, it was reported that the degree of contact had to be greater (of the order of **25%**), instead of **15%** if the theoretical value of $\beta=0.08$ was adopted, according to Lucy law for stars with convective envelopes. Moreover, in the same work [29] it is reported that there is some indication that the discrepancy between photometric and spectroscopic mass-ratios is reduced the value $\beta=0.00$ is used.

As regards semi-detached systems of *Algol* or *reverse Algol* type both normal and higher gravity-darkening values have been reported. To be more specific:

From the analysis of the infrared light-curves of **Algol** (itself, at $\lambda=1.6\mu$) [37] and it was found that the monochromatic coefficient τ_λ was **3** to **4** times larger than that resulting from the theory.

Similarly, the calculated gravity darkening values for the primary components of the *reverse Algols* -although distinctly smaller than those derived for the secondary components in semi-detached systems of normal *Algols* [29,17]- in both cases were found to be higher than the theoretical ones. Based on the mass-out-flow darkening model, these results would indicate that the rates of mass transfer in *reverse Algols* are not so high, and might imply that the systems are not in the rapid phase of mass transfer [31].

And although recently the very high values of β obtained for some semi-detached binary systems [17] were interpreted as an enthalpy transport linked with the mass exchange process [18], this might be *simply the result of the analysis method used*. This may be really the case, since these values are not supported by the recent simultaneous **uvby** observations for the **VV UMa** case [10], as well as for some other recently re-analyzed systems [31,32]. It is very important and special

attention has to be paid to the analysis method used, which has to be checked before applied to real stars [32]. If the method is not good the obtained results, either being close to the theory [38] or not being consistent with it [17, 30], might not be reliable.

Two other important subjects to consider during the light curves analysis is the spot activity, since both *W UMa-type* and *Algol-type* binaries show this kind of activity due to their magnetic fields, and the third light. The latter has not been examined in detail. As concerns the first, for two semi-detached systems, namely *LT Her* & *TV Cas*, it was found that if a spotted model is used [32] the gravity darkening exponents are consistent with the theory. Although some of the analyzed contact systems show such an activity, it has not be connected with possible abnormal values of the gravity darkening.

It is again emphasized that great attention has to be paid to the analysis method used, as well as to the specific characteristics of the chosen systems. For example some discrepancies from the expected gravity darkening values seems to exist for those systems in which both of their components are very hot [32]. This is not so, for "normal" semi-detached systems [39].

References

[1] Von Zeipel H. MNRAS 84, 1924, 702.
[2] C h a n d r a s e k h a r S. MNRAS 93, 1933, 539.
[3] T a k e d a S. Kyoto Mem. 17, 1934, 197.
[4] R u s s e l l H.N. ApJ 90, 1939, 641.
[5] K o p a l Z. Ann. N.Y. Acad. Sci. 41, 1941, 13.
[6] Lucy L.B. Z. Ap. 65, 1967, 89.
[7] A l e n c a r S.H.P. & Vaz L.P.R. A&A 326, 1997, 257.
[8] A l e n c a r S.H.P., Vaz L.P.R. & Nordlund A. A&A 346, 1999, 556.
[9] C l a r e t A. A&AS 131, 1998, 395.
[10] C l a r e t A. A&A 359, 2000, 98.
[11] S m i t h R.C. & Worley R. MNRAS 167, 1974, 199-312.

[12] S m i t h R.C. MNRAS 173, 1975, 97-102.
[13] C l e m e n t M.J. ApJ 156, 1969, 1051.
[14] W e b b i n k R.F. ApJ 209, 1976, 829.
[15] S a r n a M.J. A&A 224, 1989, 98.
[16] A n d e r s o n L & Shu F.H. ApJ 214, 1977, 798.
[17] N a ka m u r a Y. & Kitamura M. Ap&SS 191, 1992, 267.
[18] U n n o W., Kiguchi M. and Kitamura M. Publ. Astron. Soc. Japan 46, 1994, 613.
[19] K i p p e n h a h n R. A&A 58, 1977, 267.
[20] C l a r e t A. A&AS 109, 1995, 441.
[21] T s a n t i l a s S., Rovithis-Livaniou H. & Kalimeris A., Proc. 5th HELASET Meeting,
        http://astrophysics.uoc.gr/conf/proceedings.htm
[22] R o v i t h i s-L i v a n i o u H. & Tsantilas S. Proc. Summer School Belogradchik, Bulgaria
        4-11 July 2003, (in press).
[23] T s a n t i l a s S. & Rovithis-Livaniou H. Proc. 6th HELASET Conf., 2004, p. 111.
[24] K o p a l Z. Ap&SS 2, 1968, 23.
[25] W i l s o n R.E. & Devinney E.J. 182, 1973, 539.
[26] W i l s o n R.E. & Biermann P. A&A 48, 1976, 349.
[27] W o o d w a r d E.J. & Wilson R.E. Ap&SS 52, 1977, 387.
[28] K i t a m u r a M. & Nakamura Y. Ap&SS 145, 1988, 117.
[29] H i l d i t c h R.W. MNRAS 196, 1981, 305.
[30] K i t a m u r a M. & Nakamura Y. An. Tokyo 21, 1987, 387.
[31] G e o r g i a d e s N., Rovithis-Livaniou H. & Djurasevic G. Publ. COMU Ap. Research
        Center Vol. 3, 2003, 50.
[32] D j u r a s e v i c G., Rovithis-Livaniou H., Rovithis P., Georgiades N. Erkapic S. & Pavlovic
        R. A&A 402, 2003, 667.
[33] R a f e r t J.B. & Twigg L.W. MNRAS 193, 1980, 70.
[34] E a t o n M.J. AcA 36, 1986, 79.
[35] E a t o n M.J. Wu C-C & Rucinski S.M. ApJ 239, 1989, 919.
[36] K o p a l Z. Ap&SS 2, 1968, 166.
[37] B u d d i n g E. & Kopal Z. Ap&SS 9, 1979, 343.
[38] P a n t a z i s G. & Niarchos P. A&A 335, 1998, 199.
[39] Djurašević G., Rovithis-Livaniou H., Rovithis P., Georgiades N. & Erkapić S. ibid   (This
        Meeting), 2004.
[40] Djurašević G., Rovithis-Livaniou H., Rovithis P., Georgiades N. & Erkapić S. Proc. 22nd
        SPIG, (in press), 2004.

SPECTRAL OBSERVATIONS OF BRIGHT QUASARS AT NAO ROZHEN

E. Semkov[1], R. Bachev[1,2], A. Strigachev[1]

[1] *Institute of Astronomy, Sofia 1784, Bulgaria*
[2] *University of Alabama, Tuscaloosa, AL 35487, USA*

Abstract.
Optical spectra of two newly discovered bright quasars - MCG+08.17.060 and RXS J11401+4115, obtained with the 2-m RCC telescope at NAO Rozhen are shown and analysed. The spectra are published for the first time. Various parameters of the brightest emission lines along with accurate redshifts are measured and presented.

1. Introduction

We started a program of spectral observations of relatively newly discovered bright quasars, suitable for spectral observations at the 2-m class telescopes (i.e. the 2-m telescope at NAO Rozhen). Despite the number of quasar surveys, claiming relative completeness, which has been performed in the recent years, there are still many bright quasars, apparently missed in these surveys. Some of these quasars, discovered just recently, have no published spectra. In this work we present spectra for two quasars – MCG+08.17.060 and RXS J11401+4115. Both quasars are relatively nearby ($z \cong 0.05 - 0.07$, see also Tab. 1) and relatively bright ($V \cong 14\text{-}15^m$). The objects were selected from the latest Veron-Cetty & Veron (2003) quasar catalog.

2. Observations and reductions

The spectral observations of MCG+08.17.060 were performed on 19 March 2004 with the Photometrics AT200 CCD camera (1024 x 1024 pixels) and the focal reducer FORERO attached to the RC focus of the 2-m telescope. A grating prism (300 lines per mm) and 130 μm slit were used. This combination yields a resolving power $\lambda/\Delta\lambda = 250$ or about 20 Angstroms. Two 2400 sec exposure frames of the object were obtained and

combined to form the final spectrum. Two 600 sec exposure frames of a spectrometric standard - Feige 34 were obtained immediately after the quasar. The second objects, RXS J11401+4115 was observed on 20 March 2004 under the same conditions. Three 2400 sec exposure frames of the object were obtained and combined to form the final spectrum.

The spectra have been reduced using standard IRAF routines. Due to the absence of standard wavelength calibration spectra (e.g. He+Ar) the wavelength calibration has been performed based on the night-sky emission lines, allowing an accuracy of about 2-3 Angstroms. For the flux calibration a standard star (Feige 34) has been used. The redshift-corrected spectra covering 4400 – 7400 Angstroms range are shown in Fig. 1. No correction for the atmospheric absorption, redward of Hα has been applied. No correction for the instrumental profile has been performed to correct the measured widths of the lines as well; this probably accounts for the most of the [OIII] width (Tab. 1).

3. Results

Object	MCG+08.17.060			RXS J11401+4115		
Coord.	09 13 46.0 +47 42 00			11 40 03.4 +41 15 05		
z	0.0524 +/-0.0005			0.0708 +/- 0.0003		
Lines	EW	FWHM	Flux	EW	FWHM	Flux
H alpha	114	3400	8	198	2700	11.3
H beta	-	-	-	45		5.3
FeII	-	-	-	~ 55	-	-
[OIII]	25	980	1.5	9	2800	730

The redshift of the objects has been measured using Hα and O[III]λ5007. The strongest lines has been identified and measured (Tab. 1). The equivalent width (EW) of the lines is measured in Angstroms, the FWHM – in km/s, and the flux – in units of 10^{-14} erg/s.cm^2. RXS J11401+4115 shows significant FeII multiplet emission around Hβ, which is not surprising taking into account that this object is X-ray selected and has relatively narrow Hydrogen lines (e.g. Sulentic et al., 2000). An emission

RXS J11401+4115
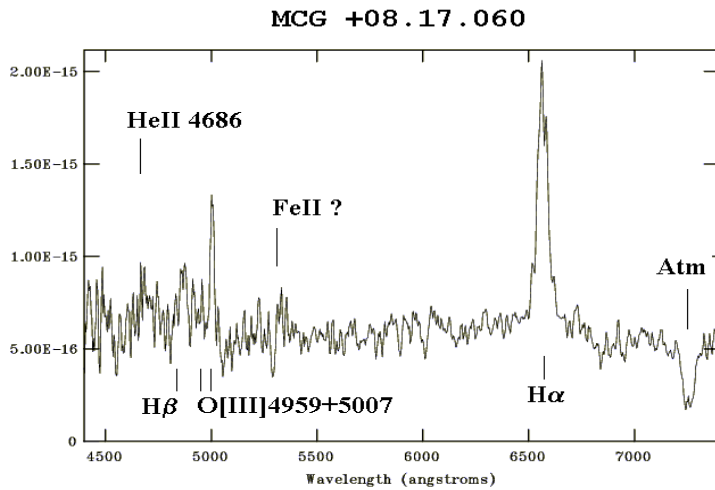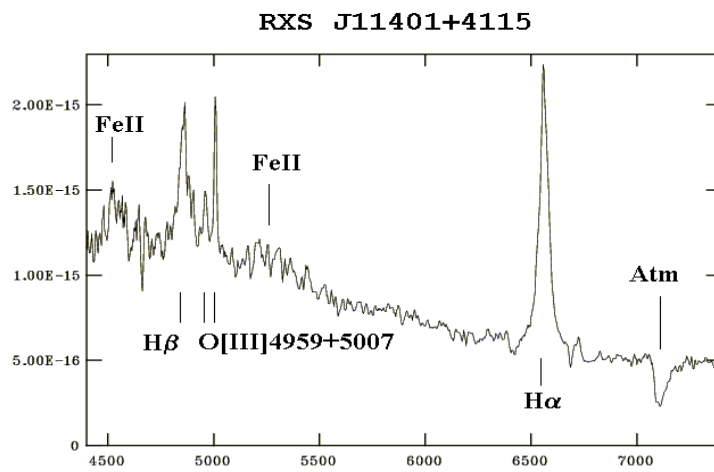
MCG +08.17.060

signature, probably corresponding to HeII 4686 is seen in the noise of the MCG+08.17.060 spectrum.

References
Sulentic J. W., Marziani P., Dultzin-Hacyan D., 2000, ARAA, 38, 521
Veron-Cetty M.-P., Veron P., 2003, A&A, 412, 399

EXPLORING THE HIGH REDSHIFT LARGE-SCALE STRUCTURE OF THE UNIVERSE: A MULTI-WAVELENGTH PERSPECTIVE.

Ivan Valtchanov

Astrophysics Group, Blackett Laboratory, Imperial College of Science, Medicine and Technology, London, United Kingdom, e-mail:
i.valtchanov@imperial.ac.uk

Abstract:

I present a short review of multi-wavelength studies of galaxy clusters and their implications for cosmology and structure formation theories. Some recent results from the XMM Large-Scale Structure Survey are used to illustrate our capability to identify and confirm clusters at high redshifts and to map the large-scale structure out to z=1. This allows us, in combination with associated observations in different wavebands, to study the evolution of the structures, to constrain cosmology and to link different aspects of galaxy formation with the environment.

Introducing the main actor – the galaxy clusters

The galaxy clusters are the most massive gravitationally bound objects in the Universe. They are composed of dark matter, gas and galaxies[1]. The mass range of clusters is about 10^{14} – 10^{15} M_{sun}. The galaxies contribute only about 5% to the total mass, the gas ~15-20% and the rest is dark matter. In general, the different constituents manifest themselves in different regions of the electromagnetic spectrum: the galaxies contribute mainly in the UV, optical and infrared domains, the hot diffuse gas in the X-ray and radio (diffuse radio halo and Syunaev-Zel'dovich effect in the radio mm range) and the dark matter through its effect on the overall cluster dynamics and via the lensing effect. Moreover, the different constituent interact with each other and only by multi-wavelength studies some violent events - like fusion shocks of accretion of galaxy groups infalling into the cluster or gas stripping off the galaxies by their

---

[1] There is an additional fourth constituent – relativistic particles, mainly electrons at very high energies [14] but they are irrelevant for this review.

interaction with the cluster potential - can be thoroughly studied. It is likely that phenomena like the active galaxy nuclei or bursts of star formation are strongly linked with the environment.

Being the largest virialized entities in the Universe, the galaxy clusters are very rare objects that have arisen from the highest peaks in the primordial density fluctuations. They form at the intersection of the large-scale filamentary structure, grow in mass by accreting gas, individual galaxies and galaxy groups, and trace the large-scale structure as is illustrated in Fig.1.
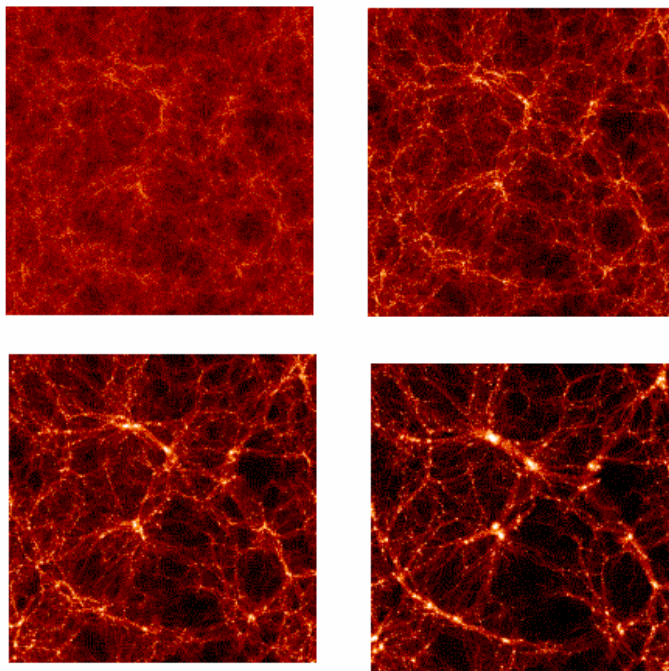
Figure 1. The evolution of 100 Mpc^3 comoving box for LCDM cosmology with dark matter only (no gas). The large-scale structure of the Universe is shown at four different redshifts: z=5 (top left), 2 (top right), 1 (bottom left) and present day (z=0, bottom right). The galaxy clusters are the bright knots in the intersection of the filamentary structure. Note how they change in contrast from z=5 to z=0. Simulations R. Teyssier, CEA/Saclay, France.

The number density of clusters as a function of the epoch (or the so called cluster abundance evolution) is very sensitive to the underlying cosmological model, and especially to the normalization of the power spectrum of the density fluctuations σ_8 (the root-mean-square of the density fluctuation in comoving spheres of 8 Mpc/h) and the matter density $\Omega m = \rho_m/\rho_c$, where ρ_m is the matter density and ρ_c is the critical density of the Universe. Hence, even the counting of clusters as function of redshift could be very important tool in cosmology (see e.g. [12,8]).

The main idea is to compare the observed number of clusters as function of redshift to the expected one for a given set of cosmological models. This can be derived following the Press-Schechter formalism (see e.g. [12] and references therein). An example of the expected cluster abundance evolution for three cosmologies: ΛCDM, OCDM and τCDM, derived for 64 deg^2 X-ray cluster survey (see the following Section) is shown in the upper panel of Fig. 2. By constructing sets of cosmological models with different parameters - σ_8, Ωm and Γ (the shape parameter of the density fluctuation power spectrum, see e.g. [12]), we can compare the differences between what is observed to what is expected and derive the confidence regions for the parameters, as shown on Fig. 2, lower panels.
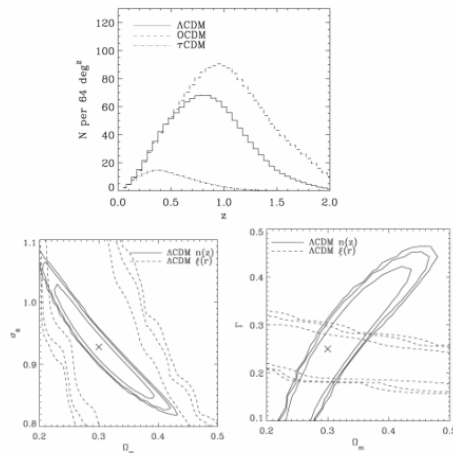
Figure 2. Upper panel: cluster abundance evolution for three cosmologies, derived from the Press-Schechter formalism and calculated for 64

deg^2 survey. Bottom panels: cosmological constraints on σ_8, Ωm and Γ, derived for a reference model and ΛCDM cosmology (see [12] for details).

We must stress that the cosmological constraints derived from the clusters are *independent and complementary* to those from cosmic microwave background (CMB) and supernovae (SNe) studies – the constraints from CMB come from analysis of the temperature fluctuations that arise at the last scattering surface in the early Universe (redshift z~1000), while those from SNe rely on the assumption that the supernovae are standard candles. In addition, the galaxy clusters are very important objects because their internal dynamics is a key to the understanding of the evolution of the large-scale structure and the structure formation.

Introducing the scenes: galaxy cluster surveys

In order to use the clusters for cosmological studies or studies of the large-scale structure evolution it is very important that we detect and subsequently confirm clusters and measure different characteristics at the highest possible redshifts. Cluster search in the optical domain is getting very difficult as we go to higher and higher redshift. There are strong projection effects and the galaxy overdensity has very low contrast with respect to the field ([5]). Although there are many optical cluster searches at high redshift (e.g. [11]), which are based on some clever algorithms, the game is rather dubious and difficult. One improvement is to use the diagram colour-magnitude and colour-redshift and search for "red-sequence" of galaxies. This technique is based on the assumption that cluster galaxies have similar colours because they evolve together and the cluster cores contain predominantly elliptical galaxies that evolve passively ([6]). In this way, by choosing convenient colours (for example R-I or V-I or R-z) we can increase the contrast for the cluster galaxy overdensity that can be very successful for redshifts as high as z~1 ([1]).

The best way to find clusters, however, is to work in the X-ray domain. Right from the beginning of the X-ray observations of the sky at high galactic latitude, it was realized that one of the most powerful objects were the galaxy clusters ([7]). The thermal X-ray emission is a proof of the existence of a deep potential well, where a diffuse gas (~10^{-3} cm^{-3}) is trapped and heated by the

gravitation to temperatures $10^7 - 10^8$ K. The X-ray emission measure $Sx \sim n_e^2$ $\sqrt{T}$ and consequently the projection effects are not important in the X-ray observations of clusters (see e.g. [13] and references therein). Thus, a chance alignment of galaxies cannot give an X-ray emission (no potential well to trap and heat the gas) while it can mistakenly be taken as cluster only based on optical 2D search. In addition, the X-ray sky at high galactic latitudes has two *distinct* types of objects[2]: super-massive black hole accretion disks (the AGNs), which are point-like unresolved sources and clusters of galaxies, which are extended sources. With the current two great X-ray observatories *Chandra* and *XMM-Newton,* the distinction between these two types of objects is relatively easy.

That is why we have proposed a survey with the XMM-Newton telescope of contiguous region of 64 deg^2 with the main objective to map and study the evolution of the large-scale structure of the Universe traced by the galaxy clusters out to z~1. The XMM Large-Scale Structure survey (XMM-LSS) is a combined effort of many astronomical institutes[3]. A detailed description of the survey may be found in [10,15]; many details are also available from the consortium web pages (see the footnote below).

Briefly, the XMM-LSS survey geometry and depth was chosen such as to allow the study of the cluster-cluster two-point correlation function in the redshift domains 0<z<0.5 and 0.5<z<1 with the same precision as the most precise present day estimation of the correlation scale from the REFLEX survey ([4]) that is based on ROSAT and goes up to z~0.2. The placement of the survey was chosen such as to be in a blank area of the sky without known big clusters and no luminous X-ray sources and, from a practical point of view, in equatorial region to allow follow-up as from the northern as well as from the southern hemispheres. The latter is really important because the follow-up programme of such a survey is enormously demanding in terms of telescope time.

---

[2] Of course there is some contamination from galactic stars, mainly X-ray binaries, nearby normal galaxies and very rarely supernova remnants.

[3] See the official web pages of the consortium:
http://vela.astro.ulg.ac.be/themes/spatial/xmm/LSS/

Detailed information on the associated surveys may be found in [10] and updates of the follow-up activities might be found in the official web pages of the consortium.

Cluster detection in XMM-Newton images

To date we have about 6.5 deg^2 observed in X-ray: 55 XMM pointings in total, some with 10 ks exposures and some of 20 ks. The X-ray data were pre-processed with the standard tools from the XMM Science Analysis System (XMM-SAS) to derive calibrated science event lists. The XMM-Newton telescope has three detectors: MOS1, MOS2 and pn which can operate simultaneously or independently. We used the three detectors for our observations and from the resulting event lists we constructed images in different energy bands for each instrument.

The detection pipeline follows the prescription of [16]. Briefly, the images in [0.5-2] keV energy band are combined to increase the signal-to-noise and filtered by multi-scale (wavelet) technique ([14]) using Poisson noise model for the significant wavelet coefficients. The sources on the filtered at 10^{-4} significance level (corresponding to 4σ in Gaussian case) images are then detected and characterised by SExtractor ([2]). Subsequently they are classified to extended (clusters) and point-like (AGNs) using three criteria – a modified stellarity index from SExtractor, full width at half max of the source and the half-light radius. This procedure is very successful at selecting candidate clusters at redshifts even well above 1 (see [16] for details).

An example of an X-ray image in raw photons, from the combined MOS1+MOS2+pn event lists together with adaptively smoothed at signal-to-noise ratio of 5 resulting image are shown on Fig.3. There are two obvious low redshift clusters at z=0.28 and z=0.35 while the great majority of the remaining sources are AGNs.
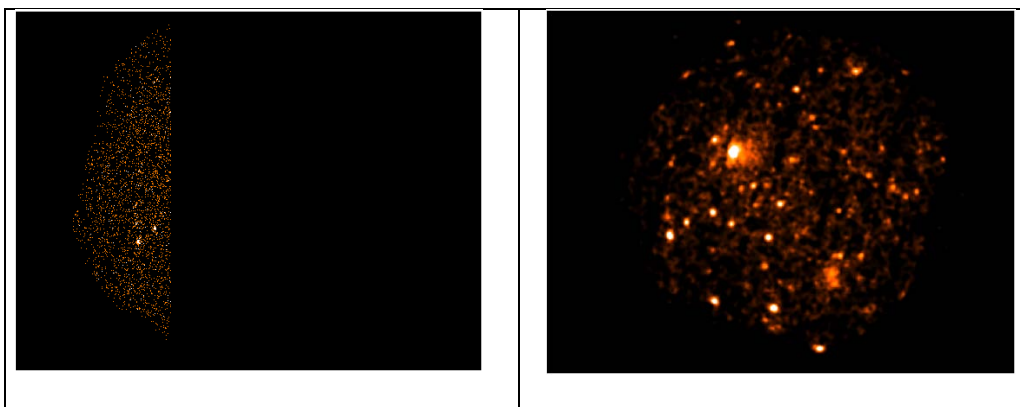
Figure 3. XMM-Newton observation. The left panel shows the raw photon image from the combined photons from the three XMM-Newton detectors MOS1, MOS2 and pn. The diameter of the field is 30 arcmin. The right panel is the adaptively smoothed image from the left panel, with signal-to-noise ratio of 5. Two "low redshift" clusters are obvious (the two extended sources) and the rest of objects are AGNs.

First results from XMM-LSS

Using the above procedure, the list of the detected extended sources is subsequently cross-identified using deep optical images from the CFHT telescope in B, V, R an I bands and all artefacts caused by detector borders were removed. The cluster candidates were divided into classes depending on their photometrical properties: *near* (z<0.5), *mid* (0.5<z<1) and *dist* (z>1). Depending on the class the candidates were allocated to different observatories for follow-up: 4-m class telescopes (CTIO, ESO-NTT) for *near* candidates; 8-m class telescopes (ESO-VLT) for *mid* and NIR telescopes (NTT-SOFI) for *dist* class.

To date we have undertaken two spectroscopic follow-up runs: fall 2002 and 2003, fall 2004 ESO-VLT (for *mid* and *dist* class) and ESO-NTT (*near*) are underway. Examples of spectroscopically confirmed clusters of each class are shown on Fig. 4. The results on redshifts are summarised on Fig.5.

108
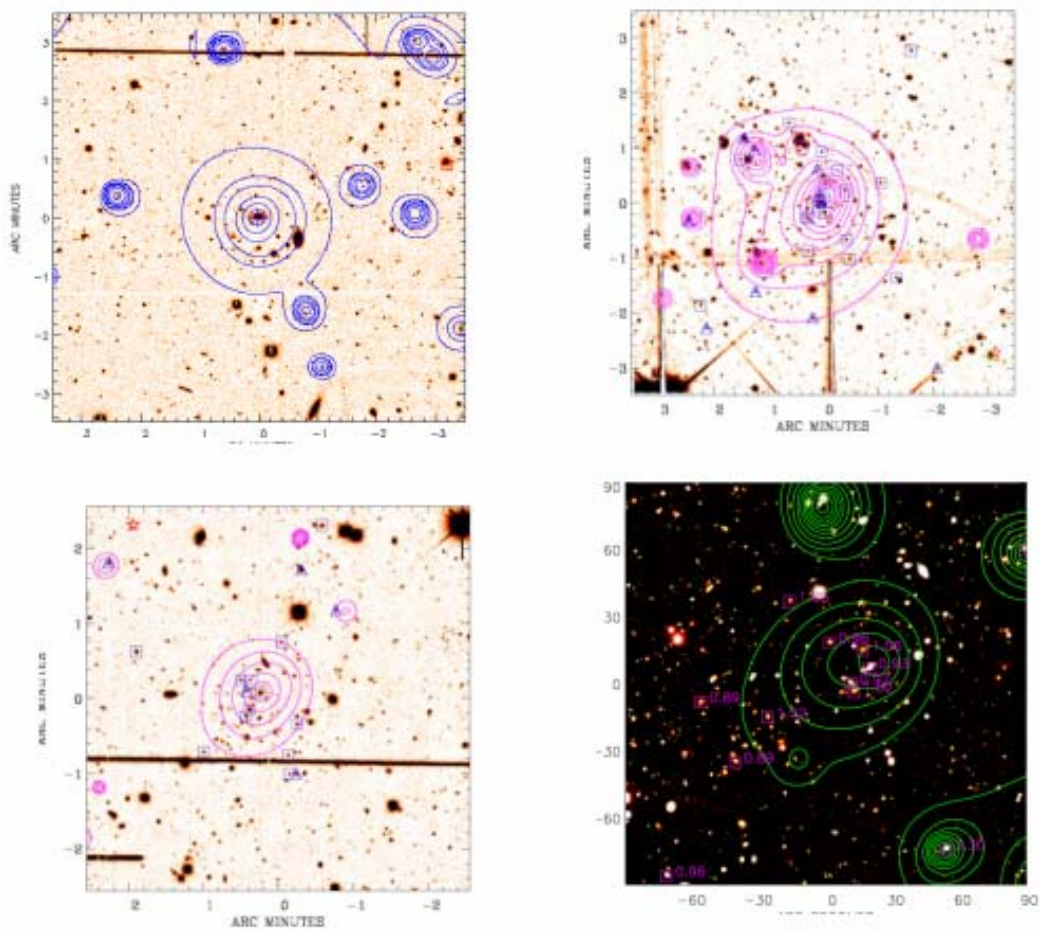
Figure 4. Example of different distance class clusters from the XMM-LSS. A *near* cluster (z=0.329, top left panel), a *mid* cluster at z=0.613 (top right), *mid* cluster at 0.84 (bottom left) and z=1 cluster (bottom right panel).
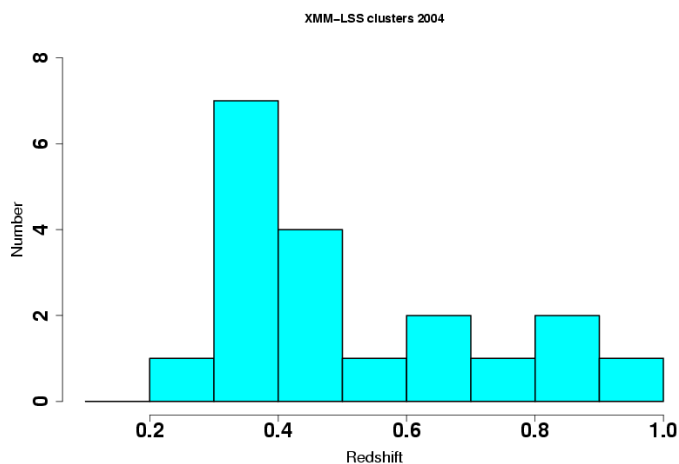
Figure 5. Redshift distribution for all spectroscopically confirmed XMM-LSS clusters for observations performed in 2002 and 2003.

The cluster at z=1 is likely to be a superposition of two clusters (see [18]).

The first results of the XMM-LSS, that show the performance of the programme and some exciting new results, are presented in [10,18,19]. Studies of the evolutionary properties of the cluster galaxies from XMM-LSS are presented in [1]. A short summary is presented below and the details may be found in:

- The pipeline procedure is highly efficient: from identification to spectroscopic confirmation we have just one failed objects from 22 candidates and one complicated and interesting case of z~1 cluster.
- The number of detected clusters per deg^2 from the first 6.5 deg^2 is consistent with the "concordant" ΛCDM cosmology: ~12 clusters per deg^2 out to z=1.

- Because of the high efficiency of our programme it was possible for 1h30m VLT time to derive the velocity dispersion of a cluster at z=0.84 based on 17 galaxies with concordant redshifts. It is worth to note that to date, there are only 5 known clusters at such high redshift with more than 10 observed galaxy members (3 of them X-ray selected).
- We detect low to moderate mass clusters – a region of the cluster mass function that is largely unexplored and that allows us to map the large-scale structure much densely.
- The combined X-ray identification and NIR observations detected the highest redshift cluster z = 1.5 known to date from X-ray observations.

Conclusions and future prospects

Clusters of galaxies are important tools in cosmological studies and in studies of structure and galaxy formations theories. To date the most complete cluster catalogues reach as far as redshift 0.2 and this hampers most of the cosmological applications of clusters. With the advent of the high throughput and high-resolution X-ray observatories like XMM-Newton and Chandra, the detection of clusters at redshifts as high as z~1 is possible in systematic manner. This can explain the wealth of X-ray based cluster surveys nowadays, most of which, however, are hunting for high redshift clusters in serendipitous observations (i.e. observations devoted to another object and the cluster happens to lie nearby). This strategy is not very useful for studies of the large-scale structure of the Universe the observations could be scattered all over the sky. Instead, we have proposed a contiguous area X-ray survey with the XMM-Newton telescope – the XMM large-scale structure survey, which can be attained with not so big a demand for observational time. The results of the XMM-LSS, however, will be fundamentally important and impossible for serendipitous clusters even at higher redshift.

The future prospects are all based on routine follow-up of the first 6.5 deg^2 of the XMM-LSS. The highest priority is to get a complete cluster sample from this area, to confirm and place the clusters on the 3-D redshift space, and to use this catalogue following the methodology of [12] to derive cosmological constraints. Another important study is to compare different cluster selection

procedures (optical, colour based, infra-red, X-ray) in order to establish if cluster properties influence the cluster detection.

And finally, the link of galaxy formation with the environment with the Spitzer infra-red observations already acquired from the SWIRE Survey ([9]).

References

[1] Andreon S., Willis J., Quintana H., et al., 2004, MNRAS, 353, 353
[2] Bertin E. & Arnouts S., 1996, A&AS, 117, 393
[3] Borgani, S., Rosati, P., Tozzi, P., et al., 2001, ApJ 561, 13
[4] Collins C., Guzzo L., Böhringer H. et al., 2000, MNRAS, 319, 939
[5] Dickinson M., 1997, in *The Early Universe with the VLT*, ed. J. Bergeron, p. 274. Berlin:Springer
[6] Gladders M. & Yee H., 2000,AJ, 120, 2148
[7] Gursky H., Kellogg E., Murray S., et al., 1971, ApJ, 167, L81
[8] Haiman Z., Mohr J. & Holder G., 2001, ApJ, 553, 545
[9] Lonsdale C. et al., 2003, PASP, 115, 89
[10] Pierre M., Valtchanov I., Altieri B., 2004, JACP, submitted (astro-ph)
[11] Postman M., Lubin L., Gunn J., et al., 1996, AJ, 111, 615
[12] Refregier A., Valtchanov I. & Pierre M., 2002, A&A, 390, 1
[13] Rosati P., Borgani S. & Norman C., 2002, ARAA, 40, 539
[14] Sarazin C., 1999, ApJ, 520, 529
[15] Starck J.-L. & Pierre M., 1998, A&AS, 128, 397
[16] Valtchanov I. & Pierre M. 2004, AN,
[17] Valtchanov I., Pierre M. & Gastaud R., 2001, A&A
[18] Valtchanov I., Pierre M., Willis J., et al., 2004, A&A, 423, 75
[19] Willis J., Valtchanov I., Pierre M. et al., 2004, A&A, submitted

EXTINCTION STUDIES IN M31

P. Nedialkov[1], A. Valcheva[1], T. Veltchev[1],
I. Stanev[1], Ch. Dyulgerov[1] & A. Kostov[1,2]

(1)Department of Astronomy, Sofia University, Bulgaria
(2) Institute of Astronomy, Bulgarian Academy of Sciences, e-mail:
japet@phys.uni-sofia.bg

Abstract.

In this paper we examine the gas-to-dust ratio in M31 galaxy combining radio emission data on neutral hydrogen (HI) and carbon oxide (CO) with the recent extinction estimates of young stellar groups (OB associations and open clusters). The fraction of sightlines where the observed $N(HI)/2E_{B-V}$ ratio is outside the typical Galactic range is only 1/10; however, the correlation between these two quantities remains weak. A radial dependence of this ratio, twice flatter than previous estimates, indicates absence of a strong metallicity gradient. Detection of objects behind the disk of M31 allow pencil beams estimates of the total extinction. The results confirm the plausibility of a disk model with exponentially decreasing optical thickness in radial direction.

Nearly constant gas−to−dust ratio in the Galactic interstellar medium in the few kpc vicinity of the Sun [1] shows that dust and gas are well mixed and the grain properties do not vary essentially. One comes to this conclusion taking into account the existing tight correlation between the star light extinction and the observed total gas column density $N(HI+2H_2)$. Local Galactic value of the gas-to-dust ratio is often adopted for regions outside the Solar neighborhood or in other spiral galaxies; yet, it is difficult to prove directly its universal applicability. One promising test is to perform comparison between the properties of dust and gas in nearby galaxies.

The nearest giant spiral, M31, is an attractive target for comprehensive study of the ISM. Its proximity allows for construction of a detailed picture of stars', dust, and gas distributions. However, any extensive survey is time-consuming because of the large angular size of M31 ($4.5° \times 1.5°$; see Fig. 1).

The new CO($1 \rightarrow 0$) map [2] with an angular resolution of 23″ at $\lambda = 2.6$ mm, combined with the HI map of [3], yields excellent opportunities for comparative studies of dust and cool gas, representative for the whole

body of M31. We examine here the gas-to-dust ratio in M31 galaxy using pencil beam columns from these maps toward the centers of young stellar groups (OB associations and open clusters) and new mean extinction estimates, based on HST observations. Extinction data are summarized in Table 1. Their radial distribution is shown in Fig. 2, compared with the averaged radial distribution of the total gas column density. Because of the large extinction spread, even within a single stellar group, no clear pattern is evident.
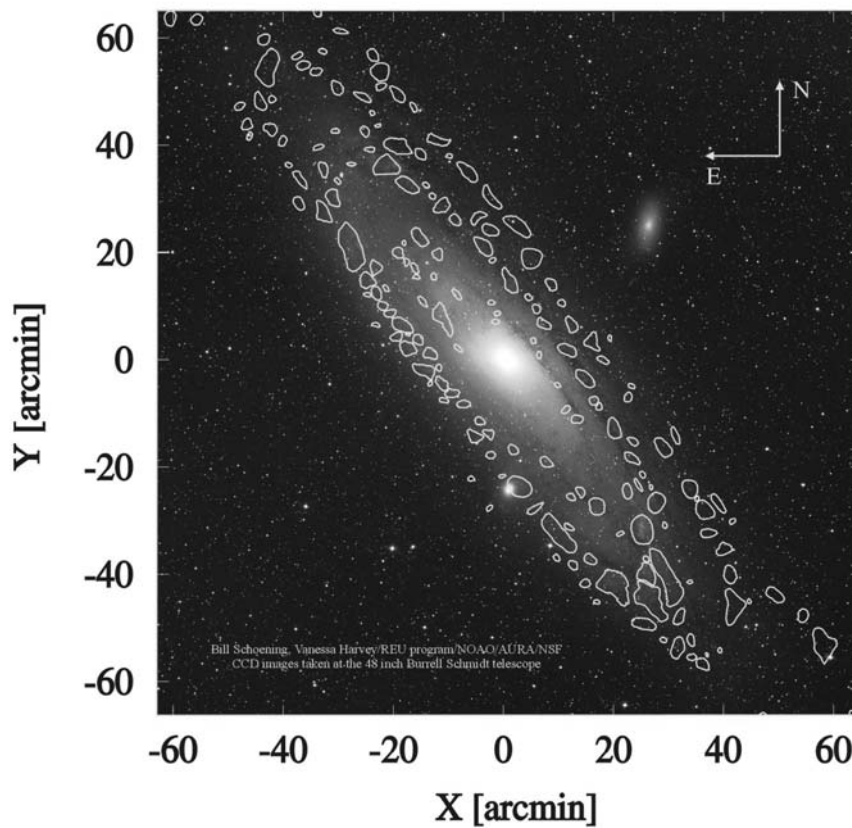
Figure 1: OB associations in M31 (as outlined by van den Bergh /1964/) superimposed on a mosaic CCD image, obtained by Bill Schoening. Note the striking overlap between their boundaries and the dark clouds which testifies that young stars and dust are well mixed.

The corresponding relationships `atomic gas-dust' and `total gas-dust' are illustrated in Fig. 3. A constant gas-to-dust ratio in M31 would yield a good correlation within an expected range, delineated with dashed lines on Fig. 3. This is the case in the Milky Way (cf. Fig. 2 in [1]). Although the fraction of sightlines with observed $N(HI)/2E_{B-V}$ ratio outside the Galactic range is only 1/10, these quantities do not correlate. Several reasons for a weakened correlation were pointed out in [11]. First, the gas-to-dust ratio may depend on the galactocentric distance. Increase of metallicity toward the center of M31 is expected to be inversely proportional to the gas-to-dust ratio. The check of this possibility showed, however, that the radial gradient of the $2E_{B-V}/N(HI)$ ratio is much flatter than that of metallicity. Second, the fraction of gas density associated with dust may vary locally (not exactly 1/2) – stellar groups, located in front of or behind the disk mid-plane, will exhibit strong deviation from the mean gas-to-dust ratio. Yet there is no doubt that young stellar groups are located at or close to the mid-plane of M31 disk. The poor angular resolution of the neutral gas maps is inappropriate for individual extinction estimates of a star or a cluster but would not influence severely the correlation in case the stellar groups' sizes are of the same order. Despite the fact that ~300 "higher resolution values" of the gas-to-dust ratio, extracted from Fig. 4 in [4], fall within the Galactic range, the correlation is still absent, even on a log-log graph. It was in [12] also found that the 2D extinction map based on CCD photometry of OB stars exhibits neither correlation nor anticorrelation when directly compared with the distributions of cold dust emission and gas column density.

Table 1. Modern extinction data for stellar groups in M31 galaxy

Stellar group type	Total number of estimates	Technique	References
OB-associations	7	Isochrones method	[4]
Brightest stars	5	Q-method + spectroscopy	[5]
OB-associations	80	SFH (MATCH package)	[6]
Young clusters	29	SFH (MATCH package)	[7]
OB-associations	9	SFH (MATCH package)	[8]
OB-associations	4	Q-method (+ Strömgren	[9]

		vby photometry)	
OB-associations	20	Fitting of the MS + varying R_v	[10]
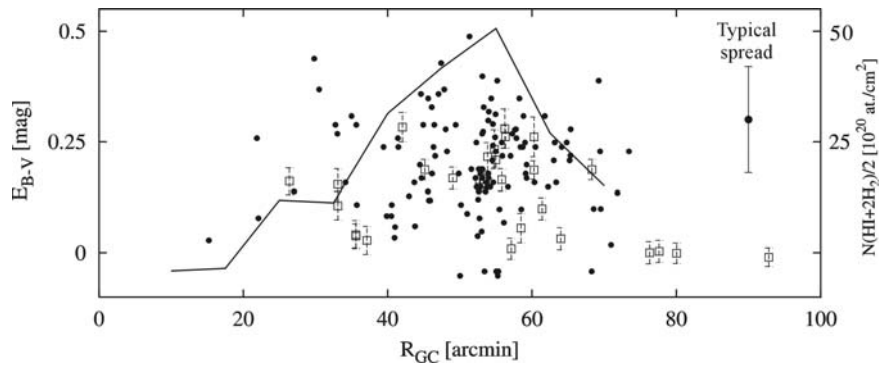
Figure 2: Radial distribution of the mean internal extinction in M31 stellar groups, listed in Table 1. The values for OB-associations ([4,5,6,8,9,10]; filled circles) and for the young clusters [7]; open squares) are plotted; the typical spread within the associations is given at the top right corner. The averaged radial distribution of the total gas column density is drawn with thick line for comparison. No clear pattern could be traced due to the significant extinction variations even within a single stellar group.

The most plausible explanation for the lack of correlation remain the limitations of the techniques applied and hence the rough extinction estimates. For example, when a modeled optical thickness is considered, the distribution of the individual extinction estimates seems to confirm an opaque disk, at least in the spiral arms of M31. Thus, the average extinction could not be representative for the true optical depth along the sightlines toward young stellar groups. The exponentially decreasing total optical thickness outward the galactic center, as obtained by [13] is represented in Fig. 4 with filled circles. The most direct way to check the model is to compare its predictions with extinction estimates, equivalent to pencil beam optical
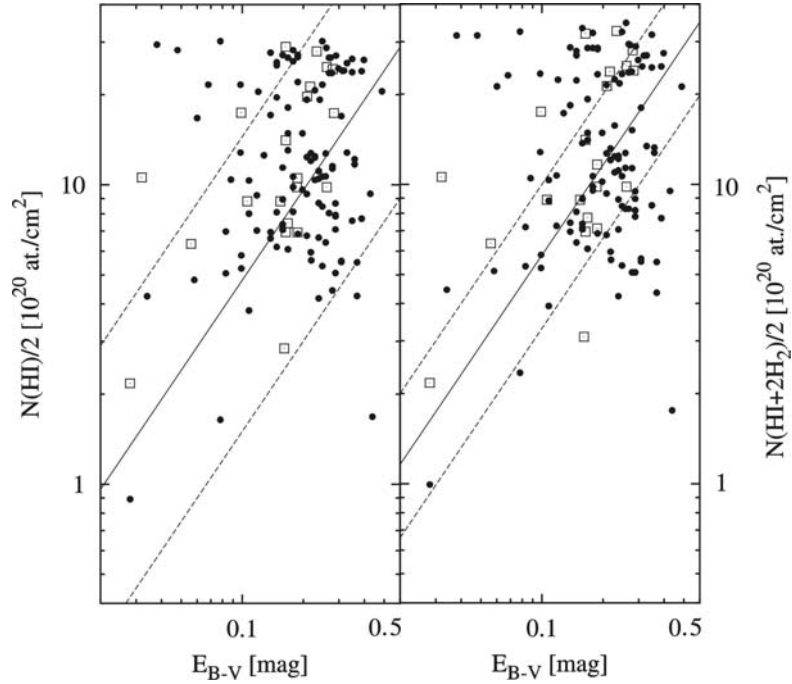
Figure 3: The relationships 'hydrogen (left: atomic; right: total) column density - mean extinction' in young stellar groups in M31 (see also Table 1 and Fig. 1). Mean Galactic gas-to-dust ratios (thick line; [1]) and the expected range of values (dashed) are shown. Note the quite weak correlation.

depths, for objects behind the disk (Fig. 4). Such objects are: distant galaxies beyond the M31 outskirts [14]; globulars, probably lying behind the disk [15]; the "remarkable" globular 037-B327, seen through one of the western spiral arms [16] and a cluster of galaxies [17], hidden behind the NE part of M31. Not all optical depths detected confirm the model of exponentially decreasing optical thickness, especially the globulars in [15] at distance $R_{GC}<50'$, which can be explained with the clumpiness of ISM leading to a selection bias: only globulars along less obscured sightlines have been detected first. We note also that the extinction value of [14] at $R_{GC}=115'$ indicates a smaller radial scale-factor of exponential decrease of the extinction than the model of [13].
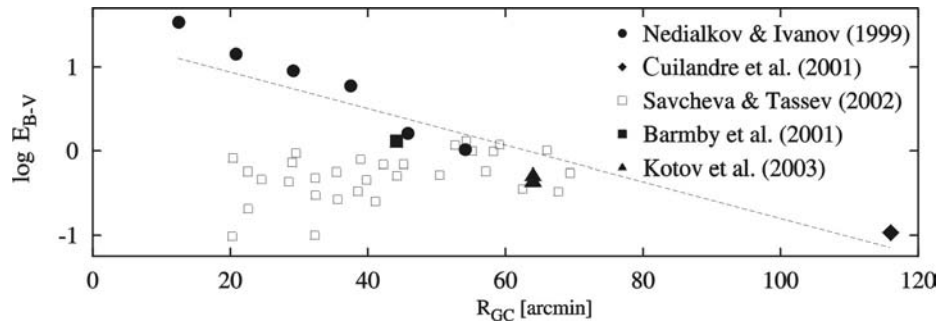
Figure 4: Total optical thickness of M31 disk versus projected galactocentric distance. Filled circles represent the predicted exponential decrease, according to Nedialkov & Ivanov (1999). Other pencil beam optical depths are given with different symbols as indicated in the figure. The dashed line fits all data, denoted with filled symbols (see text for details).

Significant optical thickness of the inner disk of M31 galaxy and deficiency of both atomic and molecular gas seems a quite unrealistic combination. The only natural explanation is that most of the hydrogen might be in molecular phase, frozen on dust grains at temperatures not very different from the temperature of the cosmic microwave background [18].

Acknowledgments

References

[1] B o h l i n R., B. S a v a g e, J. D r a k e, A survey of interstellar H I from L-alpha absorption measurements. II, 224, 1978, ApJ, 132 - 142
[2] G u é l i n M., C. N i e t e n, N. N e i n i n g e r, S. M u l l e r, R. L u c a s, H. U n g e r e c h t s, R. W i e l e b i n s k i, Distribution and properties of the molecular clouds in M31, Aachen, 232 Interstellar medium in M31 and M33 Eds: E. M. Berkhujsen, Rainer Beck and R. M. Walterbos, 2000, 15 - 20
[3] B r i n k s E., W. S h a n e, A high resolution hydrogen line survey of Messier 31. I Observations and data reduction , 55, 1984, A&AS, 179 – 251
[4] M a g n i e r E., P. H o d g e, P. B a t t i n e l l i, W. L e w i n, J. v a n P a r a d i j s, Hubble Space Telescope observations of M31 associations, 292, 1997, MNRAS, 490 – 498
[5] M a s s e y P., .Evolved Massive Stars in the Local Group. I. Identification of Red Supergiants in NGC 6822, M31, and M33, 501, 1998, ApJ, 153 – 174
[6] W i l l i a m s B., P. H o d g e, Identification and Analysis of Young Star Cluster Candidates in M31, 559, 2001, ApJ, 2, 851 - 863

[7] W i l l i a m s B. F., Clues about the star formation history of the M31 disc from WFPC2 photometry, 331, 2002, MNRAS, 293 - 312

[8] W i l l i a m s B. F., Comparing young stellar populations across active regions in the M31 disc, 340, 2003, MNRAS, 143 - 159

[9] K u r t e v R., UBV and vby&beta stellar photometry in the eastern part of M31, 324, 2003, AN, 265 - 270

[10] V e l t c h e v T., P. N e d i a l k o v, G. B o r i s o v, Initial mass function in the South-Western part of M31, A&A, 2004, (in press)

[11] N e d i a l k o v P., T. V e l t c h e v, Red Supergiants in M31: extinction, mettalicities and gas-to-dust ratio, 2002, 73, PAOB, 219 – 230

[12] N e d i a l k o v P., E. B e r k h u i j s e n, C h. N i e t e n, M. H a a s, Relationships extinction-dust emission and extinction-gas density in M31, Aachen, 232 Interstellar medium in M31 and M33 Eds: E. M. Berkhujsen, Rainer Beck and R. M. Walterbos, 2000, 85 – 88

[13] N e d i a l k o v P., V. I v a n o v, On the Absorption of Light from the Brightest Stars in M31, 17, 1999, A&AT, 367 - 391

[14] C u i l l a n d r e J - C., J. L e q u e u x, R. A l l e n, Y. M e l l i e r, E. B e r t i n, ApJ, 554, 2001, 1, 190 - 201

[15] S a v c h e v a A., S. T a s s e v, Probing the extinction law and gas-to-dust ratio in M31 via globulars behind the disk, 2002, 73, PAOB, 219 - 230

[16] B a r m b y P., K. P e r r e t t, T. B r i d g e s, The `remarkable' M31 globular cluster 037-B327 revisited, 329, 2001, MNRAS, 461 - 464

[17] K o t o v O., S. T r u d o l y u b o v, W. T. V e s t r a n d, astro-ph/0307223, 1 – 18

[18] L o i n a r d L., R. A l l e n, Cold Massive Molecular Clouds in the Inner Disk of M31, ApJ, 499, 1998, 227 - 233

STUDIES OF SELECTED VOIDS. SURFACE PHOTOMETRY OF FAINT GALAXIES IN THE DIRECTION OF 1600+18 IN HERCULES VOID

G.Petrov [1] , A.Y.Kniazev [2] , and J.W. Fried [2]

[1] *Institute of Astronomy, Bulgarian Academy of Sciences, 72 Tsarigradsko chaussee, 1784 Sofia, Bulgaria;*
[2] *Max Plank Institut for Astronomy, Koenigstuhl 17, D 69117 Heidelberg, Germany*

Abstract:

Based on photographic plates obtained with 2m RCC telescope at National Astronomical Observatory Rozhen (Bulgaria) we inspected an area of ~1 sq.degree in the direction of the Hercules void with automatic object detection software. As our first result we present a list of ~1800 detected galaxies in the wide range of magnitudes $13^m \leq B \leq 21^m$ and effective surface brightnesses $16 \leq \mu_{eff}(B) \leq 24$ mag arcsec^{-2}.

Introduction

The presence of voids in the distribution of galaxies has been discovered in early redshift surveys of galaxies - see e.g. [1, 2]. Further studies show that the largest voids are those delineated by rich clusters and superclusters of galaxies [3, 4]. The Hercules region has attracted the attention of astronomers since [5] discovered the Hercules supercluster covers a large area of the sky north of celestial equator in the range ascension range between $12^h < \alpha < 18^h$. A collaboration project between the Institute of Astronomy of Bulgarian Academy of Sciences and Max Plank Institute for Astronomy (Heidelberg, Germany) is devoted to investigate some known voids [6]. We present here the first results of a study of faint galaxies in the direction of Hercules void.

Observations

The observations were done during the nights of 27 and 28 June 1991. The Ritchie camera of the 2m RCC telescope at National Astronomical Observatory ″Rozhen″ (Bulgaria) was used to get two plates centered on RA(2000): $16^h 01^m 58^s$ and DEC: +17°57′30″ (No.1830 hereafter) and RA: $16^h 02^m 15^s$ and DEC: ++17°51′34″ (No.1831 hereafter).

The unvignetted field is ~50 sq.arc minutes for each plate and the common unvignetted field is ~1x1 sq.deg. The exposure time for each plate was 180 minutes, enough to detect objects fainter than 21 mag. Neutral wedge was exposed for 40 minutes on each plate after the main exposure. The seeing during the observations was very stable and varied only in the range of 1-1.5″. ORWO plate ZU21 30x30 sq.cm and Schott filter GG 385 were used to realize the standard B-system. To calibrate these data CCD frames in B and R were taken with 1024 x 1024 Photometrics camera, attached to the prime focus on the 2m RCC telescope during the night on July 28th 2003. M92 standard fields were observed twice during the same night.

Reduction

The two plates were scanned in the former Astronomical Institute, University of Muenster on PDS 2020 GMplus scanning machine with 25x25 mkm square slit and 20 mkm step, getting
14400 x 14400 sq.px with scale 0.25 ″/pixel. The linearization of the images was performed
with the photometer wedge and the program INTENAIP from the Astrophysical Institute of Potsdam (AIP) package [7, 8] added to the ESO MIDAS package.

We used a package of automatic procedures described in detail in [9] to detect objects above the background, to reject false detections, and to produce astrometry and integrated and surface photometry of detected galaxies. This software was created to work with Sloan Digital Sky Survey [10] data and was fitted for our purpose. The output data consist of a MIDAS table that contains all information about the detected galaxies: accurate positions (plate, X, Y, α(2000), δ(2000)), total and integrated magnitudes with their uncertainties, effective radii (R_{eff}; in arcsec), effective surface brightnesses (μ_{eff}; in mag arcsec^{-2}), radii of the regions containing 90% of the integrated (R_{90} ; in arcsec), concentration indices $C=R_{90}/R_{eff}$, position angle (PA), axial ratio (b/a), exponential fit scale lengths (α; in arcsec) with their uncertainties (in arcsec) for bulge and disk components, exponential fit central surface brightnesses ($\mu_{E;0}$; in mag arcsec^{-2}) with their uncertainties for bulge and disk components and total magnitudes, integrated out to infinity.
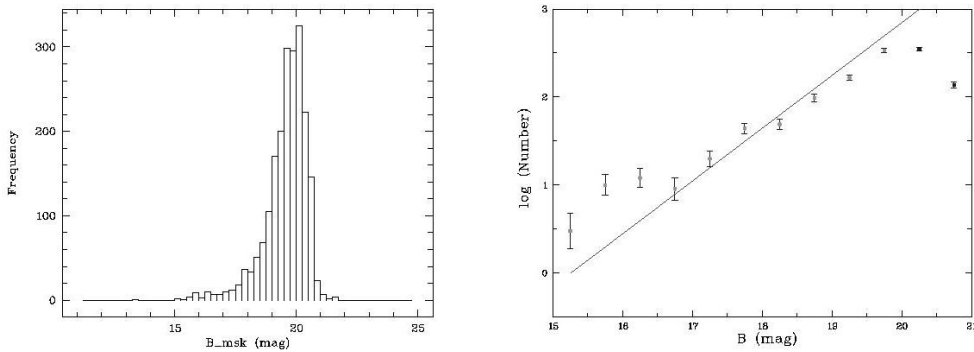
Figure 1: Left panel: Distribution of apparent magnitudes for all galaxies detected with

our programs. Right panel: Number counts of all galaxies detected with our programs as a

function of apparent magnitude. The errors bars on the galaxy counts are Poissonian. The

line shows the count-magnitude relation expected for a homogeneous galaxy distribution

in a universe with "Euclidean" geometry: $N(B) = A_B . 10^{0.6B}$.

    Integrated photometry: A code for fitting the sky background from the AIP package for adaptive filtering is used, which constructs the background within the masked regions. This algorithm iteratively fills the background inside the mask by interpolating the background from the regions outside the mask [7, 8] and it is used twice: 1) to subtract any contaminating sources like foreground stars or background galaxies and 2) to fit and subtract the sky background. During the next step we iteratively checked all detected objects by eye to identify multiple and false objects. After that the apparent is measured inside the same mask on the background-subtracted images. The instrumental is transformed into the apparent magnitude in the standard photometric system (see Fig.1). Firstly, we used the NED magnitudes for the bright galaxies in the our field to calibrate the data and finally we got M92 calibration frames (see above).
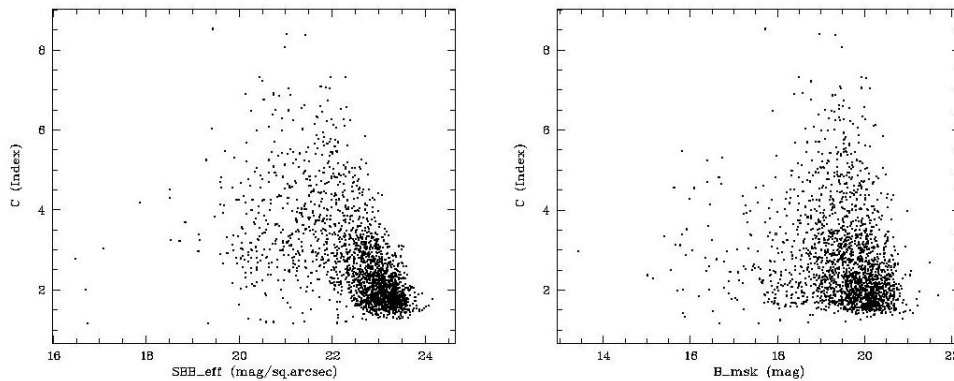
Figure 2: Relations between the concentration index and effective surface brightness (left panel) and the integrated magnitude (right panel).

Morphological types and concentration index: Our programs calculate a number of global parameters for every galaxy. Some of these may be useful for morphological galaxy classifications [11]. A particularly useful parameter is the concentration index, defined as the ratio of the radii containing 90% and 50% of a galaxy's light. For the classical de Vaucouleurs profile C is ~5.5 and for pure exponential disks C~2.3. These values are valid for the idealized seeing-free case (see Fig.2).

Creation of surface brightness profiles (SBP): The software generates SBP by measuring magnitudes in circular apertures. After a SBP is created, the effective radius R_{eff}, R_{90} and the concentration index C are calculated. Using the multilevel mask approach and ellipse fitting we also determine the PA of the major axis and the axis ratio *b/a*.

First Results

The data for all 1814 galaxies in the field - coordinates, aperture and surface photometry,
position angles, diameters, axis ratio and concentration are available under question or on- line in FITS format at
http://www.astro.bas.bg/~petrov/papers/hercules/v16t1.fits.

Giant Low Surface Brightness galaxies (LSBG): An interesting aspect of this pilot study is the identification of a substantial number of luminous distant galaxies. In Fig.3 the relations between the concentration index and the effective surface brightnesses μ_{eff} and the integrated magnitude are plotted. Some LSBGs could be selected there - bright

galaxies with B~15.5-18 mag or such ones with large diameters (> 40 arcsec) and SB > 22 mag/sqr.sec.

Galaxy Number Counts: The number counts of galaxies as a function of magnitude is one of the classical cosmological tests. We did it for our data and the result is plotted on the right panel of Fig.1. Galaxy number counts are shown in 0.5 mag bins. The errors bars correspond to
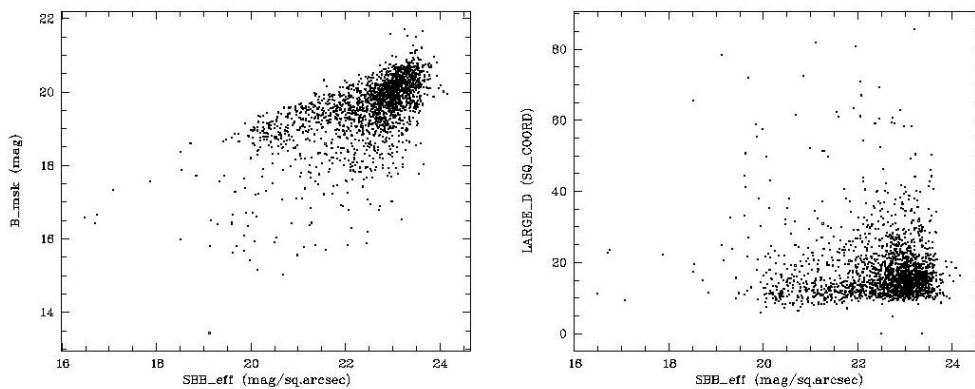
Figure 3: Left panel: Relation between the effective surface brightnesses and integrated
magnitude. Right panel: Relation between the effective surface brightnesses and major diameter of galaxies.

Poisson noise. The line in Fig.1 shows a fit to the galaxy counts-magnitude relation expected in a homogeneous universe assuming Euclidean geometry for three-dimensional space. The observed galaxy counts are quite consistent with this line for $17^m \leq B \leq 20^m$ and even fainter up to B=20.5 mag. It means that we have complete data up to this magnitudes. With our data we found big excess of bright galaxies (B<17.0^m).

References

[1] C h i n c a r i n i, G. & H.J. R o o d. The cosmic tapestry, Sky and Telescope, 59,1980,364

[2] G r e g o r y, S.A. & L.A. T h o m p s o n. Superclusters and voids in the distribution of galaxies, Sci. Am., 246, 1982, 106

[3] O o r t, J. Superclusters, Ann.Rev.A&Ap., 21, 1983, 373

[4] R o o d, H.J. Voids, Ann.Rev.A&Ap., 26, 1988, 631

[5] S h a p l e y, H. On some structural features of the metagalaxy, MNRAS, 94, 1934, 791

[6] P e t r o v, G., B. K o v a c h e v, & A. S t r i g a t c h e v. A search for galaxies in voids – first results, Astron.Ges. Abstr.Ser., 9, 1993, 46

[7] L o r e n z, H., G.M. R i c h t e r, M. C a p a c c i o l i, & G. L o n g o. Adaptive Filtering in Astronomical Image Processing – P1- Basic Considerations and Examples, A&A, 277, 1993,321

[8] K n i a z e v, A.Y. Ph.D. Thesis, Special Astrophys. Obs., Nizhnij Arkhyz, 1997

[9] K n i a z e v, A.Y., E.K. G r e b e l, S.A. P u s t i l n i k, A.G. P r a m s k i j, T.F. K n i a z e v a, F. P r a d a & D. H a r b e c k. Low-Surace-Brightness Galaxies in the Sloan digital sky survey. I. Search method and test sample, AJ, 127, 2004, 704

[10] Y o r k, D.G., J. A d e l m a n, J.E. A n d e r s o n et al. The Sloan Digital Sky Survey: Technical Summary, AJ, 120, 2000, 1579

[11] S t r a t e v a, I., Z. I v e z i c, G.R. K n a p p et al. Color Separation of Galaxy Types in the Sloan Digital Sky Survey Imaging Data, AJ, 122, 2001, 1861

MRK 1040 AND ITS COMPANION LEDA 212995

L. Č. Popović[1,2], K. Y. Stavrev[3], K. Tsvetkova[3], M. Tsvetkov[3], D. Ilić[4], S. F. Sanchez[2] and G. M. Richter[2]

[1] *Astronomical Observatory, Volgina 7, 11160 Belgrade 74, Serbia*
[2] *Astrophysikalisches Institut Potsdam, An der Sternwarte 16, D-14482 Potsdam, Germany*
[3] *Institute of Astronomy, Bulgarian Academy of Sciences, 72 Tsarigradsko Shosse Blvd., BG-1784 Sofia, Bulgaria*
[4] *Department of Astronomy, Studentski trg 16, 11000 Belgrade, Serbia*

Abstract

The Sy 1 galaxy Mrk 1040 and its close companion LEDA 212995 have been observed in several narrow spectral bands, as well as in the U and I bands, in order to look for possible interaction between them. The analysis of the observations shows a very strong point-like innermost center of Mrk 1040 that is from AGN, an irregular structure of the companion expected in the case of a star-forming region, and different star-forming regions in the stellar disk of Mrk 1040. No tidal tail of young stars between Mrk 1040 and LEDA 212995 has been identified.

1. Motivation

The influence of interactions on the fueling of the nuclei of AGNs, as well as of HII galaxies, has been the topic of several studies (see [1] and references therein). There are two interesting questions: (1) the origin of the gas that fuels the nuclear black hole, and (2) the mechanisms responsible for making the gas lose angular momentum and move from galactic scales down to the innermost central region of the AGN. Several mechanisms have been suggested to explain how it is possible to transport gas from the disk of a spiral galaxy to its nucleus. One of them is interaction between two galaxies.

One of visually galaxy pairs is Mrk 1040 and LEDA 212995. The companion LEDA 212995 is a small galaxy with emission lines indicating a star-forming region (HII lines, see [2]). Its dimensions are 0.20' x 0.10' and its magnitude is >19. The galaxy is visually located near the Sy 1 galaxy Mrk 1040 ($z = 0.01665$, [3]).

Afanas'ev & Fridman [4] pointed out that an analysis of the (*B-R*) color distribution in the galactic disk and the presence of a distinct dust lane in the disk show that 'the northeast side of the galaxy is farther away, and the companion, which is bluer than the disk of Mrk 1040, is closer to the observer'. The spectroscopic observations of Mrk 1040 and LEDA 212995 are given in [5], where the asymmetry in the velocity field of the companion is found and it is assumed that this asymmetry is due to interaction of the two galaxies. According to the redshift of the companion 0.0169±0.00015 estimated by Popović et al. [2], it seems that the two objects are close to each other.

Mrk 1040 is a Sy 1 galaxy with different star-forming regions in stellar ring. The close companion LEDA 212995 is also under star-formation. It is not clear if the companion is under interaction or not, and if the star-formation in it and the nuclei activity in Mrk 1040 are caused by the interaction of the two galaxies. To ascertain
this, we observed the pair in several narrow and broad spectral bands.

2. Observations

The observations have been made at the National Astronomical Observatory Rozhen with the 2 m Ritchey-Chretien-Coude telescope. We observed Mrk 1040 and LEDA 212995 in November 2003 and in January 2004. The dates of observations and the used spectral filters are given in Table 1.

Table 1. Observations of Mrk 1040 and LEDA 212995

RA DEC	Redshift	Date of observation	Spectral line	Number of images	Exposure time [s]
2h 28m 14.3s +31° 18′ 40.4″	0.016652	16-Jan-04	HeII	3	600, 900, 1200
		16-Jan-04	[OIII]	2	600
		16-Jan-04	U band	2	900
		17-Jan-04	I band	5	120, 300, 420
		17-Jan-04	Continuum	2	300, 600
		17-Jan-04	[SII]	1	600

Standard reduction procedures including bias subtraction, trimming and flat-fielding have been performed with the help of the IRAF software package. Here we present results only from the processing of the

observations in the *U* and *I* broad bands and in the HeII 4686 and [OIII] 4959, 5007 narrow bands, as well as the comparison of the narrow bands with the continuum ($\lambda = 5757$ Å).

3. Results

In order to find any evidence of interaction we have processed the images as follows:

(1) A surface brightness analysis over the narrow-band images has been applied assuming an elliptical isophotic model, based on the technique given by Jedrzejewski [6]. We used own code (Sanchez) for the analysis, which provides us with a model (for Mrk 1040) of the smooth component in the images. This model has been subtracted from the images (in different narrow bands). After subtraction we obtained an image where the substructures in the objects can be seen, as well as structure(s) that may indicate interaction between the objects (see Figs. 2 and 3, panel top-left).

(2) We have modeled Mrk 1040 using GALFIT [7]. The galaxy model has been done including three components: the nuclear point-like source, a bulge and a disk. This model has been subtracted from the images in order to detect the substructures (Figs. 2 and 3, panel down-left).

(3) We have scaled the continuum image to the narrow-band images, and subtracted it from them. It provides us with images of the pure HeII and [OIII] emission lines (Fig. 4, bottom-right).

(4) We have divided the *U*-band image by the *I*-band image, in order to get a *U-I* color image (Fig. 4, top-right).
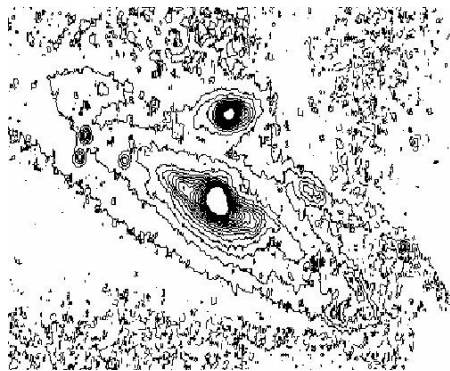
Fig. 1
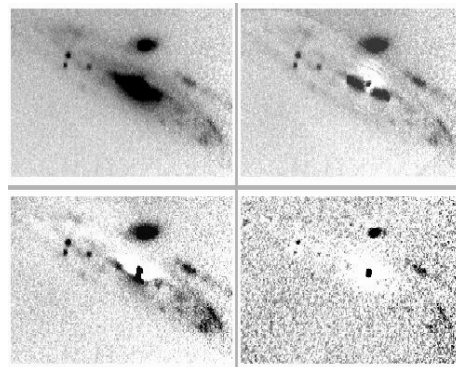
Fig. 2

Fig. 1. The brightness of Mrk 1040 and companion in the [OIII] 4959, 5007 lines.

Fig. 2. Original narrow-band image in [OIII] (top-left); residual image once subtract- ed the model obtained by the surface brightness analysis (top-right); residual image once subtracted the model obtained using GALFIT (bottom-left); residual image once subtracted the continuum scaled image (bottom-right).
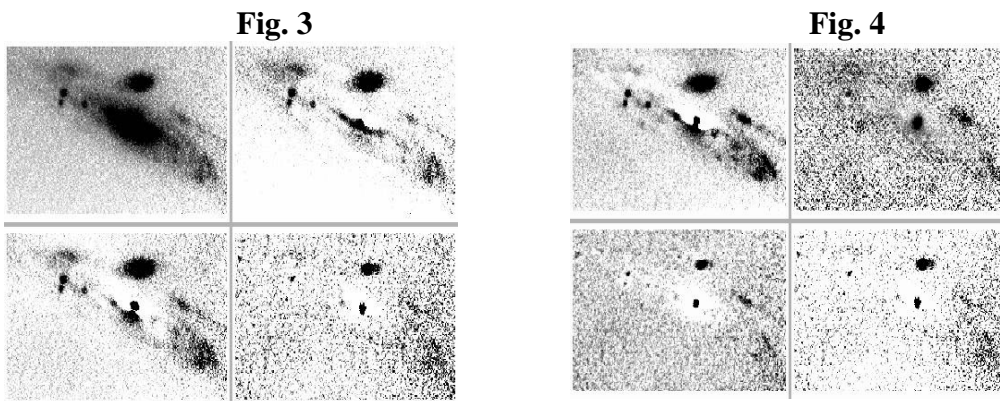
Fig. 3

Fig. 4

Fig. 3. Same as in Fig. 2, but for the HeII line.

Fig. 4. The original continuum narrow-band image (top-left); *U-I* color image (top-right); the [OIII] line regions after subtracting the continuum (bottom-left); the HeII 4686 line region after subtracting the continuum (bottom-right).

As one can see from Figs. 2-4, the substructures seen in all images are remarkably similar, indicating that: (i) There is a very strong point-like innermost center of Mrk 1040 that is from AGN. The companion has irregular structure that is expected in the case of star-forming region. (ii) Different star-forming regions in the disk of Mrk 1040 galaxy are seen in the western part of the arm. (iii) From our preliminary analysis we can conclude that there is no tidal tail of young stars in between Mrk 1040 and LEDA 212995.

References:
1. Schmitt, H.R., 2001, AJ 122, 2243.
2. Popović, L.C., Mediavilla, E., Bon, E., Ilić, D., Richter, G., 2004, Astron. Nachr. 325, 376.
3. Huchra, J.P., Vogeley, M.S., Geller, M., 1999, ApJS 121, 287.
4. Afanas'ev, V.L., Friedman, A.M., 1993, Astron. Lett. 19, 319.
5. Amram, P., Marcelin, M., Bonnarel, F., Boulesteix, J., Afanas'ev, V.L., Dodonov, S.N., 1992, A&A 263, 69.
6. Jedrzejewski, R.I., 1987, MNRAS 226, 747.
7. Peng, C.Y., Ho, L.C., Impey, C.D., Rix, H.-W., 2002, AJ 124, 266.

THE RADIAL BRIGHTNESS PROFILES OF THE GALACTIC DISKS

Tsvetan B. Georgiev

Institute of Astronomy, Bulgarian Academy of Sciences

Abstract.

A brief review of the problems and methods concerning modeling of the radial profiles of the galaxies is given. It is shown that the Sersic's (1968) formula, with an exponential number N between 1 and 3, adequately represents the convex disk profiles. Our results show that the disk profile convexity correlates more with the relative mass of the bulge than with the absolute mass of the galaxy. Examples of iterative decomposition of both the profiles of the galaxies M 33 (with almost exponential disk), UGC 1400 (visible edge-on, with possible ring-like disk) and simulated profiles as well as a comparison of B,J and K profiles of the galaxies M 51 and M 74, are given.
Key wodrs: *galaxies – structures; galaxies – fundamental parameters*
PACS number: 98.52.-b, 98.52.Nr

The investigations of the galaxies structure components include modeling of their brightness profiles. The aim of this approach is to find (1) an universal method for measuring galaxies sizes and magnitudes; (2) quantitative description of the Hubble sequence and scaling relations (e.g. fundamental plane), as well as (3) to reveal photometric indicators for the galaxy's "giantism" applicable in multidimensional Tully-Fisher type methods for distance estimation.

The simplest model of a spiral galaxy consists of bulge and disk components, whose observing radial brightness profiles could be presented by the Sersic's (1968) formula:

$$(1) \qquad I_R = I_0 \exp(-(R/H)^N) \quad \text{or} \quad \mu_R = \mu_0 + C\, R^N$$

Here I_0 is the central intensity, $\mu_0 = -2.5 \log I_0$ is the central surface brightness, the exponential number N defines the shape of the profile, H is the radial scale

length (the characteristic distance from the center at which the intensity decreases e-times) and C = $(1.087\ H)^{1/N}$ is coefficient in the magnitude representation of the profile. The de Vaucouleurs (1948) "1/4 law" for the giant elliptical galaxies and bulges of the early type galaxies, as well as the Freeman (1970) "exponential law" (suspected by de Vaucouleurs (1959)) for the disks are particular cases of (1) with N=1/4 and N=1, respectively.

Great amount of galactic profiles has been decomposed in the last 30 years by use of de Vaucouleurs model for the bulge and Freeman's model for the disk (van der Kruit 2002; Anderson et al. 2004). However, in many cases of early type galaxies the central region of the disk seems to have plateau or depression. Thus the disk model with inner truncation may be applied (Kormendy 1977, Anderson et al. 2004). On the other hand, the contemporary investigations show that less massive bulges of late type galaxies (as well as less massive elliptical galaxies) tend to have more compact periphery than the de Vaucouleurs law predicts (Andredakis et al 1995). Such radial profiles may be modeled by (1) with N>½ , up to N = 2 (Gaussian function).

The deep observations helped to figure out also that the faint peripheral regions of the disks seem to be truncated and can be modeled with outer "cutt-off radius" (van der Kruit & Searle 1981, Barteldrees & Dettmar 1994). However, the deepest observations published by Pohlen et al (2002), show that the disks really has not truncation radius, but has convex brightness profiles. Pohlen et al. (2002) has modeled such profiles using two exponents – inner, corresponding to the Freeman's model and outer – steeper (see also Pohlen et al. 2004).

Generally, the contemporary data shows that the disk brightness profiles are smoothly convex (even in the cases of the LSB and dwarf galaxies, independently of the environments); and in some cases of early type or bar galaxies the central brightness of the disks has a depression. Any modern model of the disk brightness profile must account for such features. However, the model of Freeman (1970) describes disk with (1) well prominent peak of the central brightness, (2) linear radial decrease of the brightness in magnitude scale and (3) infinite size. In the model with inner truncation (Kormendy 1977) the central peak may be absent, even if the disk has a ring-like shape, but the periphery remains infinite. In the model with sharp outer truncation (van der Kruit & Searle 1981) the central peak remains sharp and the cut-off-radius

depends on the deepness of the observation. Finally, the central peak in the two exponent model of Pohlen et al. (2002) remains sharp and the profile is "broken".

Recently I began to model the galactic disk profiles using the Sersic's (1968) formula (1) and also generalized this formula by adding 2nd and 3rd order terms. The 1st order formula (1) is well describing smooth convex profiles without strong central peak. The 2nd order can describe the disk's profile with strong central depression, even in the case of ring-like disk. The 3rd order formula is able to describe the whole profile of a galaxy with prominent bulge and disk and its inflex point is the natural dividing point between the bulge and disk profiles. This point is necessary for the decomposition. The 3rd order formula has the form

$$(2) \qquad I_R = I_0.\exp(-(R/H_1)^N -(R/H_2)^{2N}-(R/H_3)^{3N})$$

$$\text{or} \qquad \mu_R = \mu_0 + C_1.R^N + C_2.R^{2N} + C_3.R^{3N}$$

The decomposition procedure in the spirit of Kormendy (1977), but using the Sersic's formula both for the bulge and disk, is realized as C-language program.

The intermediate results of the profile decomposition of the galaxies M 33 and UGC 1400 into bulge and disk components are shown in Figure 1, according to the number of the iterations, given at the top of the graph. For the disk component the upper (overestimated) model curves correspond to the 1st iteration and for the bulge - the 1st iteration provides the most left (underestimated) profile. The short vertical line shows the position of the dividing point. In the case of the classic profile of M 33 in B-band (from de Vaucouleurs 1959) the final corresponding exponential numbers N for the bulge and disks are 1.07 and 1.80. In the case of the edge-on galaxy UGC 1400 in R-band, based on an isophote map, published by Karachentsev et al. (1992), the decomposition using 2nd order Sersic's formula is applied. It seems that this galaxy has disk with significant central depression. The optimal derived exponential number for the disk is N = 1.35. A decomposition with the 1st order Sersic's formula (1) provides results, which are very close to the presented results of the 1st iteration for UGC 1400 and the corresponding exponential bulge and disk numbers N are 2.22 and 2.84, respectively. These data correspond to the truncated bulge plus disk with inner and outer truncations.
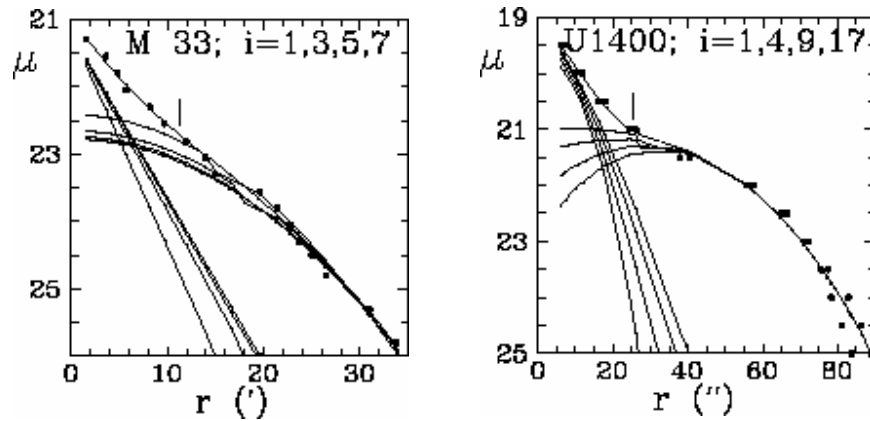
Fig.1. Intermediate results of the decomposition in the case of M 33, with almost exponential profile, and UGC 1400 (visible edge-on), with possible ring like disk. The number of the iterations is given at the top of the graph. The short vertical line shows the position of the dividing point between the bulge and disk components of the profile.

Decomposition of the simulated profiles where both bulge and disk profiles are fitted by the Sersic's formula (1) and normal noise with standard deviation 0.2 mag is added to the result profile, are shown on Figure 2. The simulated profiles experiments spread out on situations when the central intensity of the bulge is 3-50 times higher than that of the disk and when the scale length of the bulge is 5-20 times less than that of the disk. In such cases the decomposition technique provides good results. Unfortunately, the noise somewhat crucially affects the choice of the dividing point. Though, both the numerical simulations and the comparison of the results for nearby galaxies (Georgiev 2004) give evidences that the standard error estimations of the values N and μ_0 are about 25% and 0.3 mag for the disk.

Here we present the first application of this approach for 22 profiles of the nearby galaxies M 31, MW (model), M 33, LMC, SMC and M83, published by different authors (cf. Georgiev 2004) and for 22 published profiles of near

edge-on galaxies (Georgiev & Stanchev 2004a). The results show that the formula (1), with $1 < N < 4$, is a good tool for "measuring" and comparing galactic disks. The conclusion is that the shape parameter N of the disk profile increases with the mass of the disk. Another more complete sample of 119 northern edge-on galaxies with a size between 2 and 7 arcmin, homogeneous distribution of the bulge-to-disk ratio and luminosity was studied by Georgiev et al. (2004a). They claimed that the convex shape of the disk profile is connected with the relative giantism of the bulge – the disks of spiral galaxies of earlier type tend to have more convex disk shapes. The conclusion is that the bulge-disk interaction results in a convex shape of the disk. Detection of ring-like disks using the 2nd order Sersic's formula is presented by Georgiev & Stanchev (2004b). Other examples are given by Georgiev et al. (2004b).

The comparison between the radial profiles of the face-on galaxies M 51 and M 74 is shown in Figure 3. The data from different sources show that these galaxies have radial disk profiles with convex shapes.
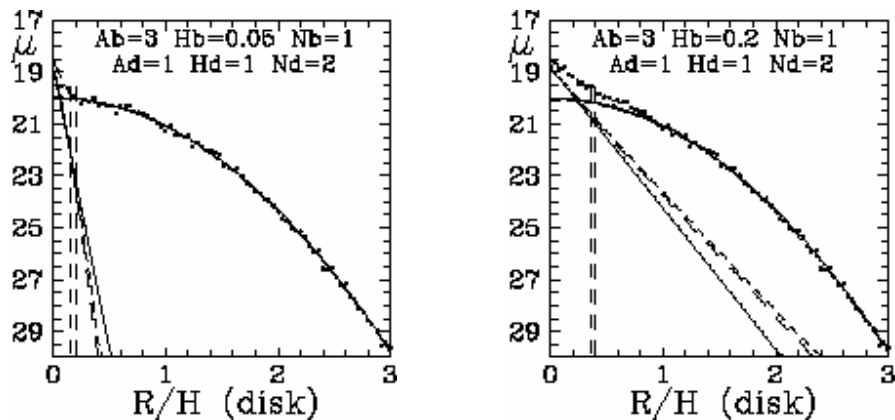
Fig. 2. Decompositions of simulated radial profiles of galaxies. The bulge and disk components (solid curves) are modeled through the 1st order Sersic's formula with exponential numbers Nb = 1 and Nd = 2.The other parameters are given in the top of the plots. Strong normal noise with standard deviation of 0.2

mag is added to the superposition of the bulge and disk models (dots). The results of decomposition using disk model according to the 1st or 2nd order Sersic's formula are presented with long dashes and short dashes, respectively. The vertical dashed lines indicate the dividing interval between the bulge and the disk.
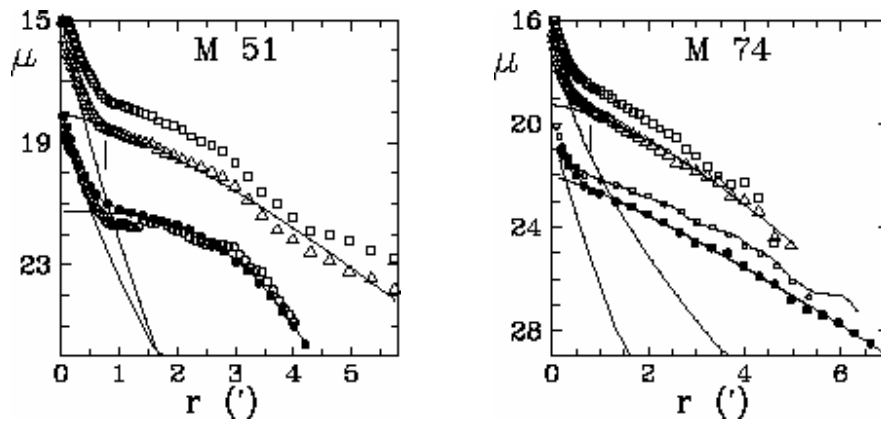
Fif. 3. Comparison between the radial profiles of the galaxies M 51 and M 74 in B, J and K bands. The B-band data for M 51 are taken from the papers by Okamura et al. (1976, dots, decomposed) and Boroson (1981, circles) and in the case of M 74 – from Natali et al. (1992, dots, decomposed), Shostak & van der Kruit (1984, circles) and Wevers et al. (1986, solid curve). The J and K data from 2MASS (Jarret et al. 2003) are presented by triangles (decomposed) and squares.

The encouraging results when fitting the convex disk profiles with the Sersic's formula, with an exponential number $N_d > 1$, gives possibilities to reanalyze many published galaxies profiles. In the future we intend to investigate the scaling relations for the disk components of the spiral galaxies using deep observations, both published and our own.

The author is gratefull to P. Nedialkov for the valuable discussions.

References:

A n d e r s o n K. S., S. M. B a g g e t t, W. F. B a g g e t t , 2004, AJ 127, 2085

A n d r e d a k i s Y.C., R. F. P e l e t i e r, M. B a l c e l s, 1995, MNRAS 275, 874

B a r t e l d r e e s A., R.-J. D e t t m a r, 1994, A&AS 103,475

B o r o s o n T., 1981, ApJ 46,177

d e V a u c o u l e u r s G., 1948, Ann. Astrophys. 11, 247

d e V a u c o u l e u r s G., 1959, ApJ 130, 728

F r e e m a n K.C. 1970, ApJ 160, 811

G e o r g i e v T. B., 2004, Aerospace researches in Bulgaria, in print

G e o r g i e v T. B., O. I. S t a n c h e v, 2004a, Bulgarian Journal of physics, in print.

G e o r g i e v T. B., O. I. S t a n c h e v, 2004b, Publ. Astron. Obs. Belgrade, in print

G e o r g i e v T. B., O. I. S t a n c h e v, P. L. N e d I a l k o v , 2004a,
        Annuaire d'Universite de Sofia, in print

G e o r g i e v T. B., O. I. S t a n c h e v, P. L. N e d i a l k o v , I. Y. G e o r g i e v, N. A. K o l
e v a, 2004b, in this issue,.

J a r r e t T. H., T. Chester, R. Cutri, S. E. S c h n e i d e r, J .P. H u c h r a, 2003, AJ 125, 525 .

K a r a c h e n t s e v I., T. G e o r g i e v, S. K a j s i n, A. K o p y l o v, V. S h e r g i n, V. R y
a d c h e n k o, 1992, Astron. Astrophys. Transactions. 2, 265

K o r m e n d y J.., 1977, ApJ 217, 406

M e s t e l L., 1963, MNRAS 126, 553

N a t a l i G., F. P e d i c h i n i, M. R i g h i n i, 1992, AA 256, 79

O k a m u r a K., T. K a n a z a v a, K. K o d a i r a, 1976, PASJ 28, 329

P o h l e n M., R.-J. D e t t m a r R.-J., R. L u e t t i c k e, G. A r o n i c a, 2002, A&A 392, 807

P o h l e n M., J. B e c k m a n, S. H u t t e m e I s t e r, J. K n a p p e n, P. E r w i n ,R.-J. D e t t
m a r, arXiv:astro-ph/0405541, 2004

S e r s i c J.-L., Atlas de Galaxies Australes 1968 (Obs. Astron.Univ.Nat.Cordoba)

S h o s t a k G. S, P. v a n d e r K r u I t, 1984

V a n d e r K r u i t P. C . 2002, in eds. G.S. da Costa and E.M.Sad ler, Dynamics, Structures
        and History of the Galaxies, ASP Cof. Serr. Vol.273 P.7

v a n d e r K r u i t P. C., L. S e a r l e 1981, A&A 95, 105

W e v e r s B. M.H. R., P.C. v a n d e K r u i t, R. J. A l l e n, 1986, A&AS 66, 605

ANALYSIS OF THE COLOR-MAGNITUDE DIAGRAMS OF THE DWARF GALAXIES UGCA 105 AND UGCA 86

T. B. Georgiev[1], I. Y. Georgiev1[1,2], N. A.Koleva[1,2], P. L. Nedialkov[2], O .I. Stanchev[1].
[1]Institute of Astronomy, Bulgarian Academy of Sciences
[2]Departament of Astronomy, Sofia University "St. Kliment Ohridski"

Abstract.
The method of the brightest star color distributions on the color-magnitude diagram is applied order to determine the foreground extinction toward two Im galaxies, seen through the Milky Way disk. The accuracy of the derived extinction values is estimated to be about 0.2 mag. The CCD photometry in V and I bands published by Karachentsev et al. (1997) is used. The extinction estimates toward UGCA 105 and UGCA 86 are 0.94 mag and 5.33 mag, respectively. They are significantly different from the catalogue values, 1.35 mag and 4.06.mag (Schlegel et al. 1998), but the most appropriate respective isochrones explain better the apparent color-magnitude diagrams. It seems that the brightest disk region of UGCA 86, known as VII Zw 9, is located along a sightline of lowered extinction (3.29 mag).

The IC 342/Maffei complex galaxies are situated very close to the plane of the Milky Way (MW) and their study is strictly limited by the foreground extinction and foreground star contamination (see Karachenstev et al. 1997, Buta & McCall1999). In such cases the foreground extinction may be estimated on the basis of the mean color of the blue plume of the color-magnitude diagram (CMD) of the studied galaxy. For this purpose we build the differential distribution of the brightest resolved galaxy stars according to the color index, called here the color function (CF). This approach is applied on published photometry of Karachentsev et al. (1997), based on observations with the Nordic Optical Telescope.

The average color index of the OB stars on the CMD (as well as the position of the respective local maximum of the CF) depends weakly on the metal abundance. Our preliminary studies show that the mean color indexes of the blue plume is $(B\text{-}V)_0 \approx (V\text{-}I)_0 \approx$

−0.1. In the case of low metallicity the mean color index of the red plume is $(B\text{-}V)_0 \approx 1.5$ or $(V\text{-}I)_0 \approx 1.7$ (see Georgiev 2002 and references therein). The error estimation of the CF local maximum determination and of the color excess (here $E(V\text{-}I)$) is about 0.05 mag. Therefore the standard error of the extinction in B band is $A_g = E\,(V\text{-}I)/0.32 \approx 0.2$ mag. The mean color of the top of the red plume on the CMD could be used as check for derived value A_g, as well as for the selection of the isochrones set with an appropriate metallicity. Unfortunately, the plume of the red stars is highly inclined and its mean color index is in principle poor defined.

In the case of observation through MW disk an additional important information about the foreground extinction may be obtained from the mean color index of the foreground stars, as follows. The number of the stars in front of the majority of the absorption medium must be significantly less than the number of the stars behind it. Therefore big part of the strongly reddened stars, mainly KM dwarfs, must be MW stars placed behind the absorption medium. According to the model of the MW's stellar population of Robin et al. (2003) the main true color index of the CF peak of the MW stars is $(V\text{-}I)_f \approx 0.8$.

The method applied here consists of 5 steps, as follows: (1) We construct the CMD in coordinates (V-I) – V and had determined the upper limiting magnitude V_0 of the brightest blue stars suspected as members of the studied galaxy. (2) Next we build CFs with upper limit V_0 and magnitude interval (this work) $\Delta V = 3$ mag, with step and interval along the color index axis of $(V\text{-}I) = 0.05$ and 0.1 mag (this work), respectively. Further we smoothed the CFs accounting for three neighboring points with weights of 0.25, 05 and 0.25. If the photometry is deeper, we may build a set of CFs with $\Delta V = 3$ mag, increasing V_0. Also in cases of severe foreground star contamination we build the CF of the stars brighter than V_0. (3) We derive the apparent mean color indexes $(V\text{-}I)_b$, $(V\text{-}I)_r$ and $(V\text{-}I)_f$, corresponding to the blue, red and foreground plumes of the CMD. (4) A corrections for the foreground extinction and the distance modulus (DM) of the galaxy was applied. (5) Having estimation of A_B and DM we superimpose set of isochrones with a fixed metallicity over CMD in order to obtain the best fit of the galaxy stellar population. The preliminary analysis of the CMDs of the studied galaxies showed that the red plumes are slightly shifted, corresponding to $(V\text{-}I)_0 = 1.75$ and thus, the isochrones with Z=0.008 we considered to be are the most appropriate.

Table 1 summarizes the gross-properties of the studied galaxies, available from the LEDA data base – the size of the galaxy a in arcminutes,

the axial ratio *b/a*, the total magnitude B_t, the foreground extinction in B-band A_g, HI line width W_{50}, as well as the expected mean color indexes the blue and red plumes, *(V-I)$_b$* and *(V-I)$_r$*, according to the A_g, adopted in LEDA. The last three columns contain the distance modulus DM, the total absolute magnitude M_B and the galactic latitude b_{MW} (in degrees). In the case of UGCA 105 the DM is derived by Karachentsev et al. (2002) according to the location of the Tip of the Red Giant Branch (TRGB). In the case of UGCA 86 Karachentsev et al (2003) does not found the TRGB and we adopt the distance estimation of Karachentsev et al. (1997) based on the brightest galaxy stars, corrected with the value for A_g adopted in LEDA.

Table 1. Basic data of the studied galaxies.

Galaxy M_B	*a* b_{MW}	*b/a*	B_t	A_g	W_{50}	*(V-I)$_b$*	*(V-I)$_r$*	DM
UGCA 105 16.70	5.5 13.7	0.64	12.14	1.35	118	0.33	2.18	27.49 -
UGCA 86 17.94	4.5 10.6	0.69	13.50	4.06	83	1.20	3.05	27.38 -

The data in Table 1 shows that the two studied Im galaxies are very similar to each other, however, the less massive and strongly obscured galaxy UGCA 86 has surprisingly high luminosity. One possible explanation is an overestimated distance modulus. Further we will consider separately the south-eastern part of the frame of UGCA 86, published by Karachentsev et al. (1997), constrined by the pixel values X>600 and Y>600, and called here UGCA 86b. It covers the brightest part of the disk of UGCA 86, known also as object VII Zw 9. The gas velocity field published by Robin et al (2003), shows that VII Zw 9 is a part of the disk of UGCA 86s. The UGCA 86b area covers 37% of the frame and contains 254 stars (57% of all measured). The rest part of the frame here is called UGCA 86a.

Table 2 contains the quantities derived in this work – the mean color indexes of the blue, red and foreground stars plumes on the CMDs, *(V-I)$_b$*, *(V-I)$_r$* and *(V-I)$_f$* , respectively, the foreground extinction $A_g = (V-I)_b/0.32$ and the distance modulus *DM*, corresponding to Table 1, but corrected with A_B, obtained in this work. The data given in Table 2 concerns UGCA 86b only, because our UGCA 86a data is identical to UGCA 86 data.

Table 2. The quantities, derived in this work.

Galaxy	$(V-I)_b$	$(V-I)_r$	$(V-I)_f$	A_g	DM	M_B
UGCA 105	0.20	2.05	0.97	0.94	27.67	-16.47
UGCA 86	1.60	3.45	2.35	5.33	26.11	-17.94
UGCA 86b	0.95	2.80	-	3.29	28.15	-

The CMDs and CFs of the galaxies UGCA 105 and entire UGCA 86 are shown in Figure 1. Some of the stars (the total numbers are 568 and 444, correspondingly) fall outside the selected CMD limits. The upper brightness V_0 is determined to be 20.4 mag for UGCA 21.8 mag – фор UGCA 86. In the case of UGCA 105 we show also two "deep" CF, with upper limitc 21.9 mag and 22.4 mag, respectively. Each rectangle in Figure 1, delineated with a solid line, has a width of 1 mag and encompasses the brightest parts of the blue and red plumes in the galaxy, populated by supergiant candidates. They are centered on the derived here values for $(V-I)_b$ and $(V-I)_r$, given in Table 2. The isochrones of Padova group (Z=0.008 and ages between 13.6 and 31.6 Myr), corrected with the values of A_g and DM, adopted in Table 1 (dashed curves) and Table 2 (solid curves) are superimposed. The "main" CFs are represented by solid curves. The foreground stars and UGCA 105 CFs, are plotted with short dashed curves. Dashed vertical lines demarcate the expected mean color indexes of the blue and red plumes, corresponding to the extinction given in Table 1, but solid vertical lines - the apparent mean color indexes $(V-I)_b$, $(V-I)_r$ and $(V-I)_f$, given in Table 2.

In the case of UGCA 105 we found two well defined plumes of the blue and red stars and the derived extinction (0.94 mag) is less than that given in catalogue data (1.35 mag) (Schlegel et al. 1998). The position of blue plume on the CMDs, obtained with the Hubble Space Telescope (Karachentsev et al. 2002, 2003) confirms the derived estimations. The position of the foreground star plumes gives even slightly smaller value of the foreground extinction. In Fig.1 the isochrones, corrected with our extinction value (solid curves) explain slightly better the populated parts of the CMD, too. Generally, we may conclude that in the last 10-15 Myr UGCA underwent a new starforming event, while during the past such period has finished roughly 30 Myr ago.
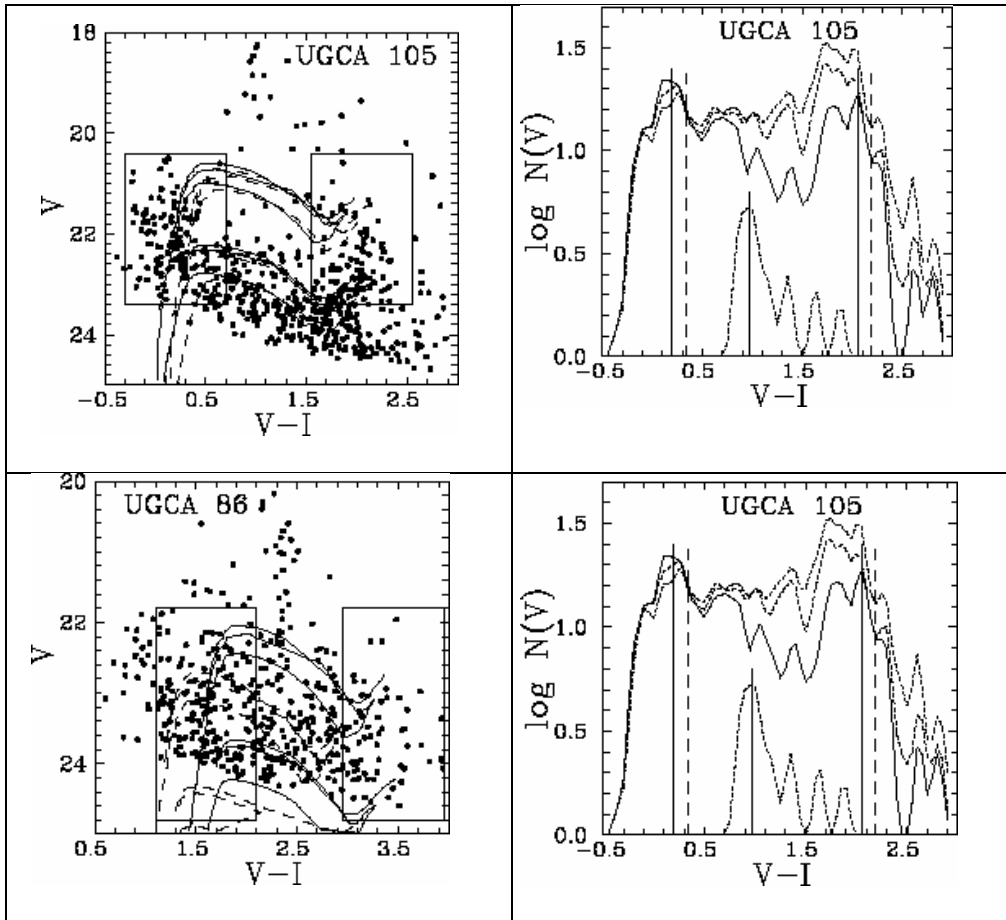
Fig. 1. Color-magnitude diagrams and color functions for the brightest stars in UGCA 105 and UGCA 86 (see the text).

The UGCA 86 CF shows many local maximums. The positions of the two of them are in a good agreement with catalogue extinction value in LEDA of 4.06 mag (Schlegel et al. 1998). However, the positions of the highest maximum and the position of the foreground stars plume, correspond to a higher extinction – 5.33 mag. The expoected well-pronounced maximum of the red stars is missing, but this could be explained with the limited depth of the observation in V-band. Moreover, the most populated parts of the CMDs are better fiited by the color indexes of the isochrones with a higher extinction correction (solid curves) applied. However, if we adopt such a high extinction, the distance modulus, based on

the brightest stars selected by of Karachentsev et al. (1997), becomes too small – 25.75 mag.
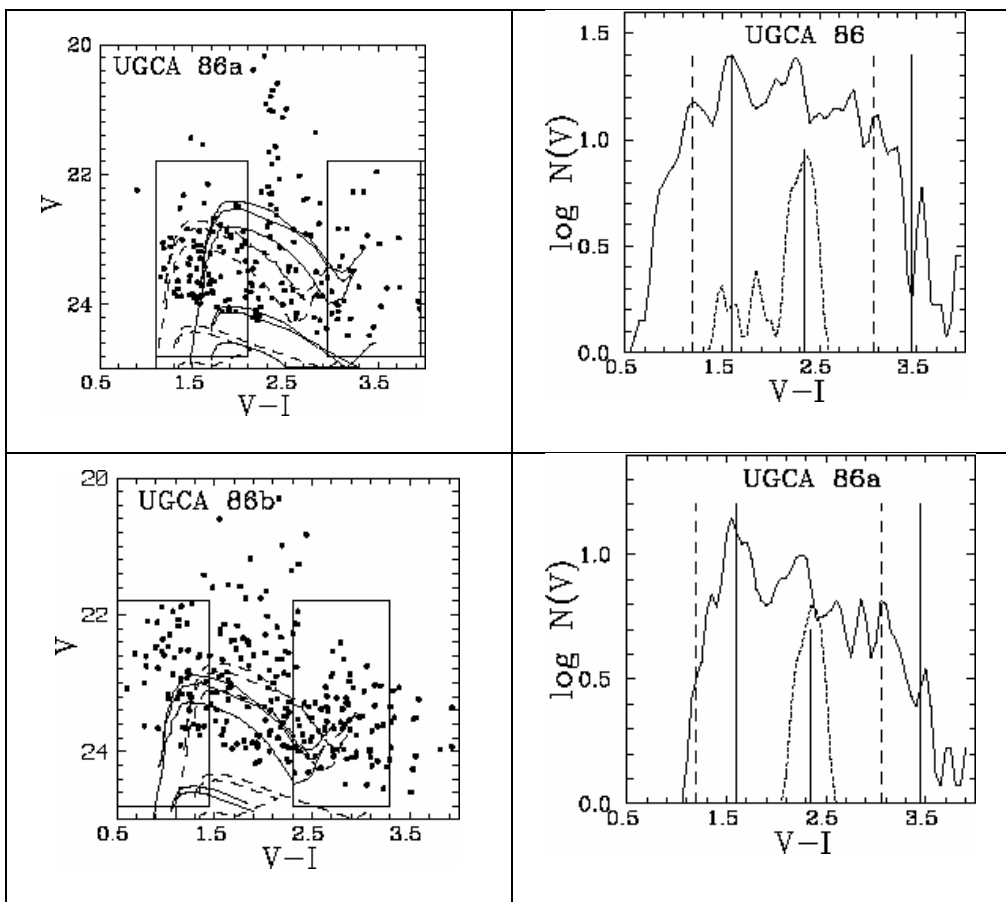
Fig. 2. Color-magnitude diagrams and color functions for the brightest stars in two parts of the galaxy UGCA 86 (see the text).

In Fig.2 we compare two CMDs of UGCA 86 – for UGCA 86a and UGCA 86b. The derived quantities for UGCA 86a are identical with those for the whole galaxy. However, the derived data about UGCA 86b are significantly different. The extinction value is significantly lower (3.29 mag), the foreground stars plume is missing and the respective corrected distance modulus occurs to be too high – 28.15 mag. The superimposed isochrones does not explain the observed CMD of UGCA 86b. Therefore, we could suspect that the brightest part of UGCA 86 is a stellar complex seen through relatively transparent "window" of MW having significantly

lowered extinction along that sightline. Generally, UGCA 86 continues to seem similar to UGCA 105, but the lack of coherent distance determinations strongly limits the possibilities for a more detailed study.

Here we reported a brief analysis of CMDs of two strongly obscured galaxies using the CFs method. Our aim was to derive an extinction estimate based mainly on photometry criteria. In the case of UGCA 105 we obtained rough estimates about the star forming history. We conclude also that the MW extinction in direction toward UGCA 86 galaxy is similar to UGCA 105 and is strongly inhomogeneous. Thus, a deeper photometry is necessary to figure out the problem with the distance modulus.

References

B u t a R. J., M. I. M c C a l l, 1999, AJ 124,33

G e o r g i e v T. B., 2002, Publ. Astron. Obs. Belgrade No. 73, 143

S c h l e g e l D. I., D. P. F i n k b e i n e r, M. D a v i e s, 1998, ApJ 500, 525

K a r a c h e n t s e v I. D., I. D r o z d o v s k y, S. K a j s i n, (7 authors), 1997, A&ASS 124,559

K a r a c h e n t s e v I. D., M. E. S h a r i n a, I. D. M a k a r o v et al (11 authors) 2002, A&A 389, 812

K a r a c h e n t s e v I. D., M. E. S h a r i n a, A. E. D o l p h i n, E. K. G r e b e l, 2003, A&A 408, 111

R o b i n A. C., C. R e y l e, S. D e r r r e re, S. P i c a u d , 2003, A&A 409, 523

DECOMPOSITION OF THE PROFILES OF 20 GALAXIES

T.B.Georgiev[1], I.Y.Georgiev1[1,2], N.A.Koleva[1,2], P.L.Nedialkov[2], O.I.Stanchev[1].

[1]*Institute of Astronomy, Bulgarian Academy of Sciences*
[2]*Departament of Astronomy, Sofia University "St. Kliment Ohridski"*

Abstract.

Decomposition technique in the spirit of Kormendy (1977), but where both bulge and disk profiles are modeled using Sersic's (1968) formula, is applied on 20 published galactic disks profiles. The result of Andredakis et al (1995) that the radial bulge profiles of the early type galaxies are close to the de Vaucouleurs (1948), but the bulges of the later galaxies have more compact shapes, is confirmed. We also confirm our previous results that the radial disk profile shapes of the later galaxies are close to the Freeman's (1970) model and only slight convex, in contrast to those of the early galaxies which shapes are obvious convex. The most deep profiles shows that the minimal observation depth sufficient enough to study the true shape of the radial disk profile in B,V, R, I, J, H and K band should be about 27.5, 26.5, 26,25.5,25,24.5 and 24 mag/arcsec^2, respectively.
Key words: *galaxies – structure; galaxies – fundamental parameters*
PACS number: *98.52.-b., 98.52.-Nr*

In the last decades much work has been done in order to improve the methods for ascertaining the main components (bulge and disk) of the disk galaxies based on their optical photometric profiles. The papers of Freeman (1970), Kormendy (1977), Boroson (1981),Shombert & Bothum (1987), Kent (1987), Capaccioli et al (1987), Andredakis & Sanders (1994), de Jong (1986), Moriondo et al (1997), Anderson et al (2004) etc. leads to a gradual progress in resolving this difficult topic. In all these studies, except the works of Kormendy (1977) and Anderson et al. (2004) the disk shape is modeled as exponential, following Freeman (1970).

In our previous papers (Georgiev 2004a, Georgiev & Stanchev 2004, Georgiev et al. 2004 and Georgiev 2004b) we introduced modeling of the smooth convex profiles of the galactic disks by means of the Sersic's (1968) formula. The decomposition in the spirit of Kormendy (1977) was made using

the Sersic's (1968) formula for both the bulge and the disk shapes in order to find the optimal exponential numbers (see Georgiev 2004b). Here we give the results after applying of this approach for 20 galaxies profiles, taken mainly from classical papers.

The data about of the galaxy profiles are summarized in Table 1 where the first 8 profiles are taken from our previous studies. The column content is as follows: 1 – the name of the galaxy, 2 – the morphological type code (LEDA), 3 – axial ratio (LEDA), 4 – photometry band of the profile, 5 – limiting surface magnitude of the profile, 6 – exponential number of the bulge (see (1) in Georgiev 2004b), 7 – optimal exponential number of the disk (see (1) in Georgiev 2004b), 8 – predicted central surface magnitude of the disk, 9 – logarithmic disk-to-bulge scale length ratio, 10 – difference between the computed total magnitudes of the bulge and the disk and 11 – references for the profiles and decomposition parameters.

Table 1. Basic data about the galaxies' profiles

Name	Type	a/b	Band	Lim	N_b	N_d	μ_{d0}	$\log(H_d/H_b)$	M_b-M_d	References
1	2	3	4	5	6	7	8	9	10	11
MW	4.0	–	–	–	0.48	2.09	–	1.94	6.07	1,18
LMC	9.0	2.2	B	25.8	0.64	1.03	21.92	0.95	2.35	2,18
SMC	9.0	1.1	B	25.3	1.09	1.25	21.64	1.09	3.90	2,18
M31	3.0	3.0	B	26.8	0.32	1.75	22.11	3.26	5.89	3,18
M33	5.8	1.7	B	25.8	0.50	1.41	21.83	1.58	4.51	4,18
M51a	4.2	1.4	B	25.6	0.74	2.87	21.18	1.44	2.79	5,19
M74	5.2	1.1	B	28.9	1.17	1.22	22.05	0.98	2.54	6,19
M83	5.1	1.1	B	23.8	0.50	1.90	20.12	1.90	4.84	1,18
N300	6.9	1.4	B	27.0	0.40	1.57	22.36	1.74	5.09	7,20
N1313	6.9	1.3	B	27.1	1.20	1.14	21.73	0.50	1.96	8,20
N1566	4.1	1.4	B	26.5	0.44	2.24	22.33	2.35	4.73	9,20
N6744	3.8	1.9	B	26.9	0.86	0.95	21.36	1.25	3.37	10,20
N7793	7.4	1.6	B	26.6	0.83	2.72	21.90	1.12	3.32	11,20
M51b	5.3	1.2	B	25.6	0.27	1.63	21.43	3.72	7.81	5,20
M101	5.9	1.0	B	24.1	0.34	1.35	21.84	2.83	6.92	5,20

N2403	6.0	2.0	B	25.0	0.67	1.28	20.89	1.18	4.07	12,20
M74	5.2	1.1	R	28.1	0.31	1.23	21.20	3.53	7.20	6,20
N5434	4.9	1.0	R	29.4	0.89	1.43	20.69	1.24	3.98	13,20
N5923	3.9	1.1	R	29.6	0.38	2.00	21.50	2.71	5.27	13,20
U9837	5.1	1.0	R	28.8	0.60	1.82	21.84	1.58	3.17	13,20
N4459	-1.5	1.3	B	26.2	1.91	1.00	21.43	0.26	0.13	1,20
N7457	-2.9	1.7	B	25.8	0.31	1.34	21.60	2.75	5.34	14,20
1Zw21	–	1.0	B	25.5	0.50	2.31	23.63	2.16	2.55	14,20
7Zw303	-2.0	1.0	B	25.2	0.75	2.20	22.59	1.43	1.35	14,20
N4216	2.8	4.5	B	25.3	1.58	6.46	22.46	0.64	-0.47	15,20
N4945	6.1	4.7	B	26.8	2.48	3.57	23.12	0.41	-0.45	16,20
U5389	6.0	10	R	26.0	1.54	4.31	22.19	0.58	-0.18	17,20
U9568	3.1	7.2	R	26.0	1.63	2.76	21.04	0.85	0.02	17,20

Sources: 1 - Freeman (1970), 2- de Vaucouleurs (1960), 3- de Vaucouleurs (1958), 4 – de Vaucouleurs (1959), 5 Okamura et al (1976), 6 - Natali et al (1992), 7 - de Vaucouleurs & Page (1962), 8 - de Vaucouleurs (1963a), 9 - de Vaucouleurs (1973), 10 - de Vaucouleurs (1963b), 11 - de Vaucouleurs (1980), 13 – Pohlen et al (2002), 14 – Kormendy (1977), 15 – Hamabe & Okamura (1982), 16 – de Vaucouleurs (1964), 17 – Karachentsev et al. (1992), 18- Georgiev (2004a), 19 – Georgiev (2004b), 20 – this work

The decompositions of all 20 profiles, published mainly in classical papers are illustrated in Fig.1 – 5. The disk shape is not convex only in the case of NGC 4459, NGC 6744, and in the case of NGC 7793 it is strongly truncated. In the most cases the 1st and 2nd order of the Sersic formula give almost identical results for the disk. Figure. 5 unifies edge-on galaxies that show evidences of ring-like disks. They are recognized after applying the second order Sersic formula for the disk shape (dashed line, see also the previous papers).
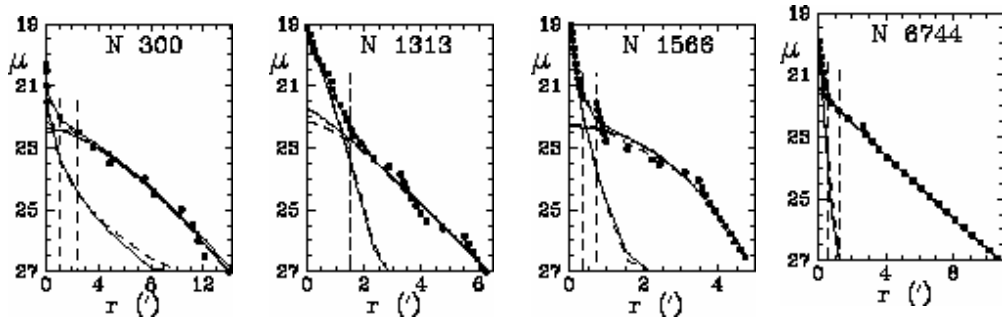
Fig.1: Profile decomposition of large galaxies in B-band, published by de Vaucouleurs. The solid curves represent the optimal model for the bulge, the disk and the restored profile based on the 1st order Sersic's formula for the disk modeling. The dashed curves represent the results when the disk is modeled by 2nd order Sersic's formula. The vertical dashed lines show the last point of the bulge region and the first point of the disk region of the profile, used as limiting points in the decomposition.
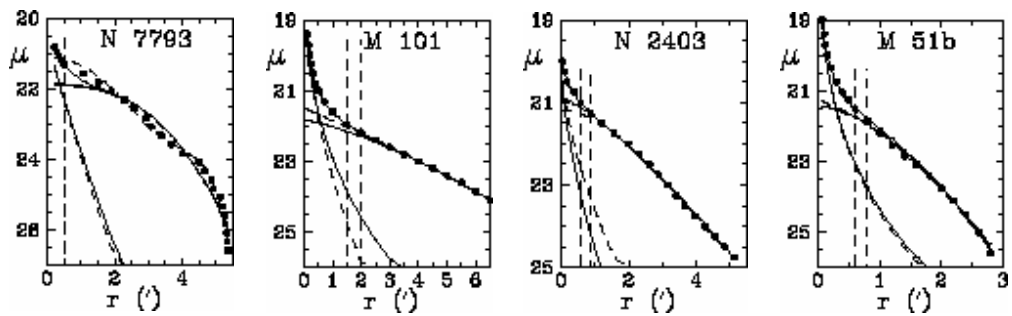
Fig. 2: Profile decomposition of other published large spiral galaxies in B-band. (see also Fig. 1).
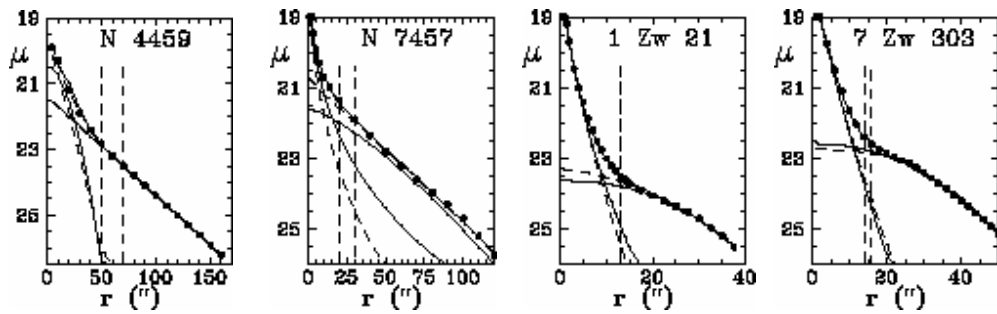
Fig. 3: Decomposition of published profiles of S0 galaxies in B-band (see Fig. 1).
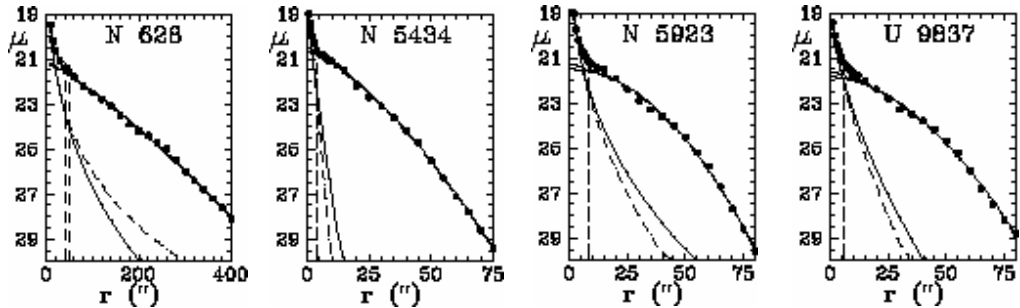
Fig. 4: Decomposition of deep profiles of Sb–Sc galaxies in R-band (see Fig.1).

We had used the deepest observations of face-on galaxy profiles, shown in Fig.3, to study the influence of the depth of the profile on the shape parameters, retrieved by our techniques. The results are given in Fig.6, where the deep face-on profiles of Natali et al (1992) and Pohlen et al. (2002) shows that the minimal deepness of the observations in order to study the true shape of the radial disk profile must be about 26 mag/arcsec^2 in R-band. Assuming the typical disk colour indexes the minimal deept must be about 24, 25, 25.5, 26.5 and 27.5 in K, J, I, V and B-band, respectively.

The correlation between the morphological type of the galaxy and the bulge/disk parameters is shown in Figure 7. Note, that the S0 galaxies from Fig. 4 and the edge-on galaxies from Fig. 5 are not used. The most left plot in
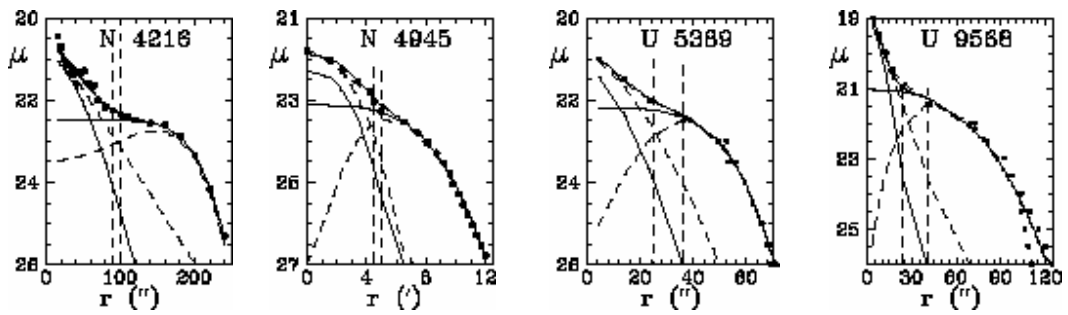
Fig.5: Decomposition of B-band profiles of edge-on galaxies with possible ring-like disks (see Fig. 1).
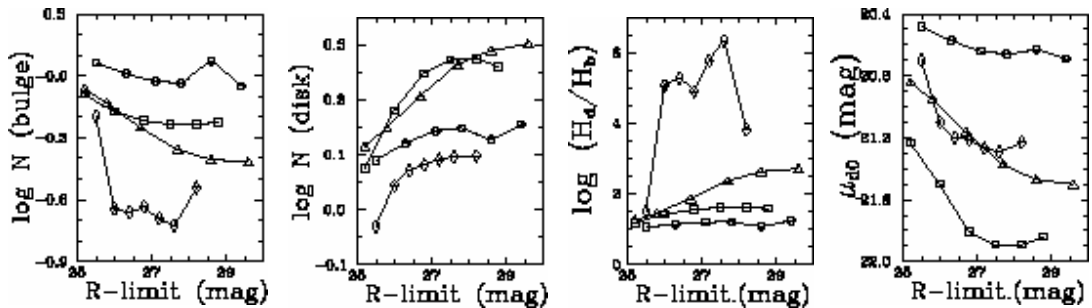
Fig.6. The correlation of the profile parameters according to artificially limited profile magnitude in the case of the galaxies M 74 (NGC 628, diamonds), NGC 5434 (circles), NGC 5923 (triangles) and UGC 9837 (squares).

Fig. 7 confirms the results of Andredakis et al. (1995), that the early type galaxies have bulge profiles close to the de Vaucouleurs (1948) "1/4 law" but the late type galaxies have more compact bulges. The middle plot of the left confirms our result – the disk profiles of the early type spiral galaxies are convex and that of the late type galaxies are flat, close to the Freeman's (1970)

law (Georgiev 2004a, Georgiev et al. 2004). The other plots in Fig. 7 demonstrate how the disk-to-bulge scale length ratio and the difference between the computed total magnitudes of the bulge and the disk correlate with the morphological type,.
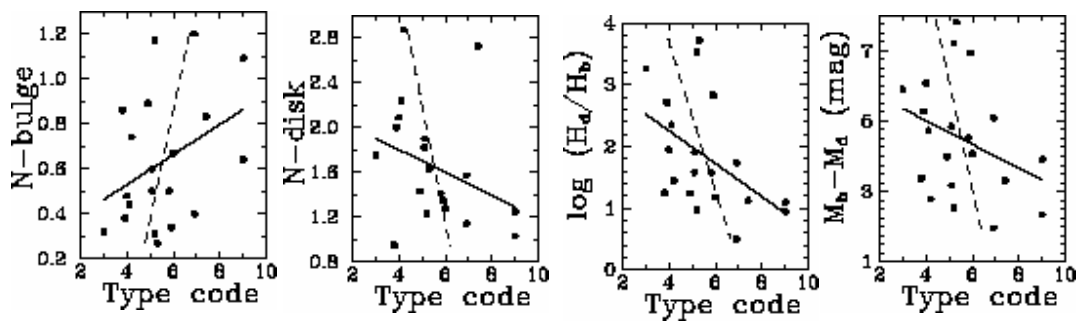
Fig.7. Correlation between the morphological type code and the bulge and disk exponential numbers, scale length ratio and difference between the magnitudes

Thus, in the case of 20 galaxies the disk profile shapes are modeled adequately through the Sersic's formula. This approach allows to recognize the disks of early type galaxies through their convex shapes, as well as to suspect for ring-like disks. It is a theoretical problem the shapes and the peculiarities of the disks to be explained.

References

A n d e r s o n K. S., S. M. B a g g e t t, W. E. B a g g e t t, 2004, AJ 127, 2085
A n d r e d a k i s Y. C., R. F. P e l e t i e r, M. B a l c e l s, 1995, MNRAS 275, 874
A n d r e d a k i s Y.C., R. M. S a n d e r s, 1994, MNRAS 267, 283
B o r o s o n T., 1981, ApJS 46, 177
C a p a c c i o l i M., E. V. H e l d, J.-L. N i e t o, 1987, AJ 94, 1519
d e J o n g R. S. 1996, A&AS 118, 557
d e V a u c o u l e u r s G., 1948, Ann. Astrophys. 11, 247
d e V a u c o u l e u r s G., 1958, ApJ 128, 465
d e V a u c o u l e u r s G., 1959, ApJ 130, 728
d e V a u c o u l e u r s G., 1960, ApJ 131, 574

d e V a u c o u l e u r s G., 1963a, ApJ 137, 720
d e V a u c o u l e u r s G., 1963b, ApJ 138, 934
d e V a u c o u l e u r s G., 1964, ApJ 139, 899
d e V a u c o u l e u r s G., 1973, ApJ 181, 31
d e V a u c o u l e u r s G., E. D a v o s t, 1980, ApJ 239,783
d e V a u c o u l e u r s G., J. P a g e, 1962, ApJ 136, 137
F r e e m a n K. C. 1970, ApJ 160, 811
H a m a b e M., S. O k a m u r a, 1982, Ann. Tokyo Astron. Obs. 15, 191
G e o r g i e v T. B., 2004a, Aerospace researches in Bulgaria, in print
G e o r g i e v T. B., 2004b, in this issue
G e o r g i e v T. B., O. I. S t a n c h e v, 2004, Publ. Astr. Obs. Belgrade, in print.
G e o r g I e v T. B., O. I. S t a n c h e v, P. L. N e d i a l k o v, 2004,
        Annuaire d'Universite de Sofia, in print.
K a r a c h e n t s e v I., T. G e o r g i e v, S. K a j s i n, A. K o p y l o v, V. S h e r g i n,
        V. R y a d c h e n k o, 1992,   Astron. Astrophys. Transact. 2, 265
K o r m e n d y J.., 1977, ApJ 217, 406
M o r I o n d o G., G. G i o v a n a r d i, L. K. H u n t, 1997, A&AS 130, 81
N a t a l i G., F. P e d i c h i n i, M. R i g h i n i, 1992, A&A 256,79
O k a m u r a K., T. K a n a z a v a, K. K o d a i r a, 1976, PASJ 28, 329
P o h l e n M., R.-J. D e t t m a r, R. L u e t t i c k e, G. A r o n i c a, 2002, A&A 392, 807
S h o m b e r t J. M., G. D. B o t h u m, 1987, AJ 92, 1, 60

STAR FORMATION TIMESCALES IN SPIRAL GALAXIES

Ivana Damjanov[*], *Milan M. Ćirković*

Astronomical Observatory, Volgina 7, 11000 Belgrade
Serbia and Montenegro

Abstract.
We investigate the impact of different models of global gaseous infall onto "normal" spiral disks on their gas consumption time scales. The old idea of Spitzer about the infall from gaseous galactic haloes was revived with the discovery of the low-redshift population of Lyα absorbers and first steps made in understanding of the transition between the high-redshift intergalactic and the low-redshift predominantly galactic population of QSO absorption systems, as well as improved understanding of the nature of so-called high-velocity clouds. It turns out that large quantities of gas which has not been astrated or has been astrated only weakly are bound to galaxies at later epochs. Such aggregates present a potential reservoir of gas not only for solution of the classical gas consumption puzzle in spiral disks, but also as a fuel for the future star formation. We present results of analyzes performed on the sample of 61 "normal" spiral galaxies used by Kennicutt (1998) for studying the form of global star formation law. Adopting the Schmidt star formation law with index n ≈ 1.3 (the average value of a sample of observational surveys), we compare the consumption time scales of the galaxies from the sample for two scenarios of their evolution: "naive" model with neither recycling of interstellar gas nor gas infall from galactic haloes, and a more realistic one with parameters that control the recycling and infall of gas.

1. Introduction

Star formation histories of spiral galaxies are determined by the interplay between incorporation of baryons into collapsed objects (stars, stellar remnants and smaller objects, like planets, comets or dust grains) and return of baryons into diffuse state (gaseous clouds and intercloud medium). The latter process can be two-fold: (i) mass return from stars to the interstellar medium (henceforth ISM) through stellar winds, planetary nebulae, novae and supernovae, which happens at the local level; and (ii) net global infall of baryons from outside of the disk (if any). The former process is a well-known and firmly established part of the standard stellar evolution

---

[*] Corresponding author: idamjanov@aob.bg.ac.yu.

lore (e.g. [1]), and although details of mass-loss in a particular stellar type may still be controversial, there is nothing controversial in the basic physics of this process. The latter process—global baryonic infall—is, however, far more controversial. Although the infall in the disk is visible through 21cm, optical recombination emission or absorption against high latitude stars, the compensating outflow is mainly hidden, being presumably very hot, rarefied, X-ray emitting gas expelled from the disk by Galactic supernovae (e.g. [2,3]), and, possibly, central nuclear source. It is easy to show [4] that the process (i) is insufficient to support continuous star formation in future for a time interval similar to the Hubble time.

Therefore, in investigation how long can the present stelliferous epoch [5] in the history of the universe last, we have to take into account both of these processes. The availability of fresh gas for fueling the star formation must also be considered as a limiting factor for the length of this epoch (sometimes in literature dubbed Roberts' time; see [6]). Two factors are crucial in this regard: (1) dependence of the rate of star formation on the gas density (encompassed by the empirical Schmidt law), and (2) empirically discovered star formation thresholds. While it is still unclear whether observed thresholds will continue to be valid at later epochs, when the overall star formation rate decreases, and ISM generally becomes colder (Fred C. Adams, private communication), we use the observed values as the working hypotheses. In addition, we apply the simplest ("toy") models to a previously studied sample of galaxies in order to get a better hold on the dependence of Roberts' time on the index of Schmidt law and thresholds.

2. Data

Sample used in our analysis contains 61 "normal" disk galaxies used by Kennicutt ([7], Table 1) with their mean gas and star formation rate (SFR) surface densities. When considering the sample properties, the main criterion was availability of CO and H_I maps. CO emission was used as a tracer for molecular hydrogen, the mean surface densities were averaged within the optical radius of the disk and average surface densities of the gas were obtained by summing H_I and H_2 surface densities. Integrated SFRs were derived from measurements of the H_α emission-line flux and then divided by deprojected area within the optical radius of the disk to derive mean SFR surface densities.

3. Different evolutionary models

a) Gas Consumption Timescale

Gas consumption timescale is defined as

$$\tau_g \equiv \left| \frac{M_{gas}}{\dot{M}_{gas}} \right| , \qquad (1)$$

where M_{gas} denotes available gas mass in the interstellar medium (ISM), and

$$\dot{M}_{gas} = \frac{dM_{gas}}{dt} \qquad (2)$$

presents the star formation rate (SFR in $M_\odot$ yr^{-1}) defined as the mass of stars formed out of gas in ISM per unit time. If we consider it constant for all cosmic times and equal to the observed value for each galaxy, the resulting timescales for subsample of 42 "normal" spiral galaxies, presented in a histogram in Figure 1, show almost no difference when comparing to a histogram of Larson et al. [4] sample in Figure 2.
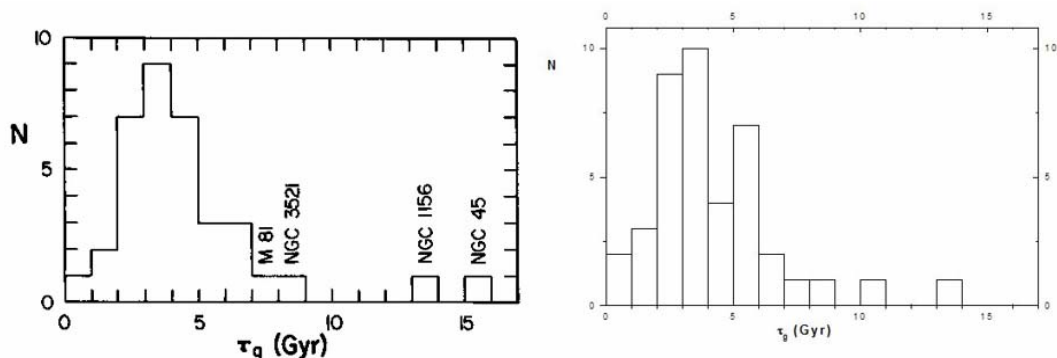
Fig. 1. – *left:* Histogram of gas consumption timescales for a sample of "normal" galaxies. Galaxies with long timescales are labeled (Larson et al. 1980); *right:* Histogram of gas consumption timescales for a sample of 42 spiral galaxies. The largest values are for late-type spirals. Used data from Kennicutt, Tamblyn and Congdon [8].

b) Star Forming Era I

We used the galaxy sample from [7] to compare the impacts that three different scenarios of their evolution:

(i)   "naïve" one, with closed-box galactic disk,
(ii)   one which takes recycling of gas into account, and
(iii)   more realistic one with parameters that control the recycling and infall of gas

have on the length of era of continuous star formation from interstellar gas in the disk of normal spiral galaxies. The term in the equation for the evolution of ISM that is present in all of these scenarios is Schmidt law [9]. In the case of "naïve" model, that is the only term:

$$\frac{d\Sigma_{gas}}{dt} = -A\Sigma_{gas}^{1.3} \ ,$$ (3)

where Σ_{gas} is mean gas surface density (units $M_{\odot}$ pc^{-2}), while A = 0.48 Gyr^{-1} denotes star formation efficiency (value taken from [7]). Integrating this equation over time interval τ_R that corresponds to the duration of star forming era, we obtain

$$\tau_R = \frac{\Sigma_{gas}^{-0.3}(\tau_R) - \Sigma_{gas}^{-0.3}(\tau_i)}{0.3A} ,$$ (4)

using $\Sigma_{gas}(\tau_i)$ for the present value of mean gas surface density and $\Sigma_{gas}(\tau_R)$ = 6 $M_{\odot}$ pc^{-2} for the threshold value, i.e. the minimum mean gas surface density required for continuing star formation process. This constant value was taken from [10]. Histogram of estimated duration of star forming era for Kennicutt sample of "normal" spiral galaxies [7] is shown in Figure 2a.
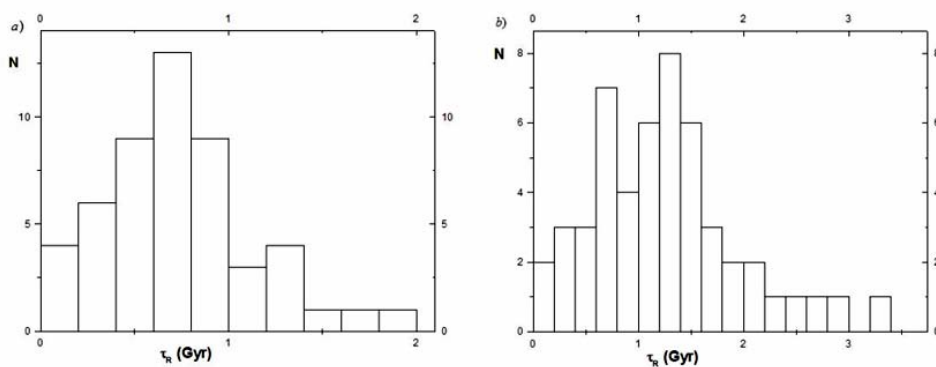
Fig. 2. –Histograms of star forming timescales in case that evolutionary model
    contains *a)* pure Schmidt law; *b)* Schmidt law with recycling.

156

The next step is to take into account recycling of gas, i.e. mass return from stars to ISM through stellar winds, planetary nebulae, novae and supernovae. The equation for the evolution of ISM now takes the following form:

$$\frac{d\Sigma_{\text{gas}}}{dt} = -(1-r)A\Sigma_{\text{gas}}^{1.3}. \tag{5}$$

Factor 1 - r denotes the lockup rate, i.e. the rate at which ISM transformed into stars is permanently locked up in low mass and dead stars. The return fraction of gas to the galactic ISM through mass-loss and supernovae, integrated over the classical Miller-Scalo [11] Initial Mass Function (IMF) is $r = 0.42$. In this way the duration of star forming era is prolonged for a factor of ~ 2, as presented in the Figure 2*b*.

The final step in this analysis would be adding to the right side of eq. (5) a term that corresponds to the net global infall of baryons from outside of the disk.

c) *Infall of baryons into the disk*

Arguments for taking into account the baryonic infall from galactic halo onto the disk can be divided into two major groups: theoretical reasons and observational constrains. In the former, ones of great importance are:
(i)   Galaxy formation theories imply prolonged baryonic cooling and infall (e.g. [12,13]);
(ii)   Infall is necessary to solve G-dwarf problem and other problems of chemical evolution of the Galaxy;
(iii) Morphological evolution along the spiral sequence in the sense Sd $\rightarrow$ Sa requires that at least a part of the dark matter must be gaseous;
(iv)   Cooling flow-type phenomena seem to be generic in the best theoretical models.
Among observational constrains we should emphasize the following:
(i)   High-velocity clouds as observed primordial infall (e.g. [14]); [unsolved problem: how big fraction of the observed infall is part of the Galactic fountain, i.e. already processed in the disk?]
(ii)   QSO absorption lines in the low-redshift regime are often located in haloes of normal luminous galaxies (e.g. [15]);
(iii) In observations of merging galaxies, it has been noted for some time that quantity of visible gas in such events is larger than coadded

estimates for each galaxy (as judged by luminosity and morphology) before merger occurred.

d) *Star Forming Era II*

The true equation of global ISM to be integrated is

$$\frac{d\Sigma_{gas}}{dt} = -(1-r)\Psi(t) + I(t),$$ (6)

where $\Psi(t)$ represents the SFR surface density at epoch t and, according to Schmidt law [9], can be rewritten as

$$\Psi(t) = A\Sigma_{gas}^{1.3},$$ (7)

while the term $I(t)$ is the infall function, i.e. denotes the net exchange rate of gaseous matter of the spiral disk with its environment:

$$I(t) = \Delta_{in}(t) - \Delta_{out}(t)$$ (8)

with $\Delta_{in}(t)$ and $\Delta_{out}(t)$ as infall and outfall rates of gas. Following the arguments given in Prantzos and Silk [16] we adopted Gaussian form of the infall function:

$$I(t) = \frac{\mu}{\sqrt{2\pi}\sigma} e^{-\frac{(t-t_0)^2}{2\sigma^2}} \quad \text{and} \quad \mu = I_0\sqrt{2\pi}\sigma e^{\frac{(T-t_0)^2}{2\sigma^2}},$$ (9)

where μ is the normalizing mass scale for the infall, I_0 present-day infall and T the age of the Milky Way, with the value of T =13.5 Gyr [17]. The characteristic epoch of infall peak t_0 and temporal width σ are assumed to be equal, according to [16]. In the course of modeling, we have been changing the values of Gaussian parameters I_0, t_0 and σ. Resulting timescale is impossible to give in a closed analytical form and numerical methods had to be used. Histogram presented in the Figure 3, obtained for the values of $t_0 = \sigma = 8$ Gyr, shows that the duration of star forming era is prolonged for a factor of ~ 2, 3, 4, or even 12, depending on the used value for present-day infall I_0. Finally, Figure 4 ilustrates the dependence of the mean value for duration of star forming era $<\tau_R>$ on the value of present-day infall.

4. Instead of conclusions

We have investigated a broad range of models of the evolution of the
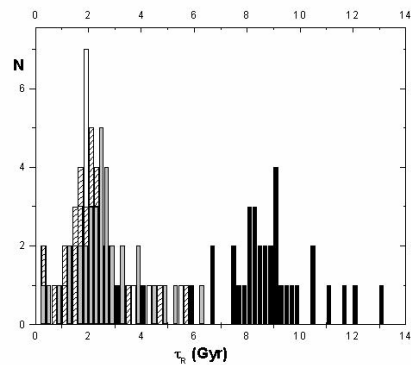
Fig. 3. – Star forming timescales for the Kennicutt sample of "normal" spiral galaxies [7] if the baryonic infall is taken into account. The form of infall function is Gaussian, with the values of characteristic epoch of infall peak t_0 and temporal width σ equal to 8 Gyr and the value of present-day infall I_0 equal to: *white bars* $-1/\sqrt{10^3}$ $M_\odot$ yr^{-1}, *slashed bars* - 1/10 $M_\odot$ yr^{-1}, *grey bars* $-1/\sqrt{10}$ $M_\odot$ yr^{-1} and *black bars* - 1 $M_\odot$ yr^{-1}.
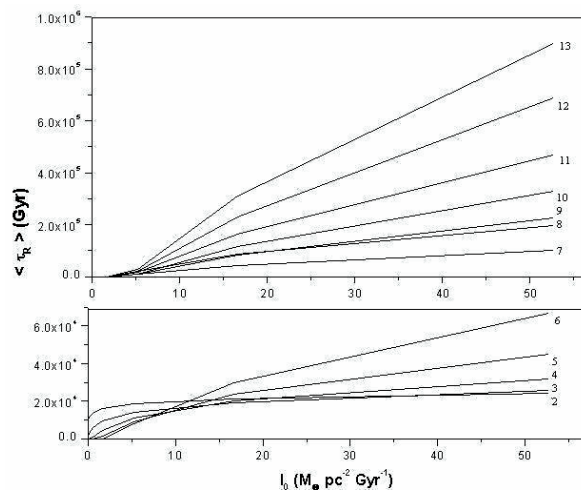
Fig. 4. – Predictions for duration of star forming era in the Gaussian infall model, as a function of present-day infall I_0, for different values of the infall peak (characteristic) epoch t_0. Numbers at the ends of the curves corespond to different values of t_0 (in Gyr).

global star formation rate in spiral disks with fixed threshold applied to Kennicutt's sample of disk galaxies. Recycling and application of Schmidt's law do not significantly change the duration of the stelliferous era for all models considered. This – contrary to previous claims – does not solve the "anthropic" part of the classical gas consumption puzzle: we seemingly live near the end of the stelliferous era. True solution has to be found in the baryonic infall into the disk. The magnitude of the present-day infall and, especially, the value of the star formation threshold do significantly impact the resulting values for τ_R. Fixed threshold with the Gaussian infall prolongs the duration of the stelliferous era for a factor of ~3, at least, in comparison to the "naive" values. In the course of the future work, we shall investigate the case of spatially varying threshold, as well as influence of the infall on other global galactic properties, like color and metallicity.

References

1. Chiosi, C. and Maeder, A. *Ann. Rev. Astron. Astrophys.* **24**, 1986, 329
2. Shapiro, P. R. and Field, G. B. *Astrophys. J.* **205**, 1976, 762
3. Benjamin, R. and Danly, L. *Astrophys. J.* **481**, 1997, 764
4. Larson, R. B., Tinsley, B. M. and Caldwell, C. N. *Astrophys. J.* **237**, 1980, 692
5. Adams, F.C. and Laughlin, G. *Rev. Mod. Phys.* **69**, 1997, 337
6. Roberts, M. S. *Ann. Rev. Astron. Astrophys.* **1**, 1963, 149
7. Kennicutt, R.C. *Astrophys. J.* **498**, 1998, 541
8. Kennicutt, R.C, Tamblyn, P. and Congdon, C.W. *Astrophys. J.* **435**, 1994, 1, 22
9. Schmidt, M. *Astrophys. J.* **129**, 1959, 2, 243
10. Elmegreen, B.G. *Astrophys. J.* **577**, 2002, 1, 206
11. Miller, G. E. and Scalo, J. M. *Astrophys. J. Supplement Series*, **41**, 1979, 513
12. Mo, H. J. and Miralda-Escude, J. *Astrophys. J.* **469**, 1996, 589
13. Chiappini, C, Matteucci, F. and Gratton, R. *Astrophys. J.* **477**, 1997, 765
14. Wakker, B. P. et al, *Bull. Amer. Astron. Soc.* **31**, 1999, 887
15. Chen. H, Lanzetta, K. M, Webb, J. K, Barcons, X. *Astrophys. J.* **498**, 1998, 77
16. Prantzos, N. and Silk, J. *Astrophys. J.* **507**, 1998, 1, 229
17. Boissier, S. et al. *Mon. Not. R. Astron. Soc.* **346**, 2003, 4, 1215

THREE DIMENSIONAL NUMERICAL MODEL OF ACCRETION FLOW IN CLOSE BINARY – PROBLEM DEFINITION

Maria Dimitrova

Space Research Institute, 6 Moskovska str., Sofia 1000, Bulgaria,
e-mail:maria@soace.bas.bg,, http://sri-head.hit.bg/members/cv/cvmaria.html

Abstract
We present the basic equations and approximations in descriptions of accretion flow in close binary system. Then we discuss the most useful geometry for numerical simulations. We introduce to numerical method and program language we choose. Finally we discuss the reason for building such a model.

Basic Equations
The accretion flow is a gas flow, which moves in the gravitational and magnetic fields of both stars and trough the there radiation.

The basic equation described this motion are:
1. The equation of mass conservation:

$$\frac{\partial \rho}{\partial t} + \nabla.(\rho V) = 0$$

2. The equations of motion (one for each space coordinate).

$$\rho \frac{\partial V}{\partial t} + \rho V.\nabla V = -\nabla p + F$$

3. The equation of energy conservation.

$$\frac{\partial}{\partial t}\left[\varepsilon + \frac{V^2}{2}\right] = -V\nabla\left[\varepsilon + \frac{V^2}{2}\right] + div\left[\lambda.gradT + V.\sigma + W\right]$$

4. The equation of state

$$p = p(\rho, T)$$

5. The equation of radiation transfer:

$$W = \int\limits_{0}^{\infty} d\nu \int\limits_{4\pi} \Omega I_{\nu} d\Omega$$

We use the approximation of irradiative thermo-conduction. It means that we accept that the flow is optically thick. In this case (Chetverushkin 1985):

$$W = \chi T^3 . gradT$$

To complete the system we need to know the forces and the descriptions of the viscosity and temperature exchange.

As in our previous investigations, we will use functions for viscosity of this kind:

$$\nu(\rho, T) = \nu_0 .. \rho^a . T^b \ , \ \chi(\rho, T) = \chi_0 .. \rho^c . T^d \ , \ \lambda(\rho, T) = \lambda_0 .. \rho^e . T^f$$

and the equation of state for perfect gas.

We build our model for binary systems with weak magnetic fields and do not involve the electromagnetic forces in equations.

The geometry

In the case of close binary, the gas flow from primary star moves toward the secondary and rotate around it. In the same time, the binary ac whole rotates with its own angular velocity around the mass center of the system.

This gives us a reason to choose a non-inertional cylindrical reference frame with the center – secondary star, which rotates with velocity, equal to those of the binary system.

In this frame, the equations of motion of a fluid with small change of viscosity from point to point becomes as follows (Landau, Lifshic 1986):

$$\frac{\partial \rho}{\partial t} = -\rho. \left(\frac{\partial V_r}{\partial r} + \frac{\partial V_\varphi}{r \partial \varphi} + \frac{\partial V_z}{\partial z} + \frac{V_r}{r} \right)$$

$$\frac{\partial V_r}{\partial t} = -V_r \frac{\partial V_r}{\partial r} - \frac{V_\varphi}{r} \frac{\partial V_r}{\partial \varphi} - V_z \frac{\partial V_r}{\partial z} + \frac{V_\varphi^2}{r} - \frac{1}{\rho} \frac{\partial P}{\partial r} + F_r +$$

$$\nu \left(\frac{\partial^2 V_r}{\partial r^2} + \frac{1}{r^2} \frac{\partial^2 V_r}{\partial \varphi^2} + \frac{\partial^2 V_r}{\partial z^2} \frac{1}{r} \frac{\partial V_r}{\partial r} - \frac{2}{r^2} \frac{\partial V_\varphi}{\partial \varphi} - \frac{V_r}{r^2} \right)$$

$$\frac{\partial V_\varphi}{\partial t} = -V_r \frac{\partial V_\varphi}{\partial r} - \frac{V_\varphi}{r} \frac{\partial V_\varphi}{\partial \varphi} - V_z \frac{\partial V_\varphi}{\partial z} + \frac{V_r V_\varphi}{r} - \frac{1}{\rho r} \frac{\partial P}{\partial \varphi} + F_\varphi +$$

$$\nu \left(\frac{\partial^2 V_\varphi}{\partial r^2} + \frac{1}{r^2} \frac{\partial^2 V_\varphi}{\partial \varphi^2} + \frac{\partial^2 V\varphi}{\partial z^2} + \frac{1}{r} \frac{\partial V_\varphi}{\partial r} - \frac{2}{r^2} \frac{\partial V_r}{\partial \varphi} - \frac{V_\varphi}{r^2} \right)$$

$$\frac{\partial V_z}{\partial t} = -V_r \frac{\partial V_z}{\partial r} - \frac{V_\varphi}{r} \frac{\partial V_z}{\partial \varphi} - V_z \frac{\partial V_z}{\partial z} - \frac{1}{\rho} \frac{\partial P}{\partial z} + F_z +$$

$$\nu \left(\frac{\partial^2 V_z}{\partial r^2} + \frac{1}{r^2} \frac{\partial^2 V_z}{\partial \varphi^2} + \frac{1}{r} \frac{\partial V_z}{\partial r} - \frac{\partial^2 V_z}{\partial z^2} \right)$$

F = F$_{g1}$ + F$_{g2}$ + F$_{cr}$

Here each space component of F contains gravitational and magnetic forces from both stars and centrifugal force. Gravitational forces are:

$$F_{g1} = \frac{GM_1}{(r^2 + R_{12}^2 - 2rR_{12} \cos \varphi + z^2)^{1/2}} \qquad F_{g2} = \frac{GM_2}{(r^2 + z^2)^{1/2}}$$

And its r, φ and z components are:

$$F_{g1}(r, \varphi) = F_{g1} \cos \beta \qquad\qquad F_{g1}(z) = F_{g1} \sin \beta$$

$$F_{g1}(\varphi) = F_{g1}(r, \varphi) \sin(\varphi + \gamma) \qquad\qquad F_{g1}(r) = F_{g1}(r, \varphi) \cos(\varphi + \gamma)$$

$$F_{cr} = \Omega^2 R_{cr} \qquad\qquad \Omega = (\frac{G(M_1 + M_2)}{R_{12}^3})^{1/2}$$

$$R_2 = \frac{M_2}{M_1 + M_2} R_{12} \qquad\qquad R_{cr} = (r^2 + R_2 - 2rR_2 \cos \varphi)^{1/2}$$

F_{cr} has only radial and tangential components, which we can write using similar picture

$$F_{cr}(r) = F_{cr}(r, \varphi) \cos(\varphi + \beta) \qquad\qquad F_{cr}(\varphi) = F_{cr}(r, \varphi) \sin(\varphi + \beta)$$

Using equation for perfect gas

$$p = \frac{R}{\mu} \rho T \qquad\qquad \varepsilon = \int_0^T c_v dT \Rightarrow d\varepsilon = c_v dT$$

$$\frac{\partial T}{\partial t} = -V\nabla T - \frac{1}{c_v} \left\{ \frac{d}{dt}\left[\frac{V^2}{2}\right] + div\left[\left(\lambda + \chi T^3\right)gradT + V.\sigma\right] \right\} = -V\nabla T - \frac{V}{c_v}\frac{dV}{dt} +$$

$$\frac{1}{c_v}\left\{ div\left[\left(\lambda + \chi T^3\right)gradT + V.\sigma\right] \right\} = -V\nabla T - \frac{V}{c_v}\frac{dV}{dt} + \frac{1}{c_v}\left\{ \chi T^3 div.gradT + 3\chi T^2.grad^2T + div(V.\sigma) \right\}$$

Finally in most cases we can accept that we can neglect all second derivatives, so we find:

$$\frac{\partial T}{\partial t}=-V_r\frac{\partial T}{\partial r}+\frac{V_\varphi}{r}\frac{\partial T}{\partial \varphi}+V_z\frac{\partial T}{\partial z}+\frac{1}{c_v}\left\{.V_r\left[\frac{1}{\rho}\frac{\partial P}{\partial r}+\frac{1}{\rho}F_r+\nu\left(-\frac{1}{r}\frac{\partial V_r}{\partial r}-\frac{2}{r^2}\frac{\partial V_\varphi}{\partial \varphi}-\frac{V_r}{r^2}\right)\right]\right.$$

$$+\frac{.V\varphi}{r}\left[\frac{1}{\rho r}\frac{\partial P}{\partial \varphi}+\frac{1}{\rho}F_\varphi+\nu\left(+\frac{1}{r}\frac{\partial V_\varphi}{\partial r}-\frac{2}{r^2}\frac{\partial V_r}{\partial \varphi}-\frac{V_\varphi}{r^2}\right)\right]+V_z\left[\frac{1}{\rho}\frac{\partial P}{\partial z}+\frac{1}{\rho}F_z+\nu\frac{1}{r}\frac{\partial V_z}{\partial r}\right]+$$

$$+3\chi.T^2\left[\left(\frac{\partial T}{\partial r}\right)^2+\left(\frac{1}{r}\frac{\partial T}{\partial \varphi}\right)^2+\left(\frac{\partial T}{\partial z}\right)^2\right]-\frac{\partial V_r}{\partial r}p-V_r\frac{\partial p}{\partial r}-\frac{\partial V_\varphi}{r\partial \varphi}p-\frac{V_\varphi}{r}\frac{\partial p}{\partial \varphi}-\frac{\partial V_z}{\partial z}p-V_z\frac{\partial p}{\partial z}$$

$$+\frac{\partial \nu}{\partial r}\left[2.V_r\frac{\partial V_r}{\partial r}+\frac{V_\varphi}{r}\frac{\partial V_r}{\partial \varphi}+V_\varphi\frac{\partial V_\varphi}{\partial r}-\frac{V_\varphi^2}{r}+V_z\frac{\partial V_r}{\partial z}+V_z\frac{\partial V_z}{\partial r}\right]+$$

$$+\frac{\partial \nu}{r\partial \varphi}\left[V_r\frac{1}{r}\frac{\partial V_r}{\partial \varphi}+V_r\frac{\partial V_\varphi}{\partial r}-\frac{V_rV_\varphi}{r}+2.V_\varphi\frac{1}{r}\frac{\partial V_\varphi}{\partial \varphi}+2\frac{V_rV_\varphi}{r}+V_z\frac{\partial V_\varphi}{\partial z}+\frac{V_z}{r}\frac{\partial V_z}{\partial \varphi}\right]+$$

$$+\frac{\partial \nu}{\partial z}\left[Vr\frac{\partial V_r}{\partial z}+V_r\frac{\partial V_z}{\partial r}+V_\varphi\frac{\partial V_\varphi}{\partial z}+V_\varphi\frac{1}{r}\frac{\partial V_z}{\partial \varphi}+2.V_z\frac{\partial V_z}{\partial z}\right]+$$

$$+\nu\left[\begin{array}{c}2\left(\frac{\partial V_r}{\partial r}\right)^2+\frac{2}{r}\frac{\partial V_\varphi}{\partial r}\frac{\partial V_r}{\partial \varphi}+\left(\frac{\partial V_\varphi}{\partial r}\right)^2+\left(\frac{\partial V_z}{\partial r}\right)^2+3\frac{\partial V_r}{\partial z}\frac{\partial V_z}{\partial r}-2\frac{V_\varphi}{r}\frac{\partial V_\varphi}{\partial r}+\frac{1}{r^2}\left(\frac{\partial V_r}{\partial \varphi}\right)^2-\frac{V_\varphi}{r^2}\frac{\partial V_\varphi}{\partial \varphi}+ \\ +\frac{2}{r^2}\left(\frac{\partial V_\varphi}{\partial \varphi}\right)^2+\frac{2}{r}V_\varphi\frac{\partial V_r}{\partial \varphi}+\frac{2}{r}V_r\frac{\partial V_\varphi}{\partial r}+\frac{2}{r}\frac{\partial V_\varphi}{\partial z}\frac{\partial V_z}{\partial \varphi}+\frac{1}{r}\left(\frac{\partial V_z}{\partial \varphi}\right)^2+2\left(\frac{\partial V_r}{\partial z}\right)^2+\left(\frac{\partial V_\varphi}{\partial z}\right)^2+2\left(\frac{\partial V_z}{\partial z}\right)^2\end{array}\right]\left.\right\}$$

We can neglect the second derivatives in the equation of motion too and the squares of derivatives. But this will be in the future.

Numerical method

To be able to compare the results with our 2D simulations (Dimittrova et.al 1990, 1997, 2002), we will use the same numerical method – large particle method (Belotsercovskiy 1985).

In our first works (Dimittrova, Filipov 1990) we prove that this method is very quick.

We build the model using C++ programming language.

Building this model, we search for each point the ρ, T and tree components for V(r, φ, z) as a function of time and some parameters.

Parameters are: M_1, M_2, R_{12}, T_{inf}, ρ_0, ν_0, λ_0, χ_0, a, b, c d, e and f. Here T_{inf} and ρ_0 are the temperature and density at the first Lagrangian point.

Altering these parameters, we will investigate haw they effect on the dynamics of the flow and will try to understand which of them are responsible for some physical processes.

The purpose
We begin building of 3D numerical model because of following easons:
1. ***To find more detailed picture of accretion flow.***
2. ***With a hope that we can find the origin of some structures formation.***
3. ***To confirm the role of physical parameters over the formation and dynamics of flow structures.***
4. ***Searching some origin of the instabilities.***
5. ***To understand whether or not 2D model is useful and where it is.***
6. ***To prove that angular momentum transfer is really as result of spiral structure formation.***

References:
1. Belotsercovskiy O.M., "Computational methods in Mechanics of Continuous Mediums", 1985, Moskow, Science
2. Chetverushkin B.M., "Mathemathical modeling of dynamics of irradiating das", 1985, Moskow, Science
3. Dimitrova M.M., Filipov, L.G., "Structure of accretion flow in close binary system - a two-dimensional model", 1990, ESA SP-311, 255
4. Dimitrowa M.M., "Structure of accretion flow in close binary as a function of radial inflow velocity - 2D numerical simulation", 1997, Aerospace Research in Bulgaria, 13, 27
5. Dimitrova M.M., Filipov L.G., Andreeva D.V.,"Pattern formation and angular momentun transport in accretion flows", 2002, 3-th Serbian-Bulgarian Astronomical Meeting, 13-15 May, Giuletchica, Bulgaria
6. Landau L.D., Lifshic E.M., "Hydrodynamics", 1986, Moskow, Scienc

INFLUENCE OF THE MAGNETIC FIELD OF THE COMPACT OBJECT ON THE ACCRETION DISK – RESULTS

Krasimira Iankova, Lachezar Filipov

Space Research Institute - Bulgarian Academy of Sciences

Abstract:
In this paper we will show our results. We consider the development of accretion flow and its interaction with the field of the star. We discuss the appear and the behavior of the instabilities.

Introduction

In the first part is construct non-stationary, non-axisymmetric, one-temperature MHD model of Keplerian accretion disk with advection in the normal dipole magnetic field of the central object. We used cylindrical co-ordinates (r, φ, z; t). Present is the mass continuity, magnetic flux conservation, equation of motion, angular momentum conservation, hydrostatic balance, the three components of magnetic induction, heat balance and using approximations. System is prepared for computer treating. Here we will see and comment obtaining analytic solution. The results show open view only along r, because we assume periodical dependencies for variables φ and t with coefficients depended from r .

Results and interpretation

System is non-linear and we solved with iterations. Second step is appropriate approximation for the system:

$$(1) \quad f_1(x) = \frac{4 + c_2}{6x^6} + \frac{1 + c_1 + c_3}{x^{15/2}}\left[1 - (x - x_g)\right] + \frac{2 - c_2}{6}$$

$$(2) \quad f_2(x) = (c_2 + 4)(x - 1) + 1$$

$$f_3(x) = \frac{c_6}{7}x^7 + \frac{x^3}{3}\left(c_7 - \frac{(3+c_2)}{2}c_5\right) - \frac{(3+c_2)}{6x^3} -$$

(3) $$-\frac{1}{2}c_5(1+c_1+c_3)x^{3/2}(x-x_g-1) +$$

$$+\frac{1+c_1+c_3}{2x^{9/2}}(x-x_g-1) + 1 - \frac{c_6}{7} - \frac{c_7}{3} + \frac{(3+c_2)(1+c_5)}{6}$$

(4) $$f_4(x) = (1 - c_{13} - c_{14})x^2 + \frac{c_{13}}{x^6} + c_{14}(x - x_g)$$

(5) $$f_5(x) = \frac{1+c_4}{x} - c_4$$

(6)

$$f_6(x) = -\frac{c_{10}x^2}{2c_9} - (x-1) - \frac{c_8}{2c_9x^{7/2}} - \left(\frac{3c_8}{2c_9} - \frac{1}{c_9}\right)\frac{1}{x^{9/2}} + \frac{1+c_1}{2c_9x^5} + \frac{2\alpha c_{11}}{c_9x^{11/2}} +$$

$$+\frac{9\alpha c_{11}}{4c_9x^{13/2}} + \frac{\alpha c_{12}}{c_9x^{17/2}} + \left[\left(\frac{3c_8}{2c_9} - \frac{1}{c_9}\right)\frac{1}{x^{9/2}} - \frac{9\alpha c_{11}}{4c_9x^{13/2}} - \frac{\alpha c_{12}}{c_9x^{17/2}}\right](x-x_g) +$$

$$+\left[\frac{c_8}{2c_9x^{7/2}} - \frac{2\alpha c_{11}}{3c_9x^{9/2}} - \frac{1+c_1}{2c_9x^5} - \frac{2\alpha c_{11}}{c_9x^{11/2}}\right]\frac{1}{(x-x_g)} + \frac{2\alpha c_{11}}{3c_9x^{9/2}}\frac{1}{(x-x_g)^2} + \frac{2c_9 - c_{10}}{2c_9}$$

$$f_7(x) = -\frac{c_2+4}{c_1x} + \frac{c_{16}+c_{12}}{c_1x^5} + \left[-\left(\frac{c_3}{2c_4} + c_3\right)\frac{1}{c_1x^{3/2}} + \frac{c_{17}}{c_1x^{9/2}}\right]\frac{1}{x-x_g} -$$

(7)

$$-\frac{c_3}{c_4c_1x^{1/2}}\frac{1}{(x-x_g)^2} + 1 - \frac{c_{17}}{c_1} + \frac{c_3}{c_1} + \frac{c_2+4}{c_1} - \frac{c_{16}+c_{12}}{c_1} + \frac{3c_3}{2c_4c_1}$$

$$f_8(x) = \frac{c_{15}x^2}{2c_4c_{11}} + \frac{c_4+1}{c_4c_{11}}x - \frac{1}{c_4x} - \frac{c_{16}+c_{12}}{3c_4c_{11}x^3} - \frac{1+c_1+c_3}{c_4c_{11}x^{1/2}}(x-x_g-1) +$$

(8)

$$+1 - \frac{c_{15}}{2c_4c_{11}} - \frac{c_4+1}{c_4c_{11}} + \frac{1}{c_4} + \frac{c_{16}+c_{12}}{3c_4c_{11}}$$

Where $f_1(x)$, $f_2(x)$, $f_3(x)$, $f_4(x)$, $f_5(x)$, $f_6(x)$, $f_7(x)$, $f_8(x)$ is corresponding of parameters ρ, v_r, v_s, H, B_r, B_φ, ω, k_φ, and c_i is constants.

Then if we compare $f_5(x)$ with $f_6(x)$ (fig.1) :
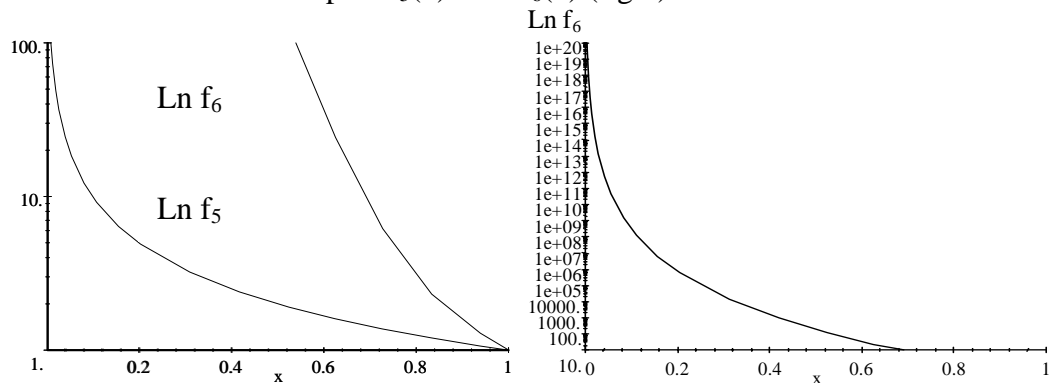
Fig.1

We can see that $f_6(x)$ increase very faster from $f_5(x)$. That is precondition $B_\varphi > B_r$ for all disk and magnetosphere. And because B_r intensification MHD turbulence and $B\varphi$ repress it [6], we have (Qmag / Q^+) <1 for all disk. This indicate that disk attain to central object and does not destroy in magnetosphere.

We can see also, that $f_2(x)$ decrease (fig.2):
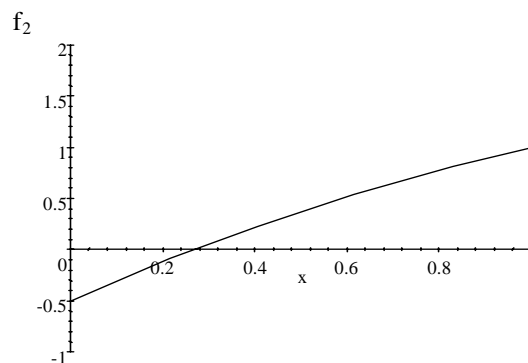
Fig.2

That is connect with delayed of the flow from magnetic field, which is a reason the plasma going off through equatorial window and may accreting.

Conclusions

In this paper we obtain dimensionless parameters of magnetic disk and coefficients of periodical dependencies from φ and t , k_φ and ω,

corresponding from dimensionless variable for distance x. We showed, that magnetic dissipation is not surpass viscosity dissipation. This permit on the flow to stay thin , to run to most inner region and to accreting over object without the disk to destroy.

We see that v_r and v_s go down inward to the centre as a result from powerful field. Dipole field transfer basic part of angular moment inward to star, what accelerate the rotation and intensify the field. v_s decrease faster from v_r, that denote supersonic accretion and sonic waves along r, too.

v_a for difference from v_r and v_s grow up very fast. We know that:
1. for $v_s >> v_a$: v_s fast and v_a slow alfenic magneto-sonic waves is appear in fluid;
2. $v_s << v_a$: v_s slow sonic and v_a fast magneto-sonic waves [7],

for us in outer edge $v_{s0} >> v_{a0}$. Jump in v_a from rotation $\pm\ v_a$ generate fast sonic, slow alfenic and slow magnetic shock waves – magnetic turbulence.

ω, k_φ grow up very fast, too. That means in inner region MRI is most effective and exalting with time, or with other words the disk proceed to new steady state with forming of structure. This transition is irreversible.

References:
1. Iankova Kr., Filipov L.,"Accretion flow and magnetic field", f-1, p.524, WDS 2003 - Proceedings of Contributed Papers, Prague, 2003.
2. Iankova Kr. D., Filipov L. G.,"Influence of the magnetic field of the compact object on the accretion disk", July 4th - 11th, 2003, Belogradchik, BULGARIA, in press.
3. Iankova Kr. D., Filipov L. G.,"Proiavi na vzaimodeistvieto na techenieto s magnitnoto pole v i izvun diska – osobennosti na modela", in press, (Bulgarian).
4. Nakao Yas., Publ.Astron.Soc.Japan 49,652-672, 1997
5. Kauling T., Magnitnaia gidrodinamika, 1978, Atomizdat, Moskva(rus).

TOWARDS IMPROVING THE QUALITY OF STELLAR PHOTOMETRY - SPATIALLY DEPENDENT ERRORS IN STELLAR MAGNITUDES

Haralambi Markov

Institute of Astronomy and National Astronomical Observatory
Bulgarian Academy of Sciences, *e-mail: hmarkov@astro.bas.bg*

Abstract

Systematic errors in stellar photometry as a function of spatial distribution of stellar images over the CCD chip have been investigated. New terms in the calibration equations aimed to reduce these errors are suggested. It is shown that this procedure improves the scatter in magnitudes and refines the photometry zero-point.

Introduction

An important procedure in stellar photometry is the transformation of instrumental magnitudes to a standard photometry system. The equations commonly applied have the following general form:

$$m = M + m_0 + f(X,CI)$$

Here **m** marks instrumental stellar magnitudes, **M** are the corresponding standard magnitudes and **m_0** the photometry zero-point, **X** is airmass at which target is observed, **CI** is the standard star color index. Coefficients in this equations are established for standard star magnitudes applying the least squares method. As a rule standard stars instrumental magnitudes are derived by means of the aperture photometry.

Accounting that the competitive method for assessment stellar brightness based on the PSF model of stellar image is spatially dependent ([1] Stetson, DAOPHOTII) we developed a method reducing aperture magnitudes for possible positional dependence. Sec.2 describes the observations; Sec.3 presents the method and basic results and Sec. 4 is devoted to the solution of the problem and conclusions.

2   The observational strategy

To detect probable spatially dependent systematic errors one have to ensure uniformly spread over the CCD chip stellar images which brightness is well known. This could be reached in two ways: a) multiple images of one and the same standard star to be taken moving the telescope between exposures in order stellar image to be suited at different regions of the focal field or b) rich uniformly populated standard fields to be used. The former approach is very time consuming as well observing as reducing the images because we prefer the second one. Suitable Stetson's standard fields ([2] Stetson) were observed multiple slightly moving the telescope between consecutive exposures in one and the same pass-band. Observations were taken in the RC focus of the Bulgarian National Astronomical Observatory 2-m telescope. Image reduction and data analyze were performed with IRAF. When this was possible some frames were summed before photometry process.

3   The methodology and main results

For every single frame standard stars were detected and their aperture magnitudes derived. In order to account the changes in photometry conditions during separate runs and even during the night (atmospheric transparence and extinction), instrumental magnitudes for every frame have been reduced to the standard system with some average for that sample value. This manner instrumental magnitudes from different frames have been set to a common photometry zero. However all they still are instantly disturbed from color and spatial dependencies if any. To establish the value of probable spatial dependence the differences "instrumental (commonly reduced) minus standard magnitudes" (hereafter residuals) as a function of stellar image position on the chip have been investigated. Fig.1 demonstrates these relations along columns (X direction, down panel) and rows (Y direction, upper panel) of the CCD chip in the case of V pass-band. Significant spatial dependence of stellar magnitudes could be easy detected. Fig. 2 shows the same relation for sparse field in the same pass-band but only for one direction. It demonstrates the importance of the quantity of standard stellar images in a single field. Sparse fields should be taken multiple in one and the same pass-band moving the telescope between

172

exposures in order standard star images to be detected at different regions of the chip.
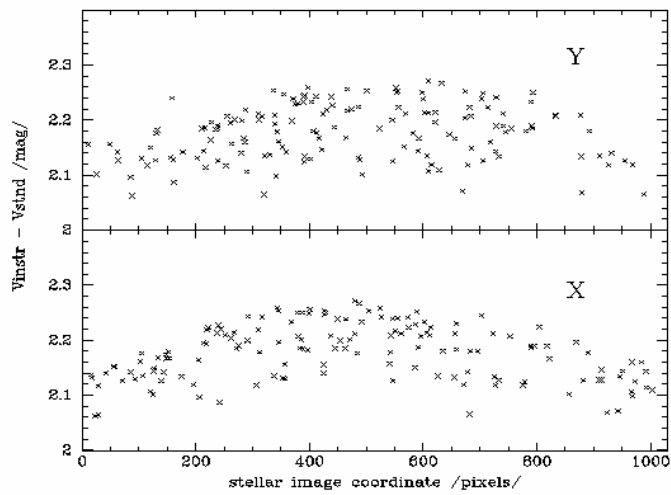
Fig.1. Spatial dependence of residuals (instrumental minus standard magnitudes) along columns (upper panel) and rows (down panel) for the case of rich standard field in V pass-band. Coordinates in both directions (abscissa) are in pixels and are related to the CCD frame. Residuals (ordinate) demonstrate significant spatial dependence
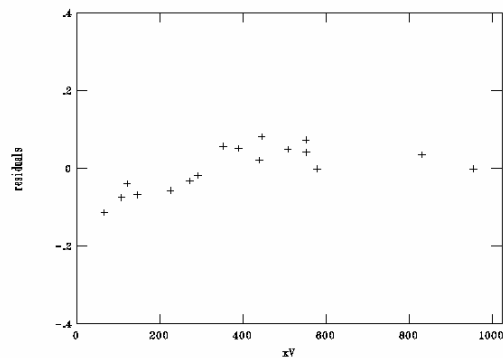
Fig.2. Spatial dependence of residuals for the case of sparse standard field in V pass-band. The meaning of the two axes is like in fig.1. Here is demonstrated spatial dependence only along the columns

4 Solution of the problem and conclusions

To reduce stellar magnitudes for these systematic errors we suggest terms dependent on stellar image position on the chip to be involved in the equations transforming instrumental magnitudes into standard system. The new terms suggested are:

$$c_1*(x/512.5-1)^2 + c_2*(y/512.5-1)^2$$

Here c_1 and c_2 are column and line oriented positional coefficients respectively but x and y are stellar image center coordinates. In this presentation the stellar image coordinates related to the CCD frame are normalized in the range [-1, 1]. At this stage we solve equations only for spatial dependence neglecting color terms. The coefficients m_0, c_1 and c_2 were derived by means of least squares method and their values for different observing runs are listed in Table 1.

V pass-band			
RUN	m_0	c_1	c_2
1	0.095±0.004	-0.158±0.014	-0.138±0.015
2	0.072±0.002	-0.145±0.004	-0.135±0.005
3	0.042±0.007	-0.128±0.014	-0.044±0.014
4	0.036±0.004	-0.104±0.010	-0.077±0.009

B pass-band			
RUN	m_0	c_1	c_2
1	0.056±0.005	-0.154±0.022	-0.135±0.014
2	0.063±0.003	-0.129±0.006	-0.114±0.007
3	0.054±0.006	-0.109±0.014	-0.116±0.015
4	0.049±0.005	-0.102±0.014	-0.107±0.013

Table 1: The values of transformation equation coefficients and their instrumental uncertainities for different observing runs. Column 1 presents observing run, column 2 the photometric zero-point, but columns 3 and 4 the 'spatial dependent' coeffitients.
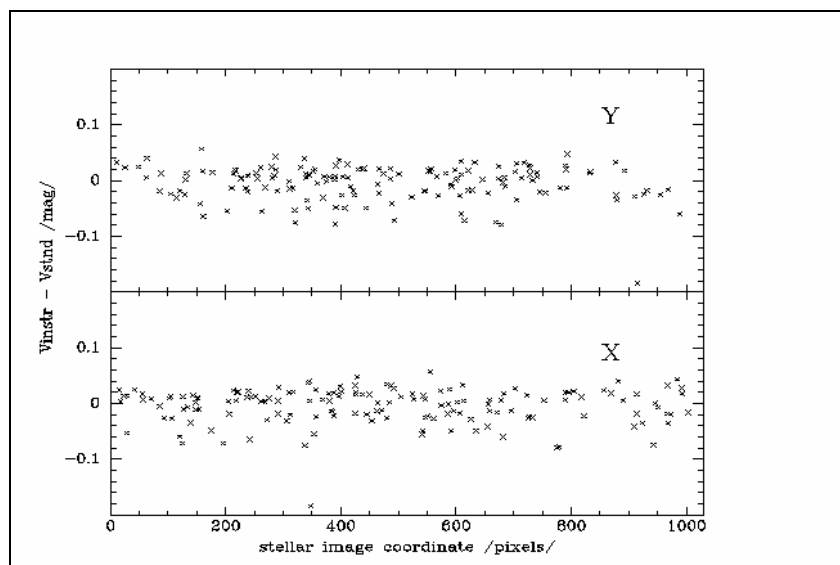
Fig.3. Spatial dependence of residuals after instrumental magnitudes were corrected. The meaning of the axes is like in the above figures. Apart from the straight form of the dependence the scatter is significantly lowered that hints on better photometric quality

m_0 variation from run to run (Tab. 1 column 2) is an important result in our investigation. It points that neglecting the spatial dependence of stellar magnitude leads to uncertainty in photometry zero-point up to 0.1 mag.

Fig. 3 demonstrates results after correcting instrumental magnitudes for spatial dependence. Comparing Fig. 3 and Fig. 2 it gets evident that the method we offer improves the quality in stellar photometry. It should be applied taking care for good signal/noise level of stellar images and their uniform spread over the CCD chip.

References

[1] P.B.Stetson, (1992), "User's manual for DAOPHOTII"
[2] P.B.Stetson, PASP 112 (2000) 925, "Homogeneous photometry for star clusters and resolved galaxies. II. Photometric standard stars"

DYNAMIC CHARACTERISTICS OF THREE ERUPTIVE PROMINENCES

P. Duchlev, K. Koleva, M. Dechev, J. Kokotanekova, N. Petrov

Institute of Astronomy of Bulgarian Academy of Sciences

Abstract:

The kinematics and dynamics of eruptions of three prominences was studied. The properties of their dependence of the height on time, as well as of horizontal expansion on time during the eruption was analyzed and compared.

1. Introduction

The eruption process of the prominences develops in two main phases. In the first pre-eruptive phase, the prominence slowly rises with approximately constant velocity of several km/s (Rompolt, 1990). At some critical height the prominence erupts and a large part of its material is lifted into the corona and into the planetary space. The velocity of the ejected prominence ranges from several km/s at the beginning phase of the eruption to several hundreds km/s at the late phase of the eruption (Rompolt, 1990).

Besides the eruption in the vertical direction, some eruptive prominences (EPs) exhibit expansion in the horizontal direction. Most of them show constant velocity (Rompolt, 1984; Rudawy et al., 1994). The velocities of the horizontal expansion are in the range from 15 to 80 km/s (Rompolt, 1998).

According to Vršnak's classification (Vršnak, 1998), there are three classes of EPs in dependence of the fine structure of the eruptive phase. Class **A** when the prominence material often remains constant after the initial acceleration. Class **B** when after the acceleration and the constant velocity follow deceleration of the EP material. Class **C** when the initial acceleration of the EP continues up to the prominence disappearing in H_{α}.

There are two basic types of EPs according to Rompolt's classification (Rompolt, 1990). Both types EPs are embedded in the lower part of huge magnetic system (HMS). The EPs of type I have shape of a large arch at the bottom of the HMS that rising up into the corona during the eruption. The EPs

of type II are located in one leg of the HMS loop. The inclination of the prominence body to the solar limb grows up to vertical position during the eruption.

2. Observational Data

The H_α filtergrams of three EPs observed with Small Coronagraph of Wroclaw Astronomical Institute were used. The EP of May 5, 1980 is classical example of type I EP (Figure 1a). The EP of May 8, 1979 EP is a classical example of an EP of type II (Figure 1b). The third EP of August 14, 1979 (Figure 1c) by morphology and eruption evolution is more similar to the EPs of type II. All H_α filtergrams were processed with the automatic Joyce-Loebl MDM6 microdensitometer at the National Astronomical Observatory – Rozhen, Bulgaria.
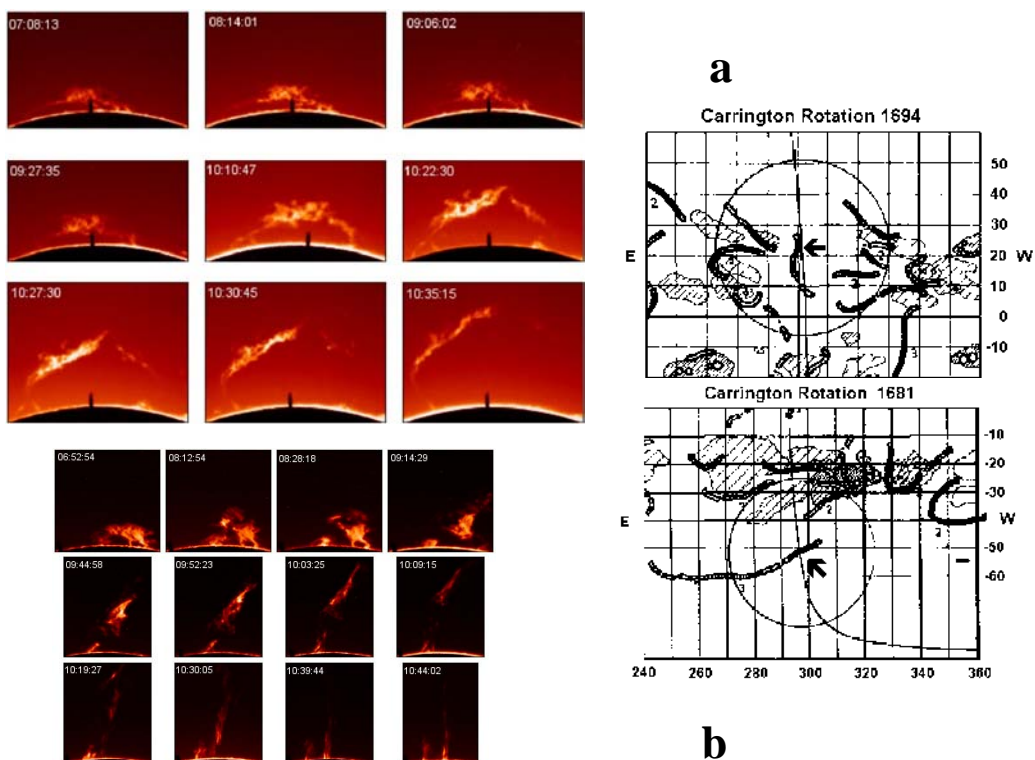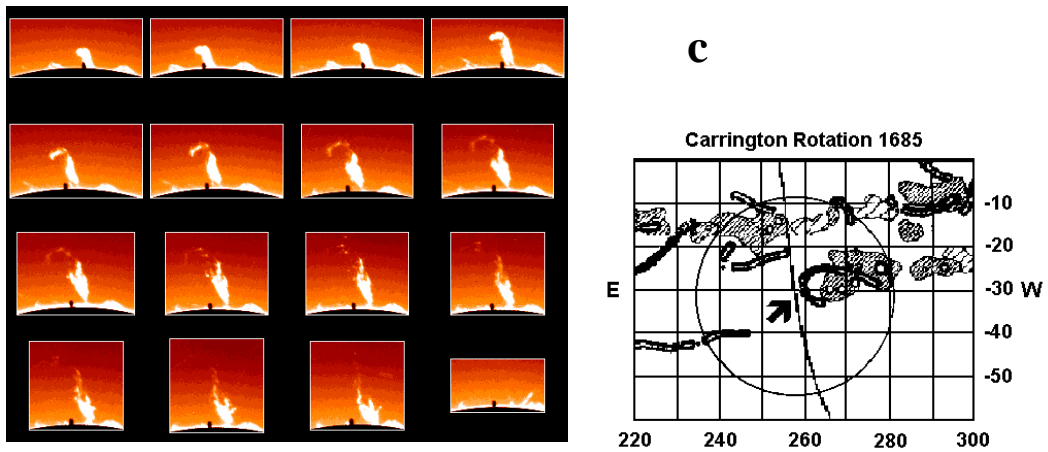
Fig. 1. A sequence of H$_\alpha$ filtergrams of the three EPs and the associated with them filaments in the synoptic maps - (a) I type EP of May 5, 1980; (б) II type EP of May 8, 1979; EP of August 14, 1979.
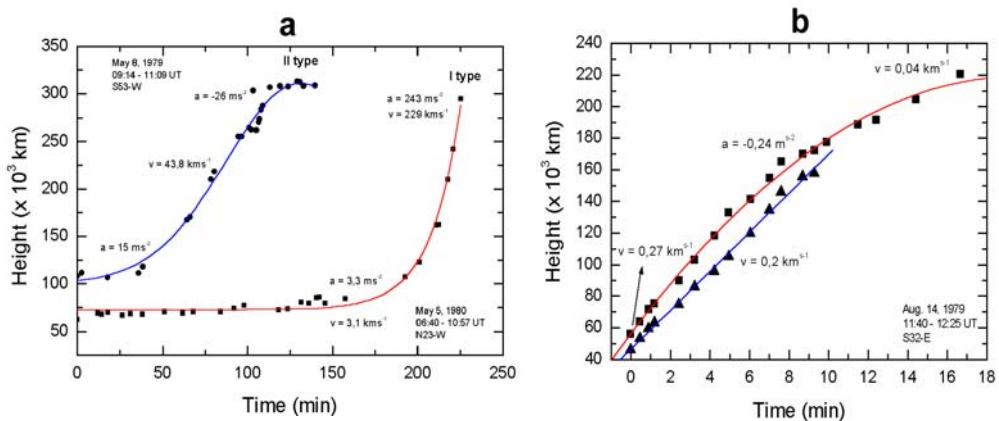
Fig 2. Height-time diagrams of the EP of I type (May5, 1980) and the EP of II type (May 8, 1979), as well as of the EP of August 14, 1979.

3. Height-Time Diagrams

Figure 2a represents height-time diagrams of the EPs of I and II type. The dependence of the height on time for these two EPs is essentially different. The curve of EP of I type shows two distinct phases during the eruption: pre-eruptive phase and eruptive phase. During the pre-eruptive phase, throughout the 146-min time interval, the EP slow rises from 65 000 km to 85 000 km with velocity of 1.8 km/s. After some critical height of about 90 000 km the prominence eruption enters on the acceleration phase. The height of the prominence arch grows very fast up to the prominence disappearing. In the frame of the acceleration phase the velocity of the EP increases from 3.1 km/s to 228.8 km/s, and the acceleration increases from 3.3 m/s^2 to 243.2 m/s^2.

The curve of the EP of II type shows three distinct phases during the eruption: acceleration, constant velocity and deceleration. During the acceleration phase this EP rises with acceleration of 15 m/s^2 and it reaches a maximal velocity at height of 170 000 km. After acceleration the EP raises with constant velocity of 43.8 km/s during 40-min time interval. At height of 106 550 km, the EP evolution enter in the deceleration phase. The negative acceleration of the EP material during this phase increases from –9.2 m/s^2 in the beginning to –35.5 m/s^2 just before the EP to reach a maximal height of 325 750 km.

Figure 2b represents the height-time diagram of the EP of August 14, 1979. The longer curve is more representatives for the prominence eruption. It clearly shows deceleration of prominence material during the eruption. The velocity of the EP rise decreases from 0.27 km/s in the beginning to 0.04 km/s to the end of the eruption. The negative acceleration during the eruption is –0.24 m/s^2.

The eruption processes of the EPs of I and II type are pronouncedly different as regards their fine structure, as well as by their dynamic parameters. These differences most probably reveal the specific evolution of the different parts of the HMS where the EPs of I and II type are embedded. From the dynamic point of view the third EP has essentially different eruption process than those of the EPs of I and II type. To a certain degree it is more close to the EP of II type as far as its eruption is similar to the last, deceleration phase of to the EP of II type. On the other hand, as in the case of the EP of II type, the

prominence material of the third EP falls back into the chromosphere after the prominence eruption.
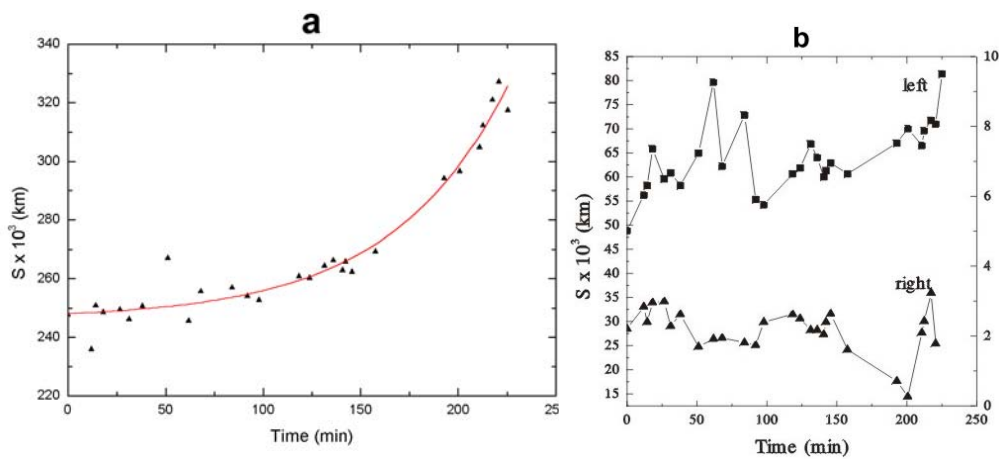
Fig.3 Horizontal expansion between the prominence arch feet (a) and between the feet of the magnetic tubes consisting left and right arch leg of type I EP (May 5, 1980).

4. Horizontal Expansion

During the eruption in vertical direction the EP of I type shows two kind of horizontal expansion. The first is between the prominence arch feet and the second is between feet of intertwisted magnetic tubes composing the left and right arch leg of the EP. Figure 3a represents the horizontal expansion between the EP leg feet as a function of time. During pre-eruptive phase the velocity slow increases from 0.6 km/s to 5.8 km/s and acceleration slow increases from 0.2 m/s^2 to 1.6 m/s^2. During eruptive phase the velocity quickly grows from 7.1 km/s to 22.3 km/s and the acceleration quickly grows from 2 m/s^2 to 6.3 m/s^2.

During the eruption of the EP of I type the magnetic tube feet in every prominence leg undergone horizontal displacement. Figure 3b represents the distance between magnetic tube feet in the left and right EP leg as a function of

time. In the process of the prominence eruption the magnetic tube feet in the left and right leg show alternative change of the direction of the horizontal expansion. While the horizontal expansion of the prominence legs is a result of prominence arch stretching, the specific horizontal expansion between the tube feet in the EP legs are most probably connected with the changes in the internal structure of EP arch during its stretching.

During the eruption of the EP of type II the prominence body consisted of two main intertwisted bundles untwists. Along with the growing of the prominence height the feet of main bundles move away each from other, showing horizontal expansion. Figure 4 shows the horizontal expansion of the bundle feet of EP body as a function of time. The mean velocity of horizontal expansion is estimated of 15.5 km/s. The onset of horizontal expansion is registered 100 min after the onset of the prominence eruption. During the 18-min time interval the bundle feet show uncertain horizontal expansion as a result of alternative change of the direction of horizontal displacement. When the two bundles of the EP body are completely untwisted, they show apparent horizontal expansion, moving away each from other. Hence, this special feature of the EP of II type horizontal expansion is close connected with the process of simplification of the prominence magnetic configuration that is a part of HMS.
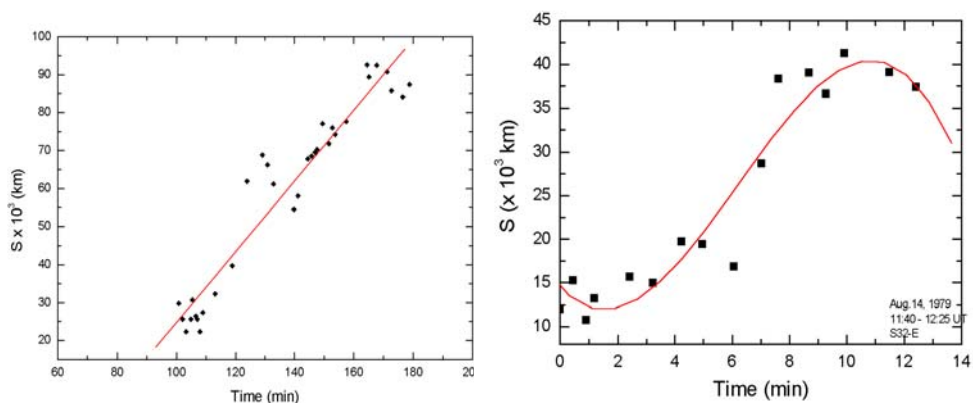
Figure 6 shows the horizontal expansion of the EP of August 14, 1979 as a function of time. The behaviour of the curve suggests that the horizontal expansion of this EP has periodical character, i.e. the EP foot probably oscillates about mean point at the solar surface. Hence, the pattern of the horizontal expansion of this EP is different than those of the horizontal expansion of the EPs of I and II type.

4. Conclusions

The eruption processes of the EPs of I and II type have different patterns as in respect to the fine structure of the eruption evolution, as well as in respect to the dynamic parameters. The eruption of the EP of II type is consisted of distinct phases of acceleration, constant velocity and deceleration and after the eruption the prominence material falls back into the chromosphere. The EP of I type shows only two distinct phases: pre-eruptive phase and acceleration.

The horizontal expansions of the EPs of I and II type have also different patterns. The EP of II type shows the horizontal expansion between two bundles consisting the prominence body whereas the EP of I type shows two kind of horizontal expansion: between the prominence arch legs and between magnetic tubes consisting left and right prominence leg.

The eruption process of the EP of August 14, 1979 is presented only of deceleration. Its horizontal expansion is characterized with specific oscillation of the prominence foot about mean point at the solar surface.

Reference

Rompolt, B.: 1984, *Adv. Space Res.* **4**, No. 4, 357.

Rompolt, B.: 1990, Hvar Obs. Bull. 14, 37

Rompolt, B.: 1998, in *New Perspectives on Solar Prominences*, D. Webb, D. Rust and B. Schmieder (eds.), IAU Colloq. 167, ASP Conference Series vol. 150, 330.

Rudawy, P., Rompolt, B., Kotrc, P., Heinzel, P. and Knizek, M.: 1994, in *Solar Magnetic Fields*, Proceedings of the international conference held in Freiburg, Germany, June 29-July 2, 1993. M. Schüssler and W. Schmidt (eds). Cambridge: Cambridge University Press, 372.

Vršnak, B.: 1998, in *New Perspectives on Solar Prominences*, D. Webb, D. Rust and B. Schmieder (eds.), IAU Colloq. 167, ASP Conference Series vol. 150, 302.

PASCHEN LINES SURVEY OF LAMBDA BOOTIS TYPE STARS

Ilian Kh. Iliev[1], Ivanka K. Stateva[1], Ernst Paunzen[2], Ina S. Barzova[1]

1) Institute of Astronomy, National Astronomical Observatory, P. O. Box 136, BG-4700 Smolyan, Bulgaria
2) Astronomisches Institut der Universität Wien, Türkenschanzstrasse 17, A-1180 Wien, Austria

The small group of stars named after the prototype Lambda Bootis comprises of Population I late-B to early-F type stars with metal deficient atmospheres. The deficit of Fe-peak elements is moderate to strong and reaches up to 2 dex. The abundance of light elements like C, N, O, and S is normal (solar). As a group Lambda Bootis type stars occupy almost the same place in the Herzsprung-Russell diagram as "classical" Am-stars and cool Ap-stars which in opposite exhibit metal-enriched spectra. The attempts to illustrate the question why are Lambda Bootis type stars so interesting are presented in the Table 1. Some of the general characteristics of four different types of stars are reviewed there. Even a simple analysis of the Table 1 shows how important can be the rotation and magnetic fields. The reality is much more complex because other general characteristics of these types of stars such as effective temperature, masses and kinematics are the same. So, what makes the puzzle so variegated?

The region bounded by effective temperature between 10000 K and 7000 K and by absolute magnitude between –1 and +2 is without any doubt the most crowded place in the Herzsprung-Russell diagram. Even the short list contains four types stars from the Table 1 plus field blue strugglers, BHB and HAEBE stars, F-weak, intermediate Population II stars, pre-MS stars, and, of course, Delta Scuti pulsators. Founding the physical reason for each of these groups is a challenging task. Our recent results show that Lambda Bootis type phenomenon occurs under limited physical conditions that puts strong constrains to many important astrophysical processes as radiatively driven diffusion, slow accretion, mass-loss and non-radial pulsations [1, 2].

	Rotation	Metals	Mag. Field	Variability
Normal A-stars	normal	normal	no	no, Delta Scuti
Cool Ap-stars	slow	excess	yes	sp, ph, puls
Am-stars	slow	excess	no	no
LamBoo stars	normal	deficient	no	puls

Fig.1

Some of the leading concepts [3, 4] suggest the crucial role of the interaction with the interstellar (or circumstellar) matter. Both gas and dust around the stars either from proto-stellar debris or from the clouds are considered as a main reason for the observed abundance anomalies. In connection with this we promoted a project targeted to some sensitive spectral lines such as NaD doublet, H-alpha and higher Paschen lines as tracers of ongoing slow accretion of circumstellar matter on the stellar atmospheres. Only the results of our Paschen lines survey are presented here.

Seven bright and pronounced Lambda Bootis type stars were observed in two overlapping spectral frames in the region between the lines Pa13 and Pa22 (centered at ca. 8500 angstroms). Observations were carried out with the coude-spectrograph of the NAO "Rozhen". Photometrics CCD (1024 x 1024, 24 microns) attached to the Third camera was used to provide the data with signal-to-noise ratio of about 300 and spectral resolution R ~ 25000.

Well-known Inglis-Teller formula connects the electron density Ne with the last resolved hydrogen line number: $\log Ne = 22.7 - 7.5 \log nmax$. Thus obtained value of Ne is typical for the uppermost atmospheric layers where the optical depth is close to 0.1. To determine Ne means to find where the appropriate central depth (or equivalent width) of a given hydrogen line approaches zero. Corrections should be made to bare numbers of nmax in order to take into account most of all the overlapping of the line wings due to rotation. In faster rotating cases the lines will "disappear" at smaller nmax values. As a rule, the internal error in nmax determination is about 0.2.

A0-F0	ZAMS	mid-MS	TAMS	sub-giant
nmax	17	18.5	20	21

Fig. 2

Just for comparison in the Table 2 we present the typical values of nmax for A0-F0 stars on different stages of their main sequence evolution. Our results together with some basic information about the stars studied are presented in Table 3. Last two columns (marked with IB) contain data taken from our paper [5]. Rozhen photographic plates and Balmer lines have been used there. Even if we take into account the big differences in the signal-to-noise level only, a conclusion can be drawn that the discrepancy between new CCD and old photographic data is not very large. As it can be seen most of the stars have Ne (and nmax) values typical for the normal A-stars. Only for the HD192640 and for the HD221756 larger nmax numbers can be interpreted as signs of an extended "giant-like" atmosphere. Does it mean that the accretion around other stars in our list is already ceased? To answer this question future observations are badly needed.

HD	T_{eff}	log g	vsini	n_{max}	$logN_e$	n_{max} (IB)	$logN_e$ (IB)
31295	8920	4.20	123	20.0	13.24	18.7	13.16
91130	8135	3.78	152	19.9	13.25	--	--
110411	8970	4.36	154	19.8	13.28	18.2	13.25
125162	8720	4.07	115	17.8	13.63	--	--
183324	8950	4.13	100	17.5	13.67	18.3	13.23
192640	7940	3.95	80	21.1	13.08	19.9	12.96
221756	8510	3.90	105	20.5	13.17	19.7	12.99

Fig. 3

The last paragraph is addressed to a topic far beyond the scope of this contribution. Here we want to share our experience to observe spectroscopically in the near-infrared. Nearly a dozen years after the end of the Photographic Era high-resolution stellar spectroscopy continues like "rhapsody in blue". The winning policy, in our opinion, is to behave as the light detector does. CCD observations are much more efficient in red and infrared regions simply because the chip is much more sensitive at those wavelengths. Even the lower resolution (because of having lower order spectra) is good prise for it. We agree that looking for new spectral regions and new sets of convenient lines with well-studied atomic constants in red and infrared for many chemical elements is not an easy task, but the result always is worth the efforts.

REFERENCES

1. I l i e v, I. Kh., Paunzen, E. Barzova, I., Kamp, I., Griffin, R., Claret, A., Koen, C. First orbital elements for the Lambda Bootis spectroscopic binary systems HD84948 and HD171948, Astron. & Astrophys., 381, 2002, 914-922

2. P a u n z e n, E., Iliev, I. Kh., Kamp, I., Barzova, I. The status of Galactic field Lambda Bootis stars in the post-HIPPARCOS era, Monthly Notices of RAS, 336, 2002, 1030-1042

3. V e n n, K.A., Lambert, D.A. Chemical composition of three Lambda Bootis stars, Astrophys. J., 363, 1990, 234-244

4. K a m p, I., Paunzen E. The Lambda Bootis phenomenon: Interaction between a star and a diffuse interstellar cloud, Monthly Notices of RAS, 335, 2002, L45-L49

5. I l i e v, I. Kh., Barzova, I. Shell signs in the hydrogen-line spectrum of some Lambda Bootis-type stars, CAOSP, 27, 1998, 441-445 (IB)

HIGH-RESOLUTION SPECTROSCOPY AT ROZHEN:
HUNT FOR SB2 MARKS IN THE SPECTRA OF
Am BINARIES

Ilian Kh. Iliev[1], Marian Fenovcik[2], Jan Budaj[3,4] and Ina S. Barzova[1]

1) *Institute of Astronomy, National Astronomical Observatory, P. O. Box 136, BG-4700 Smolyan, Bulgaria*
2) *P. J. Safarik University, SK-04001 Kosice, Slovakia*
3) *Dept. of Astronomy and Astrophysics, Penn State University, Davey Lab. 525, University Park, 16802 PA, USA*
4) *Astronomical Institute, SK-05960 Tatranska Lomnica, Slovakia*

Metallic-line A stars (or well-known Am stars) constitute a subgroup of chemically peculiar stars on the upper main sequence. Abnormally strong metallic and unusually weak Ca and Sc lines are typical for their spectra. Observed peculiarities are due apparently to slow selective diffusion driven mainly by the fine-tuned balance between radiation pressure and gravity. The diffusion operates first below the deepest HeII convection zone until it disappears because of He settling and then proceeds much higher and more effectively below the H+HeI convection zone. Rotation was found to play a key role in this process as it induces large scale mixing which can disturb the microscopic diffusion process. Recent sophisticated calculations indicate clearly that a rotational velocity less than about 90 km/s is required for diffusion to prevail and Am phenomenon to occur. There are also indications that Am peculiarity may depend on the orbital elements of a binary system [1, 2]. It is more pronounced in systems with higher eccentricities and possibly also at longer orbital periods. Since Am stars are found very often in binary systems (see discussions in [3, 4]) they offer an unique possibility to study the importance of tidal interactions on the stellar hydrodynamics and diffusion process.

Some years ago we started an extended multilateral observational project concerned especially with Am stars in binary systems. Its main aim is to collect spectroscopic data of high quality enough to fulfil the rigorous requirements of the spectrum synthesis procedures. First of all, this means S/N ratio of 300, 400 and more. Soon after the first observations we realised

that results go far beyond the scope of the project – some of the spectra exhibited clear signs of secondary components. Later on we were able to register the evolution due to orbital motion as well. Resolving SB1 systems became the second aim of our project. Here we report on the new SB2 systems found among selected Am binaries. The fact that we discovered SB2 signatures in 5 out of 28 stars simply shows that high resolution CCD spectroscopy of slow rotating binary stars offers really new opportunity to shed more light on their orbits, physical parameters and evolution.

Our spectroscopic observations were carried out with the 2-m RCC telescope of the Bulgarian National Astronomical Observatory in the frame of our observational program on Am-stars in binary systems. Photometrics AT200 camera with a SITe SI003AB 1024 x 1024 CCD chip, (24 microns pixels) was used in the Third camera of the coude spectrograph to provide spectra in two different spectral regions 100 angstroms wide and centered on 6440 angstroms and 6720 angstroms with resolving power R = 32000. The typical S/N ratio is about 300. Wavelength calibration has the r.m.s. error of 0.005 angstroms IRAF standard procedures have been used for bias subtracting, flat-fielding and wavelength calibration. Telluric lines have been removed using spectra of hot, fast rotating stars.

About thirty Am binaries were selected: 1) to be brighter than 7-th magnitude in V; 2) to have declination > +10 deg.; 3) to have orbital periods between 10 and 180 days. This assures a full range of original eccentricities that did not undergo circularization during the evolution on the main-sequence. We put no constraint on the rotational velocity and included one more broad line normal star for testing the analysis on highly rotating stars.

Only the main results with figures are reviewed here, for much more information we address the reader to the original papers where they are published.

HD434. This star (HIP728, V=6.5 mag) is well known SB1 system. Latest orbital elements are P=34.26 days, e=0.475, K=24 km/s, gamma=2.6 km/s. Our observations [5, 6] revealed pronounced secondary spectrum. It is shown with "b" in the Figure 1.
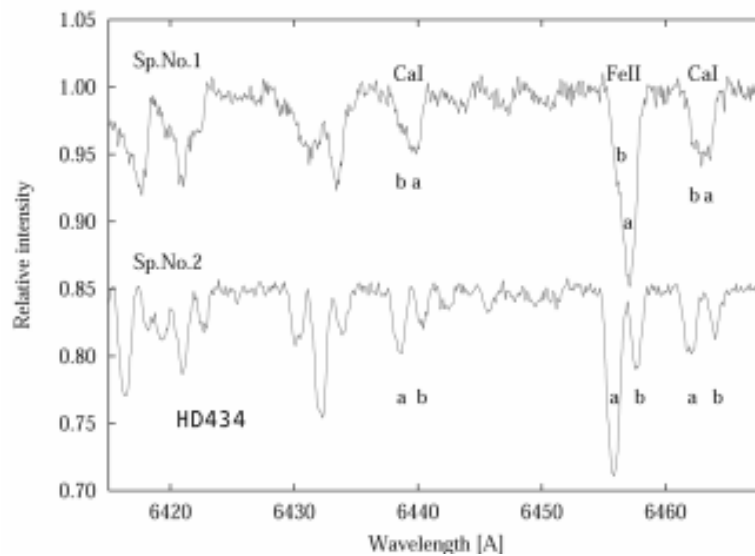
Fig.1

HD861. This star (HIP1063, V=6.6 mag) is well known SB1 system again, it is close and bright. The orbital elements are P=11.215 days, e=0.22, K=45 km/s, gamma=-12.5 km/s. Two successive spectra of this star [7] are shown in the Figure 2. While the strong lines of the primary "a" are shifted to the blue, weak but sharp lines of the secondary "b" moved to the red, as it is marked with arrows. To resolve the secondary signal-to-noise ratio of about 300 is reached. In this case high signal-to-noise ratio is as important as the high resolution.

HD108642. The next star in our sample (HIP60880, V=6.4 mag.) is SB1 system with P=11.784 days, e=0.0, K=41 km/s, gamma=-0.7 km/s. Its SB2 nature was only suspected. Slow rotation of both components facilitates the resolution of the secondary [6]. Our observations are presented in the Figure 3. Both systems of lines are well separated and recognized. As a result of the orbital motion "a" and "b" lines exchange their places.

HD216608. Fourth in a row, this star (HIP113048, ADS 16345 AB) is a visual binary system. Component B (a F6V star) orbits the primary with a period of 105 years. There is also an optical C companion, faint star of 11- th magnitude. Brightest member HD216608 A is a SB1 binary system,
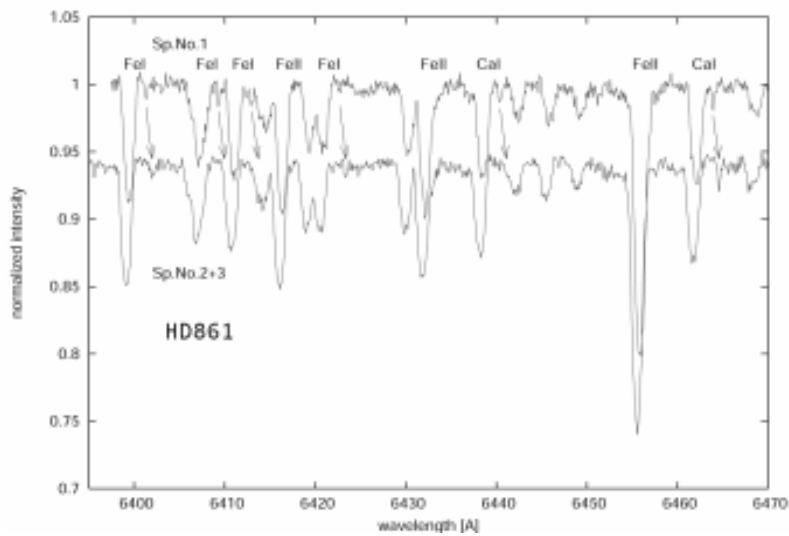
Fig.2
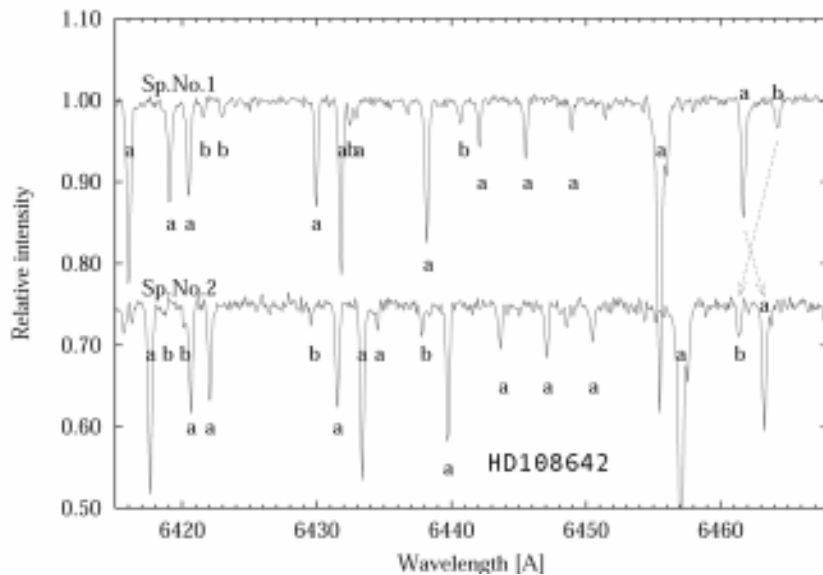
Fig.3

it is an Am star and thus, was our main target to study. Orbital elements are: P=24.164 days, e=0.2, K=10 km/s. Results of our spectroscopic observations [8] are shown in the Figure 4.
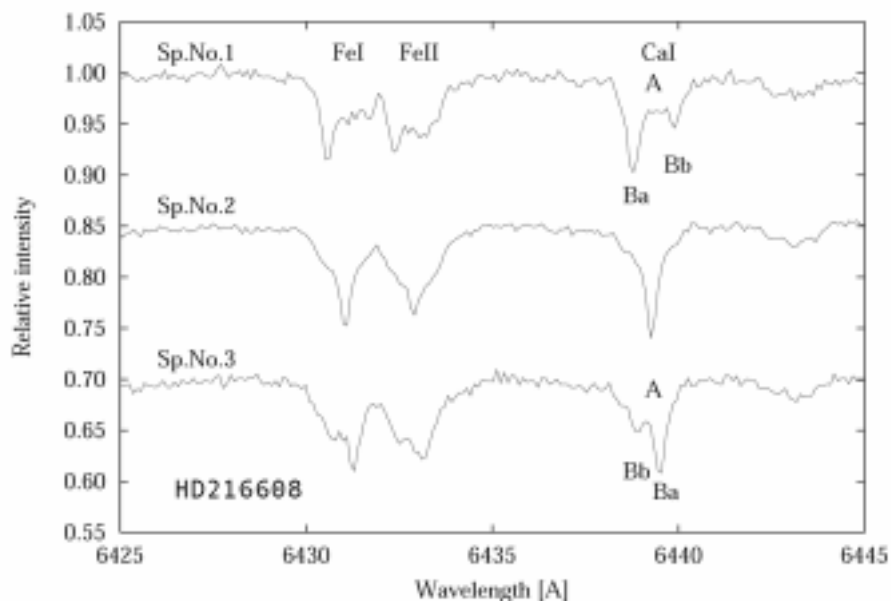
Fig. 4

HD178449. The star (17 Lyr, HIP93917) was included in our target list in order to use it as reference object for synthetic spectra procedures at high rotational velocities. This object is known SB1 system, it turned out to be very interesting and we spent large amount of observing time to solve the case [9]. Small portion of its spectrum is shown below in the Figure 5.
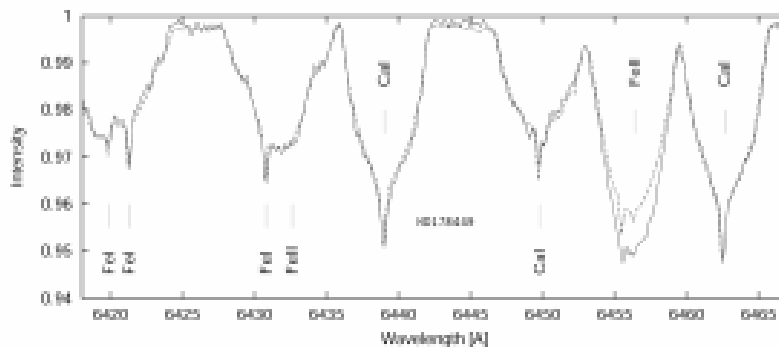
Fig. 5

The comprehensive investigation including sophisticated synthetic spectra calculations (presented with dashed line in Figure 5) shows that weak sharp "noses" belong to the newly discovered Ab component of this

system. To reject their interstellar or shell origin observations with signal-to-noise level of about 1700 were carefully collected and matured for more than 10 hours of accumulated exposure time.

Review shown here illustrates once again that the coude-spectrograph in operation at Rozhen is efficient and convenient for studying the spectroscopic binary systems. Some of our previous results in this field [10, 11, 12] could be used as reference what kind of spectroscopic investigations can be successfully carried out at NAO Rozhen.

REFERENCES

1. B u d a j, J. On the nature of the Am phenomenon or on a stabilization and tidal mixing in binaries II. Metalicity and pseudo-synhronization, Astron. Astrophys., 326, 1997, 655-661

2. I l i e v, I., Budaj, J., Zverko, J., Barzova, I., Ziznovsky, J. Lithium and metal abundances in long period Am binaries, Astron. Astrophys. Suppl., 128, 1998, 497-505

3. N o r t h, P., Ginestet, N., Carquillat, J.-M., Carrier, F., Udry, S. Binaries among Ap and Am stars, CAOSP, 27, 1998,179-183

4. D e b e r n a r d i, Y., Mermilliod, J.-C., Carquillat, J.-M., Ginestet, N. Binarity of Am stars in Preasepe and Hyades, Astron. Astrophys., 354, 2000, 881-891

5. I l i e v, I., Budaj, J., Ziznovsky, J., Zverko, J. Discovery of a secondary spectrum in the SB1 system HD434, IBVS, 2001, 5051

6. B u d a j, J., Iliev, I., Barzova, I., Ziznovsky, J., Zverko, J., Stateva, I. Direct mass ratio determination in the SB2 systems HD108642 and HD434 , IBVS, 2003, 5423

7. B u d a j, J., Iliev, I., Fenovcik, M., Barzova, I., Richards, M.T., Geordzheva, E. Discovery of the secondary in the spectrum of the SB1 system HD861, IBVS, 2004, 5509

8. I l i e v, I., Budaj, J., Ziznovsky, J., Zverko, J., Stateva, I., Geordzheva, E. Detection of a ternary spectrum in HD 216608, IBVS, 2001, 5199

9. B u d a j, J., Iliev, I. Abundance analysis of Am binaries and search for tidally driven abundance anomalies I. HD33254, HD178449, HD198391 , Monthly Notices of RAS, 346, 2003, 27-36

10. D u e m m l e r, R., Pelt J., Korhonen P., Iliev I. Kh. Is Beta Crateris a Sirius-like system?, Astron. Astrophys. 328, 1997, L37-L39

11. D u e m m l e r, R., Iliev I., Iliev L. The radial velocities and physical parameters of HD553, Astron. Astrophys. 395, 2002, 885-890

12. I l i e v, I. Kh., Paunzen, E. Barzova, I., Kamp, I., Griffin, R., Claret, A., Koen, C. First orbital elements for the Lambda Bootis spectroscopic binary systems HD84948 and HD171948, Astron. Astrophys., 381, 2002, 914-922

CCD PHOTOMETRIC STUDY OF THE OVERCONTACT ECLIPSING BINARY SYSTEM V1363 Ori

Kosmas Gazeas, Panagiotis Niarchos

Department of Astrophysics, Astronomy and Mechanics
National and Kapodistrian University of Athens
GR 157 84 Zografos, Athens, Greece

Abstract.

New BVRI light curves of the eclipsing binary system V1363 Ori, based on CCD observations made at the University of Athens Observatory, are analyzed using the Wilson-Devinney light curve synthesis code and new geometric and photometric elements are derived. These elements are used together with the available spectroscopic data to compute the absolute elements of the system. The evolutionary status of the system is also discussed.

1. Introduction

The eclipsing binary V1363 Ori (GSC 4904:0531) was first was discovered by Hipparcos satellite mission (ESA, 1997). It was listed in the 74th special name-list of variable stars (Kazarovets et al. 1999) as an EW type eclipsing binary with a period of 0.431915 days. The Hipparcos observations of the system were analyzed by Selam (2004), in order to determine the mass ratio, the degree of contact and the orbital inclination. The spectroscopic mass ratio is $q=0.205$ and the spectral type is estimated to be early to mid F-type Main Sequence system (Pych et al. 2004). An O'Connell effect in the light curves of V1363 Ori was present from the day of its discovery (Gomez-Forrellad et al. 1999) and confirmed by our observations.

2. Observations

The ground-based observations of V1363 Ori were made on 7, 9, 24 February and on 6, 11, 26 March 2004. The instruments used were the 0.40 m Cassegrain reflector at the University of Athens Observatory, Greece, and a ST-8 CCD camera. The CCD camera uses a Kodak KAF-1600 CCD chip, cooled by a two-stage Peltier element, which provides a CCD working temperature of -30° C below ambient. The CCD chip has 1536×1024 useful pixels of 9×9 microns, covering an area of approximately 15×10 arcmin.

The CCD camera is equipped with a set U, B, V, R and I Bessell filters. The scale on the chip is 1.24 arcsec/pixel in 2×2 binning mode.

A total number of 724 frames were obtained in all filters. The images were processed with the AIP4WIN program of Berry & Burnell (2000). Differential magnitudes were used to determine the standard deviation of our measurements, which is 0.005 mag on average in all bands used (B, V, R, I). From the light curves it is clear that V1363 Ori is a contact eclipsing binary of W UMa type.

3. Light curve analysis
3.1. Times of minima

Although we succeeded to observe complete light curves, it was not possible to compute the period of the system, since only one primary minimum was observed. The time of this minimum was computed by the method of Kwee & van Woerden (1956) and its value (the mean value in the four filters B, V, R and I) is: Min I (HJD) = 2452705.2281 ± 0.0008. For the phase diagrams we have used the following ephemeris, where the time of minimum is the one calculated from our observations and the period is from Gomez-Forrellad et al. (1999):

$$\text{Min I (HJD)} = 2452705.2281 + 0^{d}.431921 \times E \qquad (1)$$

3.2. Unspotted solution

Our light curves were analyzed with the Wilson-Devinney DC program, running in Mode 3. One hundred normal points were formed from our observations for each filter. Due to the profound asymmetries in the light curves, we had to assume the existence of at least one cool spot on the primary component of the system, since the temperatures of both components are almost the same. In the beginning of our solution it was assumed that no spots were present on the surface of the stars, and we performed the unspotted solution by omitting the observations around the asymmetrical part of the light curve, between phases of 0.75 and 0.95.

The spectroscopic mass ratio q=0.205±0.007 (Pych et al. 2004) was used as a fixed parameter. The free parameters to be determined by the program were the following: the phase of conjunction φ, the inclination i, the temperature of the secondary star T_2, the surface potentials Ω (both $Ω_1$ and $Ω_2$) and the non-normalized monochromatic luminosities of the primary (L_1) for the four filters. The temperature T_1 had a fixed value (from spectroscopic observations). The usual values from the theory were used for

194

the coefficients of gravity darkening. The limb darkening coefficients were taken from the new tables of Claret (2000) (bolometric values) and Claret, Díaz-Cordovés & Giménez (1995), according to the spectral type and the wavelength of observation. The third light was assumed equal to zero. The results are given in the second column of Table 1. The errors given are standard deviations.

3.3. Spotted solution
Cool Spot model

In the second step of our analysis we used all the data, assuming that there is a cool spot in the primary component (spotted solution). The results are given in the third column of Table 1. The spot latitude is counted from the north pole, while the spot longitude from the line between the two components, counterclockwise.

The errors given are standard deviations. The derived parameters were used to construct the theoretical light curves which are shown along with the observed ones in Figure 1.

Hot Spot model

Since the position of the cool spot is around the neck region it was difficult to give a physical explanation. For this reason we tried to model the system with a hot spot on each of the two component. We obtained a satisfactory solution by placing the hot spot on the secondary component. But the position of this hot spot is far away from the neck region and again it was difficult to explain it physically.

The spot latitude was assumed to be 90° and the rest spot parameters were found to be: spot longitude = 57.3° ± 0.2°, spot radius = 13.9° ± 0.1° and temp. factor = 1.262 ± 0.001.

Table 1. Light curve solutions for V1363 Ori.

Parameter	Mode 3 (no spot)	Mode 3 (cool spot)
φ	-0.0041 ± 0.0002	-0.0008 ± 0.0002
i (deg)	53.84 ± 0.01	56.59 ± 0.11
T_1 (K)	6750*	6750*
T_2 (K)	6342 ± 1	6789 ± 12
$\Omega_1 = \Omega_2$	2.1191 ± 0.0001	2.1569 ± 0.0015
$q = m_2/m_1$	0.205*	0.205*
$g_1 = g_2$	0.32*	0.32*
$A_1 = A_2$	0.50*	0.50*
% overcontact	96%	73%
$L_1/(L_1+L_2)$ (B)	0.8238 ± 0.0021	0.7628 ± 0.0031
$L_1/(L_1+L_2)$ (V)	0.8147 ± 0.0018	0.7657 ± 0.0019
$L_1/(L_1+L_2)$ (R)	0.8088 ± 0.0011	0.7678 ± 0.0013
$L_1/(L_1+L_2)$ (I)	0.8015 ± 0.0011	0.7707 ± 0.0012
$X_1 = X_2$ (B)	0.706*	0.706*
$X_1 = X_2$ (V)	0.602*	0.602*
$X_1 = X_2$ (R)	0.497*	0.497*
$X_1 = X_2$ (I)	0.417*	0.417*
r_1 (vol)	0.5661 ± 0.0008	0.5540 ± 0.0012
r_2 (vol)	0.3218 ± 0.0008	0.2948 ± 0.0012
Spot Parameters		
Spot Latitude (deg)	-	127.3 ± 1.4
Spot Longitude (deg)	-	6.1 ± 0.4
Spot Radius (deg)	-	41.5 ± 0.9
Temper. Factor	-	0.77 ± 0.01
Σ w(res)^2	0.0303	0.0358

* assumed
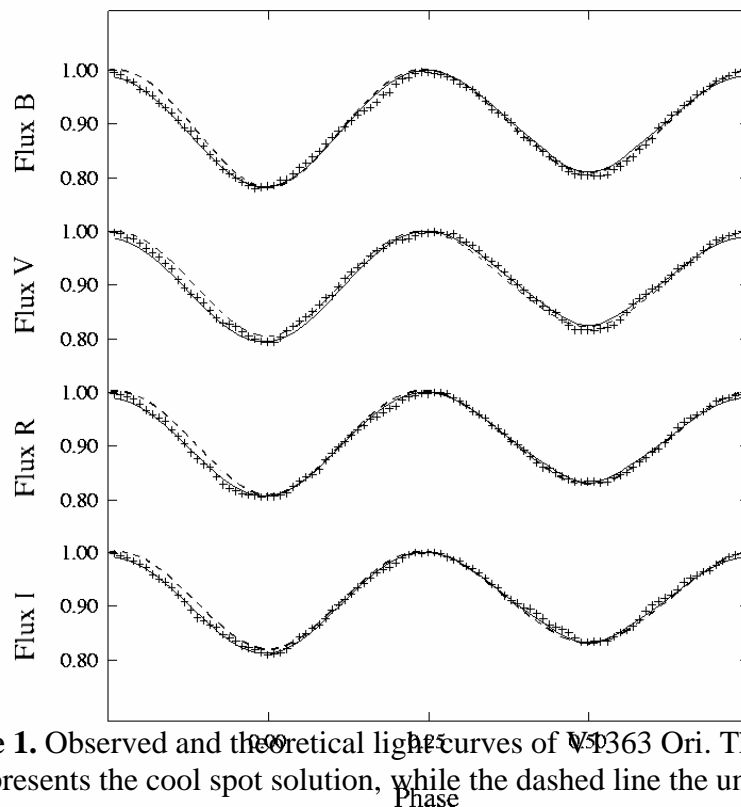
Figure 1. Observed and theoretical light curves of V1363 Ori. The solid line represents the cool spot solution, while the dashed line the unspotted.

5. Summary and conclusions

It is clear from Figure 1 that the observed light curves of V1363 Ori are rather symmetrical with some small parts of asymmetry, explained by spot activity on the stellar surfaces. There is a small difference in the depths of the two minima indicating different surface temperatures of the two components. Such a light curve is typical for W-type contact systems of W UMa type. The light curve analysis shows a highly contact configuration with a fill-out factor 73%.

The elements derived from the cool spot model of Table 1 are combined with the available spectroscopic data to compute the following absolute physical parameters in solar units (radii, masses and luminosities) of V1363 Ori: $R_1=1.665\pm0.087$, $R_2=0.886\pm0.046$, $M_1=1.314\pm0.599$, $M_2=0.269\pm0.123$,

197

$L_1=5.193\pm0.026$, $L_2=1.505\pm0.032$ and the absolute bolometric magnitudes of the components are: $M_{(bol)1}=2.960$, $M_{(bol)2}=4.305$.

By using the absolute elements of the system we tried to get a picture of its evolutionary status. By means of the M-R diagram we see that the primary component lies on the TAMS line, an indication that is not yet evolved. On the other hand, the less massive secondary, seems to be evolved, as it is well above the TAMS line.

Acknowledgements

REFERENCES

Berry, R., Burnell, J., *The Handbook of Astronomical Image Processing*, Willmann-Bell, Richmond (Virginia), 2000.

Claret, A., A&A, **363**, 1081, 2000.

Claret, A., Díaz-Cordovés, J., Giménez, A., A&AS, **114**, 247, 1995.

ESA, The Hipparcos & Tycho Catalogues, SP-1220, 1997.

Kazarovets, A. V.; Samus, N. N.; Durlevich, O. V.; Frolov, M. S.; Antipin, S. V.; Kireeva, N. N.; Pastukhova, E. N., IBVS 4659, 1999.

Kwee, K. K., van Woerden, H., Bull. Astron. Inst. of Netherlands, **12**, 327, 1956.

Pych W., Rucinski S.M., DeBond H., Thomson J.R., Capobianco C.C., Blake R.M., Ogloza W., Stachowski G., Rogoziecki P., Ligeza P., Gazeas K., AJ, **127**, 1712, 2004.

Selam S.O., A&A, **416**, 1097, 2004.

Gomez-Forrellad J.M., Garsia-Melendo E., Guarro-Flo J., Nomen-Torres J., Vidal-Sainz J., IBVS No 4702, 1999.

198

HEATING IN THE STELLAR WINDS OF HOT STARS

J. Kubát, J. Krticka

Astronomicky ustav, Akademie ved Ceske republiky, CZ-251 65 Ondrejov, Czech Republic

Ustav teoreticke fyziky a astrofyziky PrF, Masarykova univerzita,

CZ-611 37 Brno, Czech Republic

Abstract

Multicomponent radiatively driven winds in late B stars cause significant heating of the layers just above the photosphere. If heating is large enough to heat the circumstellar environment up to coronal temperatures, then a coronal wind may be present. In addition, the coronal region may be a site of significant X-ray emission being able to explain observed X-ray activity of early B stars.

Introduction

Stellar winds in hot stars are known to be radiatively driven. The radiative momentum is transferred from radiation to a gas by means of absorption. Not all chemical elements are equal absorbers, so some elements are accelerated more than the others. In the case that there is enough collisions that may redistribute the momentum over the entire gas (basically elastic collisions), the radiatively driven stellar wind behaves like a one-component fluid. This issue has been discussed by Castor et al. [1] and for the case of O star winds they concluded that the amount of collisions is sufficient to maintain the wind as a one-component flow. Corresponding continuity and momentum equations read

$$\frac{\mathrm{d}}{\mathrm{d}r}\left(r^2 \rho v\right) = 0,$$

$$v\frac{\mathrm{d}v}{\mathrm{d}r} = f^{\mathrm{rad}} - f^{\mathrm{grav}} - \frac{1}{\rho}\frac{\mathrm{d}p}{\mathrm{d}r},$$

Where f^{rad} is the radiative acceleration, is the gravitationa acceleration, p is the gas pressure, ρ is the density, and v is the flow velocity. The one-component approximation was then used in a majority of radiatively driven wind model calculations and computed models gave successful comparison with observations (for a review see Kudritzki & Puls [2]).

The possibility of a lower momentum transfer by collisions was first discussed by Springmann & Pauldrach [3]. First multicomponent hydrodynamic calculations of a radiatively driven stellar wind were performed by Babel [4,5]. Porter & Drew [6] studied the multicomponent wind using a simplified beta-velocity law. Later, Porter & Skouza [7] discussed the possibility of a wind reaccretion after its decoupling. Consistent hydrodynamic calculations of a multicomponent wind were performed by Krticka & Kubát [8,9,10]. The stability of such a wind has been discussed by Owocki & Puls [11] and Krticka & Kubát [12].

Multicomponent monotemperature winds

In a real radiatively driven wind the chemical species may be divided into three basic groups according to the ability to absorb radiation. The first group consists of radiatively accelerated particles that have enough ability to absorb radiation and, consequently, are significantly accelerated by absorption of radiation in spectral lines. The second group involves particles whose contribution to the radiative force is almost negligible compared to the first group. This group is taken along by friction with the first group. Since its role in the stellar wind is passive, we call this group as a passive component. In real stars it consists of hydrogen and helium. The third group are free electrons, which are accelerated by Thomson scattering and by friction as well. Each component is described by a set of equations

200

of continuity, motion, and energy (here a stands for i - accelerated ions, p - passive component, and e - electrons),

$$v_{ra}\frac{dv_{ra}}{dr} = g_a^{\mathrm{rad}} - g - \frac{1}{\rho_a}\frac{dp_a}{dr} + \frac{q_a}{m_a}E + \frac{1}{\rho_a}\sum_{b\neq a}R_{ab},$$

$$\frac{3}{2}k\frac{dT}{dr}\sum_a v_{ra}\frac{\rho_a}{m_a} + \sum_a a_a^2\rho_a\frac{1}{r^2}\frac{d}{dr}\left(r^2 v_{ra}\right) =$$
$$= Q^{\mathrm{rad}} - \frac{1}{2}\sum_a\sum_{b\neq a}R_{ab}\left(v_{ra} - v_{rb}\right),$$

Where subscript denotes variables corresponding to the component a, T is the temperature, E electric polarisation field, and R_{ab} is the frictional force. The radiative force in the CAK approximation for the multicomponent wind reads (see Krticka & Kubát [9])

$$g_i^{\mathrm{rad}} = \frac{1}{\mathfrak{D}_i}\frac{\sigma_e L}{4\pi r^2 c}f\left(\frac{n_e/W}{10^{11}\mathrm{cm}^{-3}}\right)^{\delta}k\left(\frac{\mathfrak{D}_i}{\sigma_e v_{\mathrm{th}}\rho_i}\frac{dv_{ri}}{dr}\right)^{\alpha},$$

with Abbott [13] force multipliers, f is the finite disk correction factor, W is the stellar dilution factor.

The main driving force for the passive plasma, namely the frictional force between charged particles reads

$$R_{ab} = -n_a n_b k_{ab}G(x_{ab}),$$

where x_{ab} is the dimensionless velocity difference,

$$k_{ab} = \frac{4\pi \ln \Lambda q_a^2 q_b^2}{kT} \frac{v_{ra} - v_{rb}}{|v_{ra} - v_{rb}|}$$

is the friction coefficient and *G(x)* is the Chandrasekhar function (see Fig. 1).
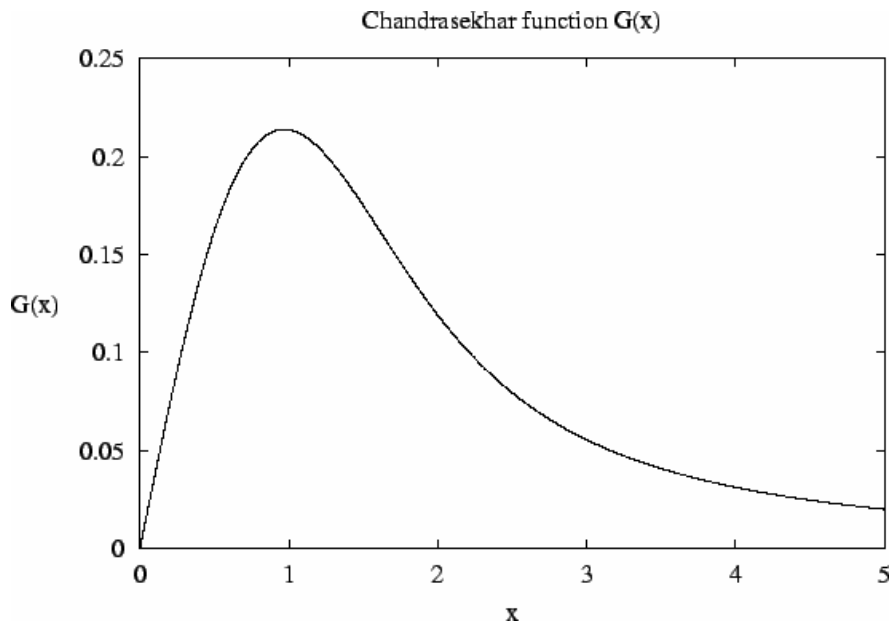
Figure 1: The Chandrasekhar function *G(x)*
The radiative energy term involves free-free heating, free-free cooling, bound-free heating, and bound-free cooling due to hydrogen.

Calculations of the three-component wind models show the same results as for the one component wind for the case of galactic O stars, which means that the one-component approximation is an adequate one for winds of these stars. On the other hand, there is a relatively large heating for lower effective stellar temperatures, namely for the main-sequence B type stars. An interesting fact is that for lower effective temperatures we obtain higher wind temperatures, a consequence of a frictional heating, which rises with decreasing effectiveness of elastic collisions. Detailed results of the three component calculations as well as the complete list of equations are

presented in Krtička & Kubát [9].

Multitemperature winds

A more general treatment of the three-component wind adds the possibility of different temperatures for different components. The basic difference is in the energy equation, which now reads

$$\frac{3}{2}kv_{r_a}\frac{\rho_a}{m_a}\frac{\mathrm{d}T_a}{\mathrm{d}r} + a_a^2\rho_a$$
$$+ \frac{1}{\sqrt{\pi}}\sum_{b\neq a}K_{ab}\frac{2k\,(T_b}{m_a}$$

Common processes which influence all components are advection cooling, adiabatic cooling, heat exchange by collisions, and friction. However, not all heating and cooling processes are effective for all wind components. Radiative bound-free and free-free transitions affect only electrons - they transfer energy between radiation field and electron gas. Accelerated ions are subject to the so-called Gayley-Owocki heating (sometimes also called Doppler heating), which is caused by the fact that radiation is absorbed and then reemitted at different wind velocities (and thus Doppler shifted). The energy difference is then consumed for heating the ionic gas. This effect was first discussed by Gayley & Owocki [14]. Recently, it was rederived directly from the Boltzmann kinetic equation by Krtička & Kubát [10].

Results of multitemperature calculations generally confirm monotemperature three-component results, the only qualitative difference that in the heated region the component temperatures slightly differ. There is no heating in the O star domain, as for monotemperature flows. Detailed

results may be found in Krticka & Kubát [10].

Consequences of coronal temperatures

If large heating leads to coronal temperatures (of order 10^7 K), then such medium has to emit X-ray radiation. This has been really observed, an average X-ray luminosity of main-sequence B3 stars according to ROSAT observations (Cohen [15]) is $10^{-9} L$. For our models the X-ray luminosity is 10^{-11} -10^{-7} L, so the observed X-ray energy falls into the approximate theoretical interval. It points out an interesting possibility of generation of X-ray radiation in B stars by frictionally heated plasma.

Another consequence is that high temperature totally changes the ionization structure of the wind, and, consequently, also the absorption coefficients. Then the radiation driving force may be significantly affected by these changes and the radiatively driven wind may be probably ``switched off'' due to insufficient absorption. If the temperature in the corona is high enough, a coronal wind may appear. Kubát et al. [16] named such wind as a radiation induced wind. However, they did not find enough heating from the friction in a two-component wind, so the coronal wind from B stars remains still suspicious.

Conclusions

Frictional heating and GO heating lead to substantial heating of the wind and may change the outflow velocity. Large heating may lead to formation of a coronal region. Frictional heating is another possible source of X-ray radiation in addition to shocks. There is a possibility of launching the coronal wind in hot stars, but the frictional model does not yield enough heating.

Acknowledgements:

Bibliography

[1] Castor, J. I., Abbott, D. C., Klein, R. I. 1976, in Physique des mouvements dans les atmosphcres stellaires, R. Cayrel & M. Sternberg eds., CNRS Paris, p.363

[2] Kudritzki, R. P., Puls, J. 2000, *Ann. Rev. Astron. Astrophys.* **38**, 613

[3] Springmann, U. W. E., Pauldrach, A. W. A. 1992, *Astron. Astrophys.* **262**, 515

[4] Babel, J. 1995, *Astron. Astrophys.* **301**, 823

[5] Babel, J. 1996, *Astron. Astrophys.* **309**, 867

[6] Porter, J. M., Drew, J. E. 1995, *Astron. Astrophys.* **296**, 761

[7] Porter, J. M., Skouza, B. A. 1999, *Astron. Astrophys.* **344**, 205

[8] Krticka, J., Kubát, J. 2000, *Astron. Astrophys.* **359**, 983

[9] Krticka, J., Kubát, J. 2001, *Astron. Astrophys.* **369**, 222

[10] Krticka, J., Kubát, J. 2001, *Astron. Astrophys.* **377**, 175

[11] Owocki, S. P., Puls, J. 2002, *Astrophys. J.* **568**, 965

[12] Krticka, J., Kubát, J. 2002, *Astron. Astrophys.* **388**, 531

[13] Abbott, D. C. 1982, *Astrophys. J.* **259**, 282

[14] Gayley, K. G., Owocki, S. P. 1994, *Astrophys. J.* **434**, 684

[15] Cohen, D. H., Cassinelli, J. P., MacFarlane, J. J. 1997, *Astrophys. J.* **487**, 867

[16] Kubát, J., Krticka, J., Pustylnik, I. B. 2004, *New Astron.* **9**, 215

PHYSICAL PARAMETERS FOR STARS
IN CLOSE BINARY SYSTEMS

Panagiotis Niarchos

National and Kapodistrian University of Athens, Greece

Abstract

The importance of derivation of the physical parameters for stars in close binary systems is stressed and the basic observational approaches for their study are briefly presented. The new opportunities and challenges in the study of close binaries in the 21st century, mainly based on observations from space, are also discussed.

1. Introduction

Binary stars are important for several reasons: (i) they are as common as single stars in the Universe. In the solar neighborhood more than 50% of stars are members of binary or multiple star systems; (ii) they are the primary source of our knowledge of the fundamental properties (stellar masses, radii and luminosities) of stars; (iii) they can be used as distant indicators for nearby galaxies; (iv) the evolution of binary stars helps us to explain a host of diverse and energetic phenomena such as cataclysmic variables, novae, symbiotic stars, some types of supernovae and X-ray binaries; (v) binaries in clusters are also very important since they provide the means for a detailed testing of stellar evolution theory.

Close binaries or Interacting binaries are two stars that do not pass through all stages of their evolution independently of each other, but in fact each has its evolutionary path significantly altered by the presence of its companion. Processes of interaction include: gravitational effects, mutual irradiation, mass exchange and mass loss from the system.

2. Derivation of physical parameters

The ultimate goal for observational astronomers who study the properties of binary stars is to make direct determination of the astrophysical parameters: *masses, radii, shapes, temperatures and luminosities*. These parameters also called absolute dimensions, which describe the component stars in SI units, can be derived from the analyses of light and radial velocity curves, regardless of the distances of the binaries

from us. The basic formulae used for the computation of the absolute elements are:

From double-lined binaries we get

$$m_{1,2} \sin^3 i = (1.0361 \times 10^{-7})(1 - e^2)^{3/2}(K_1 + K_2)^2 K_{2,1} P$$

where the masses are in solar masses, i is the inclination of the orbit, e is the eccentricity of the orbit, K_1, K_2 are the semi-amplitudes of the two radial velocity curves and P is the period in days.

The semi-major axes in solar radii are given by

$$a_{1,2} \sin i = (1.9758 \times 10^{-2})(1 - e^2)^{1/2} K_{1,2} P$$

For single-lined binaries the mass function can be determined by

$$\begin{aligned} f(m) &= (1.0361 \times 10^{-7})(1 - e^2)^{3/2} K_1^3 P \\ &= m_2^3 \sin^3 i / (m_1 + m_2)^2 \\ &= m_1 q^3 \sin^3 i / (1 + q) \end{aligned}$$

where $q = m_2 / m_1$ is the mass ratio.

From light curve solutions we obtain i, $r_{1,2}$, $T_{1,2}$ and the mass ratio q. Second-order parameters, such as *limb darkening, gravity darkening* and *bolometric albedos* are assigned theoretical values. The absolute radii or dimensions of the stars are given by $R_{1,2} = \alpha\, r_{1,2}$. This is the case that masses and radii are the most accurately determined fundamental parameters for stars in binaries. The relative radii determined from solutions of good light curves are accurate to $\pm 1\%$ or better, and the major source of uncertainty about masses and radii arises from the accuracies of the velocity semi-amplitudes.

One of the temperatures, usually T_1, can be adopted from other data, such as: (i) de-reddened colour indices at a total eclipse; (ii) using several values of de-reddened colour indices at different orbital phases; (iii) spectral types, or (iv) fitting of stellar-atmosphere models to tomographically separated spectra. The other temperature T_2 may be derived from the foregoing techniques and confirmed by the light-curve solutions or determined from the light-curve solutions directly.

The luminosities and absolute magnitudes of the two components are computed from the relations

$$L_{1,2} / L_{sun} = (R_{1,2} / R_{sun})^2 (T_{1,2} / T_{sun})^4$$

$$M_{bol\,1,2} = C - 5\log_{10}(R_{1,2} / R_{sun}) - 10\log_{10} T_{1,2}$$

where

$$C = M_{bol\,sun} + 10\log_{10} T_{sun} = 42.369, \; for \; M_{bol\,sun} = +4.75 \; and \; T_{sun} = 5780\,K$$

During the last two decades two distinct developments had a great impact in deriving the basic astrophysical quantities describing the close binary systems. The first was the development of the Roche model for light curve analysis, and the second one was the invention of new modern methods in deriving radial velocities for close binary systems.

3. Observational approaches of Close Binaries
3.1. Photometry

The photometric observations are made either by photoelectric photometers or by CCD cameras. Each detector has its own advantages and disadvantages, but photoelectric photometry is still the most precise and accurate means of obtaining flux measurements in optical astronomy. The CCDs have major advantages in doing photometric studies of multiple faint objects in crowded fields.

The modern synthetic light curve codes, based on Roche model, enable us to derive much more realistic and accurate physical parameters of close binary systems. These codes allow also a simultaneous solution of photometric and radial velocity curves. Among those parameters the one of main interest is the *mass ratio* of the system, which is necessary for the calculation of the absolute dimensions for single line spectroscopic binaries. Mass-ratios determined by using photometric methods are *model dependent* and, in most cases, very poor because of the weak sensitivity of the light-curve shapes to changes of q. Only for W UMa contact binaries with total eclipses the mass-ratio can be determined with relatively high accuracy by synthetic light curve techniques.

3.2 Spectroscopy

Spectroscopic studies of Close Binaries aim to spectral classification, line profile analysis and radial velocity determinations. Low resolution, usually R>1000, is used for spectral classification, higher resolutions are desirable for precision radial velocity work and highest resolution (R ~10^5) is needed for the analysis of spectral line profiles and extra-solar planet research. In any case high level of precision and accuracy in radial velocities is needed for binary star modeling.

Contact Binary systems have been difficult to study with good precision because (i) the spectral lines are very broad (V_{rot} ~150 km s^{-1}) and blended ($\delta\lambda$~ 2 Å) and (ii) also because the systems are very faint for good spectral resolution (0.01 P ~5 min). These two problems have been overcome in the last 15 years by reducing the spectra in a digitized form using modern techniques, like *Cross Correlation Technique* [2], [3], [4] and *Broadening Function Approach* [5], [8], [11]*,* and by introduction of image intensifiers and high quantum efficiency CCD detectors.

3.3 Spectrophotometry

A combination of spectroscopy and photometry can provide a rich bounty for light curve analysis. A large number of narrow pass bands can greatly improve the radiative modeling of stars, since the wavelength-dependent parameters are adjustable for each pass-band, and together provide strong leverage for the determination of the temperatures and for any thermal perturbations projected onto the disk surfaces. In addition, the weight of the non-wavelength-dependent parameters is increased by virtue of the large number of light curves. Promising techniques to disentangle the separate spectral distributions of the component stars from the composite spectrum of an eclipsing binary system have been developed by [6] and [7].

3.4. Polarimetry

The sources of polarization in interacting binaries are: scattering of starlight by interstellar dust; light of one component scattered at the surface of the other; starlight scattered by a circumstellar disk, stream, or other locus of concentrated gas; thermal bremsstrahlung in the stellar environment, (electron scattering in gas flows or in coronae); nonthermal bremsstrahlung (from flares); electron scattering in high-temperature atmospheres, and magnetic surface fields. Although polarimetric observations are very important for the study of close binaries, there are

several reasons for lack of adequate polarimetric studies. Hopefully, future investigators will pay this important field more attention and closer collaboration between model developers and observers of polarimetric data would also improve the situation.

A combination of the above observations yields the fundamental source of information about *sizes, masses, luminosities and distances or parallaxes* of stars. This information provides the means to test stellar structure and stellar evolution theories, to improve our understanding of such exotic objects as X-ray binaries, novae and Wolf-Rayet stars, to get a great wealth of knowledge from binaries in globular clusters and to solve astrophysical problems (Algol paradox, convection in stars, mass transfer and mass loss, gas streams and discs around stars, physical processes in stars, etc.).

4. Observations from Space. The GAIA mission

The GAIA mission is one of the next two "cornerstones" of ESA's science program [13]. The objectives of the GAIA mission are to build a catalogue of ~10^9 stars with accurate positions, parallaxes, proper motions, magnitudes and radial velocities. The catalogue will be complete up to $V = 20$ mag. The overall mission contain three parts: (1) extremely precise astrometry, (in the micro-arcsec regime) with the measurement of stellar position, parallax and proper motion; (2) photometry, with measurements in different spectral bands; (3) radial velocity measurements up to $V = 17$ mag.

4.1. GAIA's contribution to the study of Close Eclipsing Binaries

The GAIA large-scale photometric survey will have significant intrinsic scientific value for the study of variable stars of nearly all types, including detached eclipsing binaries, near contact or contact binaries and pulsating stars. The strength of the GAIA mission is in the numbers. GAIA will observe ~ 4×10^5 eclipsing binaries brighter than V =15 and ~ 10^5 of these will be double-lined systems. The observing fashion is quite similar to Hipparcos operational mode. Even if the stellar parameters will be determined at 1% accuracy for only 1% of them, this is still 25-times more than what has been obtained from all ground-based observations in the past [1].

4.2. Measurement Performances
• Catalogue: ~1 billion stars; 0.34×10^6 to V=10 mag; 26×10^6
   to V=15 mag; 250×10^6 to V=18 mag; 1000×10^6 to V=20 mag

• Median parallax errors: 4 μas at 10 mag; 11 μas at 15 mag;
  160 μas at 20 mag
• Distance accuracies: 2 million better than 1%; 50 million better
  than 2%; 110 million better than 5%; 220 million better than 10%
• Tangential velocity accuracies: 40 million better than 0.5 km s^{-1};
  80 million better than 1 km s^{-1}; 200 million better than 3 km s^{-1};
  300 million better than 5 km s^{-1}; 400 million better than 10 km s^{-1}
• Radial velocity accuracies: 1-10 km s^{-1} to V=16 - 17 mag.
• Photometry : to V=20 mag in 4 broad and 11 medium bands

4.3. Accuracy of fundamental parameters

GAIA will provide light curves for millions of faint eclipsing binaries and also the absolute luminosities and temperatures (from parallaxes and colours). These data, combined with the radial velocity measurements obtained from spectroscopic observations, will allow us to determine the fundamental parameters *(radii, masses, luminosities, temperatures)* of hundred thousands eclipsing systems. Although the expected accuracy will be moderate, the large amount of data will allow us to look for large deviations from the "normal" mass-radius-luminosity relations.

As mentioned above the number of Close Eclipsing Binaries discovered by GAIA will reach hundred thousands. Combined astrometric, photometric and spectroscopic observations of these systems will be reduced and analyzed by suitable codes in order reliable orbital and physical parameters are determined. There are two crucial questions regarding the reliability of the derived stellar parameters from GAIA observations:

(1) How these observations can be compared with the state-of-the-art ground-based observations?
(2) What is the accuracy to which Close Eclipsing Binaries can be investigated using GAIA data alone?

From an analysis of spectroscopic and photometric observations for a small sample of eclipsing systems, obtained by GAIA-like ground-based observing campaign (for spectroscopy) and by GAIA-like Hipparcos photometry, it was shown [10], [12], [14], [15], [16] that the orbital elements and the fundamental parameters of these systems can be determined at ~ 2% accuracy level. By no means this will have an immense impact on theories of stellar structure and evolution.

5. Prospects and expectations

- Thousands of new candidates CBs have been discovered through surveys looking for micro-lensing events, like the MACHO project, EROS, OGLE and others in very crowded fields.
- The number of observed light curves will continue to exceed the number analyzed (use of CCDs etc.) and their quality is expected to improve
- GAIA mission will observe about 1 million different EBs.
- For the future, new approaches will also be possible with highly efficient photometric searches looking for very shallow eclipses, such as those produced by Earth-like extra-solar planets.
- Space missions with the required photometric precision are currently under development in Europe and USA. The eclipses are expected to be 10^{-4} or less in depth, so that normal or even marginal stellar eclipses will be very easy to detect.
- New techniques of analyzing data should be invented and new programs to treat phenomena of extended atmospheres, semi-transparent atmospheric clouds, variable thickness disks, and gas streams should be developed.

Close binary analysis is a formidable astrophysical task. The field includes radiation physics and sometimes hydrodynamics. Physical models are required for radiation transport in the component's atmospheres and for the dynamic forces controlling the stellar mass distribution. Close binary research might initiate projects involving complicated physics and requiring sophisticated mathematics and numerical methods [9].

References

1. Andersen J., 1991, A&AR vol.3, No 2, p. 91
2. McLean B.J., 1981, MNRAS 195, 931
3. Hill G., 1982, The reduction of Spectra-IV: VCROSS, an Interactive Cross-Correlation Velocity Program, Publ. Dom. Astrophys. Obs. 16, 59
4. Hill G., Fisher W.A., Poeckert R., 1982, The reduction of Spectra-III: REDUCE, an Interactive Spectrophotometric Program, Publ. Dom. Astrophys. Obs. 16, 43-58
5. Rucinski S.M., 1992, AJ 104, 1968
6. Simon K.P. and Sturm E., 1994, A&A 281, 286
7. Hadrava P., 1995, A&AS 114, 393
8. Rucinski S.M., 1999, "Precise Stellar Radial Velocities", ASP Conf. Ser. Vol. 185, eds. J.B. Hearnshaw & C.D. Scarf, p. 82
9. Kallrath J., Milone E.F., 1999, Eclipsing Binary Stars, Springer, New York
10. Munari U., Tomov T., Zwitter T., Milone E.F., Kallrath J., Marrese P.M., Boschi F., Prsa A., Tomasella L., Moro D., 2001, A&A 378, 477
11. Rucinski S.M., 2002, AJ 124, 174
12. Niarchos P. and Manimanis V., 2003, A&A 405, 263
13. Pace O., 2003, in "GAIA Spectroscopy, Science and Technology", U. Munari ed., ASP Conf. Ser. 298, p. 13
14. Zwitter T., 2003, in "GAIA Spectroscopy, Science and Technology", U. Munari ed., ASP Conf. Ser. 298, p. 329
15. Zwitter T., Munari, U., Marrese, P. M., Prsa, A., Milone, E. F., Boschi, F., Tomov, T., Siviero, A., 2003, A&A, 404, 333
16. Marrese, P. M., Munari, U., Siviero, A., Milone, E. F., Zwitter, T., Tomov, T., Boschi, F., Boeche, C., 2004, A&A 413, 635

THE FLARE ACTIVITY OF YZ CMI IN 1999 – 2004

D. P. Dimitrov, K. P. Panov

Institute of Astronomy, BAS

YZ CMi is a spotted flare star dM4.5e/M4.5 at a distance of 5.9pc (4). Flares on YZ CMi have been detected in the optical, radio and X-ray wavebands. Chugainov (1) and Pettersen et al. (3) determined the photometric period from spot light curves, which is ~ 2.77 days. It is generally assumed that light variations of the quiescent star are due to rotational modulation of spotted star i.e. the 2.77 days period is the period of rotation.

YZ CMi was a part of a flare star monitoring program at the Rozhen National Astronomical Observatory, using the 60cm telescope and the UBV photon-counting, computer controlled photometer. The monitoring was carried out in the U band with 1s integration (73.72 hours) and with 0.1s integration (2.90 hours). In Table 1., data are presented for each year 1999 – 2004. Altogether, 97 flares have been recorded in 76.620 hours of monitoring.

Table 1

Year	T [hours]	Flares
1999	7.825	5
2000	1.764	2
2001	2.403	3
2002	6.223	12
2003	36.689	49
2004	21.716	26
Total:	**76.62**	**97**

Fig 1 shows some of the flares observed, where the flare amplitude is:

$$\frac{I_f}{I_0} = \frac{I_{0+f} - I_0}{I_0}$$

The flare energies in the U-band were obtained by the relation:

214
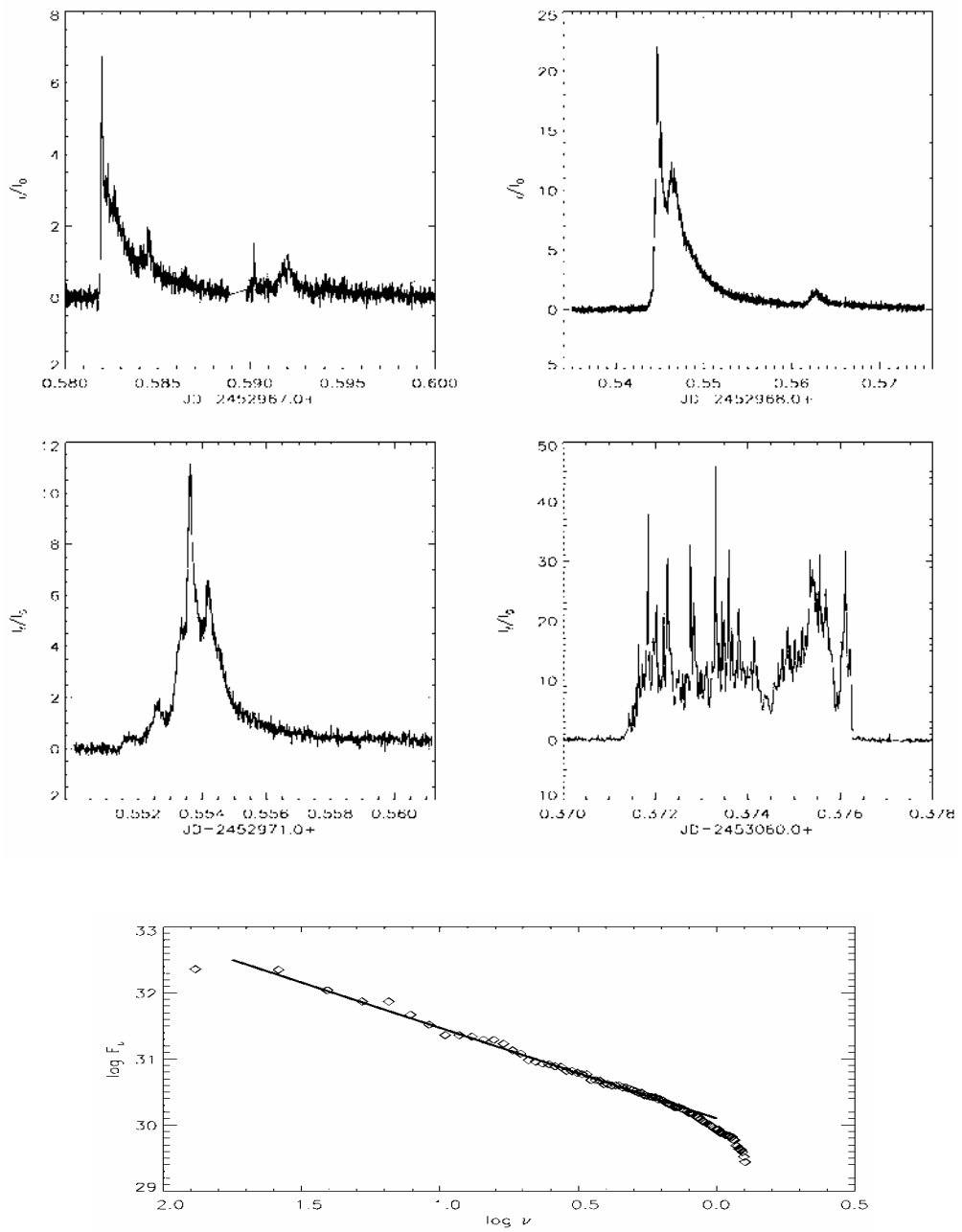
Fig 1. Light curves in the U-band of some large YZ CMi flares.

$$\log E_f = \log ED + \log E_q^U$$

and:

$$ED = \int\limits_{flare} \frac{I_f(t)}{I_0} dt$$

$$E_a^U$$
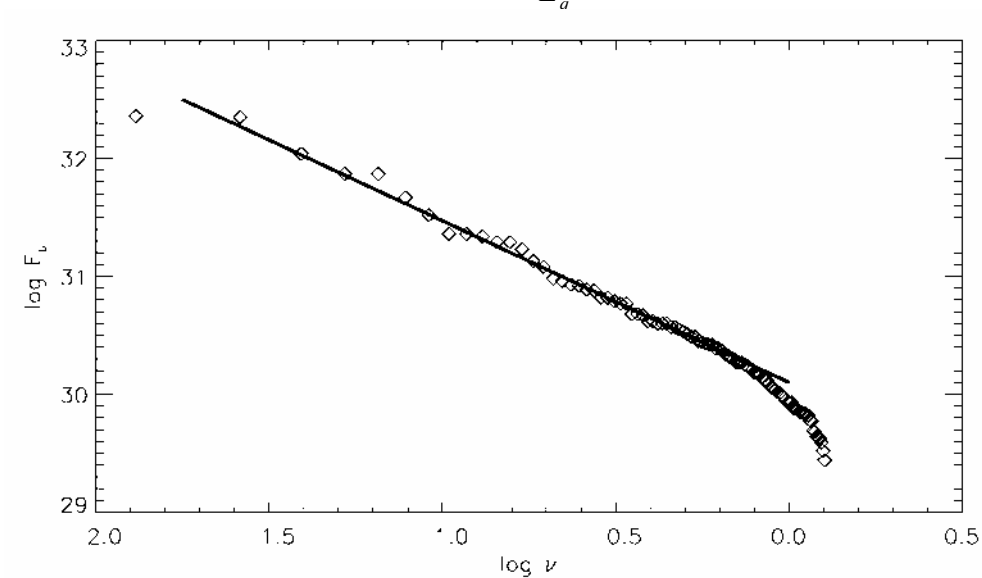
Fig 2. Cumulative flare energy distribution of YZ CMi for the sample in Table 1.

is the equivalent flare duration. The is the quiescent star luminosity of YZ CMi,

$$E_q^U = 4.11x10^{28} ergs.s^{-1} \qquad \text{Panov et al. (5)}$$

The shape of the flare JD = 2453060.374 is very unusual, showing many spikes superposed on a ~7.2 min flare.

216

Gershberg and Shakhovskaya (2) showed that the flare activity is described with a relation:

$$\log \nu = a - b.\log E_U$$

where $\nu = N/T$ is the cumulative flare frequency, E_U is the flare energy in the U band, and $\boldsymbol{a}$ and $\boldsymbol{b}$ are constants. From our flare sample we get:

$$(1) \qquad \log \nu = 22.1 - 0.73 \log E_U$$

The mean frequency of flaring from our sample is:

$$(2) \qquad \frac{N}{T} \pm \frac{\sqrt{N}}{T} = 0.78 \pm 0.10$$

Comparing our values from (1) and (2) with the respective values from Gershberg and Shakhovskaya (2), we find statistically significant agreement. Thus, we find no evidence for a variability of the flare activity of YZ CMi, over the time – period 1972 - 2003

References:
1. Chugainov P., Izv. Krymskoi Astrofiz. Obs. **52**, 1974, 3
2. Gershberg R., N. Shakhovskaya, ApSS **95**, 1983, 235
3. Pettersen B., G. Kern, D. Evans, A&A **123**, 1983, 184
4. Gershberg R., M. Katsova, M. Lovkaya, A. Terebizh, N. Shakhovskaya, A&AS **139**, 1999, 555
5. Panov K., Yu. Goranova, V. Genkov, 2000, IBVS No **4917**

LONG-TERM PHOTOMETRIC INVESTIGATION
OF FK COM

D. P. Dimitrov, K. P. Panov

Institute of Astronomy, BAS

FK Com is the prototype of a small group of G-K stars, which evolutionary status is not yet clear. FK Com is a G2III to G7III star, apparently a single giant with extremely rapid rotation, *vsini*=162.5 km/s (10). This star exhibits strong chromospheric activity, similar to the chromospheric activity of the RS CVn stars. Strong emission has been observed in H_α and *CaII H+K* lines (3, 4). The H_α emission is variable (12). Chromospheric flares have been observed in H_α (6, 17) and in broad band filters. FK Com exhibits also light variations, due to photospheric spot activity. Chugainov (1) was the first to report photometric variability, which he attributed to rotational modulation by photospheric spots. Chugainov (1) also determined the photometric period, P $= 2^d.412$, which is the period of rotation. FK Com has been detected also with ROSAT in the X-rays by Welty and Ramsey (14) and in the radio (8, 7). It is generally believed that the strong activity of FK Com is due to its rapid rotation. However, the rapid rotation is a real problem, considering the evolutionary status of the star.

Two hypotheses have been proposed, to explain the rapid rotation of FK Com. According to Walter and Basri (5), FK Com is accreting material from a small and unseen companion. The second hypothesis suggests that FK Com is a relic of a coalesced close binary star (2). Attempts to reveal the unseen companion, however, failed (10).

There is an intense photometric record of FK Com, with contributions by many authors. The light curve shows a variable amplitude and shape, on a time-scale of months. From a long-term photometric study Jetsu et al (11, 13) determined an averaged photometric period, P $= 2^d.4002466$. They also showed that the spot distribution is consistent with the existence of two long-lived active longitudes on the photosphere, which are apart by 180°. Jetsu et al (11) proposed that the active longitudes on FK Com are alternately activated, i.e. a

"flip-flop". The essential question with the "flip-flop" is how the change of the light curve is achieved. One possibility is that spots do not essentially move on the photosphere and the growth at one active longitude is related to the decay of the spot at the opposite longitude. The second possibility is the assumption of latitudinal drift and differential rotation (9).

Doppler imaging is powerful method to reveal the surface inhomogeneities. In a series of papers, Korhonen et al (16, 18, 19, 20), using Doppler imaging, studied FK Com and reached contradictory results: solid body rotation or differential rotation.

FK Com has been studied photometrically with the 60cm telescope of the National Astronomical Observatory Rozhen during the past 18 years. Fig 1 shows the light curves of FK Com in the V-band in 2000-2004. Fig 2 shows the light variation of FK Com during the past 25 years. Observations were taken from the literature and our own data, obtained in Rozhen. The dispersion of data in each observing season depicts the real amplitude of variation during that season (min to max variation). All light curves are constructed with the ephemeris:

$$\text{HJD} = 2439252.895 + 2^{d}.4002466 \text{xE} \qquad \text{Jetsu et al., (11)}$$

The search for periods with the long-term data set (Fig 2) revealed no definitive periodicities. It is, however, quite obvious that a long-term variation in the light of FK Com is real: in the min light, in the max light and in the amplitude of rotational modulation. In Fig 3, we plotted the phase of min light for the different observing seasons versus the year. Each point on that figure depicts the position of the light curve (76 different light curves altogether) on the phase diagram. It is interesting to note that the first part of the diagram shows three jumps (1982 – 1992) in the phase of min light, i.e. the "flip-flop". After 1994 the diagram is much more complex, showing evidence of both the "flip-flop" as well as phases between 0.5 and 1.0. Intermediate phases between 0.5 and 1.0 may be due to a real latitudinal drift of the spots, between the positions of the two active longitudes. A differential rotation, corresponding to that latitudinal drift could be the cause of the drift in phase in Fig 3. Assuming that interpretation of Fig 3, we could determine the range of variation of the photometric period, which is: $P_{min}=2^{d}.397071$ and $P_{max}=2^{d}.404288$. Thus as an estimate of the differential rotation from Fig 3 we have $\Delta P/P = 0.003$. This is
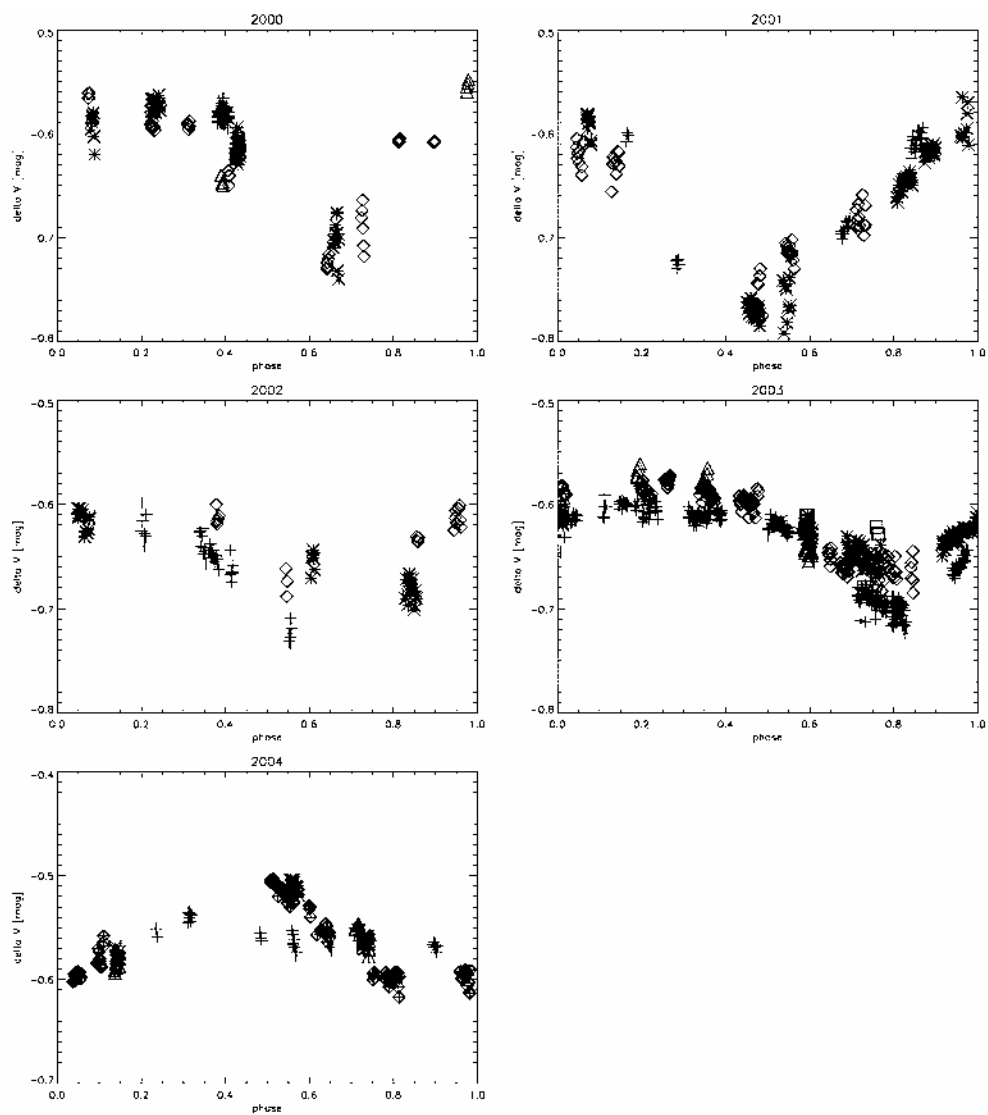
Fig 1. Light curves of FK Com in the V band. With different signs are denoted parts of the light curve from different months. The magnitude difference is:

much smaller in comparison with the respective value for the Sun (~0.2). Our estimate of the differential rotation of FK Com is different from the value
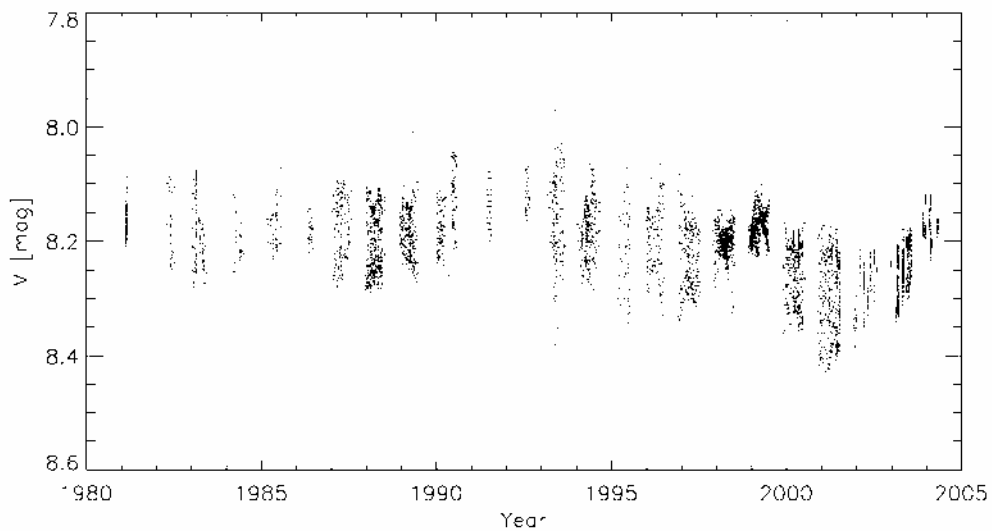
Fig 2. The long-term photometric variations of FK Com. The spread of data for each season denotes min to max variation of the rotational modulation

obtained by Korhonen et al. (20) but is similar to reported values for other BY Dra and RS CVn stars.

Fig 3 shows quite clearly periodicity in the "flip-flop", reported also by Korhonen et al (19). The analyses of data on Fig 3 with the PERIOD98 Program of the Wien University (15) reveals a cycle of 5.9 years. It means that it takes about 3 years to "switch-over" from one active longitude to the other one. In the period 1998-2000, our Fig 3 shows also light curves, which do not follow the general trend of the "flipping" (marked by crosses). The reason for these deviations is not yet clear and needs further investigation. Similar "flipping" of active longitudes has been observed also in other stars (RS CVn) and still needs a theoretical explanation.
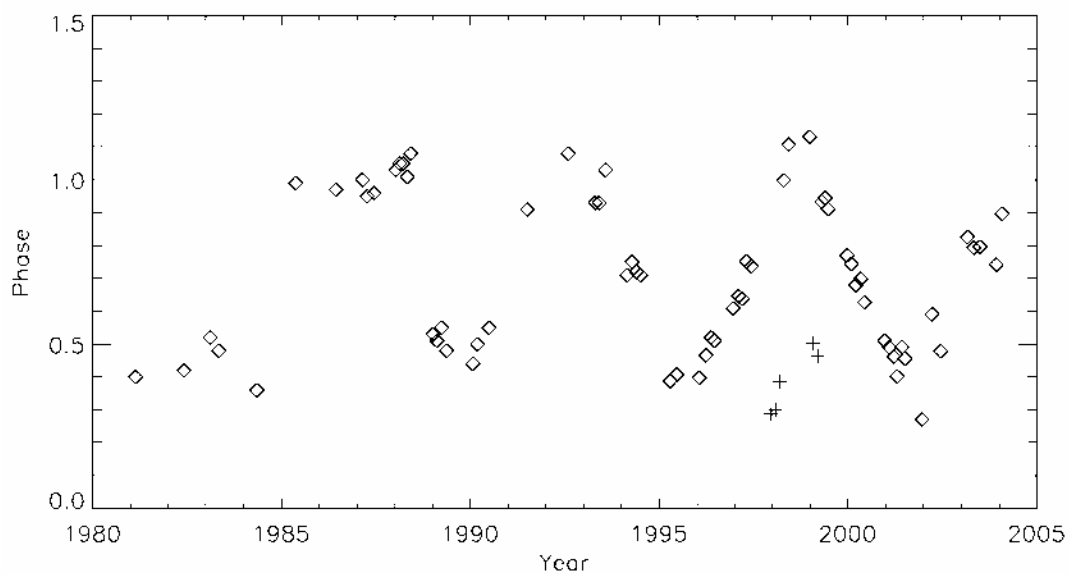
Fig 3. The phases of FK Com min light over the time: 1980 - 2004

References:

1. Chugainov, P., 1966,IBVS No **172**
2. Bopp B., S. Rucinski, in: Fundamental Problems in the Theory of Stellar Evolution, IAU Symposium 93, Sugimoto D., Lamb D., Schramm D., (eds.), Reidel, Dordrecht, 1981, p.177
3. Bopp B., R. Stencel, ApJ **247**, 1981, L131
4. Bopp B., in Proc. Second Cambridge Workshop on Cool Stars, Stellar Systems, and the Sun, SAO Special Report No. 392, I, 1982, p. 207
5. Walter F., G. Basri, ApJ **260**, 1982, 735
6. Dorren J., E. Guinan, G. McCook, PASP **96**, 1984, 250
7. Hughes V., B. McLean, ApJ **313**, 1987, 263
8. Rucinski S., AJ **101**, 1991, 2199
9. Panov K., A. Antov, in Lecture Notes in Physics, **397**, 1992, p.322
10. Huenemoerder D., L. Ramsey, D. Buzasi, L. Nations, ApJ **404**, 1993, 316
11. Jetsu L., J. Petl, I. Tuominen, A&A **278**, 1993, 449
12. Welty A., L. Ramsey, M. Iyengar, H. Nations, D. Buzasi, PASP **105**, 1993, 142

13. Jetsu L., I. Tuominen, A. Antov, B. Bopp, P. Chugainov, K. Grankin, S. Linnaluoto, S. Melnikov, L. Nations, K. Panov, V. Shevchenko, A&ASS **103**, 1994, 183
14. Welty A., L. Ramsey, AJ **108**, 1994, 299
15. Sperl, M., Comm. In Asteroseismology **111**, 1998, 1
16. Korhonen H., S. Berdyugina, T. Hackman, R. Duemmler, I. Ilyin, I. Tuominen, A&A **346**, 1999, 101
17. Oliveira J., B. Foing, A&A **343**, 1999, 213
18. Korhonen H., S. Berdyugina, T. Hackman, K. Strassmeier, I. Tuominen, A&A **360**, 2000, 1067
19. Korhonen H., S. Berdyugina, I. Tuominen, M. Andersen, J. Piironen, K. Strassmeier, K. Grankin, S. Kaasalainen, H. Karttunen, S. Melnikov, V. Shevchenko, M. Trisoglio, J. Virtanen, A&A **374**, 2001, 1049
20. Korhonen H., S. Berdyugina, I. Tuominen, A&A **390**, 2002, 179

BIFURCATION SOLUTIONS OF VORTICAL TRANSPORT EQUATION PARAMETERS, AS A MECHANISM OF DETECTING AN INSTABILITY IN THE ACCRETION DISCS

Andreeva Daniela[1], Filipov Lachezar[2]

[1,2]*Space Research Institute, BAS, Sofia, Bulgaria*
[1]danvasan@space.bas.bg; [2]lfilipov@space.bas.bg

Abstract

The vortices play a very important role for the existence of accretion discs. Usually they arise under the influence of different kind of instabilities. One basic equation that describes these processes is the reaction-diffusion equation and its prototype in our case – vortical transport equation. Here using the bifurcation analyses of the presented equation we receive some bifurcation solutions, which are the mechanism of the vortical formations, locally in the accretion discs.

Introduction

The vortical equation received from consecutive transformations of the basic hydro-dynamical equations is our analog of the reaction-diffusion type equation for the accretion discs. The equation, which we received [1], has some difference in the expression from the well known vortical equation [4].

It is follows from the fact that we represent the reaction-diffusion equation with quantities, describing the accretion disc. We consider the terms and processing in thin non-axisymetrical accretion discs.

In this paper we will turn our view on the ruling parameter, which variation and extremum are the reason for the arising of instability. We have to determine here this parameter for the vortical transport equation and find the bifurcation solution for the different kind of bifurcation.

The bifurcation changes the qualitative behavior of the system, when the parameter of the system reached its critical value [5], which is known as a bifurcation point. Passing trough this point, the system turns from stable state to unstable state or to another stable situation.

For most cases, the analytical and numerical results show [3] that the locations of fixed points are determined by the parameters and these fixed points are either structurally stable or unstable.

Analyses and results

I. Bifurcations and amplitude equations.

It is used in the bifurcation analyses a specifically quantities and non-linear equations. We mentioned above for the critical value of the control parameter of the system. We denote it here with λ_c, which is in fact a bifurcation point. When the given system passed trough this bifurcation point, it may lose its stability and there are conditions to forming structures in these places. The obtaining results have to be of global character, but they have an effect of local behavior.

When we talk about bifurcation, we have to specify that there are exist a different kind of its evince. The essence of different kind of bifurcation is defined from relevant amplitude equation. We present in this section amplitude equations of basic type of bifurcations.

1. Transcritical bifurcation:

$$\frac{dw}{dt} = (\lambda - \lambda_c)Q_1 w - Q_2 w^2 \qquad \text{There are two fixed points and the solution}$$

is:

$$w_{S0} = 0, w_{S1} = (\lambda - \lambda_c)\frac{Q_1}{Q_2}$$

2. Pitchfork bifurcation:

$$\frac{dw}{dt} = (\lambda - \lambda_c)Q_1 w - Q_3 w^2 \qquad \text{The fixed points in this case are three:}$$

$$w_{S0} = 0, w_{S1} = \pm[(\lambda - \lambda_c)\frac{Q_1}{Q_3}]^{\frac{1}{2}}$$

3. Hoph bifurcation:

$$\frac{dw}{dt} = (\lambda - \lambda_c)Q_1 w - Q_3 |w|^2 w$$

Here the coefficients Q_1 and Q_3 are complex quantities and they are expressed as:

$Q_1 = Q'_1 + iQ''_1$ and $Q_3 = Q'_3 + iQ''_3$

The Hoph bifurcation has a periodically character. We have to introduce here for the amplitude w polar coordinates, so: $w = qe^{i\phi}$

Because of this we receive the solutions for q and they are in the form:

$$q_{S0} = 0, q_{S1} = \pm\left[\frac{(\lambda - \lambda_c Q'_1)}{Q'_3}\right]^{1/2}$$

The basic denotations in this section:

λ - the control parameter;

λ_c - the critical value of the control parameter;

Q_1, Q_2, Q_3 - the numerical coefficients, determined entirely by the structured of the initial equations and solutions;

II. Basic equations, vortical transport equation.

In our examination for the accretion discs we have to determine the coefficients Q_1, Q_2, Q_3 from the solution of the next system of equations. These are the basic equations being in the studying of the accretion discs dynamics.

1. The first equation is the well known from the hydrodynamics continuity equation:

(5) $\dfrac{\partial \rho}{\partial t} + \nabla.(\rho v) = 0$

2. The second two equations present the development of the Navier-Stokes equation in cylindrical coordinates in the terms of r, φ:

(6)
$$\frac{\partial v_\varphi}{\partial t} + v_r \frac{\partial v_\varphi}{\partial r} + \frac{v_\varphi}{r} \frac{\partial v_\varphi}{\partial \varphi} - \frac{v_r v_\varphi}{r} = -\frac{1}{\rho r} \frac{\partial P}{\partial \varphi} + \frac{1}{\rho} F_\varphi +$$
$$\nu \left(\frac{\partial^2 v_\varphi}{\partial r^2} + \frac{1}{r^2} \frac{\partial^2 v_\varphi}{\partial \varphi^2} + \frac{1}{r} \frac{\partial v_\varphi}{\partial r} - \frac{2}{r^2} \frac{\partial v_r}{\partial \varphi} - \frac{v_\varphi}{r^2} \right)$$

Where $F_\varphi = \frac{1}{2} \left(\Omega \times r \right)^2$

(7)
$$\frac{\partial v_r}{\partial t} + v_r \frac{\partial v_r}{\partial r} + \frac{v_\varphi}{r} \frac{\partial v_r}{\partial \varphi} - \frac{v_\varphi^2}{r} = -\frac{1}{\rho} \frac{\partial P}{\partial r} + \frac{1}{\rho} F_r +$$
$$\nu \left(\frac{\partial^2 v_r}{\partial r^2} + \frac{1}{r^2} \frac{\partial^2 v_r}{\partial \varphi^2} + \frac{1}{r} \frac{\partial v_r}{\partial r} - \frac{2}{r^2} \frac{\partial v_\varphi}{\partial \varphi} - \frac{v_r}{r^2} \right)$$

Where $F_r = \frac{1}{2} \left(\Omega \times r \right)^2 + G \frac{m_1 m_2}{r_1 + r_2}$

3. The energy conservation equation here is in the form:

(8) $\frac{\partial}{\partial t} \left(\frac{1}{2} \rho v^2 + \rho \varepsilon + \rho g z \right) + div \left[\left(\frac{1}{2} \rho v^2 + \rho \varepsilon + P \right) v \right] = 0$

where $\frac{1}{2} \rho v^2$ - the kinetic energy per unit volume,

$\rho \varepsilon$ - is the internal or thermal energy per unit volume.

$\rho g z$ - is the potential energy / z is the unit vector over z-direction /

4. We represent here our view of vortical transport equation, which is in fact a vortical evolution law. We obtain this equation after taking the curl of Navier-Stokes equation and some transformations of the reaction-diffusion equation.

227

$$(9) \quad \frac{\partial \Psi}{\partial t} = (\nabla . v_r) \Psi_r - (\nabla . \Psi_\varphi) v_\varphi + \frac{D_r}{D_\varphi} \nabla^2 \Psi$$

5. Because of the important role of angular momentum in the accretion discs, the next equation presents it the form:

$$(10) \quad \frac{\partial}{\partial t}(\rho r v_\varphi) + \nabla . r \rho v_\varphi + \nabla . r P - \nabla . \left[\frac{1}{3} r v (\nabla . v) + v r^2 \nabla \frac{v_\varphi}{r} \right] = 0$$

Where the denotations for all equations are:

ρ - is the mass density of the flow;

v - is the velocity of the flow / over r and φ direction /;

P - is the pressure;

Ψ - is the vorticity / over r and φ direction /;

r - is the radius of the disc;

D - is the diffusion coefficient (or matrix of the transport coefficient);

III. A graphical view of the bifurcation solutions.

After receiving the solutions for Ψ, D, v, r we use them to express the bifurcation equations in the term of the above equations. We show here the graphical view of the new form of these equations:
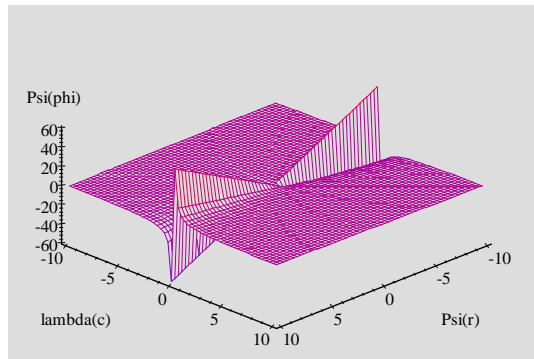
Figure 1. Graphical solutions of the transcritical bifurcation.
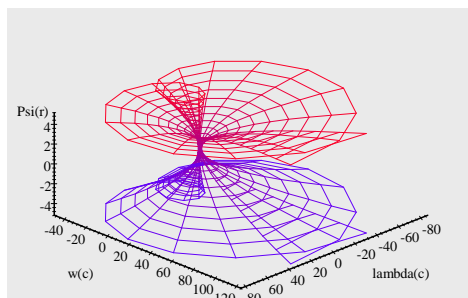
Figure 2. A graphical view of the pitchfork bifurcation solutions
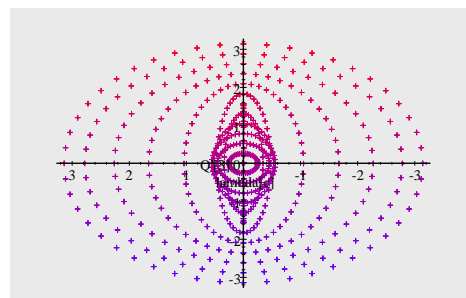
Figure 3. Graphical solutions of the Hoph bifurcation.

Conclusion

We presented here the behavior of bifurcation control parameter in the terms and solutions of the basic hydrodynamical equations and vortical transport equation, ruling the accretion disc flow. We showed the graphical view of this parameter for the three types of bifurcation. It is important to note that in the places where the bifurcation acts, there are conditions for arising of instability. This instability may give rise to structure formations, locally in accretion disc. Such structures, as vortical formations play an important role in the angular momentum transfer.

R e f e r e n c e s:

1. A n d r e e v a D. V., F i l i p o v L. G., D i m i t r o v a M. M., 2002, Turing formations in accretion disc - as a reaction-diffusion system, Publ.Astron.Obs.Belgrade, **73**, 67-71

2. B o r c k m a n s P., D e w e l G., W i t A. De., W a l g r a e f D., 2001, Turing bifurcations and Pattern selection, submitted in *Chemical Waves and Patterns*

3. C h a n, H.S.Y., C h u n g, K.W., D o n g w e n, Qi, 2001, Some bifurcation diagrams for limit cycles of Quadratic differential systems, Int. J. Bifurcation and Chaos 11, 197-206.

4. D e b n a t h L., Nonlinear Water Waves, 1994, Acad. Press, Dept of Math, UCFl

5. N i c o l i s G., 1994, Introduction to nonlinear Science, Brussels

MASS-LOSS AND WIND MOMENTUM RATES OF HOT LUMINOUS STARS.
THE EFFECTS OF WIND CLUMPING AND VARIABILITY IN GALACTIC O-TYPE STARS.

Markova, Nevena [1], Markov, Haralambi [2]

1) Institute of Astronomy, Bulgarian Academy of Sciences
2) Institute of Astronomy, Bulgarian Academy of Sciences

1. Introduction

About six years ago a project to study wind variability of hot massive stars (HMS) in our Galaxy and in the Local group was initiated at the National Astronomical Observatory (NAO) of the Bulgarian Academy of Sciences. Almost since the onset of our investigation we have collaborated with Dr. Puls (University of Munich, Germany) and Dr. Scuderi (Catania Obs., Italy). In this talk I'm going to present results derived trough our HMS project and in particular those which refer to Galactic O-type stars.

Why is it important to study massive stars? First of all because these stars are the main engines of the cosmic evolution. In the present cosmos, they provide most of the metals and the energy. In the distant Universe they dominate the UV light from the young galaxies. The very first generation of these objects (very massive stars, Population III) might have been responsible for the re-ionization of the early Universe. At the endpoint of their evolution, massive stars suffer a gravitational collapse and explode as supernova (of type II or Ib,c). Eventually a Gamma-Ray-Burst emerges, the most energetic cosmic flash. Thus our knowledge about massive stars and their evolution is crucial for our understanding of the Universe as a whole.

On the other hand, studies of HOT massive stars (HMS) are particularly important because they may provide a unique opportunity to derive distances from purely spectroscopic tools. Indeed, the radiation driven wind theory

predicts a simple relation between the "modified wind-momentum rate", $\mathbf{D_{mom}}$ $= \boldsymbol{M}_{\mathbf{dot}} \; \boldsymbol{V}_{\mathbf{inf}} \boldsymbol{R}_{\mathbf{star}}{}^{\mathbf{0.5}}$, and the stellar luminosity, L, in the form :

$$\log \mathbf{D_{mom}} \; = \log \mathbf{D_0} \; + 1/\alpha \; (\log \boldsymbol{L/L_{\odot}})$$

where $\boldsymbol{M}_{\mathbf{dot}}$, $\mathbf{V_{inf}}$ and $\boldsymbol{R}_{\mathbf{star}}$, are mass-loss rate, wind terminal velocity and stellar radius, respectively, and α is the power law exponent of the line strength distribution function. This relation is known as the Wind-momentum Luminosity Relationship (WLR) [1]. If properly calibrated - the coefficients of the WLR are expected to vary with spectral type and metallicity - the WLR can give very accurate distances (within 10%) out to the Virgo and Fornax clusters of galaxies [2].

2. Mass-loss rate estimates

To determine mass-loss rates the observed Hα profiles of 30 O-type stars have been fitted using the approximate method, developed by Puls et al. [3], which we modified to account for the effects of line-blocking and blanketing. Detailed information about the actual fit procedure can be found in [4] while in the following we will focus on the final results only.

a
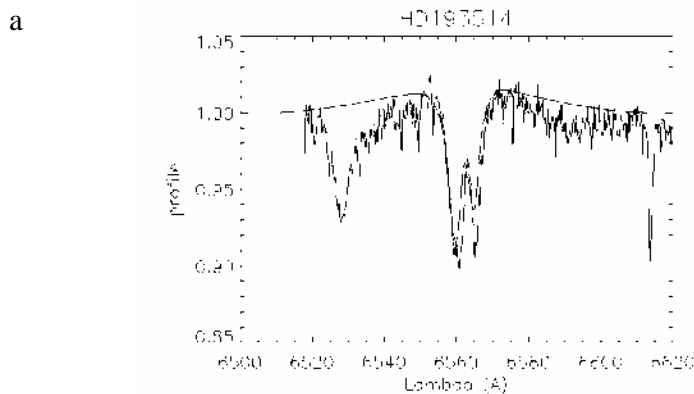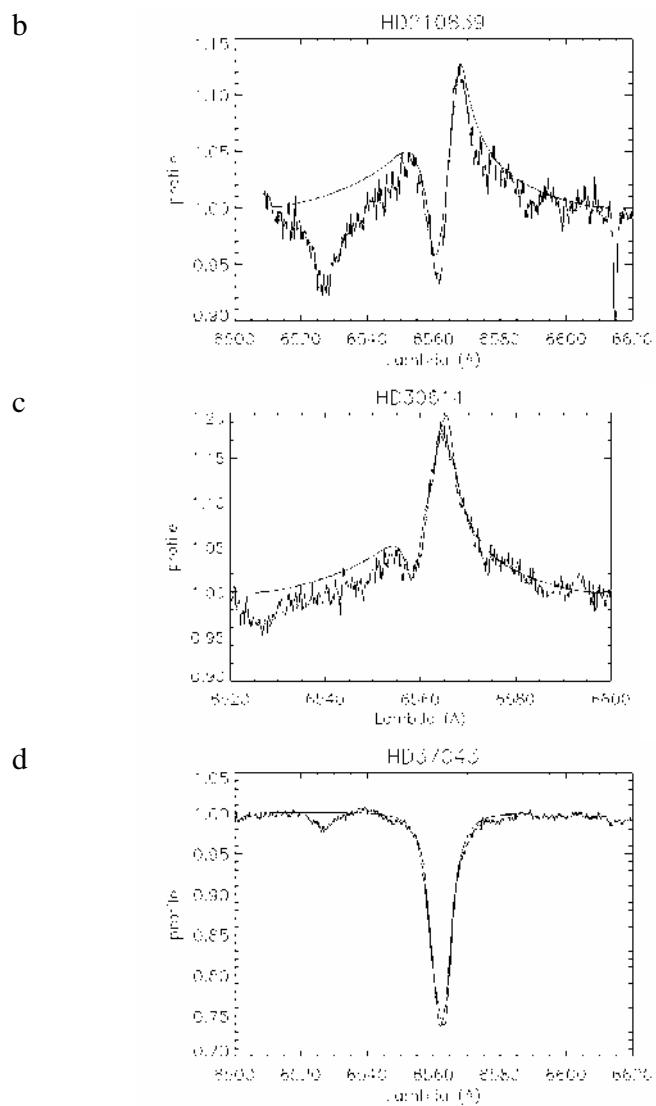
Fig. 1 Examples of differently shaped Hα profiles with the corresponding model fits.

In Fig. 1 typical examples of differently shaped Hα profiles together with the corresponding model fits are shown. Evidently, the agreement between observations and theoretical calculations is quite good and in particular does not depend on the strength of the wind. This finding however is somewhat leading away because and if mass-loss rate determinations, M_{dot}, are to be concerned one would find estimates of different accuracy for profiles in absorption (weaker winds) and in emission (stronger winds). The later result can be easily understood if one takes into account that in case of profiles in absorption the velocity exponent β cannot be constrained from the corresponding fit and thus makes M_{dot} more uncertain [3,4].

3. Wind-momentum Luminosity Relationship for Galactic O-type stars

Having mass-loss rates of the target stars already determined one can calculate the corresponding wind momenta and subsequently to derive the WLR. The WLR for Galactic O-type stars is shown on Fig. 2. In order to improve the statistics and thus, to reduce the effect of uncertain distances [see 4], in addition to our data similar data from other investigations [5, 6] have been incorporated. The results illustrated in Fig. 2 clearly indicates that the WLR for luminosity class III/V objects strictly follows the theoretical predictions (dashed line) while the relation for the supergiants shows a vertical offset corresponding to an average factor of roughly 0.25 dex. This result is strikng because it contradicts the radiation-driven theory which predicts an unique relation (for all luminosity classes) instead.
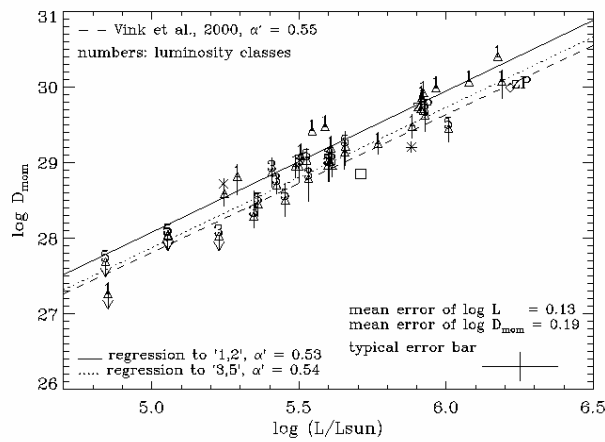
Fig. *2 WLR for Galactic O-type stars. Data from observations*.

4. WLR for Galactic O-type stars as a distant indicator.
The effects of spectral variability and wind clumping.

The possibility to use the WLR as a distant indicator is directly related to the accuracy of the derived M_{dot} estimates. There are several physical processes that may effect and significantly modify the observed mass-loss rates, of which the most important are spectral variability and wind clumping.

The uncertainty in both mass-loss and wind-momentum rates caused by wind variability turnes out to be rather insignificant [8]. This result seems somewhat astonishing, especially in those cases when drastic changes in the Hα profile shape have been observed. Note, however, that for not too low wind densities small changes in thus M_{dot} give rise to large changes both in the profile shape and the equivalent width [3]. In fig. 3 the WLR for Galactic O-supergiants are shown. Vertical lines represent the error in the wind momenta introduced by wind variability. Obviously, wind variability can only increase the local scatter without changing the concept of the WLR. This result is in full agreement with an investigation by Kudritzki [9] who reported 0.15 dex as an error in the wind momentum rates of one A-supergiant caused by wind variability.
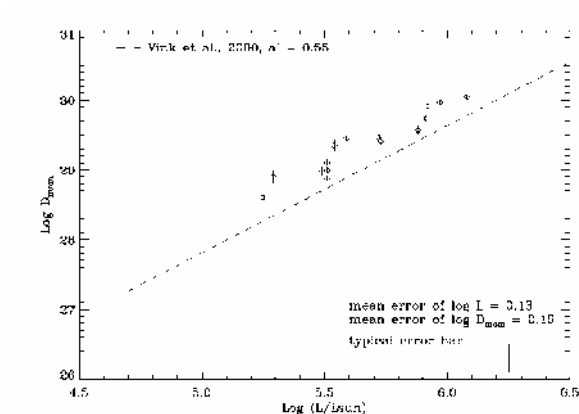
Fig. 3 WLR for Galactic O-supergiants. Vertical lines represent the error introduced by wind variability.
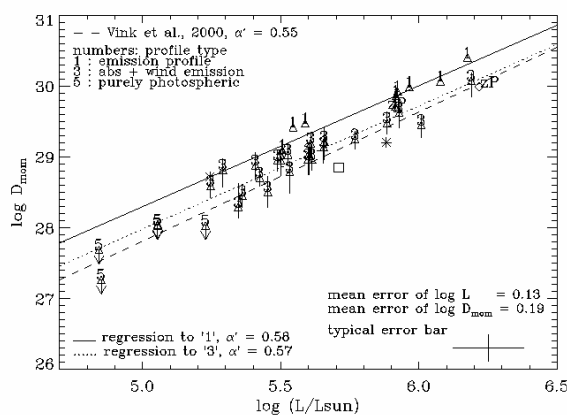
Fig. 4 WLR for Galactic O-type stars but with regression in dependence of profile type.

On the other hand, it turned out that wind clumping might be responsible for the established disagreement between observations and theory. This possibility seems to be supported by the fact that the majority of stars with higher wind momenta show Hα in emission (see Fig. 4). Indeed, it may be that in objects with Hα in emission one can 'see' the effect of wind clumping (due to the larger contributing volume) which then mimics higher mass-loss rates (and thus wind momentum) then actually present. In objects with Hα in

absorption, on the other hand, only contribution from the innermost (not clumped) wind are present and, thus M_{dot} is observed at its actual value.

5. Future perspectives

The possibility to use the WLR as an indicator of wind clumping in O-star winds is very exciting but needs to be proven independently. One way to check this possibility is to compare mass-loss rates derived from Hα, IR and radio fluxes. In case the wind is clumped and if the predictions of the hydro-dynamical simulations about the radial stratification of the clumping factor are correct – this factor is expected to be higher in

the inter-mediate part of the wind and should decrease inwards and outwards [7] - these estimates should differ significantly [4].

In order to investigate this point in detail we have started a multi-wavelength observational campaign to derived IR and radio-continuum fluxes for our Hα targets.

The observations in radio domain have been already complete and consist

of fluxes measured at 0.7, 2.0, 3.5 and 6 cm by means of VLA. Part of the targets

have been observed in the near IR domain (at JHKLM) at the Crimea Obs. While observations in the far IR domain (at 24, 70 and 160 μk) are planned for Spitzer observatory.

References
1. Kudritzki, R.-P., Lennon, D.J., Puls, J.,
"Quantitative spectroscopy of luminous blue stars in distant galaxies" Proc. of the ESO
Workshop "Science with the VLT", eds. J.R. Walsh & L.J.Danziger (Springer Verlag), 1995,
246
2 Kudritzki, R.-P., Puls, J., Lennon, D.J., et al.
"The wind-momentum luminosity relationship of galactic A- and B-supergiants"
A&A 350, 1999, 970
3 Puls, J., Kudritzki, R.-P., Herrero, A., et. al.
"O-star mass loss and wind-,o,emtum rates in the Galaxy and the megellanic Clouds.
Observations and theoretical predictions."
A&A, 305, 1996, 171

4. Markova, N., Puls, J., Repolust, T. and Markov, H., "Bright OB stars in the Galaxy.I Mass-loss and wind momentum rates of O-type stars. A pure Hα analysis accounting for line-blanketing", A&A 413, 2004, 693

5. Herrero, A., Puls, J. and Najarro, F.
"Fundamental parameters of Galactic luminous OB stars. Temperature, masses and WLR fof Cyg OB2 supergiants" A&A 396, 2002, 949

6. Repolust, T., Puls, J. and Herrero, A.
"Stellar and wind parameters of Galactic O stars. The influence of line blocking/blanketing", A&A415, 2004, 349

7. Owocki, S., Runacres, M.C. and Cohen, D.H.
"Outer wind evolution of instability-generated clumped structures in hot-star winds" in Thermal and ionization aspects of flows from hot stars: Observations and theory, eds. Lamers & Sapar, ASP Conf Ser. 204, 2002, 183

8. Markova, N.,Puls, J., Scuderi, S. and Markov, H.
"Bright OB stars in the Galaxy. II. Wind variability in O supergiants as traced by Hα"
 A&A, 2004, in press

9. Kudritski, R.-P. , "The wind momentum - luminosity relationship of blue supergoiants"
 in Proc. IAU Coll. No. 169, eds. B. Wolf, O. Stahl & A.W. Fullerton, Sprimger Verlag, 1999, p. 4

ECLIPSING BINARY SYSTEM V376 AND: OBSERVATIONS AND SOLUTIONS

A. Dumitrescu[1], M.D. Suran[1], L. Iliev[2], V. Tudose[1]

[1]*Astronomical Institute of the Romanian Academy, Bucharest*
[2]*Astronomical Institute of the Bulgarian Academy, Sophia*

Abstract:

We present ground-based photoelectric observations of the newly discovered eclipsing binary system V376 And. The observations were carried out at Bucharest Observatory (Romania) and Rozhen Observatory (Bulgaria). Six times of minima and a new ephemeris are presented. The orbital parameters of the system are determined by modeling the light curves obtained.

Introduction

V376 And is a W UMa type variable star identified as such by the Hipparcos/Tycho mission. It has a period of 0.798669 days and a magnitude oscillating between 7.683 and 8.002 [1]. The system was spectroscopically investigated in [2]. Several times of minima are given by [3] and [4]. Systematic optical observations in B and V filters have been carried out in [5] and [6].

Observations

The observations were performed in Rozhen and Bucharest with a 60/750 cm Cassegrain telescope and a 50/750 cm Cassegrain telescope, respectively, both equipped with single channel photometers. The date, place and phase coverage of observations are listed in Table 1 [6].

Table 1. Phase coverage.

Date	Observatory	Phases	Date	Observatory	Phases
11/16/2000	Rozhen	0.61-0.83	10/13/2003	Bucharest	0.08–0.28
11/17/2000	Rozhen	0.96-0.11	11/08/2003	Bucharest	0.54-0.75
09/22/2003	Bucharest	0.90-0.10	11/13/2003	Bucharest	0.85-0.06

09/23/2003	Bucharest	0.14-0.36	11/21/2003	Bucharest	0.82-0.07
09/28/2003	Bucharest	0.43-0.62	11/22/2003	Bucharest	0.23-0.36
10/10/2003	Bucharest	0.36-0.52	12/17/2003	Bucharest	0.45-0.55

Table 2. Times of minima for V376 And.

Min HJD	Error	Type	Filter	Reference
2448500.7420	0.001	I	Hp	[1]
2451510.5408	0.0014	II	R	[3]
2451510.5419	0.0010	II	V	[3]
2451510.5421	0.0008	II	B	[3]
2451644.3215	0.0028	I	spec	[2]
2451865.53952	0.00018	I	V	[5]
2452595.5273	0.0006	I	BV	[4]
2452905.42037	0.00014	I	V	[5]
2452911.41258	0.00021	II	V	[5]
2452957.33934	0.00041	I	V	[5]
2452965.31396	0.00024	I	V	[5]
2452991.28162	0.00028	II	V	[5]

The light curves show a significant O'Connell effect in both colors (Fig.2 and Fig.3). The B-V values suffer a jump around the secondary maximum in the color index-phase space (Fig.1). Unfortunately, this region was scanned only on November 16, 2000 and partially on November 8, 2003, and even though the measurements were made with different instrumentation, at this moment we can not exclude the possibility of this being an artifact of some errors in the data acquisition process. Our skepticism is also partly motivated by the results of the analysis of the light curves, which will be discussed in the next section. Further observations are planned in the attempt to settle the issue. A compilation of all times of minima available in literature are presented in Table 2. Using the whole set of primary minima a new ephemeris was obtained [6]:

$$\text{Min I} = \text{HJD } 2452905.4178 \pm 0.0030 + 0^d.798672 \pm 0.000001 \text{ E}$$
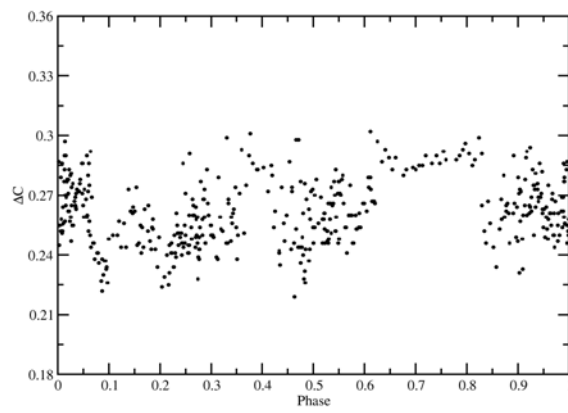
Figure 1. B-V values for V376 And.
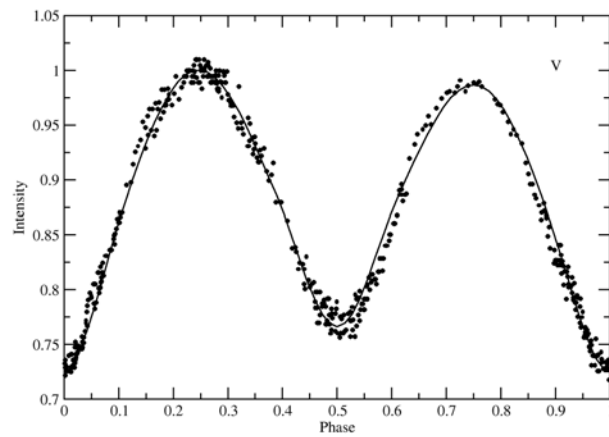
Figure 2. Normalized light curve of V376 And in filter V and the best fit model with parameters from Table 3.
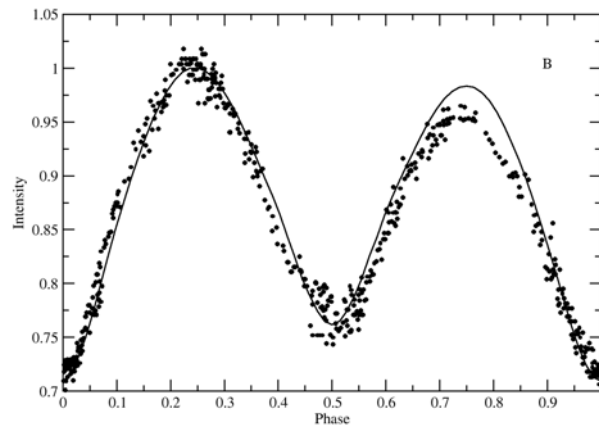
Figure 3. Normalized light curve of V376 And in filter B and the best fit model with parameters from Table 3.

Solutions

The observed intensity difference between the B and V filters can be in principle easiest explain by hypothesizing the presence of spots on the surface of stars. In particular, we took the most mathematically economic case, that is a circular (15° radius) cold spot (1000 K bellow the surface's temperature) in the plane containing the line that connects the centers of the stars ($\beta_{spot} = 0°$) on the surface of the primary component of the system.

We further assumed that the orbits are circular, the rotation axis of both stars are perpendicular on the orbital plane, the system has the property of synchronism (with the revolution counter-clockwise), the convection processes are dominant (gravity-darkening coefficient g=0.32) and the albedo A has a value of 0.5. In order to obtain the parameters of the system, a custom-made code based on the algorithm of [7] was used. Given the availability of spectroscopic observations [2] we put strong constraints on the mass ratio q=0.30 and the temperature of the primary component T_1=9600 K (using tables from [8]). The Roche lobe fill-out factor f, the orbital inclination with respect to the line of sight i, the temperature of the secondary T_2 and the longitude of the spot λ_{spot} (measured clockwise with respect to the line connecting the centers of

241

the two stars) were free parameters. Table 3 presents a summary of the best fit parameters for V filter data. The attempt to use the same parameters to overall fit the B filter data fails completely (Fig.2 and Fig.3).

Table 3. Best fit parameters for V filter data.

f	0.44 ± 0.04	T_2	8800 K
i	$65°.7 \pm 0°.5$	λ_{spot}	315°
$\Omega_1 = \Omega_2$	3.72	$\Sigma(O-C)^2$	0.00014

Discussion

Using the best fit parameters from V filter data to account for the observations in the B filter reveals reasonable compatibility in the phase range of the primary maximum, but is inconsistent with the rest half of the light curve. The reasons for this discrepancy can be divided in two categories: either, as previously mentioned, the data for the secondary maximum were somehow contaminated by yet unknown instrumental errors, or some of the assumptions employed (notably the ones related to the presence of the spot) are not correct. Further observations of this system are required.

References

[1] ESA. The Hipparcos and Tycho Catalogue, vol.12, 1997
[2] Rucinski, S. M., Lu, W., Mochnacki, S. W., Ogloza, W., Stachowski, G.. Radial velocity studies of close binary stars. V., Astron. J., 122, 2001, 1974-1980
[3] Keskin V., Yasarsoy B., Sipahi E.. Times of minima of some eclipsing binaries, Inf. Bull. Var. Stars, 4855, 2000
[4] Tanriverdi T., Kutdemir E., Elmasli A., Senavci H.V., Albayrak B., Selam S.O., Aydin C., Aksu O., Bulca I., Cinar D., Kara A., Demirhan M., Yilmaz M., Cetintas C., Gozler A.P., Karakas T., Sezgin A.S., Turhanoglu B.. Photoelectric minima of some eclipsing binary stars, Inf. Bull. Var. Stars, 5407, 2003
[5] Dumitrescu A., Iliev L., Tudose V.. New observations of variable stars, to appear in Inf. Bull. Var. Stars, 5599
[6] Dumitrescu A., Iliev L., Tudose V.. Photometric observations of the eclipsing binary V376 And, to appear in Rom. Astron. J.
[7] Djurasevic, G.. An analysis of active close binaries (CB) based on photometric measurements. I - A model of active CB with spots on the components, Astrophys. Space Sci., 196, 1991, 241-265
[8] Morton, D.C., Adams, T.F.. Effective temperatures and bolometric corrections of early-type stars, Astrophys. J., 151, 1968, 611.

ORBITAL PERIOD CHANGES OF THE ECLIPSING BINARIES *OO AQUILAE* AND *V471 TAURI*

Rovithis-Livaniou H.[(1)], Tsantilas S.[(1)], Kalimeris A.[(1)] & Rovithis P.[(2)]

(1) Section of Astrophysics, Astronomy & Mechanics, Dept. of Physics, Athens University, Panepistimiopolis, Zografos 157 84, Athens, Greece. e-mail: elivan@cc.uoa.gr

(2) Institute of Astronomy & Astrophysics, National Observatory of Athens, P.O. Box 20048, Athens 118 10, Greece. e-mail: rovithis@astro.noa.gr

Abstract

*The orbital period changes of the systems **OO Aql** and **V471 Tau** are investigated. Long variation terms –decreasing for the first and increasing for the latter system– were found. While, the detected periodic terms might not be real for both systems.*

Introduction

Continuing to study the orbital period behavior of close binaries, using the method we proposed ten years ago[1], we present here our results for the systems **OO Aql** and **V471 Tau**.

OO Aql is a rare contact binary that belongs to the *A sub-class* of the well-known *W UMa*-type group. It is a *G5 V* binary with an unusually high mass-ratio, ($q = 0.843$).

V471 Tau is an eclipsing binary consisting of a *white dwarf* (of T≈35000K and R≈7000Km), and a *cool K2V* star (of T≈4900K and R≈520000Km). Moreover, its membership to the Hyades cluster[2], makes it very important to study various problems of stellar astrophysics.

2. Orbital Period Study of *OO Aquilae*

Using all times of minimum light of **OO** Aql, its (O-C) diagram was constructed based on the linear light elements[3]:

$$\text{Min I} = 2438239.664 + 0.5067887 \cdot E$$

Then, following the first continuous method[1], we found that this diagram can be best described by a fifth order polynomial, (Fig. 1), the

coefficients of which are given at Table I. Then, the real orbital period changes of **OO Aql** –in terms of the **P(E)-P$_e$**, where **P$_e$** is the constant period of 0.5067887 *days* used to construct the (O-C) diagram of the system- and its rate of change were calculated and are presented in Fig. 2 and Fig. 3, respectively.

Table I

Coefficients of the 5th order polynomial used for the (O-C) diagram description of OO Aql

$c_0 = 0.0485$	$c_2 = -0.7174$	$c_4 = 1.7712$
$c_1 = 0.1403$	$c_3 = 0.4151$	$c_5 = -1.4913$

scale constant 5×10^4

From Fig. 2, where the **P(E)-P$_e$** function is presented, a *long-term variation* of the order of: **–1.43x10d/E**, corresponding to **–1.03x10d/y,** or to **–0.0088s/y** was detected, (dashed straight line). Moreover, a periodicity of **55** years (or double) is obvious.

Fig. 1

	Fig. 2
	Fig. 3
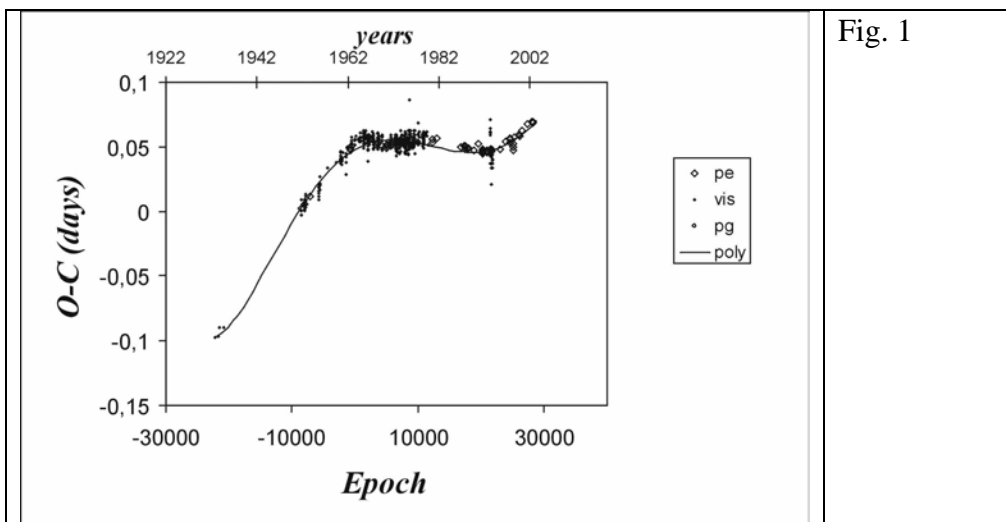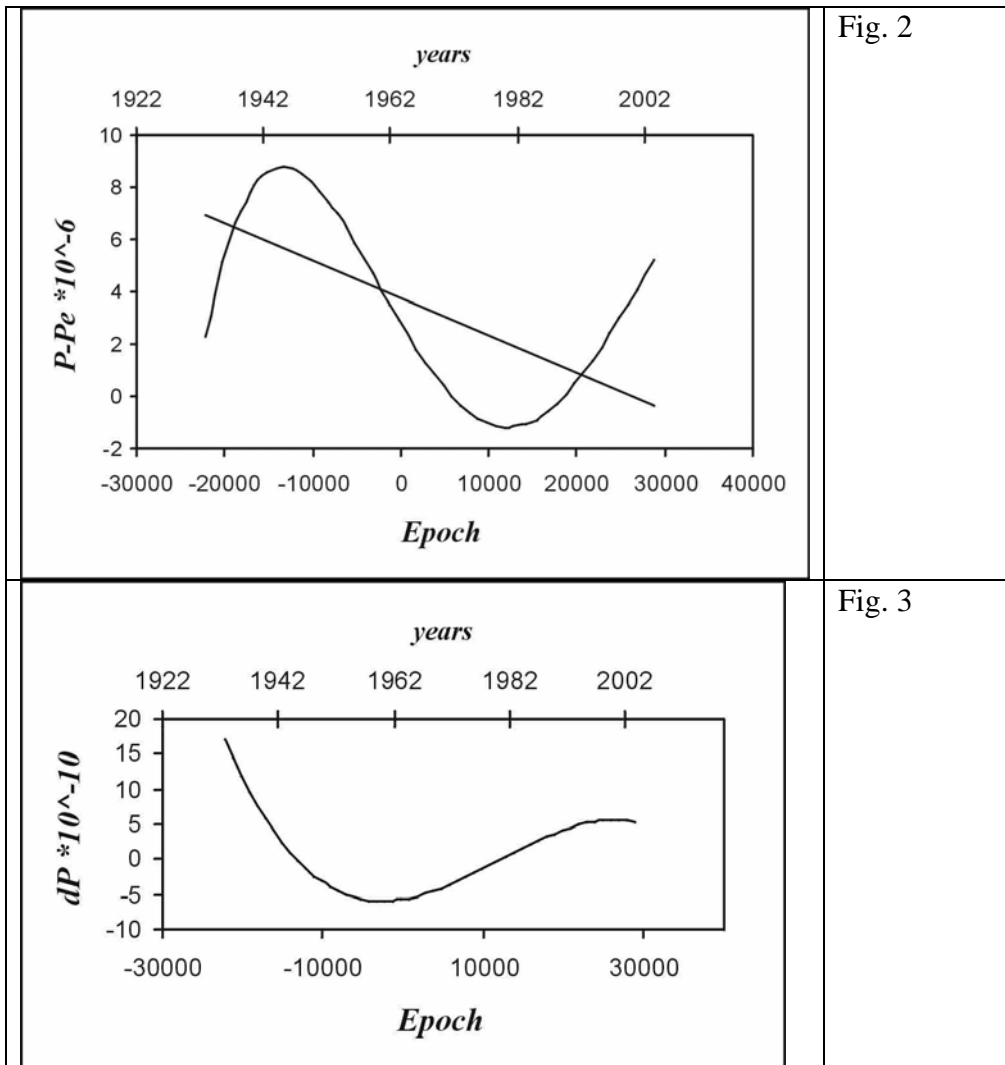
3. Orbital Period Study of *V471 Tauri*

From all times of minimum light of **V471 Tau**, its (O-C) diagram was constructed based on the linear light elements[4]:

$$\text{Min I} = 2440610.06413 + 0.52118334 \cdot E$$

Repeating the same procedure as previously, it was found that the (O-C) diagram of **V471 Tau** can be best described by a sixth order polynomials, (Fig. 4), the coefficients of which are given at Table II. While,

Figs. 5 & 6 are similar to 2 & 3, presenting the real period changes and the rate of change but for *V471 Tau*.

From Fig. 5, a *long-term variation* of the order of: **4.03x10d/E**, corresponding to **2.82x10d/y**, or to **0.0024s/y** was detected, (dashed straight line). Moreover, a periodicity of about **22.8** years was detected by applying discrete Fourier transform to the **P(E)-P_e** function of *V471 Tau*.

Table II
Coefficients of the 6th order polynomial used for the (O-C) diagram description of V471Aql

$c_0 = 0.0006$	$c_2 = 0.0025$	$c_4 = 0.6962$
$c_1 = 0.0061$	$c_3 = -0.2318$	$c_5 = -0.7859$
	$c_6 = 0.3136$	scale constant 1.7×10^4

Fig. 4

Fig. 5
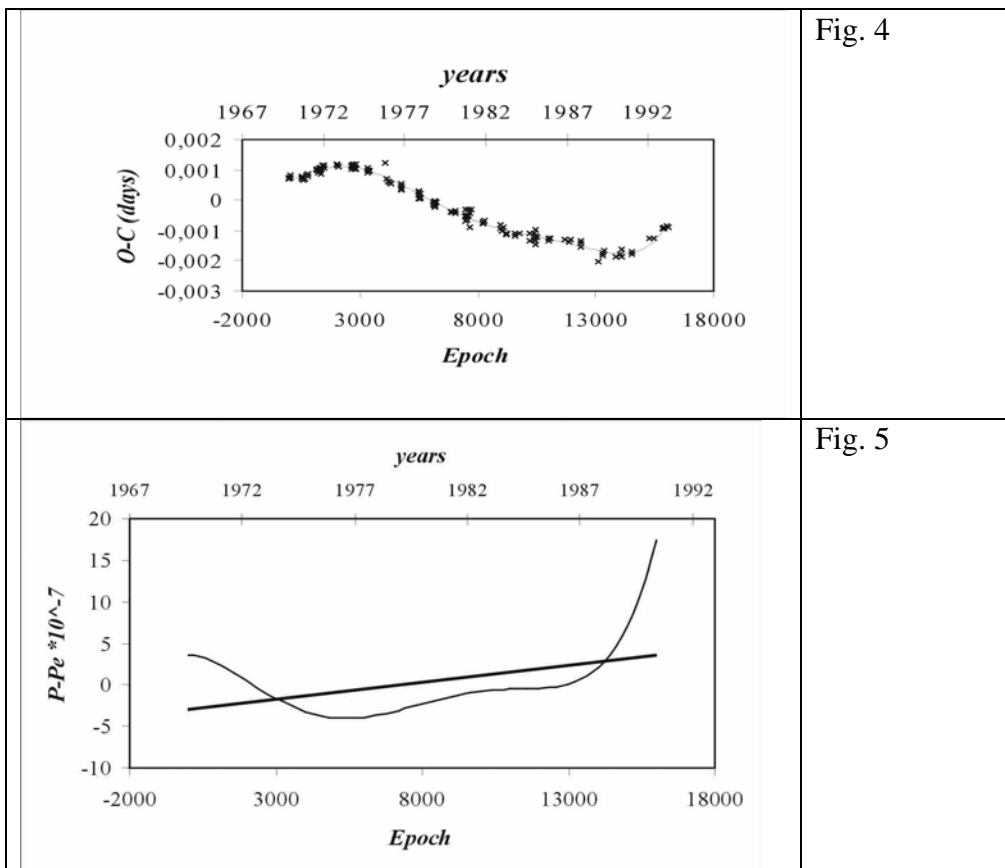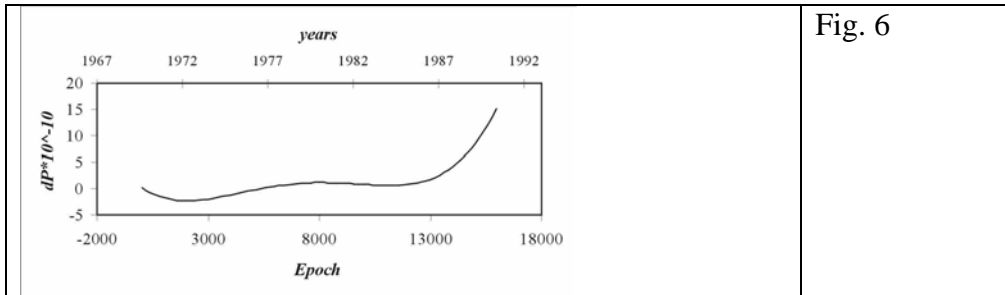
Fig. 6

4. Discussion

The orbital period changes of both systems presented here, have been also studied by some other investigators[3],[2]. Considering our and their results, we note that although the sets of observational data used -in both cases- were not the same, the detected periodic terms correspond to either the time interval covered by the analyzed observations, or to half of it. *So, they might be not real*. For this reason, we limit ourselves to present the period changes (and their rates of changes) only.

Moreover, for *OO Aql*, as is obvious from Fig. 2, there is not any period jump around 1963, as has been reported[3]. And it is better to wait and see if its observed period variations are due to the presence of a third body, to magnetic activity cycles[5], or if there is not any periodic term at all.

The same is true for *V471 Tau*, although if the periodicity is real and suppose that is due to the light-time effect, it yields to a very interesting result concerning the third body's mass: it is very small, a sub-solar mass like that of a *brawn dwarf*. But even so, we have to wait to get reliable results.

References

[1] K a l i m e r i s A., Rovithis-Livaniou H. & Rovithis P. On the orbital period changes in contact binaries, A&A 282, 1994, 775-786.

[2] G u i n a n E.F., Ribas I. The best brown dwarf yet? A companion to the Hyades eclipsing binary V471 Tauri, ApJ 546, 2001, L43-L47.

[3] D e m i r c a n, O. & Gurol B. Light curves and period changes of OO Aquilae, A&ASS 115, 1996, 333-338.

[4] B o i s B., Lanning H. H., Mochnacki S.W. Spectroscopy of 471 Tau. I - Review of basic properties, AJ 96, 1988, 157-164.

[5] A p p l e g a t e, J. H. A mechanism for orbital period modulation in close binaries, ApJ 385, 1992, 621-629.

ANGULAR MOMENTUM EVOULUTION OF INTERACTING BINARY STAR SYSTEMS

Osman Demircan

Çanakkale Onsekiz Mart University
Astrophysics Observatory
Çanakkale Turkey, e-mail:demircan@comu.edu.tr

Abstract:
The orbital angular momentum distribution of interacting binary star systems and the important role of mass loss and theAlfven radius in effective spin down and orbital shrinkage (and thus in the orbital angular momentum evolution) of these systems are reviewed.

1. Definitions

The spin angular momentum H_s of a star with mass M, radius R, and spin period P_s:

$$(1) \qquad H_s = k^2 R^2 M P_s^{-1}$$

where k is the gyration constant varying between 0.07 and 0.15 depending on the density distribution inside the star

The orbital angular momentum H_o of an interacting binary system with component masses $m_{1,2}$ and orbital period P_{orb}, is given by

$$(2) \qquad H_0 = \left(\frac{G}{2\pi} \right)^{1/3} \frac{m_1 m_2}{(m_1 + m_2)^{1/3}} P_{orb}^{1/3}$$

where G is the universal gravity constant.

2. The angular momentum loss (AML) and slow-down of a single star.

The H of a star is lost by stellar winds.. However for cool stars with convective envelopes $(m \leq 1.6\ m_o)$, the mass loss through the stellar wind occurs not from the photospheric surface but from the top of closed magnetic loops (Alfven radius). If H of a cool star with toroidal magnetic loops differentiated with respect to P_s and m, respectively, on the surface,

and on the Alfven radius of the star by considering that the stellar wind leaves the star at Alfven radius, we obtain

$$(3) \qquad \frac{dH}{dt} = k^2 R_A^2 P_s^{-1} \frac{dM}{dt} = -k^2 R^2 M P_s^{-2} \frac{dP}{dt}$$

which reveals the magnetic braking law of single cool stars as

$$(4) \qquad \frac{dP}{dt} = \left(\frac{R_A}{R} \right)^2 \frac{P}{M} \frac{dM}{dt}$$

as noted first by Schatzman (1959), Kraft (1965), and Mestel (1968). It is known that the R_A is an order of magnitude larger than R in Eq.(3) and Eq.(4). Therefore (due to the large R_A)   a relatively small amount of mass loss becomes sufficient to spin down the cool stars. Such efficient spin-down was first observed by Skumenich (1972) in cool stars, and by Uesugi and Fukuda(1982) in different spectral-type field stars.

3. AM evolution of RS CVn systems into contact binaries.

In RS CVn type binaries with late type (mostly G or K) evolved components it is expected that the enhanced AML from the component stars is fed by H_o by the process of tidal friction so that a strong braking torque on the individual components causes the binary orbit to shrink, and eventually spiraling into forming a contact binary system (see e.g. Van't Veer 1993, and Guinan and Bradstreet 1988). In order to understand the process , Demircan (1999) formed the H_o-P_{orb} diagram of 40 well known RS CVn systems. He derived the semi-empirical relation

$$(5) \qquad \frac{dM}{dt} = 0.068 \frac{m_1 m_2}{\left(m_1 + m_2 \right)^{1/3}} P^{-2/3} \frac{dP}{dt}$$

between the wind driven mass loss and the orbital period decrease of these systems, where the masses are in scalar unit and the orbital period in days. The time scale for the RS CVn systems to evolve into contact binaries is estimated by integrating Eq.(5) between t_o and t:

$$(6) \qquad t(yr) \cong \frac{0.204}{\dot{M}} \frac{m_1 m_2}{\left(m_1 + m_2 \right)^{1/3}} \left(P_o - P_t \right)^{1/3}$$

where P_t is the orbital period at a given age t after t_o. Note that for $t > t_o$ the P_t is always smaller then P_o. The $\dot{M}$ in Eq.(6) is the mass loss (in $m_\odot / yr$) from the system. Demircan's (1999) example of the orbital period evolution of the system RT And for five different assumed initial periods P_o obtained by using Eq.(6) is repreduced in Fig 1., where $\dot{M}$ was assumed to be 10^{-10} $m_\odot / yr$.

Fig.1. confirms that it would take take a few billion years for the RS CVn systems to evolve into contact configuration by the considered process(see also Guinan and Bradstreet 1988).

4. AM evolution of massive binaries

The magnetic breaking process is not present for stars with radiative envelopes. These stars are generally more massive than $1.6 m_\odot$. However, it is well known that they also spin-down effectively (cf. Uesugi and Fukuda, 1982) due to probably higher rate of stellar wind flow, and probably large (comparable with the Alfven radius) co-rotating distance of the wind material. The massive components in a close binary systems can not spin down due to strong tidal forces, but the total AML is driven from the orbit by a process of tidal friction, so that the binary orbits must shrink just as in the case of binaries with cool components.

5. Discussion

The well known spin-down of single stars due to AML requires the orbital shrinkage (period decrease) in close binary star systems. Thus, we expect the AM evolution of close binary systems towards smaller orbits. For this process to be effective, the spin orbit coupling ($P_s \cong P_{orb}$) is the necessary condition. Thus, the relatively longer period ($P_o \geq 10d$) binaries are not expected to evolve into shorter period systems. On the other hand, the more massive component of a short period binary may fill its Roche lobe and start transferring mass to the other component, while the system is evolving towards shorter periods under the wind driven mass loss and spin-orbit coupling mechanism. When Roche lobe overflow starts, then the control in AM evolution of the binary is dominated by the mass transfer and

until mass-ratio reversal, the orbital period should decrease, but during the second stage after mass ratio reversal, it is expected to increase.
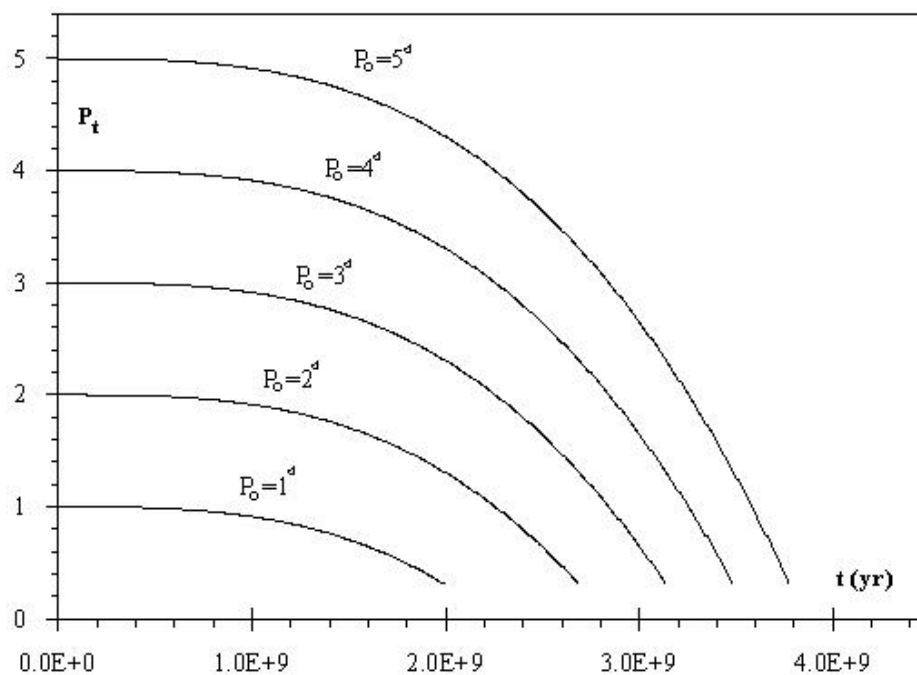
Fig.1. Dynamical evolution of the system RT And from detached to contact stage, for five different initial orbital periods P_o (extracted from Demircan 1999).

References:
Schatzman E. 1959 Ann. Astrophys. Suppl. 8,129
Kraft R. P. 1965 Ap J. 142,681
Mestel L. 1968 MNRAS 138, 359; 140, 177
Skumenich A. 1972 Ap J. 171,565
Demircan O.   1999 Tr. J. of physics 23,425
Van't Veer F.   1993 Comments Astroph. 17,1
Guinan E.F.,Bradstreet D.H. 1988 in Formation and
        Evolution of Low Mass Stars, eds.A.K.Dugree, M.T.V.T. Lago,Kluwer, p345.
Uesugi A., Fukuda I. 1982 Revised Catalogue of Stellar Rotational Velocities

THE ACTIVITY OF THE SYMBIOTIC BINARY Z AND AT THE END OF 2002

Nikolai A. Tomov[1], Mima T. Tomova[1], Olga G. Taranova[2]

[1]*Institute of Astronomy, National Astronomical Observatory Rozhen,*
P.O. Box 136, 4700 Smolyan, Bulgaria
[2]*Sternberg Astronomical Institute, Moscow University,*
Universitetskii pr. 13, 119899 Moscow, Russia

Abstract

Broad-band UBVRJHKLM photometric data taken at the time of the optical maximum of the symbiotic binary Z And during its small-amplitude brightening in the end of 2002 are analyzed. The spectral energy distribution of each component of the binary has been obtained. The analysis shows that the energy distribution of the compact companion was changed very small, it was remained a hot object emitting mostly in UV as in the quiescent state of the system. On the basis of this result the brightening is supposed to be due to a slow expansion to about two times its quiescent size as a result of an accretion rate increase.

Introduction

The symbiotic system Z And consists of a normal cool giant of spectral type M4.5 [1], a hot compact component with temperature higher than 10^5 K [2] and an extended circumbinary nebula formed by the wind of the giant and partly photoionized by the hot component.

The last major brightening of Z And began in the end of August 2000, the optical light reached maximum in December and gradually decreased to its typical quiescent value till the summer of 2002 [3, 4, 5]. In August 2002 there was not any indication of activity of the system and the light was in a deep minimum determined by an eclipse of the hot component [5]. After that time the light increased again and reached maximum in November, but the *UBV* amplitudes were not great ~1^m. In the same time, however, the IR emission was heavily enhanced - to the level close to that in December 2000. The star underwent an outburst again, but it was differing from the major outbursts when the visual emission of the hot companion predominates over the other components in its typical energy distribution – a weak *UBV* emission and relatively strong *JHKLM* one. Our study is devoted to an analysis of the continuum energy emitted in these regions of

the spectrum of Z And. The aim is to obtain the basic parameters of the hot stellar component and the surrounding nebula at the time of the light maximum.

Observations and reduction

Broad-band *JHKLM* photometry of Z And was obtained on 11 Dec. 2002 (JD 2452620.262) with the InSb photometer attached to the 125cm telescope of the Crimean Station of the Sternberg Astronomical Institute. Broad-band *UBV* photometry was obtained on 12 Nov. 2002 (JD 2452591.308) with the single channel photoelectric photometer, attached to the 60 cm telescope of the National Astronomical Observatory Rozhen. The comparison stars used were described in the work of Tomov et al. [6].

The light curves of Skopal [5] and Skopal et al. [7] show that our *UBV* estimate of November 2002 was obtained at the maximum of the light during the outburst at the end of the year 2002 (Fig. 1). For our considerations we used average *UBV* magnitudes from the photometry of Skopal and our data at that time. The collection of the data taken in eight photometric bands provides the possibility to analyse the light in a broad spectral region. Since the IR estimates were less changed they were related to the times of obtaining the *UBV* magnitudes. We also used *R* photometric data from the light curve of Skopal [5] at the epoch of our observation from November 2002. The stellar magnitudes were converted into continuum fluxes.
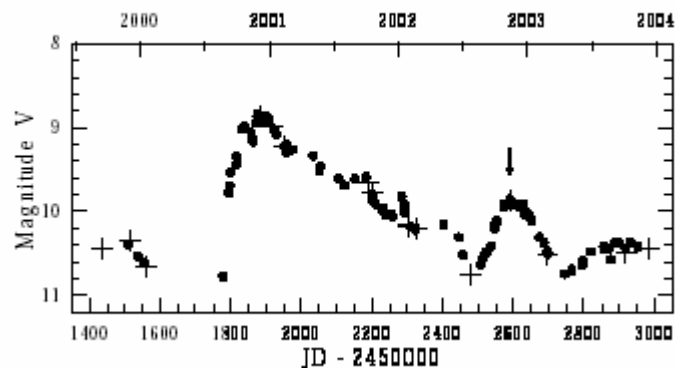
Fig. 1. The V light curve of Z And during its phase of activity after the summer of 2000. The dots indicate the data of Skopal et al. [4, 7] and the crosses our unpublished data. The arrow indicates the epoch during which we obtained our multicolour *UBVRJHKLM* data.

All fluxes were corrected for the interstellar reddening. We used the value E(B-V)=0.30 and proceeded according to the approaches of Seaton [8] and Johnson [9].

Continuum energy distribution

The basic parameters of the components of the binary can be obtained from their continuum emission. It turned out, however, that the hot component has radiated comparatively little in the region of the photometric bands used by us and mainly at the shorter wavelengths. That is why its parameters were determined also by means of some suppositions in addition to the analysis of the observed continuum.

When analyzing our data we proceeded in the following way. The giant was not variable during the time of activity after the year 2000. That is why initially we subtracted its fluxes according to the work of Tomov et al. [6] from the observed fluxes. It turned out that the rest of the emission is fitted very well by a nebular continuum in the region of the *RJHK* bands. Then we assumed that the same continuum is probably present also in the *UBV* region. In this region, however, an additional emission of a third component is present as well.

On the basis of our spectral data it was obtained that doubly ionized helium is dominant in the circumbinary nebula and we assumed that its continuum is formed by the emission of hydrogen and ionized helium.

The best fit at the wavelength positions of the *UBVRJHKL* bands for the nebular emission turned out to be continuum of gas with an electron temperature of 20000 ± 1000 K and an emission measure of $(11.7\pm0.3)\times10^{59}(d/1.12 \text{ kpc})^2 \text{ cm}^{-3}$ (Fig. 2, Table 1).

This result showed that the increase of the light of Z And at the time of its optical maximum was mainly due to the nebular emission and the energy distribution of its secondary stellar component was typical of a hot object radiating predominantly in the UV region, as in the quiescent state. In this case it would not be correct to determine its parameters on the basis only of visual data. Thus, we obtained these parameters from both the *UBV* fluxes and the companion's Lyman luminosity. It was necessary for this luminosity also to be estimated. Using the quiescent radius and effective temperature adopted in the work of Tomov et al. [6], we obtained a Lyman photon luminosity of 9.43×10^{46} phot s^{-1}. We supposed that the Lyman luminosity has increased in the same ratio of 2.5±0.2 as the emission measure of the nebula and in this case obtained $(2.36\pm0.19)\times10^{47}$ phot s^{-1}.
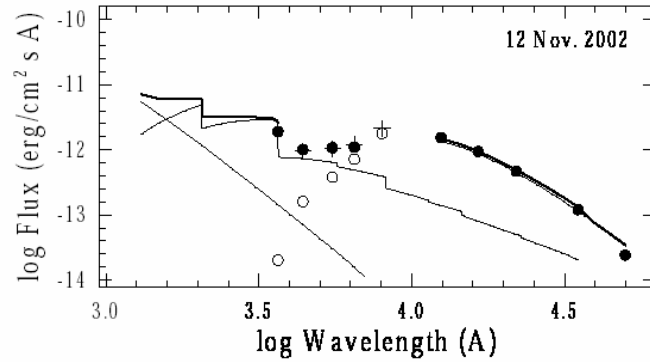
Fig. 2. The spectral energy distribution of Z And at the time of its optical maximum in November 2002. The points indicate the observed fluxes. The thin lines represent the continua of the system's components. The circles represent the *UBVRI* fluxes of the giant. The thick line represents the resulting continuum. In the region of the *BVRI* photometric bands the resulting continuum is represented by crosses, placed only at their positions, since the giant does not radiate as a blackbody in this region and its continuum is not known at the other wavelengths.

Using this value and the observed *UBV* fluxes, for the radius and the effective temperature at the time of the optical maximum we derived 0.13 ± 0.01 $R_\odot$ and 125000 ± 3000 K. The uncertainties are determined from our observed fluxes. These parameters are given in Table 1 and the fluxes of the hot component were calculated on their basis.

DATE	15.09.1999 QUIESCENT	12.11.2002 ACTIVE
Hot stellar		
T_{eff} (K)	150000 (UV data)	125000 ± 3000
R (d/1.12 kpc) $R_\odot$	0.06 (UV data)	0.13 ± 0.01
Nebular		
T_e (K)	20000 ± 1000	20000 ± 1000
n_e^2 V (d/1.12 kpc)$^2 \times 10^{59}$ (cm^{-3})	4.7 ± 0.3	11.7 ± 0.3

Table 1. Parameters of the hot stellar and the nebular components based on the observations. The parameters for the quiescent state are from the work of Tomov et al. [6].

Discussion and Conclusions

The commonly accepted view is that hydrogen steady-state burning is realized at the surface of the secondary component of Z And in its quiescent state [10]. This component is a high temperature compact object. Its expansion could then be due to an accumulation of matter not included in the burning process as a result of the growth of the accretion rate. The expansion occurs at constant bolometric luminosity [11]. The quiescent parameters used by us and the assumed increase of the Lyman luminosity by a factor of 2.5 lead to an increase of the bolometric luminosity of this hot object by a factor of about 2, which however, makes the interpretation difficult for an expansion at constant bolometric luminosity. Though, we will use the relation between the velocity of the expansion and the accretion rate of an accreting white dwarf with hydrogen burning at its surface to obtain at least a most crude estimate of the increase of the accretion rate during the active phase. This velocity is given by

$$dR / dt = R \, (d \ln R / d \ln \Delta M_1) \times ((\text{Mdot} - \text{Mdot}_{RG}) / \Delta M_1)$$

$$\approx 8 \text{ m/s } ((\text{Mdot} - \text{Mdot}_{RG}) / 10^{-6} \text{ M}_\odot/\text{yr}) \times (\Delta M_1 / 10^{-5} \text{ M}_\odot)^{-1} ,$$
(1)

where $d \ln R / d \ln \Delta M_1 = 3.1 \sim 4.1$ at $R = 1 R_\odot$ [11]. Mdot is the accretion rate necessary to trigger the expansion and ΔM_1 is the mass of the accreted envelope. Mdot_{RG} is the upper limit of the region of the accretion rates, where the accretion rate is equal to the burning rate; when the accretion rate is greater than this limit the envelope expands as a result of accumulation of mass. Using this relation we can obtain an estimate of the mean accretion rate needed for expansion of the hot component of Z And for the time of the light increase from the mean velocity of the increase of the star's radius. The typical time of the growth of the light is 100^d [5]. In this case the mean velocity of the increase of the radius from 0.06 $R_\odot$ to 0.13 $R_\odot$ is obtained to be 5.6 m s^{-1}. At a mass of the hot component of 0.6 $M_\odot$ [2, 12] the mass of the accreted envelope for burning in thermal equilibrium is 5.01×10^{-5} $M_\odot$. The upper limit of the accretion rate is 1.77×10^{-7} $M_\odot$ yr^{-1} [11]. Then using the relation (1), we derived 3.2×10^{-7} $M_\odot$ yr^{-1} for the accretion rate providing the expansion. According to Fernandez-Castro et al. [2] the quiescent accretion rate of the hot component of the Z And system is equal to 4.5×10^{-9} $M_\odot$ yr^{-1}. In this case the ratio of the two values is about 70.

We present the results of broad-band *UBVRJHKLM* observations of the symbiotic binary Z And taken during its outburst at the end of 2002. The data show that the hot component of this system was a compact object emitting mostly in UV during this time, as in quiescence. The increase of the emission of the circumbinary nebula indicates an increase of the flux of the ionizing photons from this component. We assumed that its Lyman luminosity increases in the same ratio as the emission measure of the nebula. On the basis of the Lyman luminosity estimate and the *UBV* fluxes we calculated its effective temperature and radius. The result shows that it expands to about two times its quiescent size. We also obtained a crude estimate of the mean accretion rate during the active phase.

References

1. Mürset, U., & Schmid, H. M., Spectral classification of the cool giants in symbiotic systems, A&AS, 137, 1999, 473

2. Fernandez-Castro, T., Cassatella, A., Gimenez, A., & Viotti, R., IUE observations of Z Andromedae - Spectral variations during quiescence and a physical model, ApJ, 324, 1988, 1016

3. Skopal, A., Chochol, D., Pribulla, T., & Vanko, M., UBV Photometry of the Symbiotic Star Z And During its 2000 Outburst, IBVS, 5005, 2000

4. Skopal, A., Vanko, M., Pribulla, T., et al., Photometry of symbiotic stars. X. EG And, Z And, BF Cyg, CH Cyg, V1329 Cyg, AG Dra, RW Hya, AX Per and IV Vir, Contrib. Astron. Obs. Skalnate Pleso, 32, 2002, 1

5. Skopal, A., Discovery of the eclipse in the symbiotic binary Z Andromedae, A&A, 401, 2003, 17L

6. Tomov, N. A., Taranova, O. G., & Tomova, M. T., Mass ejection by the symbiotic binary Z And during its 2000-2002 outburst, A&A, 401, 2003, 669

7. Skopal, A., Pribulla, T., Vanko, M., et al., Photometry of symbiotic stars. XI. EG And, Z And, BF Cyg, CH Cyg, CI Cyg, V1329 Cyg, TX CVn, AG Dra, RW Hya, AR Pav, AG Peg, AX Per, QW Sge, IV Vir and the LMXB V934 Her, Contrib. Astron. Obs. Skalnate Pleso, 34, 2004, 45

8. Seaton, M. J., Interstellar extinction in the UV, MNRAS, 187, 1979, 73p

9. Johnson, H. L., Astronomical Measurements in the Infrared, ARA&A, 4, 1966, 163

10. Fernandez-Castro, T., Gonzalez-Riestra, R., Cassatella, A., Taylor, A., & Seaquist, E. R., The active phase of the hot component of Z Andromedae, ApJ, 442, 1995, 366

11. Fujimoto, M. Y., A Theory of Hydrogen Shell Flashes on Accreting White Dwarfs - Part Two - the Stable Shell Burning and the Recurrence Period of Shell Flashes, ApJ, 257, 1982, 767

12. Schmid, H. M., & Schild, H., The polarimetric orbit of Z Andromedae, A&A, 327, 1997, 219

NEW AIMS OF THE SPECTRAL RESEARCH OF BE-STARS

Lubomir Iliev

Institute of Astronomy

Bulgarian Academy of Sciences
liliev@astro.bas.bg

Abstract:

An overview of the basic concepts development of the spectral research of Be stars is presented.

Adventures of one definition

First two Be-stars were observed about 140 years ago. Observations of Padre Angelo Secchi were result of implementation of "new" at that time technology – a prism spectroscope attached to refractor-telescope. In 20-s and 30-s of XX-th century large optical telescopes with standard spectrographs and high sensitivity photographic materials started the era of modern astrophysics. Not by coincidence first hypothesis about origin of Be stars was created at that time by Struve in 1931 [1]. Regular spectral observations with powerful telescopes show the fact that emission spectral lines in stars of B spectral type are common. In 1918 abbreviation Be was accepted by IAU.

In the second half of XX-th century first attempts for classification and statistics were made. First wide definition of Be-stars and related phenomenon was given by Collins in [2] as: **non-supergiant B type star whose spectrum has or had at some time, one or more Balmer lines in emission.**

More recently the term **classical Be star** is commonly used to exclude Herbig Ae-Be stars, Algol systems and other similar by appearance but obviously different by origin phenomena. In broad context Be stars are class of stars that rotate so fast that are close to the limit where centrifugal force balances with the gravity at the stellar surface. Some well known Be stars rotate at speed of more than 300 km/s. The reasons the Be-stars to rotate so fast are unknown and

represents one of the greatest challenges to the modern stellar astrophysics.

According to some recent investigations massive stars during their MS stage could significantly change some of their "surface" parameters. Outer layers could spin up as a result of angular momentum distribution as was shown by [3]. Thus Be stars became test laboratory for studying angular momentum evolution and rotationally induced instabilities.

Line-profile variations

Photospheric absorption spectra of Be-stars show normal parameters of gravity, temperature and abundance for a B type star. The only difference is the rotational broadening. Variability is the most prominent feature of Be stars.
Time scales vary from several minutes to several decades. About 1/3 of all Be stars show V/R variability connected with phase transitions and geometrical position of circumstellar disks.

Variability of the emission strength in Be stars spectra is remarkable. It may disappear completely for a certain period and in a decades develop to very high values

Shell lines presented in some late subtype Be-stars also could exhibit high degree of variability usually in connection with phase changes.

Short term variability of Be stars

In addition to the long-term and gradual variability most common for all classical Be stars, there is spectral variability of shorter term with characteristic times from several minutes to several days. Short-term spectral variations are most often found in early type Be-stars. Vast majority of LPV were found in stars of up to B6 spectral subclass.

Similar distribution was found from photometrical observations. Statistical research of several groups of investigators show that nearly 90% of stars up to B5 are variable, and only 28% of those later than B6 were found to vary. Wide implementation of cross-dispersed echelle-spectrographs boosted the research of short-term spectral variability. Because of the large spectral coverage and high accuracy new discoveries could be expected in this field.

Spectral phase transitions

The strongest variability of circumstellar envelopes and their spectral evidences are so called spectral phase transitions. Variations of the spectrum spread from complete loss of any traces of emission to fully developed complex of emission spectral lines (Balmer, FeII, He etc.). Usually transitions between emission line and shell spectrum are explained by inclination differences. They were observed in γ Cas, Pleione, 59Cyg, HR2142 and other stars.

One possible explanation is eventual precession of stellar equatorial and envelope disk planes. Transitions between emission phase and normal B phase are explained by different mechanisms of dissipation of the material in the envelopes.
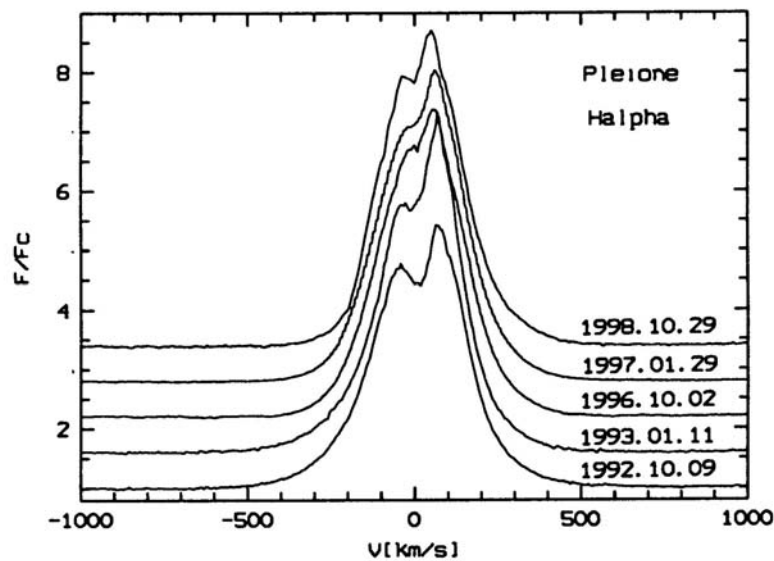
Fig. 1 Hα profile variations of Pleione from Rozhen observations taken from [4].
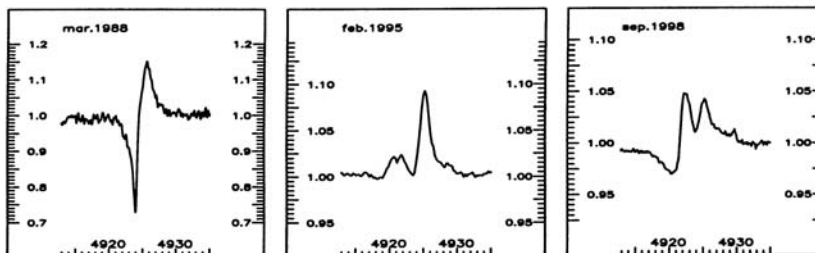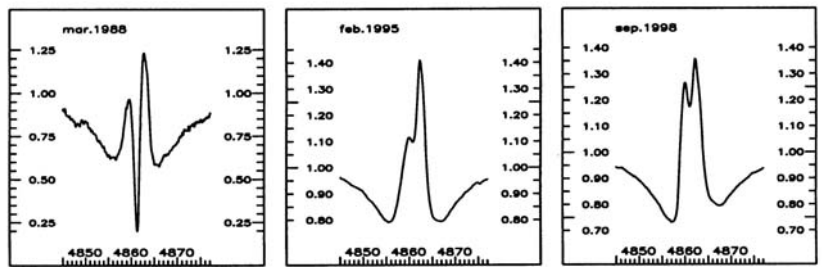
Fig. 2 Hβ profiles of Pleione as shown by [5].
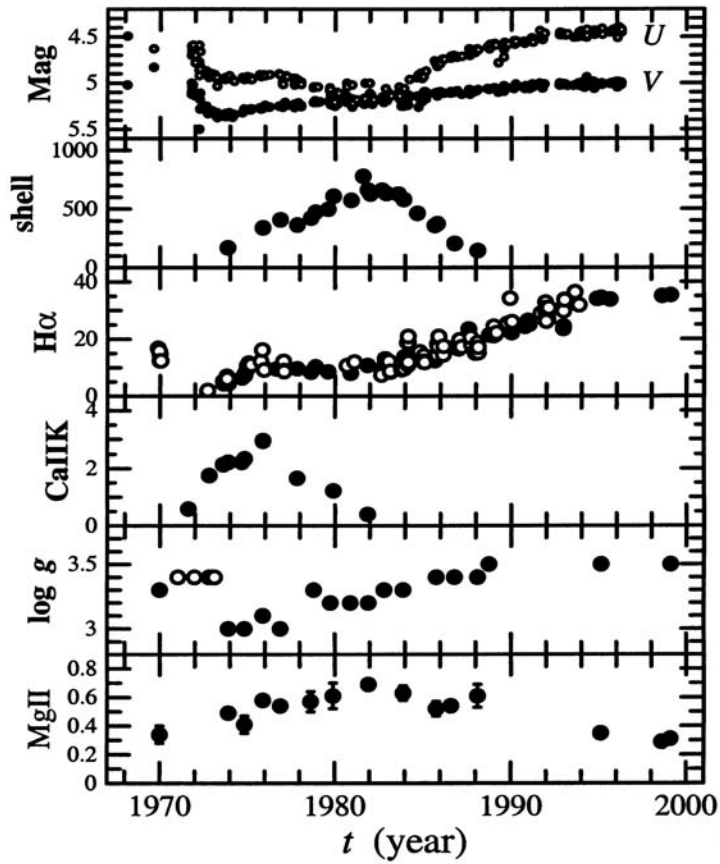
Fig. 3 Variation of other spectral features of Pleione's spectrum during last several decades from [6].

Special interest is called by Be stars that came through all 3 types of spectral phases. One example is the well known Be star Pleione, which undergone its last phase transition in 1987-88 [7]. The variation of some of the spectral evidences of the Be phenomenon in this star are shown on the panels of Fig. 3.

Rotational modulations

Rotational modulation was first proposed as hypothesis explaining observed spectral variations in Be stars. It was supposed to be caused by star spots cooler than the surrounding regions of stellar surface. Later hypotheses supposed rotation spectral modulations to originate in the circumstellar environment.

Natural way to support this type of variability is to assume existence of oblique magnetic field. This hypothesis explain well the possible transfer of angular momentum. Searches for magnetic field in Be stars is not successive till now. General detection limit is still above than the expected mean magnetic field strengths. Predicted by simulations values are about 500 G.

Rotation modulations themselves are in strong competition with NRP in explanation of small scale short term LPV.
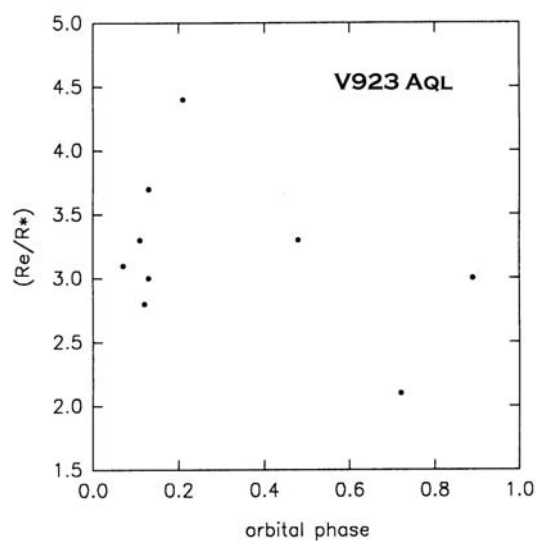
Fig. 4 Phase dependence of envelope dimensions of V923 Aql from [8].

Be-stars in binaries

[9] proposed that all Be-stars are binary systems. The secondary component is undetected and the system is at mass transfer stage. This general conclusion was not supported by the observation, but binary systems with Be star as one of the components are important tool for understanding Be phenomenon.

Influence of the binary companion may help the spin-up of the primary. Tidal forces can help the outflow of the matter from equatorial regions of the primary. The presence of the binary may impose additional conditions on the model calculations and this type of systems could be used as probes.

One good example of the variations of the parameters in the circumstellar envelope is the Be binary star V923 Aql. This type of variations were first reported by [10] and later studied in detail in the works of [7] and [11].

Concluding remarks

Despite their large number and relative closeness, Be stars continue to be significant challenge to the modern astrophysics. New accurate observations, implementation of up to date techniques supplied astronomers with new knowledge about the Be-phenomenon. In the same time this new facts turned most of previous statistical and theoretical conclusions to critical reestimation.

All above mentioned makes Be stars extremely relevant objects for international co-operation programmes. It is impossible for single observing teem on single observatory to carry out decent programme able to follow up important features of Be-phenomenon like phase transitions, variations connected with the orbital periods, etc.

New technology instrumentation is highly desirable to continue and develop new reviews embracing large number of Be stars possibly not only from our own Galaxy. This instrumentation is a challenge that could be met by united efforts of a group of neighbouring countries. (example of nordic astronomical cooperation).

References:

[1] STRUVE, O., 1931, ApJ, vol.73, p.94.

[2] COLLINS, G.W., 1987, in IAU Colloq. 92, Physics of Be Stars, ed. A. Sletteback & T.P. Snow, p.3

[3] HEGER, A & Langer, N., 2000, ApJ, vol.544, p.1016.

[4] ILIEV,L., 2000, in IAU Colloq. 175 "The Be-phenomenon in early type stars", Alicante, Spain, 28 June – 2 July, 1999, eds. M.A. Smith, H. F. Henrichs and J. Fabregat, p.566

[5] BALLEREAU, D, Chauville J., Zorec J., Morrel, N., 2000, in processings of IAU Coll. 175 "The Be-phenomenon in early type stars", Alicante, Spain, 28 June – 2 July, 1999, eds. M.A. Smith, H. F. Henrichs and J. Fabregat, p.562

[6] HIRATA, R., Shimada, M., Masuda, S., Katahira, J., 2000, in processings of IAU Colloq. 175 "The Be-phenomenon in early type stars", Alicante, Spain, 28 June – 2 July, 1999, eds. M.A. Smith, H. F. Henrichs and J. Fabregat, p. 558.

[7] ILIEV, L., Ruusalepp, M., Kovachev, B., 1988, IBVS No32

[8] ARIAS, M.L., Cidale, L.S., Ringuelet, A.E., 2000, in processings of IAU Colloq. 175 "The Be-phenomenon in early type stars", Alicante, Spain, 28 June – 2 July, 1999, eds. M.A. Smith, H. F. Henrichs and J. Fabregat, p 547.

[9] KRIZ, S, Harmanec, P., 1975, Bull. Astron. Inst. Czechoslovakia, vol.24, p.65.

[10] ILIEV, L., 1994, in IAU Symp. 162 "Pulsation, Rotation and Mass Loss in Early Type Stars, 4-8 Oct. 1993, Antibes, Juan-les-Pins, France, eds. L. Balona, H.F. Henrichs and J.M. Le Contel, p.374.

[11] ARIAS, M.L., Cidale, L.S., Ringuelet, **A.E**., 2004, A&A, vol.417, p.679.

ASTROMETRY WITH SMALL INSTRUMENTS

Petre Popescu[1], Alin Nedelcu[1], Radu Popescu[1], Octavian Bădescu[1,2]

[1]Astronomical Institute of Romanian Academy: petre@aira.astro.ro;
nedelcu@aira.astro.ro; pradu@aira.astro.ro;
[2]Technical University of Civil Engineering, Faculty of Geodesy:
octavian@aira.astro.ro

Abstract
Based on an analyze concerning Bucharest astrometric instruments, a modernization project was elaborated. There are exposed the general aims of the project and the preliminary results obtained: the selection of data from astronomical catalogues, data acquisition concerning instrument positioning and tracking, data selection from astronomical image acquisition system and data processing by means of specific procedures.

I. Observational astrometry in Romania

Main topics of research in Romanian astrometry were connected with the use of 4 instruments: Prin-Merz Astrograph, Meridian Circle Gauthier-Prin, Zeiss Transit Telescope and Danjon Astrolabe.

Meridian Circle Gauthier-Prin 19/235 cm was installed in 1926, it had an important contribution in improving, in an extended international cooperation, stellar catalogues. Zonal and local catalogues for different purposes were built using this instrument. The developments of CCD astrometry and the difficulties of financing such a special project obliged us to stop visual observations. Now the Meridian Circle is preserved and we are studying the opportunity of future modernization.

Zeiss Transit Telescope 10/100 cm was set up in 1956 and was used for Earth rotation monitoring. After using 30 years, taking into account the new development of this class of instruments we stopped the observations. In the future, such an astronomic instrument has no use, except for education.

Danjon Astrolabe 10/100 cm was borrowed from Brussels Observatory and installed in 1993. After being modified for performing CCD observations, it was used in the study of vertical deviation: geodetic and astronomical determinations were compared and a computation method was elaborated. We expect to use such class of instrument for astro-geodetic

measurements in defining the relative position of the geoid relative to WGS84 ellipsoid.

Prin-Merz Astrograph 38/600 cm is a twin telescope installed in 1911 and used for photographic astrometry a very long time. A project of modernization of this instrument is in work (October 2002 - October 2004).

II. Main topics of Romanian astrometric researches.

1. Wide-Plate Archive

A database containing 13000 plates is the result of the about 80 years observational period using the Prin-Merz Astrograph. The database contains a lot of astronomical information difficult to be evaluated. The work on this database was connected with IAU Commission 41, Wide-Plate Archives Working Group having collaborators M. Tsvetkov and K. Tsvetkova from the Institute of Astronomy of Sofia. The aim of this work was the storage and digitizing of our plate archive.

Currently, under a contract with Politechnical University Bucharest, we are developing software for high-speed identifying of the objects from the catalogues, for identifying from all the images from the plates: position, flux (magnitude) and diameter. We work also for searching of unknown objects (not contained in the catalogues). The final result will be a self-adaptive configuration database in distributed platforms (grid databases analysis).

2. Narrow-field astrometry

Astrometry of Solar System bodies is performed in international collaboration with the aim of studying mutual phenomena of planetary satellites, to contribute for improving the orbits of PHAs, to study taxonomic families of PHAs. CCD astrometry and also photometry of these bodies is included in this study.

3. Connection of Radio and Optical Reference Frames

Our institute is included in a group of collaborators: Kiev University Astronomical Observatory, Nikolaev Astronomical Observatory, and Pulkovo Astronomical Observatory. In the interval 1992 - 2000, there were observed, in photographic mode, 188 areas [1].

The topic includes the improvement of optical/radio stars' positions by narrow-field CCD observations. There were made studies concerning: the non-coincidence between radio and optical centers at least for ICRF extended sources, high accuracy densification of the optical frame in post-Hipparchos era mainly for radio-optical connection. Now is in study a first set of 12 radio-sources. There are used in the Compiled Catalogue of

Reference Stars around Extra-Galactic Radio Sources to be finalized in Pulkovo [2].

4. Vertical deviation measured with astronomical methods

In collaboration with the Faculty of Geodesy, Technical University of Civil Engineering, we are working for the introduction of a new national ellipsoid, for the compensation of geodetic net, needed for local ellipsoid special purposes. There were performed geodetic measurements (distances, directions / angles) on the surface of the ellipsoid for relative positioning of geoid-ellipsoid (WGS or Krasovsky).

In conclusion, the demands of narrow field CCD astrometry in our institute are:

- To modernize one of the most valuable instruments Prin-Merz Double Astrograph, in order to continue our astrometric tradition;
- To invest in a new instrument Geodetic Total Station and to modernize it by adding a CCD camera;
- To initiate observational programs using appropriate detection methods of the image;
- To concentrate on software development in order to balance technical improvements and low finance budget.

III. Modernization plans and results

Prin-Merz Astrograph, a 38/600-cm twin telescope, with a $2^0 \times 2^0$ field, was selected for the modernization process, being the most valuable instrument, figure 1.

Fig.1 - Prin-Merz Double Astrograph

In October 2002 we started the project, financed by Romanian Space Agency. It was included in the general idea of development and applying optoelectronic techniques of acquisition and image processing in order to improve the accuracy and efficiency of ground-base astronomical observations by using the automatic control of the positioning and data processing with appropriate software. We include INCDMF - CEFIN (Center of Fine Mechanics) as manager for this project.

The project goals were:
- The research and application of the optoelectronic observation techniques by means of a system of image acquisition with CCD camera;
- The development and use of stepper motor intelligent driver systems, use of planetary gear-box, specific mechanisms, electronic drivers;
- The development and accomplishment of a position control system with absolute encoder;
- The accomplishment of data acquisition and transmission interfaces.

Mounted on the visual telescope, the new optical system has a 7.6×7.6 arcmin field of view, an angular resolution of 0.447 arcsec / pixel which allowed to reach a limit magnitude of 18.

The CCD camera is a 1024×1024 Apogee AP47P, with pixel size 13×13μm, quantum efficiency >90% at 650nm, read noise: 7 - 9 e⁻, digital resolution: 16 bit, 50 kHz and frame transfer 20 sec, figure 2.

Fig. 2 - Apogee AP47P CCD Camera mounted on the optical telescope

The tracking system was installed on a Zeiss refractor (with a field of 14×14 arcmin) mounted on the Prin-Merz telescope. It allows real time tracking using a CCD-TV MINTRON 12V camera.

The driving system modernization includes a stepper motor and planetary gearbox electromagnetic coupled which was mounted on the declination circle. It has a rotation speed of 90 degrees/min. The position control system has an absolute encoder with a min. 20-bit resolution, mounted on the declination circle and connected with data processing system. The accuracy of the positioning is less than 5 arcsec.

The operation and data processing system consist in:

1. Selection of data from astronomical catalogues.

Projected to perform narrow-field astronomical CCD observations, the system uses USNO B1-0 Catalogue of ~ 500 million stars with good enough stellar density [3].

It is possible to use about 80 stars to compute plate solution for each frame with a mean square error of about 0.17 arcsec.
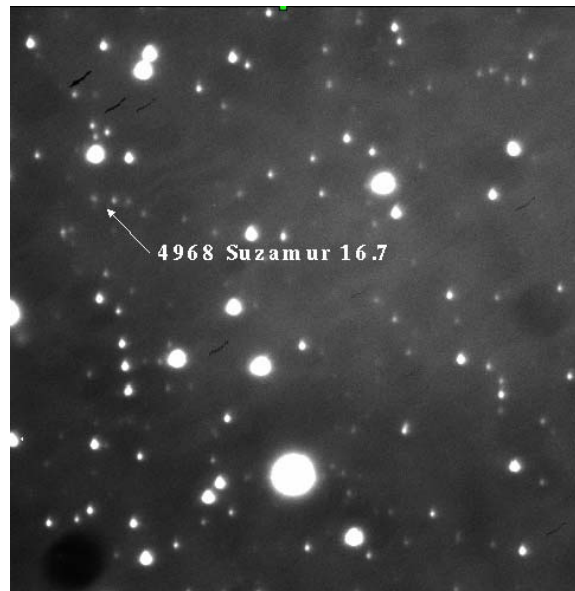
Fig. 3 - 4968 Suzamur, M=16.7

2. Data acquisition concerning instrument positioning and tracking.

The MINTRON Camera is used for positioning and tracking. The position of a star-target (up to 12th magnitude) is measured 10 times/sec and used as feedback for instrument pointing correction.
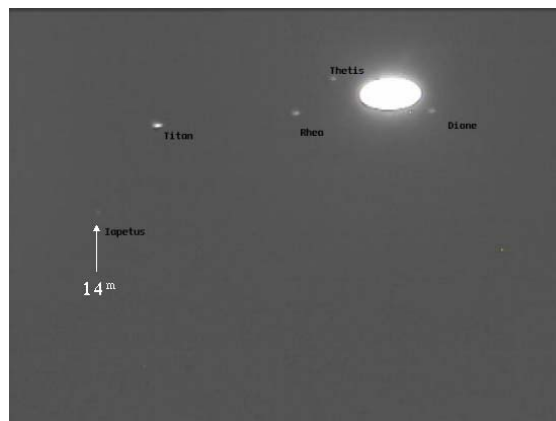
Fig. 4 Image of Saturn's satellites on Mintron Camera

3. Data selection from astronomical image acquisition system.

We showed two 1K×1K FITS files of the eclipsing binary II UMa (8th magnitude). In figure 5, the exposure time was 7 sec, which allowed reaching 16th magnitude and figure 6 with an exposure time of 10×7-sec, reaching 17.5th magnitude.
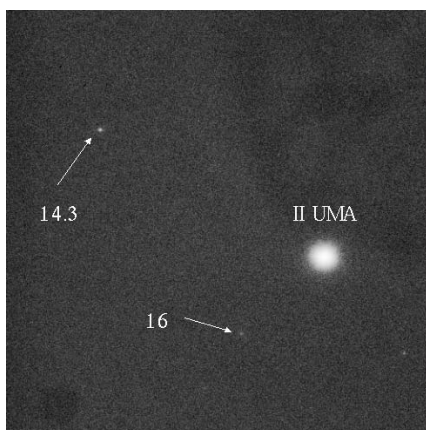
Fig. 5
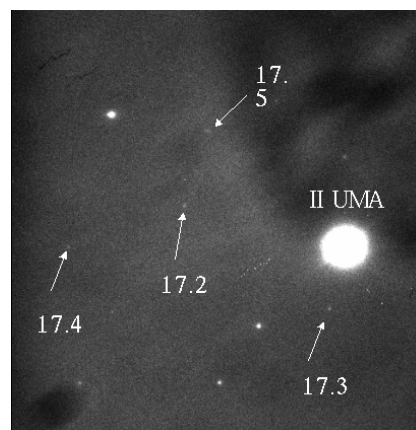
Fig. 6

Another image, figure 7, with 30×1-min exposure shows some more details and figure 8, of 18.5 - 18.9 magnitude.
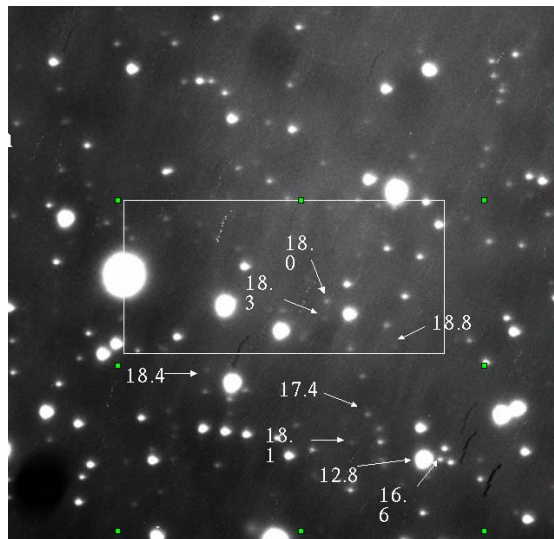
Fig. 7
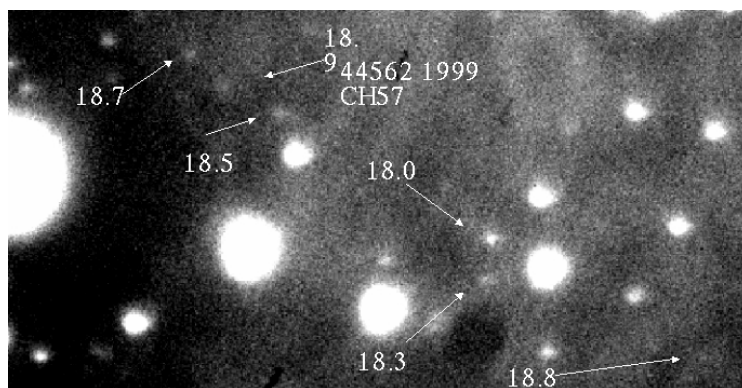
Fig. 8

4. Data processing by means of specific procedures.

The FITS frames were processed using IRAF (dark, bias, flat corrections) [4]. The image quality is to be evaluated and information used in automatic focus. The method involves short exposures that are added to

obtain up to 30 minutes of total exposure. The frames are shifted to compensate drift in image telescope tracking; this drift will be eliminated after the finder feedback loop will be set-up. This is a methodology used for fast moving object astrometry in order to obtain accurate position of asteroids from faint reference stars [5]. To facilitate the detection, we built one image (sum of 3 FITS images, one image = sum of 30×1 min frames separated by 20 min) shifted in respect with reference stars position. The same set of images were shifted in respect with asteroid position.

5. Interactive, flexible dedicates software.

Any implementation of nearly real time digital processing must relay on automated image analysis software. The automated detection, classification (centroid position, magnitude) of the objects are implemented on a hardware running system a near real-time operating system (*NIX). An intuitive interface together with IRAF package will provide a smooth, flexible and versatile system to the user. Batch-mode operation is also available for remote use of the system.

IV. Conclusions

Narrow-field CCD astrometry is possible with small instruments: the maximum magnitude detected during performing test observations allows us to initiate new observational programs. The experience in the work of this project permits the continuation of the development and accomplishment of a remote control operation system of astronomical instruments. In this idea, it is necessary to follow the modernization programs in order to maintain the capabilities of our observatories, to valorize our astronomical scientific and technical heritage: databases and instruments.

References
1. G. Bocsa, M. Birlan, Intermediate Stars in Extragalactic Radiosources Fields, Rom. Astron. J., 11/2, 2001, 181-187
2. Y. Babenko, et al, Reduction of compiled catalogue in the selected extragalactic radio source fields. Preliminary estimation. Rom. Astron. J., 13/1, 2003, 77-81
3. Monet, D. et al., The USNO B, Catalog USNO B1-0, A.J, 125, 2003, 948
4. Image Reduction and Analysis Facility IRAF, http://iraf.noao.edu/
5. A. Nedelcu, R. Popescu, O. Badescu, PHEMU observational campaign at Bucharest, Proceedings of Astronomy Summer School South-Eastern Europe Youth at the Telescope, 2003 (in print)

Gravity-Darkening in Semi-Detached Binary Systems TW And, TW Cas, AI Dra and UX Her

G. Djurašević[1], H. Rovithis-Livaniou[2], P. Rovithis[3], N. Georgiades[2] and S. Erkapić[1]

1 Astronomical Observatory, Volgina 7, 11060 Belgrade, Serbia and Montenegro
2 Dept. of Physics, Athens University, GR Zografos 15784, Athens, Greece
3 Institute of Astronomy and Astrophysics, National Observatory of Athens, P.P.Box 20048, 11810 Athens, Greece

INTRODUCTION

In this paper we are dealing with the estimation of the gravity-darkening exponent (GDE, β), which describes the dependence of the emergent flux of total radiation on the local gravity acceleration of a rotationally or tidally distorted star in hydrostatic equilibrium. Theoretical predictions for stars with purely radiative energy transfer give the value of $\beta = 0.25$ [1], while for stars with convective envelopes $\beta = 0.08$ [2]. Recently however, it was suggested that both mechanisms could act simultaneously [3], and thus any value between these two extremes is expected.

Several attempts have been made to estimate the value of β from observational data for various kinds of binary systems (see e.g. [4] and references therein).

In a semi-detached binary system the secondary component fills its Roche lobe, while the primary is well deep inside its own Roche lobe. In the analysis of such a system it is reasonable to fix the GDE value of the primary star to its theoretical value. The appropriate GDE value for the Roche lobe-filling component could be then empirically estimated from observational data by light-curve analysis.

RESULTS

Here we have performed such an analysis on four semi-detached binary systems and estimated the GDE values for their Roche lobe filling components. More details on the applied model and method of light-curve analysis can be found in [4].

273

The binary systems in question are: *TW And* (F0V + K1-3III-IV; P ~ $4^d.12$) [5] with the mass ratio q = 0.193 estimated from radial-velocity measurements by [6]; *TW Cas* (B9 + G; P ~ $1^d.428$) [7], [8] with q = 0.38 [9]; *AI Dra* (B9.6 V+ G2?; P ~ $1^d.19$; q = 0.43) [10], and *UX Her* (A2.6 + K; P ~ $1^d.549$; q = 0.248) [11].

Tables 1 and 2 comprise the results of our light-curve analyses, and Fig.1 and 2 give the graphic presentation of the obtained results. The subscripts (h,c) in the tables denote the hotter and cooler component of the system. The *Note* given below Table 1 is also valid for Table 2. For *TW And*, *TW Cas*, *AI Dra* and *UX Her* we have obtained β_c ~ 0.06, β_c ~ 0.13, β_c ~ 0.12, and β_c ~ 0.06, respectively. These values basically confirm theoretical predictions for stars with convective envelopes.

System Quantity	TW And B-filter	TW And V-filter	TW Cas B-filter	TW Cas V-filter
n	244	247	647	649
Σ (O-C)^2	0.0265	0.0244	0.0597	0.0485
σ	0.0104	0.0100	0.0096	0.0087
$q = m_c / m_h$	0.1928		0.38	
T_h	7200		12000	
β_h	0.25		0.25	
A_h	1.0		1.0	
A_c	0.5		0.5	
$f_h = f_c$	1.0		1.0	
T_c	4395±13	4466±14	5857±45	5977±29
F_h	0.322±0.001	0.321±0.001	0.583±0.003	0.584±0.003
F_c	0.999±0.001	1.000±0.001	0.994±0.001	0.994±0.001
$i [^o]$	87.17±0.03	87.12±0.04	75.66±0.03	75.64±0.03
β_c	0.05±0.01	0.06±0.01	0.12±0.02	0.13±0.02
$a^{h,c}_1$	+0.3243,+0.5289	+0.3772,+0.6891	+0.5853,+0.3929	+0.6396,+0.4350
$a^{h,c}_2$	+1.0356,-0.6472	+0.9587,-0.8787	+0.4825,+0.1973	+0.0445,+0.4293
$a^{h,c}_3$	-0.7918,+1.3420	-0.9546,+1.7082	-0.5779,+0.5639	-1.0004,+0.0051
$a^{h,c}_4$	+0.2444,-0.2800	+0.3466,-0.6172	+0.2072,-0.2901	+0.0317,-0.0885
Ω_h	6.540	6.551	4.291	4.289
Ω_c	2.216	2.215	2.645	2.645
R_h [D=1]	0.157	0.157	0.255	0.255
R_c [D=1]	0.230	0.230	0.277	0.277
$L_h / (L_h+L_c)$	0.871	0.789	0.922	0.872
$_h$ [M_s]	1.68±0.07		3.97±0.05	
$_c$ [M_s]	0.32±0.02		1.51±0.04	

$_h$ [R$_s$]	2.15±0.05	2.42±0.03
$_c$ [R$_s$]	3.38±0.09	2.79±0.03
log g $_h$	4.00±0.02	4.27±0.02
log g $_c$	2.89±0.02	3.73±0.02
M$^h_{bol}$	2.17±0.02	-0.31±0.02
M$^c_{bol}$	3.30±0.05	2.46±0.05
a$_{orb}$ [R$_s$]	13.64±0.22	9.40±0.20

Table 1. Results of the analysis of *TW And* & *TW Cas B* and V light curves obtained by solving the inverse problem for the Roche model. Gravity darkening exponent of the cooler secondary component (*β$_c$*) was a free parameter.

Note: Black-body approximation of stellar atmosphere, n – number of observations, Σ (O-C)^2 – final sum of squares of residuals between observed and synthetic light curves, σ – standard deviation of the observations, q = m$_c$ / m$_h$ – mass ratio of the components, T$_{h,c}$ – temperature of the hotter primary and cooler secondary, $\beta_{h,c}$, A$_{h,c}$, f$_{h,c}$ – gravity-darkening exponents, albedos and non-synchronous rotation coefficients of the components respectively, F$_{h,c}$ – filling factors for the critical Roche lobe of the hotter primary and cooler secondary, i [^{o}] – orbit inclination (in arc degrees), a$^{h,c}_1$, a$^{h,c}_2$, a$^{h,c}_3$, a$^{h,c}_4$ – non-linear limb-darkening of the components (Claret's formula [12]), $\Omega_{h,c}$ – dimensionless surface potentials of the components, R$_{h,c}$ – polar radii of the components in units of distance between the component centers, L$_h$ / (L$_h$+L$_c$) – luminosity of the more massive hotter star, $_{h,c}$ [M$_s$], $_{h,c}$ [R$_s$] – stellar masses and mean radii of stars in solar units, log g $_{h,c}$ – logarithm (base 10) of the system components effective gravity, M$^{h,c}_{bol}$ – absolute bolometric magnitudes of the components, and a$_{orb}$ [R$_s$] – orbital semi-major axis in units of solar radius.
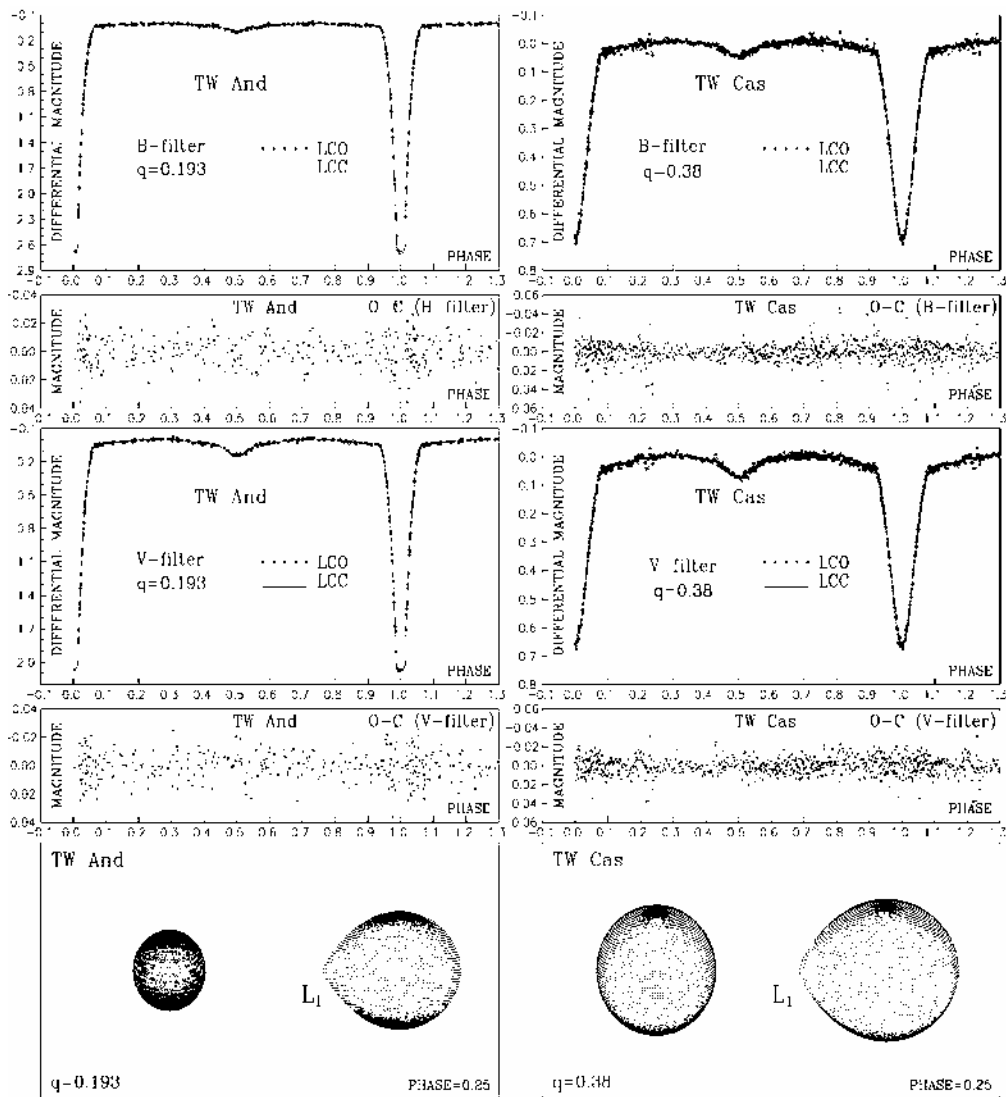
Figure 1. Observed (LCO) and final synthetic (LCC) light curves of *TW And* & *TW Cas*, with final O-C residuals obtained by analyzing their observations, and the views of the systems at the orbital phase 0.25 obtained with parameters estimated in the light-curve analysis.

276
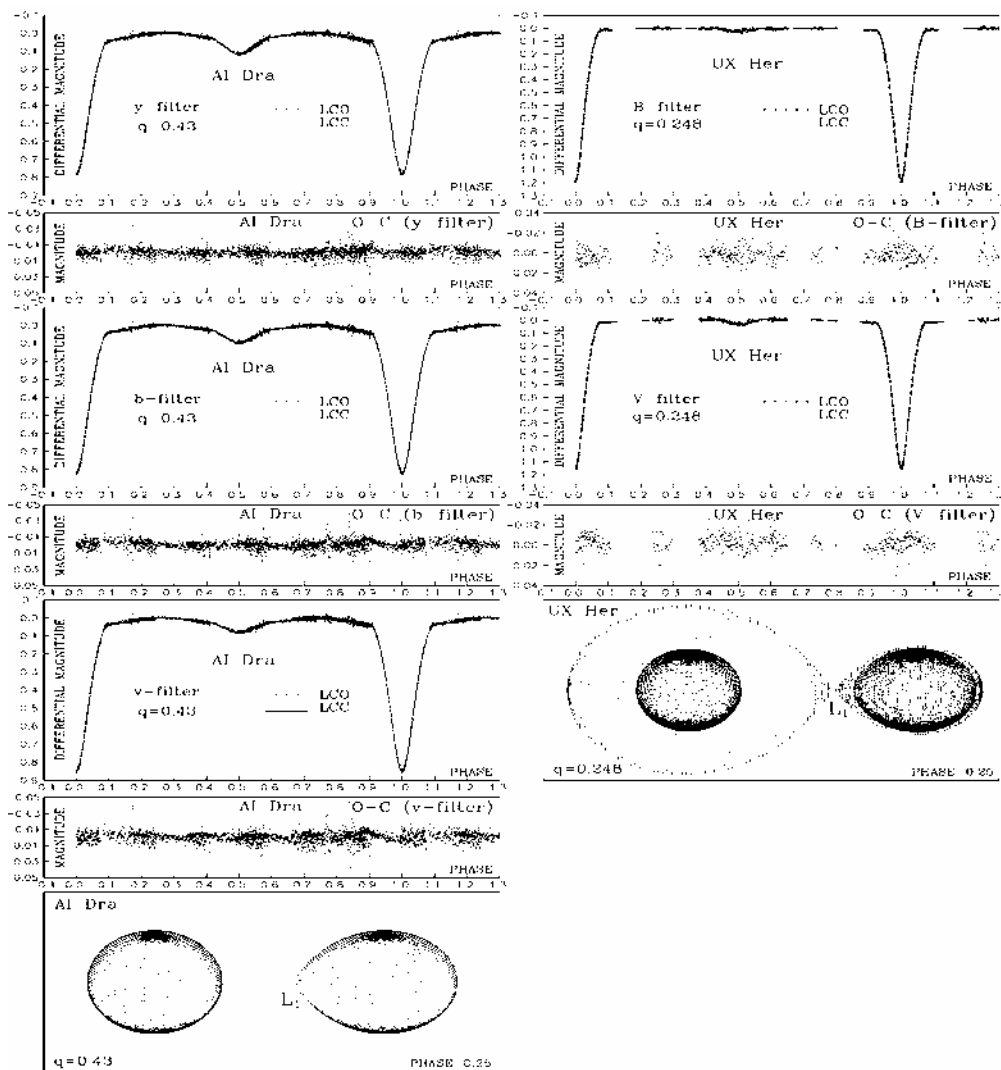
Figure 2. Observed (LCO) and final synthetic (LCC) light curves of *AI Dra* & *UX Her*, with final O-C residuals obtained by analyzing their observations, and the views of the systems at the orbital phase 0.25 obtained with parameters estimated in the light-curve analysis.

277

System Quantity	AI Dra y-filter	AI Dra b-filter	AI Dra v-filter	UX Her B,V-filters
n	2635	2635	2635	696
Σ (O-C)^2	0.0862	0.0927	0.1213	0.0344
σ	0.0057	0.0059	0.0068	0.0071
$q = m_c / m_h$	0.43			0.248±0.005
T_h	9800			9000
β_h	0.25			0.25
A_h	1.0			1.0
A_c	0.5			0.5
$f_h = f_c$	1.0			1.0
T_c	5607±15	5550±16	5445±20	4055±22
F_h	0.670±0.001	0.669±0.001	0.670±0.001	0.483±0.001
F_c	0.990±0.001	0.992±0.001	0.993±0.001	0.931±0.001
i [^{o}]	77.40±0.08	77.37±0.08	77.42±0.08	82.12±0.01
β_c	0.120±0.007	0.123±0.007	0.118±0.009	0.06±0.02
$a^{h,c}_1$	+0.5543,+0.5400	+0.4513,+0.4155	+0.4390,+0.5413	+0.4027,+0.5209 [B] +0.5877,+0.7136 [V]
$a^{h,c}_2$	+0.3222,-0.1002	+0.8004,+0.0291	+0.8980,-0.6903	+0.7907,+0.3053 [B] -0.6993,-0.9308 [V]
$a^{h,c}_3$	-0.2696,+0.8016	-0.7284,+0.8797	-0.8103,+1.7817	-0.5422,-0.1246 [B] +1.1472,+1.5821 [V]
$a^{h,c}_4$	+0.0717,-0.4229	+0.2283,-0.4501	+0.2534,-0.7090	+0.1238,-0.0076 [B] -0.0969,-0.4541 [V]
Ω_h	3.911	3.915	3.910	4.641
Ω_c	2.755	2.751	2.750	2.427
R_h [D=1]	0.286	0.286	0.286	0.227
R_c [D=1]	0.285	0.286	0.286	0.231
$L_h / (L_h+L_c)$	0.867	0.902	0.933	0.981 [B]; 0.973 [V]
$_h$ [M_s]	2.79±0.02			2.28±0.09
$_c$ [M_s]	1.20±0.02			0.56±0.11
$_h$ [R_s]	2.19±0.02			1.82±0.02
$_c$ [R_s]	2.30±0.02			1.94±0.02
log g $_h$	4.20±0.02			4.27±0.02
log g $_c$	3.79±0.02			3.62±0.02
M^h_{bol}	0.79±0.02			1.56±0.02
M^c_{bol}	3.17±0.06			4.89±0.06
a_{orb} [R_s]	7.521±0.006			7.97±0.01

Table 2. Results from the analysis of *AI Dra* (Strömgren *ybv*) light curves, and *UX Her* (BV) light curves obtained by solving the inverse problem for the

Roche model. Gravity darkening exponent of the cooler secondary component (β_c) was a free parameter.

Note: The labels are the same as in Table 1.

DISCUSSION

The light-curve analysis of the four semi-detached binary systems (*TW And*, *TW Cas*, *AI Dra*, *UX Her*) presented here, made within the Roche model and gave us the ***real possibility*** to estimate the GDE values for their secondary components ***without any additional approximations***. During the same analyzing procedure, we can estimate the systems' parameters, too, (as they are given at Tables 1 & 2). The estimated values of GDE basically confirm the theoretical predictions for stars with convective envelopes.

References
1. Zeipel, H. V., M. N. R. A. S. 84, 1924, 702.
2. Lucy, L. B., Zs. f. Ap. 65, 1967, 89.
3. Claret, A., Astron.Astrophys 359, 2000, 289.
4. Djurašević, G., Rovithis-Livaniou, H., Rovithis, P., Georgiades, N., Erkapić, S., and Pavlović, R., *A &A* 402, 2003, 667.
5. Amman, M., Walker, K., Astron.Astrophys. 24, 1973, 131.
6. Popper, D.H., Ap. J. S. 71, 1988, 596.
7. McCook, G.P., A.J. 76, 1971, 449.
8. Cester, B., Pucillo, M., Mem. Astron. Soc. Ital. 43, 1972,291.
9. Mardirossian, F., Mezzetti, M., Cester, B., Giurcin, G., Russo, G., Astron.Astrophys 39, 1980, 235.
10. Kiss, L.L. IBVS 5355, 2002.
11. Gordon, K.C., Kron, G.E., A.J. 70, 1965, 100.
12. Claret, A., Astron.Astrophys 363, 2000, 1081.

HELICAL INTERNAL STRUCTURES IN ERUPTIVE PROMINENCES

M. Dechev, P. Duchlev, K. Koleva and N. Petrov

Institute of Astronomy, 72, Tsarigradsko Chaussee Blvd., Sofia, Bulgaria
email: mdechev@astro.bas.bg

Introduction

Helical structures have been observed in many active prominences on the Sun. These structures can be roughly divided in two classes: internal (or microscopic) and external (or macroscopic). In the case of internal twist two or more fine threads with different helix radii are observed within the body of the prominence tube. In the second case, the whole body of a prominence tube shows helical twist or two or more tubes are intertwined in a rope-like structure.

Observation of twisted prominences have been reported by Jockers and Engvold [1], Rompolt [2], Wang [3], Vrsnak et al. [4] and Vrsnak et al. [5].

Twisted, helical-like patterns are more frequent in active region prominences. All these configurations can be represented by an axial current and so are equivalent to a simple twisted magnetic flux tube.

In the eruption phase, the morphology of a prominence often changes dynamically. In the late phases of the eruption usually a rather simple arch remains, frequently exposing helical-like structure. Such a behavior is described in Tandberg-Hanssen [6] and Vrsnak et al. [7].

A more detailed classification of the prominences exposing helical-like structures is made in Vrasnak et al. [5]. The authors described four main classes (Figure 1):
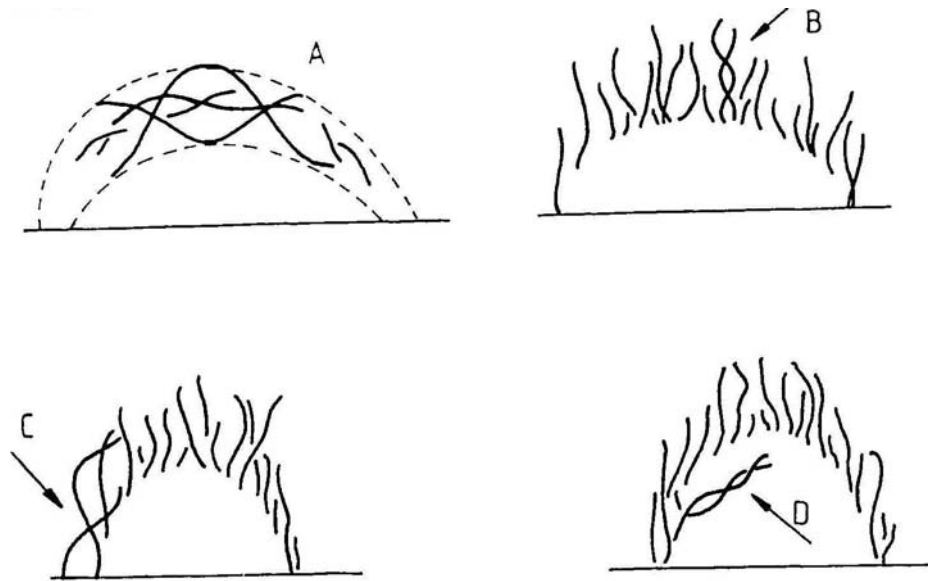
Figure 1. Classification of helical patterns in prominences
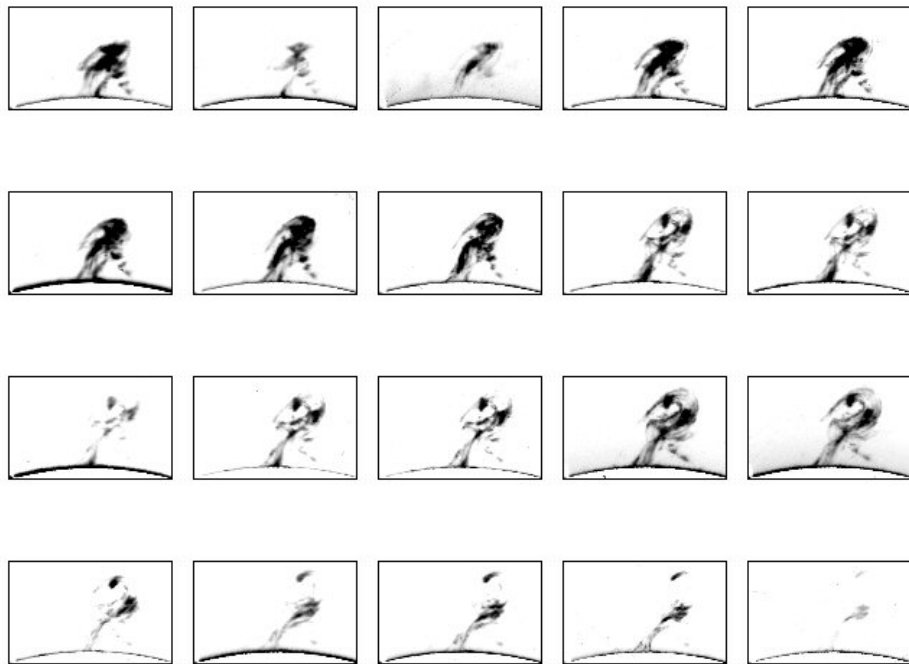
Figure 2. Eruptive prominence observed in H-alpha on May 7, 1979.

class A – pattern, where the threads are apparently twisted around the prominence cylinder axis;

class B – typical for huge QPs which have a sharp lower edge and a number of twisted threads extended upwards making the upper edge diffuse;

class C – "cross-like" structures in the legs of QPs or in the eruptive prominences;

class D – helical threads which are twisted around an axis parallel, but not coinciding whit the axis of the prominence.

There is theoretical support for the concept that the helical twisted structures are responsible for the eruption of prominences (Hood and Priest, [6]). The system becomes unstable and erupts when the twist increases to a critical value. Pneuman [7] gave adiabatic and isothermal models of a helical pinch rising in a low β atmosphere under influence of an ambient coronal magnetic field that decreases radially away from the center of the Sun.

Study of evolution of erupting helical prominences is important for a better understanding of structure, equilibrium and dynamics of prominences in general. This may also provide knowledge about stability of the other structures, which might be twisted, such as coronal loops, coronal arches and two ribbon flares.

In the following sections we discus the morphological details and evolution of the prominence eruption on May 7, 1979.

Observational material.

The eruptive prominence (Fig. 2) was observed in H-alpha on May 7, 1979 with a small coronograph at the Astronomical Institute of Wroclaw University, Poland. All H-alpha plates were digitalized with the automatic Joyce-Loebl MDM5 microdensitometer at National Observatory – Rozhen, Bulgaria.

The two-dimensional scans have a resolution of 20 µm per pixel and a step of 20 µm in both directions.

The prominence appeared on the western limb at a mean latitude of N38°. The prominence was observed between 13:38 UT and 14:26 UT. In this time interval prominence loop slowly rose and complicated its structure. After 14:24 UT it faded and disappeared.

Measurements and Results

Figure 3 represents a sketch of the measured prominence loop. With H1 is marked the maximal height point and H2 marks the height of the cross-point. Alpha is the angle between the legs of the loop.
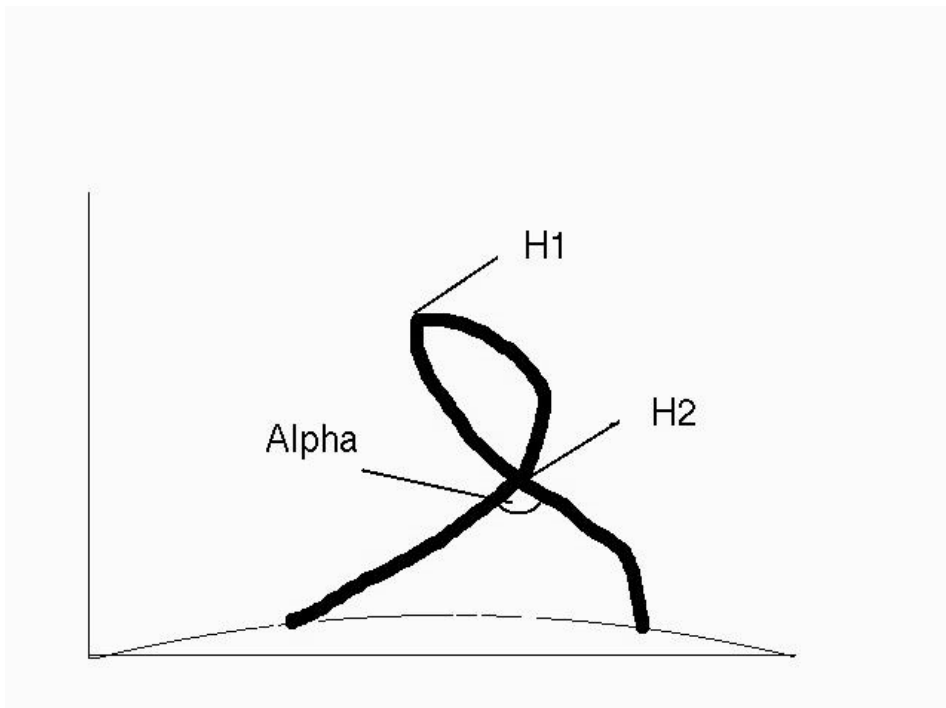
Figure 3. Sketch of the prominence loop.

On Figure 4 is presented height-time variation for these two points. Height is given in pixels (1 px is equal of 750 km). The time is given in seconds after 13:38 UT.

Figure 5 shows normalized differences between H1 and H2 as a function of time.

On Figure 6 is shown the angle variation as a function of time.

T – R periodogramme analyses of the angle variation gives two statistically significant periods of about 4 min and 14 min.

These angle variations can be result of three independent mechanisms: movements of the feet of the loop, propagation of some kind of wave mode along the loop or a shaking of the whole loop.

Our measurements showed that there are no observable movements in the legs, so the first mechanism can be excluded. If the angle variation is result of a pure wave mode propagating along the loop or a shaking of the whole loop, we should observe correlation between time variations of H1 and H2. As it is easily seen from Figure 5, there is no such a correlations.
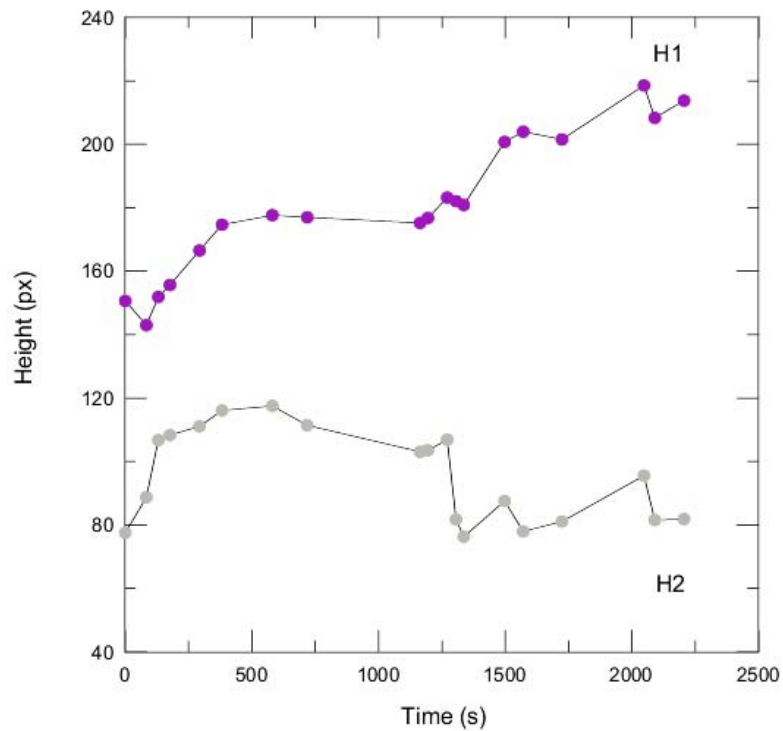
Figure 4. Variations of the measured H1 and H2 heights
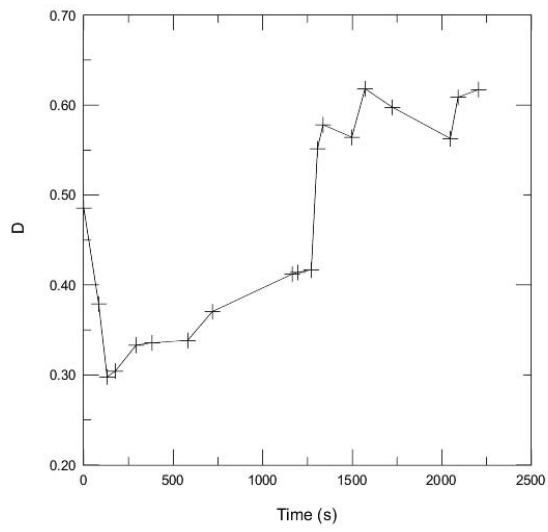
Figure 5. Normalized difference D between H1 and H2 as a function of time.
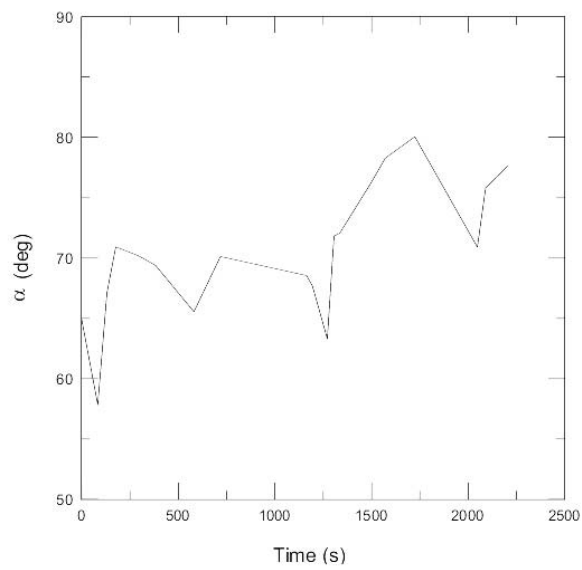
Figure 6. Angle variation as a function of time

So, the most probable explanation of the angle variation is a superpositionof propagating wave modes an a shaking of the whole prominence loop. Figure 6 demonstrates also an observable trend in the angle changes. This can be result of a mechanism of intensification of field-aligned currents, described in Nenovski et al. [8].

References

1. Jokers, K., O. Engvold, *Solar Phys*.,**44**, 1975, 44
2. Rompolt, B. *Solar Phys*., **41**, 1975, 329
3. Wang, J. L., in D. F. Neidig (ed), "The Lower Atmosphere of Solar Flares", 1986, National Solar Observatory, Sacramento Peak, Sunspot, New Maxico, USA, 466.
4. Vrsnak, B., V. Ruzdjak, R. Brajsa and A. Dzubur, *Solar Phys*., **116**, 1988, 45.
5. Vrsnak, B., V. Ruzdjak, B. Rompolt, *Solar Phys*., **136**, 1991, 151.
6. Tandberg-Hanssen, E., "Solar Prominences", 1974, D. Reidel Publ. Co., Dordrecht, Holland.
7. Vrsnak, B., V. Ruzdjak, R. Brajsa and F. Zloch *Solar Phys*., **127**, 1990, 119
8. Nenovski, P., V. N. Dermendjiev, M. Detchev, J.-C. Vial, and K. Bocchialini. On a mechanism of intensification of field-aligned currents at the solar chromosphere-quiescent prominence boundaries, *A&A*, **375**, 2001,1065.

AN ACTIVITY PATTERN OF AR NOAA 9026 DURING THE LAST HALF OF ITS EVOLUTION

K. Koleva, P. Duchlev, J. Kokotanekova and M. Dechev,

Institute of Astronomy, Bulgarian Academy of Sciences, Bulgaria

Abstract:

We have studied the evolution of active region NOAA 9026 by processing and analysis of white-light images and H_α filtergrams obtained in Astronomical Institute in Wroclaw (Poland). For determination of the full picture of activity events during the active region evolution the data from BBSO, GOES and Palma Reports were used. The sunspot evolution, filament and flare activities were summarized. The analysis of LASCO and EIT (SoHO) data suggests possible interrelations between associated with active region coronal mass ejections and filament eruption, as well as some X-flares in this region.

Introduction

The active region (AR) NOAA 9026 was observed on the solar disk from 02 to 12 June 2000. For the first time during this solar cycle, the Sun display a spectacular fireworks of many flares going off in close succession from one and the same active region.

The AR 9026 was observed in Wroclaw Astronomical Institute (Poland) from June 7, 2000 when it was located near the central meridian, to June 11, 2000. The registrations in white light and H-alpha were made. The observational data was processed with the Joyce Loeble microdencitometer in NAO Rozhen (Bulgaria).

For more detailed study of the active region evolution from its first appearance to its decay the BBSO Solar Activity Reports, GOES event list, and Palma Reports data were used.

Our aim was obtain a full picture of activity events, as well as some possible interrelations between them during the evolution of AR NOAA 9026.

Sunspot evolution:

The AR 9026 was observed for the first time at the E-limb on June 2, 2000. Its location was near N19E75. At the moment of its appearance the AR was observed as two well shaped sunspots with distinct penumbra. The

Maunt Wilson magnetic configuration was beta-gamma with possible delta configuration located on the southern edge of the leading spot.

There is a slight increase of magnetic complexity on June 5, 2000, which was change to large beta-gamma-delta region and strong delta configuration in leading spot. The leading part of the region was much larger and developed than the following one. The middle part contains a great number of sunspots with a common penumbra. The large sunspot in the eastern part of the AR has clearly expressed, regular shaped penumbra, with a magnetic polarity coincident with polarity of the polar magnetic field. This spot remains near constant in shape and dimensions over the time of observation.

On June 7, 2000 the AR 9026 was located near the central meridian at N20W02. On this date the sunspot group in AR has a complex beta-gamma-delta configuration. There is not a significant change in sunspot area and count.

A slight decrease of sunspot group dimensions is remarked on June 8. This variation is accompanied of the decaying of the leading part of the sunspot group and the breaking of the penumbra in the middle.

Rapidly decaying sunspot group shows little or no activity on June 9. The breaking of the penumbra in the middle part continues and the distance between sunspots increase. The leading part was already break up. Maunt Wilson classification has changed from β-γ-δ to β-γ.

On June 10 the sunspot group is rather simplified, containing some sunspots with penumbras.

Filament activity

Figure 1 shows the H-alpha filtergrams, made in Wroclaw Astronomical Institute. There are some quiescent filaments in the close proximity of the active region. Two of them exhibit a partial DB (disappearance brusque or sudden disappearance) and DB, respectively, on June 6, according to the Synoptic Maps of Solar Activity of the Meudon Observatory. During this day the imaging telescope EIT on board of SoHO observed the flare and filament eruption beginning at about 15:12 UT. There was also an earlier X1.1 flare and filament eruption from the same region at about 13:36 UT. Some of these quiescent filaments could be used to trace the area of solar rigid rotation near the active region in our future work.
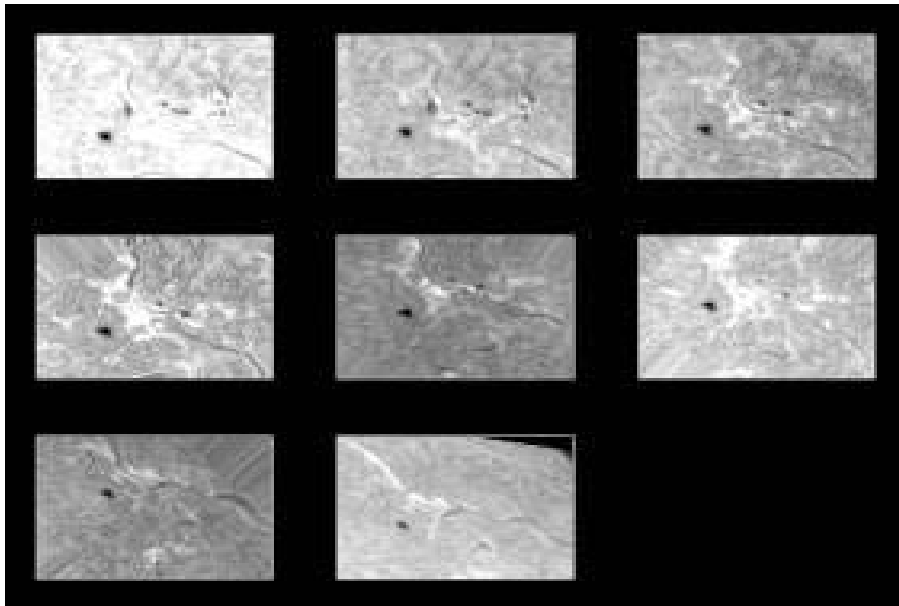
Fig 1. Filament evolution between June 7, 2000 and June 11,2000.

Flare activity:

The Table 1 shows chronologically the flares, associated with AR 9026. There are given the X-ray class of the events and the corresponding optical flares. A count of radio burst is presented too. We are used the GOAES event listing and the Palma reports.

A great series of flares was registered on June 6, 2000. The X-ray flare at 15:12 UT and this one at 13:36 UT were registered by EIT. There are another X-ray flares observed by EIT on June 7. The flare morphology was different than both X flares on June 6. It is not so much compact as the X2.3 flare and extends over a different region that the X1.1 one.

The C-class activity continues on June 8. There are not registered X-ray flares on June 9, 2000.

Fig. 2 represents H-alpha filtergram with the relative positions of the flare sites on the June 7.
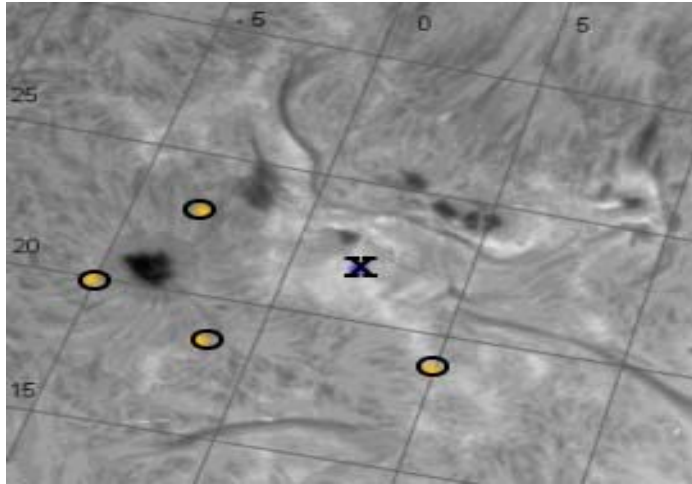
Fig. 2: Relative positions of the flare sites on the June 7, 2000. The circles marks optical flares and the cross mark X-ray flare.

Table 1.

Date	Peak time (UT)	X-ray class	Optical flare	Location	Count of Radio burst
1-JUN-00					5
2-JUN-00	19:38	M7.6			20
3-JUN-00	01:49	C7.0	SF	N20E57	11
	06:47	C4.6	SF	N20E54	
	14:24	C7.6	SF	N18E51	
	17:00	C3:0	SF	N17E49	
	19:24	M6.1	2B	N20E49	
4-JUN-00	04:32	C8.4	SF	N23E49	2
	20:18	C1.8	SF	N21E37	
5_JUN-00	11:30	C2			
	14:00	M1.5			
	18:35	C3.8	1F	N19E22	
6-JUN-00	08:36	C2.8	SF	N21E16	26
	08:51	C2.4	SF	N19E14	
	13:19	M2.7			
	13:39	M7.1			
	13:36	X1.1			
	15:25	X2.3			
7-JUN-00	15:53	X1.2	3B	N23E03	11
	15:53	X1.1			
8-JUN-00	04:36	C2.0	SF	N21W06	9
	05:28	C2.2	SF	N20W10	
	15:56	C1.7	SF	N20W11	
10-JUN-00	17:02	M5.2	3B	N22W38	13

Related activity:

Some enormous Coronal Mass Ejections (CME) were associated with active region passage on the solar disk – on 6 June, 7 June and 10 June.

On June 6, 2000 LASCO and EIT (both on board of SoHO) observed a full halo CME. The event was first visible at all position angles in C2 LASCO chronograph field of view at 15:54 UT. It appears as a bright front, particularly over the N pole, with trailing filamentary material. The plane-of-sky speed of the leading edge of the halo is about 908 km/s. It was supposed that the event was associated with an X2.3 flare and filament eruption in AR 9026 during this day.

LASCO and EIT registered another halo CME on June 7. The event was first visible as a faint diffuse front in C2-chronograph field of view at 16:30 UT. The CME was probably associated with an X1.2 flare in AR 9026, located near central meridian at about N20 E02. The plane-of-sky speed was about 411 km/s.

Conclusions

This study of AR NOAA9026 brings out the full picture of its evolution at different heights in the solar atmosphere. We follow the sunspot, filament and flare evolution in the region, as well as the coronal response.

The next step of this study will be to determine the Doppler shifts and to precise the pre-flare conditions. We will search for area of rigid rotation (pivot-point) near the region using the quiescent filaments as tracers. Because of the very high flare activity, related to this active region, the availability of pivot-point is very likely.

CARBON-CONTAINING NEUTRALS AND THEIR SPATIAL DISTRIBUTION IN THE HALLEY COMET COMA

V. Guineva, R. Werner, P. Stoeva

Solar-Terrestrial Influences Laboratory, Stara Zagora Departent,
Bulgarian Academy of Sciences, Bulgaria
e-mail: v_guineva@yahoo.com

Introduction.

Carbon plays a major role in the physical and chemical processes in the Solar system, due to its quantity and great chemical diversity and, mostly - to its great biological significance. The observations of Halley's comet show that carbon is the main constituent of the cometary nucleus. Emissions of different carbon-containing radicals and ions are registered. The C_2, C_3, CH и CN emissions are some of the strongest in the visible region. In order to investigate the separate bands with spectrophotometric observations, it is necessary to separate correctly their glow from the measured spectra.

In order to study the carbon-containing neutrals glow, the spectra in the near UV and visible region are used, registered by the three-channel spectrometer (TCS) on board the VEGA-2 Interplanetary station in the Sun coma on 9 March 1986. The spectra are totally 1035, 667 of which in mode A when the instrument scans a rectangular region with 2°x1.5°sizes, 15x7 positions and, 368 in mode B when VEGA-2 is closest to Halley's comet and TCS scans only along the central line – 15 positions, a spectrum being registered in each position.

II. Separation of the carbon-containing neutrals emissions by the TKS - registered spectra.

The correct separation of the cometary components emissions by the registered spectra is of crucial importance for the analysis of their distribution around the cometary nucleus.

The precision of a given band separation depends on the selected wave interval width, on the method for calculating the spectral index **u**, which determines the dust continuum course [1] and on the way for normalizing the dust continuum to the measurement data. A criterion for the

quality of the method for separating the column intensity of a specific emission by the measured spectra can be the type of its dependence on the projected distance to the nucleus or, the **p**-parameter (the perpendicular from the nucleus to the line of observation). The more compact this dependence (the points around a given curve are grouped more densely), the better the glow of the investigated constituent is separated.

II.1. Calculation of the spectral index *u* for each spectrum.

The spectral index **u** determines the form of the curve, describing the dependence of the dust continuum intensity on the wavelength:

$$I_d = I_s \lambda^{-u+2}$$

The investigations show that with changing parameter **u** even by 0.1, the dust continuum changes noticeably. This requires **u** to be calculated most precisely. Until now it was calculated by a linear regression on the basis of 11 dust points as the regression coefficient was determined by the least squares method. The intensity was obtained by averaging 5 consecutive pixels (30 Å), centered on the respective dust line [1].

The dust points involved in the calculations are reconsidered and the intensity average deviation values are examined for each line as well as the length of the confidence interval for parameter **u**, depending on its inclusion and exclusion.

The dust line at 4100 Å cannot be used for calculations of spectra, measured by TCS because the adjacent cometary emissions cannot be well separated in this region. Instead, the calculations include the 3760 Å line. The dust lines 4250 Å, 6770 Å и 6840 Å also drop off. The computing of the spectral index **u** is made on the basis of the following 8 dust lines: 3760, 4520, 4860, 4890, 5260, 6100, 6250, 6500 Å, as the average intensities of 3 pixels, centered along the respective wavelength in the non-deconvoluted spectra are used.

The confidence interval of 95 % for the spectral indices, thus obtained, is several times smaller and the statistical regression coefficient is several times larger than in the previous calculations. The parameter is obtained within the limits of 3÷3.4 for 95% of the spectra and, for the remaining 5 % the interval is extended from 2.1÷3.7. For all 1035 spectra $u_{cp.}$=3.1768, $du_{cp.}$=0.1896, for mode A (667 spectra) $u_{cp.}$=3.2126, $du_{cp.}$=0.2282, for mode (368 spectra) $u_{cp.}$=3.1119, $du_{cp.}$=0.1197.

II.2. Dust continuum norming to the measurement data.

So far, in order to subtract the dust continuum from a given cometary emission, it was normed to its closest dust line, as the minimum in a definite interval around this line was searched [2]. The attempts have

shown that if the dust line is not well selected (for example, 4100 Å) or, the found minimum is not suitable, considerable errors can be made in the determination of the investigated emission intensity, displayed in the large distribution of points in the **p**-parameter dependence.

To avoid this and to obtain more precise data, subject to investigation and analysis, the norming coefficient of the dust continuum is determined by a linear regression on the minima of the deconvoluted spectra in the following 7 dust intervals: 3660÷3800 Å, 4500÷4650 Å, 4819÷4915 Å, 5214÷5333 Å, 6064÷6141 Å, 6206÷6306 Å, 6450÷6600 Å.

The obtained continuum and its norming correspond well to every spectrum. Fig.1 presents 2 spectra with different intensity and the dust continuum for each of them, determined in the above-described way. Vertical lines show the seven minima of each spectrum according to which the dust continuum is normed.
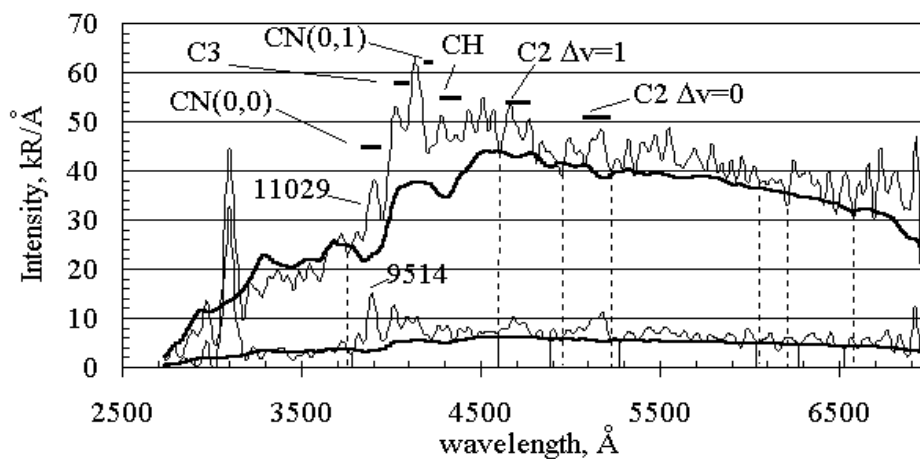
Fig.1. Two spectra on 9.03.1986 with different intensities, registered at board time 9514 sec. and 11029 sec. (board time 0 sec. corresponds to 4:12:38 UT). A darker line below the spectra marks the dust continuum, determined in the above-described way. Vertical lines show the seven minima of each spectrum according to which the dust continuum is normed. Horizontal lines mark the intervals in which the CN, C_3, CH and C_2 bands intensities are summed up

III. Determination and analysis of the emissions intensity, depending on the projected distance to the nucleus.

III.1. Determination of CN, C$_3$, CH and C$_2$ intensities.

In order to determine the carbon-containing neutrals intensities, the intensities within intervals of the processed spectra, covering almost the entire glow region of the examined bands are summed up.

The following intervals are used: CN(0,0) – pixels 343÷357, $\lambda\lambda$ 3842÷3933 Å, CN(0,1) – pixels 401÷404, $\lambda\lambda$ 4193÷4217 Å, C$_3$ – pixels 374÷382, $\lambda\lambda$ 4030÷4084 Å, CH – pixels 415÷426, $\lambda\lambda$ 4277÷4346 Å, C$_2$ $\Delta v=0$ – pixels 548÷570, $\lambda\lambda$ 5076÷5214 Å, C$_2$ $\Delta v=1$ – pixels 476÷496, $\lambda\lambda$ 4645÷4755 Å.

These intervals are marked by horizontal lines over the spectra in Fig.1.

III.2. Dependencies of the emissions intensities on the p-parameter.

In the near-nucleus region, the environment cannot be treated as optically thin. The need of an estimate of this fact is clearly seen in the case of the dust continuum (Fig.2). The continuum course with the **p**-parameter coincides the best with the curve, obtained when the optical depth of the inner coma environment is taken into account. It is obtained, that $\tau=1$ at about 200 km.
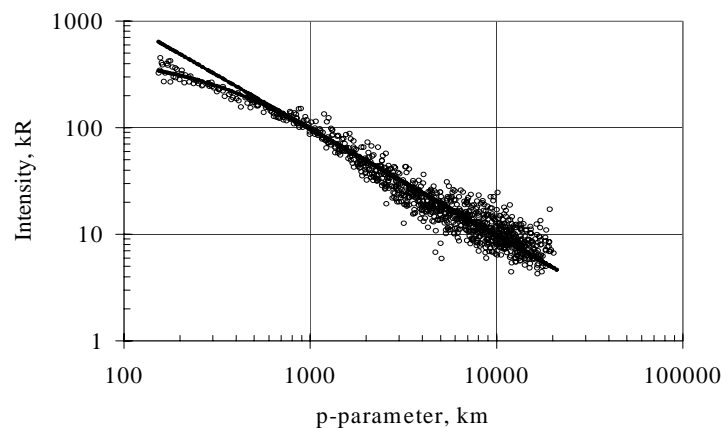
Fig.2. The measured dust continuum. The straight line presents the dependency I=1/p, and the curved in the near-nucleus region one – the same dependency, when the optical depth of the inner coma environment is taken into account. It is obtained, that $\tau=1$ at about 200 km.

The obtained dependencies of the examined emissions intensities on the **p**-parameter are more compact than those obtained in the previous way [2], especially in the cases of C_3 and CH. A larger distribution of the points is observed already with the CN(0,1) intensities which probably is due to the fact that this band is weaker and is mixed with a stronger one, which is seen in Fig. 1. It is possible such emissions to be separated by using non-deconvoluted spectra and very narrow intervals, in which to sum up the intensities.

Fig.3 shows the dependencies of CN(0,0), C_3, CH and C_2 $\Delta v=0$ intensities, corrected with the optical depth, on the **p**-parameter. The curves represent the Haser's law. The needed parameters for the different constituents are taken from [3]. For all emissions a better compliance with Hazer's law is seen than the established by Werner et al. [2] one. The deviation at **p**<1000 km, especially expressed for CN and C_3 [2], is eliminated. It obviously has been a result of incorrectly subtracted dust continuum.
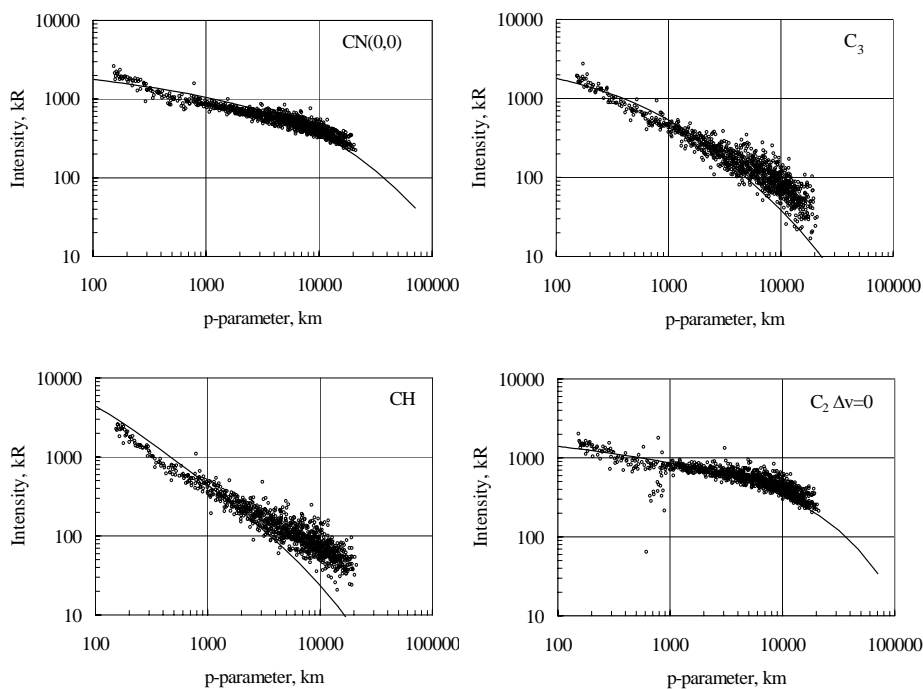
Fig.3. Intensity dependencies on the perpendicular distance, obtained from all spectra measured on 9 March. The dust continuum is extracted in the way, described in this work. Data correction with the optical depth is performed. The curves represent Haser's law.

The dependence of CH on the **p**-parameter is close to the one, obtained by Arpigny et al. [4], with ground-based observations of Halley's comet on 16 March 1986. The results for CN, C_3 and CH are similar to the ones, obtained by Umbah et al. [5], in the **p**-region, which is common for them.
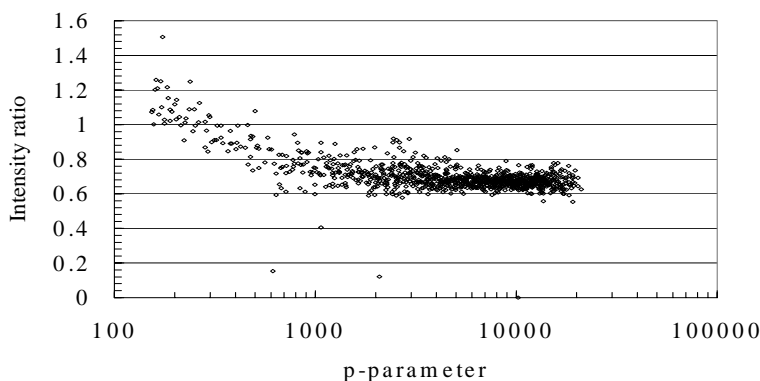
Fig.4. Intensity ratio of the $\Delta v=1$ to $\Delta v=0$ sequences of C_2. The intensity courses differ from each other to distances of about 2000 km from the comet Halley nucleus.

The obtained intensity of $\Delta v=1$ of C_2 sequence of Swan's system decreases more quickly with increase of the **p**-parameter as compared to that of $\Delta v=0$. Fig.4 shows the ratio of these sequence intensities versus **p**. It is seen that the $\Delta v=1$ and $\Delta v=0$ intensity courses differ up to about 2000 km from the Halley comet nucleus. At greater distances to the nucleus the ratio remain almost constant, its values being distributed in an interval less than 0.2. The change of this intensity ratio towards **p** is established and investigated by many authors [6] and it is explained by the cascade transitions between the singlet and triplet conditions, which allow population change of the lowest vibrational levels. The range of the change we have obtained is the same as the one, registered by Vanýsek and Valníček [6].

IV. Conclusions.

An improved method is applied to subtract the dust continuum from the spectra of Halley's comet, registered by TCS on board the Vega-2. For each spectrum, the spectral index **u** is calculated by 8 dust points, selected so as the confidence interval to be the least possible. The dust continuum is normed by 7 dust regions on the basis of a linear regression.

The evaluation of the dust continuum in this way is reliable and the intensities of the carbon-containing neutral emissions CN, C_2, C_3 and CH are obtained more precisely. The obtained dependencies of the intensity on the **p**-parameter are with higher quality. Compliance is established with Hazer's model. The peculiarities of those molecules glow, published so far, are confirmed.

References:

1. Stoeva, P., R. Werner, V. Guineva, St. Staykova, Investigation of the Halley comet dust size distribution by the Vega-2 Interplanetary station visual spectra, in Tenth International School on Quantum Electronics: Laser Physics and Applications, Peter A. Atanasov, Dimitar V. Stoyanov, Editors, Proceedings of SPIE, v. 3571, 1999, pp. 307-311
2. Werner R., V.Guineva, P.Stoeva, St.Spasov, The Spectrum of Comet Halley Obtained by VEGA - 2, Advances in Space Research, v.9, 1989, No3, pp.(3)221 - (3)224
3. Arpigny C., C.J.Zeippen, M.Klutz, P.Magain, D.Hutsemékers, On the interpretation of the CH cometary spectrum, Symposium on the Diversity and Similarity of Comets, 6-9 April 1987, Brussels, Belgium, ESA SP-278 (September 1987)
4. Krasnopolsky, V.A., M.Gogoshev, G.Moreels, V.I.Moroz, A.A.Krisko, Ts.Gogosheva, K.Palazov, S.Sargoichev, J.Clairmidi, M.Vincent, L.Bertaux, J.E.Blamont, V.S.Troshin and B.Vaníček, Spectroscopic Study of Comet Halley by the Vega-2 Three-Channel Spectrometer, Nature, v.321, 1986, No6067, pp.269-271
5. Umbah R., K.Jockers, and E.H.Geyer, Spatial distribution of neutral and ionic constituents in comet P/Halley, Astron. Astrophys. Suppl. Ser., v.127, 1998, pp.479-495
6. Vanýsek V. and B.Valníček, Flux Ratio of C_2 Swan Bands in the Innermost Atmosphere of Comets, Adv. Space Res., v.9, 1989, No3, pp.(3)191 - (3)194

WAVELET ANALISYS OF THE SOLAR ROTATIONAL ACTIVITY VARIATIONS

R.Werner (1), A.Hempelmann (2), D.Valev (1), I. Kostadinov (1,3),
At.Atanassov (1), G.Giovanelli (3), A.Petritoli (3), D.Bortoli (3),
F.Ravegnani (3)

(1) Solar-Terrestrial Influences Laboratory, Stara Zagora Department,
BAS, Bulgaria
(2) Hamburg Observatory, Hamburg University, Hamburg, Germany
(3) Institute of Atmospheric Science and Climate, Bologna, CNR, Italy

Introduction

The study of the solar activity has been of great interest for a long time. On the one hand it is important for the understanding of the Sun as an active star and on the other hand – for the investigations of the solar-terrestrial connections.

The solar magnetic field reverses approximately every 22 years, and manifests the 11-year solar cycle, in which the Sun changes its activity from its maximum to its minimum value. The activity variations, developed by the sun surface rotation in connection with the nonsymmetrical distribution of active regions over the solar disc are in a shorter time scale. As it is well known, these variations have periods of about 27 days. The amplitude of the solar irradiance variations is strongly dependent on its wavelength and increases towards shorter wavelengths. Over a solar cycle, the total solar irradiance changes with only 0.1%, yet in the UV and shorter wavelengths they exceed those by orders of magnitude [1]. The changes in this spectral range are of basic importance for the solar-terrestrial influences and require detailed analysis of the growth and decay of active regions, because the EUV solar irradiance is fully absorbed by the Earth atmosphere, and the UV irradiation is absorbed partially.

27-day Solar Cycle

In the sense of the statistical average, in the beginning of the solar cycle, the active regions originate at heliographic mid latitudes Φ and shift equatorwards with the cycle extension. The solar surface rotates with different velocity, depending on the latitude. The differential solar rotation period, observed from the Earth, can be approximated with sufficient

accuracy by: Psyn = 26.75 + 5.7 sin2Φ [2]. A wider spread of the solar activity indices is observed, however, around the 27-days period. At first, the 27 periodicity is non-sinusoidal and higher harmonics can appear in the spectra. Donnelly and Puga have shown that the second harmonic (the 13.5 day oscillation) is of physical nature and includes predominantly two groups of activity regions with a phase shift of approximately 180° [3]. A 12-14 day period is obvious in most indices, related to chromospheric emissions, such as the CaII-K plage index, but is absent in the F10.7. Generally, however, the periodicities range from 20 to 36 days. It is pointed out that the indices with "periodicities around 30-34 days shifted to about 26-28 days in 1982", when the Sun was in a maximum activity phase. Bouwer concludes that the "period is a result of the combination of active-region evolution and solar rotation (i.e. not due to the differential rotation)"[4] A reason for the widely spread periodicities around 27 days is that the dominant radiance within an active region can move rapidly forward or backward in respect to the solar surface [5]. The power spectra of projected areas of active and passive spots show the 27-day rotation, active spots besides 28 and 25, 51 and 157 day periodicities [6]. Bai remarks that the periodicity at approximately 25 and 50 days are maybe harmonics of the Rieger's period (about 150 days) [6].

Data set preparation

For our analysis we have used the CaII-K-line index from the Big Bear Solar Observatory (BBSO) for the time period from 1996 until 2003 (ftp://ftp:bbso.njii.edu/pub/archive/). The index is determined by Sun images in the K-line (393.9 nm) with a 1.5Å FWHM filter, obtained by a CCD camera. Indices are formed by integrating the brightness above thresholds of 0% (D0 index), 2.5% (D25), 5% (D50 7.5% (D75) and 10% (D100). The pixel numbers above the threshold at 7.5% produce the plage area index (D75A - index 05 in the BBSO data archive). It is expected that the correlation between the indices and the solar Lα irradiation is the best for the D0 index, since the network is more prominent in the Lα flux. While for higher thresholds weak networks are cut and plages and bright network spots are dominant, in the images stronger 27-day modulations are provided by higher D-indices. The year 1996 is approximately the solar activity minimum and in October the current 23rd solar cycle 23 begins (see Fig. 1). In particular, the analysis is carried out with the CaII-K line plage area D75A-index, which shows strong rotational modulation and for the comparison - the D0-index. To represent the 27-day rotational modulation,

the time series are divided into two parts. The first one includes the last part of the solar minimum before October 1996 and the increased solar activity phase up to the end of 1999 and, the second one includes the solar maximum and the start of the decline phase. In the data set the only missing
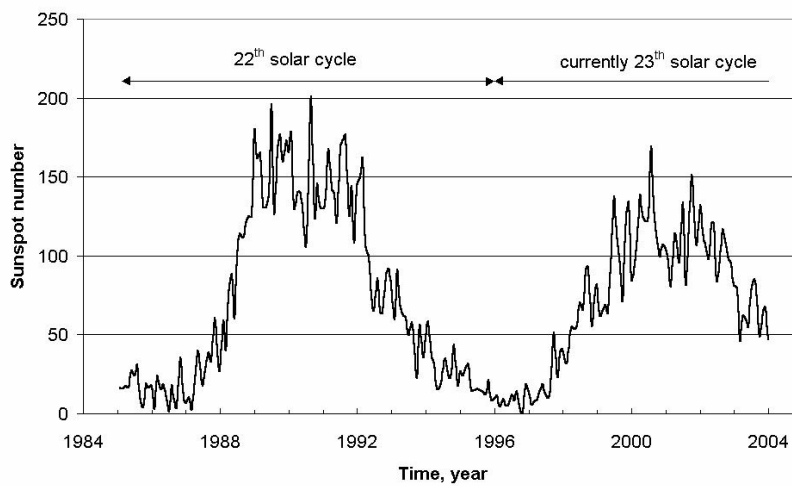
Fig 1. The 11-year solar activity evolution during the last and the currently solar cycle, expressed by the Greenwich Sun spot number. It is accepted, that in October 1996 was started the currently 23th solar cycle.
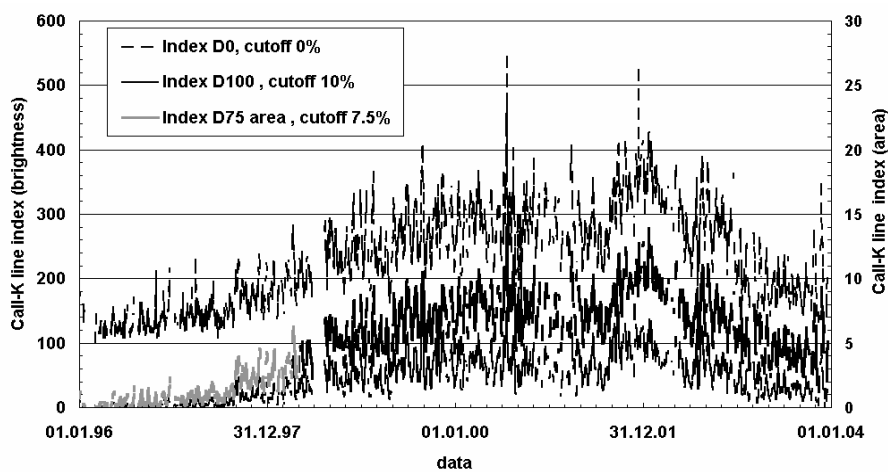
Fig. 2 Time evolution of the D00, D100 and D75A CaII-K line index from 1. January 1999 up to 31.Decmber 2003. The indices D25, D50 and D75

values (not shown) are located between D0 and D100 from greater to smaller brightness respectively to increased thresholds.

data are for successive days over a time interval of some days and very rarely of a longer period. The missing data are linearly interpolated (with the values at the interval end points) and for intervals longer than 5 days, the corresponding day number is stored. Smoothed by running mean over 41 days series were subtracted from the interpolated time series to bring out the periods about 27 days. For data gaps longer than 5 days the values of the time difference series are set to zero, because the interpolated values over larger time intervals differ strongly from the real values. As seen in Fig. 2 the rotational amplitudes are very different during the different activity phases. They are very small at the solar minimum and then they continuously increase with the activity increase. For the time period 1996-1999 the obtained 27-rotation variation of the index has been divided by solar activity, approximated by a low order polynomial. The changes of the activity indices by the Sun rotation are much more regular around the solar maximum and additional data processing is not necessary.

Simple solar activity model

The CaII K line time series shows, that the short-time periods are modulated by periods of several months (see also Fig 4 and 5). The obtained behaviour can be described in first approximation by a simple model, which consists of a harmonic oscillation with simultaneous amplitude and phase modulation:

$$B = A\,cos[(\,t - t_1\,)\,\omega\,],$$

where A is the amplitude modulation:

$$A = 1 + cos[(\,t - t_2\,)\,\omega_1\,],$$

and w is the phase modulation:

$$\omega = \omega_0\left\{1 + d * cos[(\,t - t_3\,)\omega_2]\right\},$$

and t_1, t_2, t_3 are the phase shifts. The Period of the Sun rotation is T_0 and it is chosen to 27-days and w_0 is the corresponding angular frequency. The period of the amplitude modulation w_1 is selected to several Sun rotations. We have fixed w_1 to nw0, with n=8. (n is not required to be an integer number). We have set the phase shifts t1 to $T_0/2$ and t_2 to $nT_0/2$. In that way the amplitude maximum of A is reached at the half of the period length. We have studied only the influence of the phase shift t_3. The modulation index d is fixed at 0.1. For a further simplification $\omega_1 = \omega_2$ is set. Thus, the phase

modulation describes the growth or decay of the period during the active region evolution expressed by amplitude modulation A. (For results see Fig. 3)
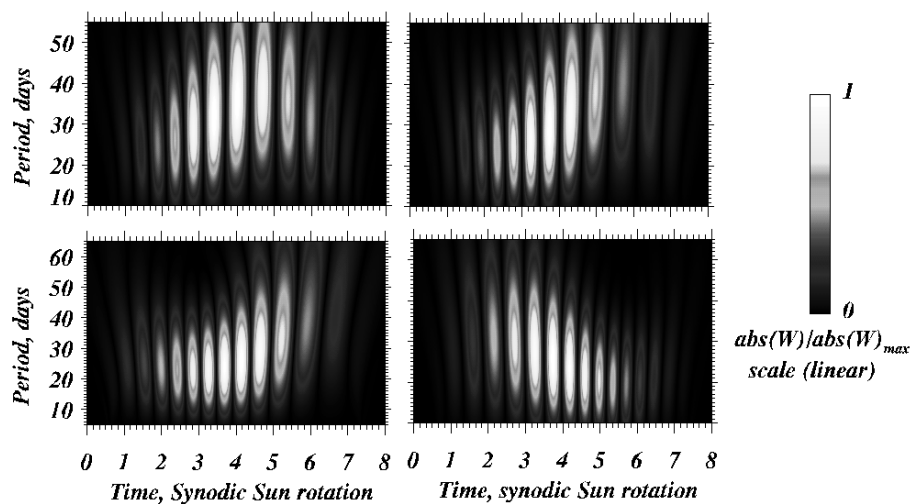
Fig. 3 Wavelet spectra of the modeled solar activity for the time of the first amplitude period for some phase shifts t1. Top: left $t_1=T_0$, the maximum of the amplitude of solar rotation activity variation is in coincidence with the maximum of the amplitude modulation located at 4 Sun rotations, right $t_1=3T_0$, the period of solar activity slowly increased, however the maximum of its amplitude is reached before the period maximum and the activity decrease suddenly, bottom, $t_1=5T_0$ the maximum of the solar activity variation is in coincidenc with the minimum of reached period, and right $t_1=7T_0$. The solar activity at the beginning of signal is relativly low but the period is high, with inceasing of the time the period is decreasing and after the transition of the activiti maximum it is decay. It is obiuse high freqency correcponding to a 20 day period.

Wavelet basics

A new tool – the wavelet analysis, is successfully applied in the last years for analysis of geophysical time series[8,9]. Hempelmann has developed a method to determine the duration of the Sun differential rotation [10] and for stars, rotating as slow as the Sun [11]. Soon and Baliunas have found by wavelet time frequency approach that the rotation of some chromospheric active stars is at least 10 years long [12]. The long-

period solar activity wavelet analysis was carried out by Le [13]. A wavelet is a function and satisfies the conditions of:

zero mean

$$\int_{-\infty}^{\infty} \psi(t)\,dt = 0$$

(i)

and additionally the normalization $\|\psi\| = 1$.

(ii)

(It should be noted that the condition (ii) under certain circumstances is equivalent to the criteria of the regularity). The continuous wavelet transformation (WT) $W\psi$ for a given mother wavelet of a time signal $f(t)$, is defined as:

$$W_\psi f(a,b) = \int_{-\infty}^{\infty} f(t)\,\psi_{a,b}^*(t)\,dt$$

with the complex conjugate wavelet function

$$\psi_{a,b} = \frac{1}{a^{\frac{1}{2}}}\psi\!\left(\frac{t-b}{a}\right),$$

where $\psi_{a,b}$ represents the mother wavelet ψ, shifted by b and dilated/compressed by a. The factor $1/a^{1/2}$ satisfies the normalization condition. Since the beginning of the eighties, when the wavelet theory was first developed, many mother wavelets have been found. The simplest of them are the Haar- and Morlet-wavelets and the Mexican hat. In the following

$$\psi = \left[1 - (ct)^2\right]e^{-(ct)^2/2}, \qquad\qquad \text{with} \quad c = 4$$

is used as a mother wavelet [14]. This is the so-called Mexican hat wavelet, because the graph of this function is similar to them. The Mexican hat is a simple real function and the calculation of WT is comparatively fast. Moreover, the function is symmetric, which is useful for identifying regions of maximum/minimum curvature [15].In analogy to FT, the spectrum is given by $\left|W_\psi f\right|$ and the power spectrum by $\left|W_\psi f\right|^2$. The result of the WT $W\psi(a,b)$ is defined in the phase plane, spanned by the time shift b and the scaling parameter a. For the chosen wavelet with $c = 4$ the scale parameter a at maximum and minimum of $W\psi(a,b)$ presents directly the

signal period. For the interpretation of the wavelet spectrum it is important to note that the frequency resolution for constant *b* is proportional to *1/a* and it decreases with the increase of ω, but the time resolution increases with the decrease of *a*. This is the typical wavelet zoom effect. In consideration of the frequency filtering of a given time series it should be noted that WT is similar to a convolution (For *a* = 1 the WT is exactly the convolution of the time signal *f(t)* with the analyzed wavelet.) The time series are filtered by a more stretched /compressed filter function (mother wavelet) by increasing/decreasing scale parameter *a*. The resulting wavelet spectra are given at the fig. 4 and 5.
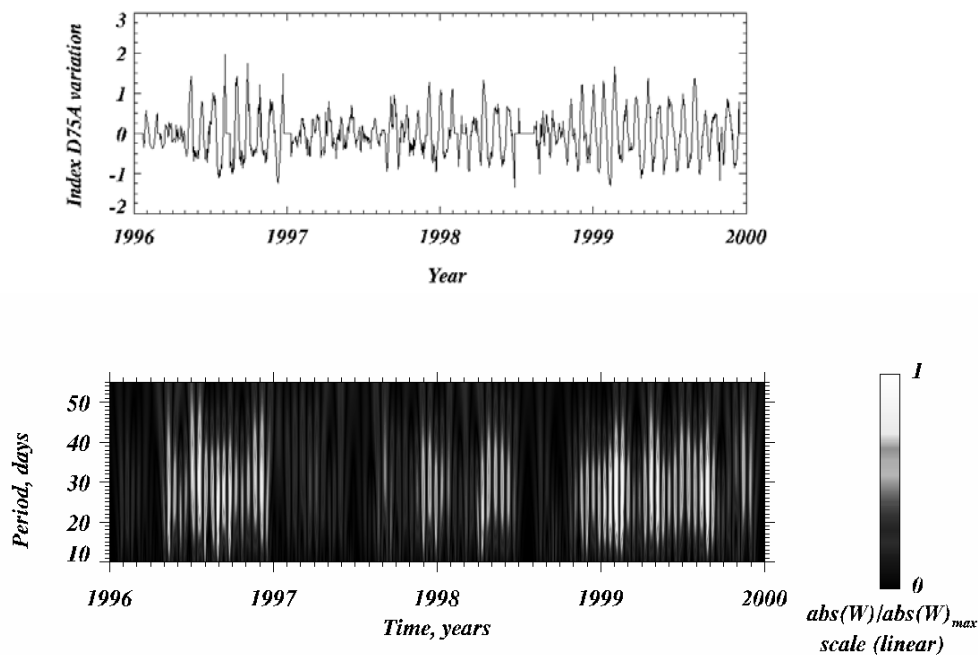
Fig 4. a) Long time removed time series of the CaII-K line core index for the minimum between the 22 and the 23rd solar cycle 1.Jan. 1996 up to increase par of the 23rd cycle 31.Dec.1999. (For processing details see the text) b) The wavelet spectrum of the time series shown at a)
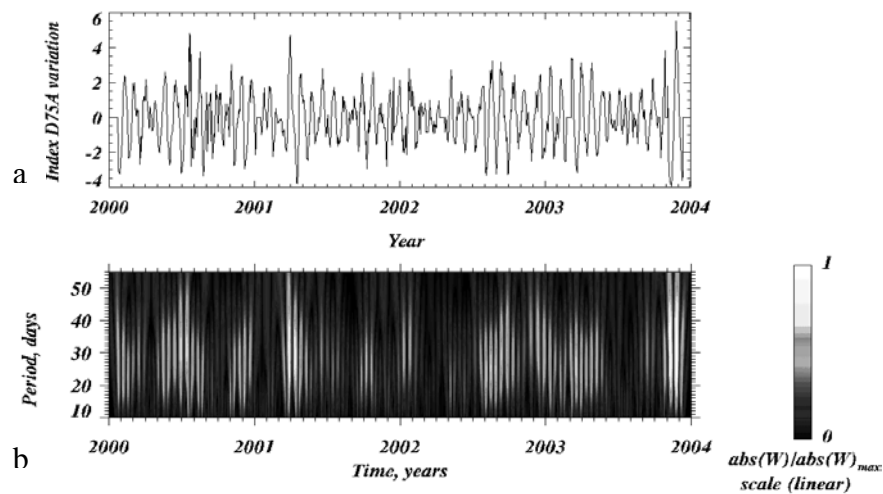
Fig 5. a) Long time removed time series of the CaII-K line core index for the maximum of the 23rd solar cycle 1.Jan. 2000 and the begin of the decreasing phase pu to 31.Dec.2003 b) The wavelet spectrum of the time series shown at a

Results

The time series have displayed obvious packets with period lengths of several months, modulating the solar activity variation caused by the rotation cycle. This period is probably related to active region growth and decay, i.e. the typical lifetime of a single spot group or an active region. The areas and the brightness of an active region decay/grow after the plage formation. The parent spot of a bipolar group of a developing region travels slightly forward with increasing the distance to the subsequent spot. With decrease of the active region, the parent spot shifts backward nearly to its initial heliographic longitude, the bright remnants always trailing behind and towards the poles. The appearance or the decay of new regions changes the activity distribution over the solar disc. These processes modify the observed rotation period. The wavelet analysis of the shows clearly a change of the period from 22 up to 34 days, which is significantly longer than that, predicted only by the differential sun rotation.

Conclusions

306

The simple solar activity model, which takes into account phase and amplitude modulations, can be used to explain that the periods due to the solar 27-rotation cycle are in a range of 22 up to 34 days and both kinds of modulation are consequence of activity region growth or decay, hence, they are a result of a variable pattern of spots and active regions on the solar surface. The areas and the brightness of an active region grow after the plage formation. The parent spot of a bipolar group of a developing region travels slightly forward with increasing the distance to the following spot. With decrease of the active region, the parent spot shifts backward nearly to its initial heliographic longitude, the bright remnants always trailing behind and towards the poles. The appearance or the decay of new regions changes the activity distribution over the solar disc. These processes modify the observed rotation period. The wavelet analysis shows clearly a change of the period from 22 up to 34 days, which is significantly longer than that, predicted only by the differential sun rotation. We have described the variability of the longer period by amplitude modulation, while the shortening and the prolongation of the solar rotation period can be modeled by a phase modulation. The superimposing modulations change the period more than twice by nonlinear effects. The proposed simple empirical model describes with good quality the separate episodes of the active region evolution. Both kinds of modulation are the consequence of activity region growth or decay and hence, they are a result of a variable pattern of spots and active regions on the solar surface.

The applied method based on wavelet analysis is very useful to study of the duration of several solar periods and its progress.

References
1. Fligge, M, S.K. Solanki, The solar spectral irradiance since 1700, Geophys. Res. Lett. Vol. 27, No. 14, 2157 – 2160
2. Lang, K.R. Astrophysical Data: Planet and Stars, Springer-Verlag New York etc., 1992, 104
3. Donnelly, R.F. and L.C.Puga, Solar Physics, vol. 130, 1990, 369
4. Bower, S.D. , Periodics of solar irradiance and solar activity indices, II, Solar Physics, 142 (1992) pp. 365 - 389
5. Kane, R.P, Fluctuations in the ~ 27-daz sequences in the solar index F10 During solar cycles 22-23, Journ. Atmosp. Solar-Terr. Phys.,65, 2003, 1169 – 1174
6. Pap, J., W.K.Tobiska, S.D.Bower, Periodics of solar irradiance and solar activity indices, I, Solar Physics, 129, 1990, 165 - 189
7. Bai, T, Periodicities in Solar Flare Occurrence: Analysis of Cycles 19-23, The Astrophysical Journal, vol.591, Issue 1, 406-415.

8. Liu, H.-S. and   B.F.Chao Wavelet Spectral Analysis of the Earth's Orbital Variations and Paleoclimatic Cycles, Journal of Atmospheric Sciences, vol 55, no.2, 1996, 227 – 236
9. Liu, P.C. Wavelet Spectrum Analysis and ocean Wind waves, Wavelets in Geophysics ed. by E.Foufoula-Georgiou and P.Kumar, Academc Press, 1994, 151 - 166
10. Hempelmann, A. and R.A. Donahue, Wavelet Analysis of Stellar Differential Rotation I. The Sun, Astronomy and Astrophysics, vol. 322, 1997, 835
11. Hempelmann, A., Wavelet Analysis of Stellar Differential Rotation: III. The Sun in white light, Astronomy and Astrophysics, vol. 399, 2003, 717-721
12. Soon, W. and Baliunas, S., Lifeteime of Surface features andStellar Rotation: A Wavelet Time-Frequency Approach, the Astrophyscs Journal, vol. 510, iss.2, 1999, L135 –L 138
13. Le, G.-M., Wavelet Analysis of Several Important Periodic properties in the Relative Sunspot Numbers, Chinese Journal of Astronomie and Astrophysics, vol. 3, No.5, 2003, 391 -394
14. Weinberg, B.L., S.R.Drayson and K.Freese, Wavelet Analysis and Visualisation of the Formation and evolution of twoi total ozone events over northern Sweden, Geophys. Res. Let., vol. 23, No. 17, August 15, 1996, 2223 - 2226
15. Hagelberg, C.R. and N.K.K.Gamage, Application of Structure preserving Wavelet Decompositions to Intermittent Turbulence: A Case Study, Wavelets in Geo-physics ed. by E.Foufoula-Georgiou and P.Kumar, Academc Press, 1994, 45-80

ON THE SOLAR ACTIVITY AND EARTH ATMOSPHERE LARGE-SCALE VORTICAL PROCESSES COUPLING

Nikolay Erokhin, Vladimir Damgov *, Liudmila Mikhailovskaya

Space Research Institute of RAS, Moscow, Russia
*Space Research Institute of BAS, Sophia, Bulgaria

Abstract

The analysis of solar activity (SA) influence on large-scale vortical processes in the Earth atmosphere (for example, tropical depressions, typhoons and hurricanes) is the important part of natural hazards and Earth climate change research. In particular, the mutual correlation functions of solar activity (SA) characteristics and tropical cyclogenesis (LVP) intensity are studied, the spectra of SA and LVP are compared and so on.

In the present paper the correlation coupling between Wolf numbers W(t) characterizing solar activity intensity with large-scale vortical perturbations (LVP) amount T(t) occurring in the Earth atmosphere is considered. In the Fig.1 the graphs of W(t), T(t) are shown for the time interval from 1983 up to 1998 years. A single point of these curves give the number of events during month period. So 192 points in the each data set were used. According to Fig.1 the behavior of oscillating functions W(t), T(t) is different, for example, the growth of W(t) not always accompanied by the T(t) increase, the peaks of these functions have different position on t and so on. So far as W(t), T(t) oscillate the mutual correlation function $Cr(n)$ was calculated where n is the temporal shift in months. Let us determine the averaging W and T values on the data sets taken

$$<T>=\left(\frac{1}{192}\right)\sum_j T_j, \quad <V>=\left(\frac{1}{192}\right)\sum_j V_j, \quad \text{where} \quad V_j = 0.02 W_j, \quad \text{and}$$

dispersions of temporal sequences considered $\sigma_t^2 =\left(\frac{1}{192}\right)\sum_j \left(T_j - <T>\right)^2$,

$\sigma_V^2 =\left(\frac{1}{192}\right)\sum_j \left(V_j - <V>\right)^2$, $0 \le j \le 191$. The mutual correlation function is determined by

$$Cr(n) = \frac{1}{192} \sum_{j=0}^{191-n} \left(T_{j+n} - <T>\right) \cdot \left(V_{j+n} - <V>\right), \quad n = 0,1.....N/2 \quad (1)$$

The plot of $Cr(n)$ is presented in Fig.1b and it shows the absence of clear correlation between fluctuations $\delta T_j = T_j - <T>$ and $\delta V_j = V_j - <V>$. For example, there are wide intervals of anti-correlations. The maximum of the first positive correlation in behavior of considered events W(t), T(t) corresponds to temporal shift of the order of 6 days. Variable trends X_j for the function V_j and Y_j for T_j one are shown in Fig.2a. The mutual correlation function $Crf(n)$ of W and T fluctuations near these trends $\delta V_j = V_j - X_j$, $\delta T_j = T_j - Y_j$ is presented in Fig.2b. It is clear that relationship of LVP with SA has a complicated nature. So the consecutive mathematical model of relationship between the solar activity and large-scale vortical processes in the Earth atmosphere must take into account a number factors of principle like large-scale instability triggering, the large vortices generation, nonlinear stabilization of instabilities, perturbations dissipative decay, the ration between typical periods of subsystems variability (SA and LVP). According to this we develop the oscillator x(t) model allowing to explain the observable features of T(t)-W(t) correlations. The basic equation is written like this

$$x_{tt} + v x_t + \omega_o^2 x = f(t) \qquad (2)$$

where ν, ω_o - are the friction coefficient and oscillator frequency respectively. It is supposed also that $f(t) = 0$, $x(t) = 0$ for t ≤ 0. The solution of (2) is determined by formula

$$x(t) = \frac{1}{\omega_1} \int_0^t d\tau f(t-\tau) \exp(-v\tau) \sin(\omega_1 \tau), \quad t > 0 \qquad (3)$$

Here $\omega_1^2 = \omega_o^2 - v^2$. Let us take T to be the temporal step so $t_k = Tk$, where k = 0, 1 ..... (N -1). From the expression (3) relationship of $x_k = x(t_k)$ with $f_j = f(t_j)$ follows as (B = T / ω_1)

$$x_k = B \sum_{j=0}^{k} f_{k-j} \exp(-\delta j) \sin(\gamma j) \qquad (4)$$

where the following denotes are introduced δ = νT , $\gamma = \omega_1 T$. The external force we take as the sum of two dispersed impulses

310

$$f_k = A_1 D_1(k) \sin \Psi_1(k) + A_2 D_2(k) \sin \Psi_2(k)$$

$$\Psi_1(k) = \Omega_1(k-m) - \varphi_1, \quad \Psi_2(k) = \Omega_2(k-s) - \varphi_2$$

$$D_1(k) = 1/\left[1 + (k-m)^2/\tau_1^2\right] \quad D_2(k) = 1/\left[1 + (k-s)^2/\tau_2^2\right], \qquad (5)$$

$$0 < m, s < (N-1)$$

The plots of the external force f_x and excited by it oscillations x_x are given in the Fig.3a for the case of parameters choice $\delta = 0.01$, $\gamma = \pi/19$, $\Omega_1 = \pi/41$, $\Omega_2 = \pi/107$, $A_1 = 1$, $A_2 = 0.7$, $\tau_1 = 40$, $\tau_2 = 90$, m = 400, s = 990, $\varphi_1 = 0$, $\varphi_2 = \pi/3$. In this case the oscillator frequency γ is significantly larger of the external force frequencies Ω_1, Ω_2 and we see the strong correlation between f(t) and x(t) behaviors. For the intermediate case $\gamma = \pi/95$, $\Omega_1 = \pi/41$, $\Omega_2 = \pi/107$ and unchanged other parameters, when the oscillator frequency value is placed between the external force frequencies Ω_1, Ω_2, the plots of f_x and x_x are presented in the Fig.3b. It is seen from this figure the anti-correlation of functions x_x and f_x at the time t < 700. But at the time t>700 the clear correlated behaviors of oscillator displacement x_x and force f_x are occurred f_x. The case presented in the Fig.3a corresponds to the non-inertial approximation in the equation (2): $x(t) \approx f(t)/\omega_o^2$. The mutual correlation functions for the both cases are shown in Fig.4a and Fig.4b respectively. Their comparison indicates that for the second case the level of mutual correlation x_x and f_x is less essentially.

Thus on the basis of the simple model considered it is possible to understand the complicated behavior of mutual x_x - f_x correlations in the dependence on ratio between oscillator frequency and external force frequencies.

From the analysis given above it is seen the necessity to develop model of LVP-intensity based on the differentiable functions. Such model allows, for example, describe correctly the phase space of LVP-intensity and to improve our understanding of possible correlation relationships between large-scale vortical processes in the Earth atmosphere and solar activity variation, to study further the physical mechanisms of solar-terrestrial relationships realization in the large-scale atmosphere dynamics [1].

Let us consider the LVP-intensity in the North-East part of Pacific Ocean for the August-October season of 1998 year. During the period 53 events (tropical depressions, storms and cyclons occurred). Take into account that the each event with its ordering number k had the development

period of duration ε_k, the quasi-stationary phase $a_k \le t \le b_k$ and the decay stage with duration τ_k. The development stage we approximate by the function

$$p_k(t) = 0.5(1 + (t - a_k) / \left[\varepsilon_k^2 + (t - a_k)^2 \right]^{1/2}$$

where t , a_k , b_k , ε_k - are measured in days. The decay stage of large-scale perturbation is approximated by the following function

$$g_k(t) = 0.5(1 + (b_k - t) / \left[\tau_k^2 + (t - b_k)^2 \right]^{1/2} .$$

Therefore, the life cycle of single LVP with number k is described by the function $f_k(t) = p_k(t) \cdot g_k(t)$, shown in Fig.5a. Now the cyclogenesis intensity may be determined like this $T(t) = \sum_k f_k(t)$, where $1 \le k \le 53$. The plot of intensity T(t) for the chosen season is given in Fig.5b. It is important that we have the analytical formula for LVP-intensity in the form of differentiable functions. This allows us to study the phase plane (T, Q), where Q(t) = dT / dt or in the discrete form we obtain now $Q_j = (T_{j+1} - T_j) / \Delta t$, where Δt is the temporal step so $t_{j+1} = t_j + \Delta t$.

The phase plane $\left(T_j, Q_j \right)$ is shown in the Fig.6 for the entire season considered and in some time intervals. These figures indicate the complicated structure of phase plane studied. In particular, if we try to develop the oscillator model driven by the external force [2] (for example, suppose $f_j = V_j$), to describe this plane then it is necessary to take into account the dissipation, the variable oscillator parameters like its frequency, a nonlinearity and so on which must determined by the background temperature, pressure, winds fields in the ocean-atmosphere system. The criterion of usefulness such model may be the correspondence of LVP-intensity profile T(t) obtained to the experimental data existed. Such model is under development now. It is necessary to note also that besides the solar-terrestrial relationships there are the external factors influence on the LVP in the Earth Atmosphere, for example, cosmic rays. лучи.

CONCLUSIONS

1. It was considered the correlation relationships between the large-scale vortical processes intensity occurred in the Earth atmosphere (the set on independent events) and the solar activity variations characterized by the Wolf numbers. The complicated dynamics of these correlations is explained

on the basis of oscillator model under influence of the external force and the ratio between the force frequencies and oscillator one is taken into account.

2. The analytical approximation of LVP-intensity based on the differentiable functions is developed and it is applied to the analysis of active cyclogenesis season August-October 1998 year for the North-East part of Pacific Ocean. The complicated structure of LVP-intensity phase plane is obtained. The approximation by the oscillator model beside the dissipation must take into account the variable system parameters like oscillator frequency and possible the system nonlinearity. The parameters variability corresponds naturally the non-stationary background fields under LVP-development.

References

1. M o i s e e v S., V.G. Pungin and V.N. Oraevsky. Nonlinear instabilities in Plasmas and Hydrodynamics, IoP Publ., Bristol and Philadelphia, 2000, 162 p.
2. D a m g o v V. Nonlinear and parametric phenomena in radiophysical systems, "Prof. Marin Drinov" Acad. Publ. House, Sofia, 2000, 450 p.

CCD PHOTOMETRY OF ASTEROIDS AT ROZHEN NATIONAL ASTRONOMICAL OBSERVATORY FROM 2001 TO 2003

Gordana Apostolovska*, Violeta Ivanova, Galin Borisov and Bonka Bilkina
*Institute of Physics, Faculty of Natural Sciences, 1000, Skopje, Republic of Macedonia,
Institute of Astronomy, Bulgarian Academy of Sciences, BG-1786 Sofia, Bulgaria

Abstract

The research is based on CCD photometric observations performed at Rozhen National Observatory, Bulgaria, in the period from 2001 to 2003. The photometric observations were made with a 0.5m/0.7m Schmidt telescope using a ST-8E CCD and with a 2m RCC telescope using a CCD camera Photometrics. The results from the photometric research are differential lightcurves of more than ten asteroids. For the first time the synodic periods of rotation for nine asteroids were determined and for five asteroids, the mean values of the color indexes were calculated. The mean values of the color indices for (300) Geraldina, (1011) Laodamia and (3443) Leetsungdao are presented.

The results gathered by photometric observation contribute to the enlargement of the database for rotational characteristics of the asteroids and their classification. These, together with the CCD observations of the asteroids from their next oppositions are expected to contribute in the search for the position of the poles, and the shape of asteroids.

Introduction

The importance of studying the asteroids could be attributed to two main reasons. The first main reason is that asteroids are considered to hold the key for understanding of the Solar system creation. Knowing the physical characteristics, the distribution and the evolution of asteroids is crucial for the understanding of the processes by which the planets were formed. The second reason is connected with the great influence of the asteroids on the evolution of the life on our planet. In order to prevent an impact and diminish the consequences of one, it is necessary to discover all Near Earth Objects and investigate their nature.

The rich metal composition has also led to asteroids being examined from an economical viewpoint, being considered as a source for metals, as well as a source or rare minerals. It makes them a new potential mineral source for humanity in the not-so-distant future, which would improve the chances for keeping the ecological balance of our planet.

The reflected sunlight from the asteroid is varying from several different factors: the variation of the distance between the Earth and the Sun, asteroid axis rotation, the albedo, the solar phase angle α. Specifics of the asteroid photometry are the continuous change of the geometry of the observations and the condition that asteroids could be observed only during short time intervals before and after the opposition. Measurements of the light flux or the magnitude with time reveals the lightcurve (*LC)* of the asteroid. The form of the lightcurve repeats with a period that corresponds to the synodic rotation period of the asteroid.

The asteroids have gone through a rich collision evolution due to which they have mostly irregular shapes. A typical lightcurve of an asteroid with shape closest to a triaxial ellipsoid is most likely to have two different minima and maxima, with a period of rotation between 4 and 12 hours. The theory shows that for asteroids with rotational period less than 2.2 hours the inertial forces from the rotation would cause the asteroid to break apart. The statistics of asteroid spin rates vs size suggest that most of the asteroids are not monolithic structures, but rather they are a conglomerate of several gravitationally bound pieces.

Observations and results

We carried out photometric observations in order to obtain optical lightcurves and calculate the synodic rotational periods of asteroids; and to determine the mean values of the color indices of chosen asteroids from the Main asteroid belt. The obtained results are based on the CCD photometric observations performed at the Bulgarian National Astronomy Observatory (BNAO) – Rozhen.

The regular photometric observations of asteroids (brighter than 13m) at BNAO Rozhen have been carrying out since 1991 with the 60 cm Cassegrain telescope equipped with the electrophotometar. The 2-m RCC telescope was used for fainter objects, in particular for relative photometry during the international observing campaign for (1620) Gegraphos.

By joint efforts of the Bulgarian Academy of Science, the Institute of Physics (Faculty of Natural Sciences) from Skopje and the Space Frontier

Foundation in 2000 a new SBIG ST8-E (Kodak KAF-1602E,1536x1024px, 1px=9μm) camera was purchased. It was mounted on the Schmidt telescope and has been used for observation of asteroids since July 2000.

A small amount of our observations during the last 3 years were carried out with the 2-m RCC telescope using a CCD camera Photometrics (CE200A-SITe, 1024x1024,1px=24μm).

The choice of the objects that were observed was based on the visibility of the objects in the assigned observation schedules, observation capabilities of the used telescopes and detectors at BNAO Rozhen. The quality of the results was, of course, influenced by the weather conditions.

From the measurements of the extinction during longer period at BNAO Rozhen [1] it is shown that out of five nights, one night is photometric, thus every fourth night, or approximately 20% of the total number of nights in a year is a high quality photometric night. On the nights with good photometric quality asteroids were observed through BVRI filters of the standard Johnson-Cousins system. The instrumental magnitudes of the asteroid were transformed into an absolute photometric system and the mean values of the color indices were determined.

The variation of the brightness of the asteroids is a periodic function and this gives the possibility of gathering and combining the lightcurves from several nights into one composite lightcurve (CLC). The size of the CCD frame enables us to choose an asteroid and at least two non variable stars in the same frame. On this way the atmospheric effects are eliminated and a very accurate lightcurve data and period of rotation of the asteroid could be determined, without using the absolute photometric system. During the constructing of the individual lightcurves the main goal is to cover the rotational phase of the asteroid as much as possible. The method for constructing the composite lightcurve, as well as for the calculation of the rotational period [2] is a semi-automatic and allows to choose and combine those lightcurves that do not differ much by the phase angle ($\Delta\alpha < 5°$) and are in a time interval of no more then 15 days.

The synodic periods are calculated for the first time for (698) Ernestina, (1019) Strackea, (4324) 1981 YA1 and (5240) Kwasan [3]. The values of color indices for (1474) Beira and it's synodic period and periods for (1309) Hyperborea and (2525) O'Steen are calculated for the first time [4]. In Table 1 the aspect data for each asteroid and each night of observations are reported. The position of the asteriod is given by the ecliptic longitude λ and the ecliptic latitude β. The fifth column contains the

316

Earth – asteroid distances Δ, the sixth column contains the Sun – asteroid distances r, and in the last column α is the phase angle.

Table 1.

Object	Date	$\lambda[°]$	$\beta[°]$	$\Delta[AU]$	$r[AU]$	$\alpha[°]$
(300) Geraldina	10.01.2002	143.46	1.01	2.406	3.276	9.4
	11.01.2002	143.33	1.01	2.399	3.276	9.1
	25.03.2003	210.80	0.34	2.445	3.370	7.4
(698) Ernestina	13.02.2002	126.83	18.24	1.630	2.556	9.6
(1000) Piazzia	22.08.2003	348.8	9.93	2.123	3.086	6.9
	23.08.2003	348.50	10.00	2.121	3.089	6.6
	26.08.2003	347.86	10.30	2.118	3.096	5.7
(1011) Laodamia	9.02.2002	177.49	4.99	0.709	1.612	21.5
	11.02.2002	177.41	5.26	0.704	1.617	20.3
	26.06.2003	295.89	-3.16	2.187	3.157	6.7
(1019) Strackea	16.06.2001	219.44	47.91	1.070	1.783	30.4
	17.06.2001	219.46	47.62	1.073	1.783	30.5
	22.06.2001	219.75	46.00	1.091	1.782	31.0
	24.06.2001	219.96	45.38	1.099	1.781	31.2
	26.06.2001	220.21	44.72	1.107	1.781	31.5
(1309) Hyperborea	12.01.2002	141.41	-14.63	1.904	2.788	10.8
	14.01.2002	141.10	-14.69	1.894	2.789	10.2
(1474) Beira	24 08.2003	22.44	27.42	0.806	1.607	31.5
	25.08.2003	22.79	28.00	0.799	1.602	31.5
	21.09.2003	30.79	47.54	0.672	1.493	33.5
(2525) O'Steen	23.09.2003	20.72	-3.95	1.778	2.545	17.8
(3443) Leetsungdao	16.07.2001	316.28	26.94	0.713	1.655	20.2
	18.07.2001	316.07	26.87	0.708	1.656	19.4
	20.07.2001	315.82	26.76	0.704	1.657	18.8
	21.08.2001	310.85	20.80	0.726	1.689	16.0
(4324) 1981 YA1	18.09.2001	40.34	13.10	1.232	2.062	20.4
	19.09.2001	40.34	13.18	1.224	2.062	20.1
	18.10.2001	36.82	14.77	1.075	2.044	8.9
	19.09.2001	36.79	14.78	1.073	2.044	8.5
	20.09.2001	36.39	14.79	1.071	2.043	8.2
(5240) Kwasan	20.12.2001	82.4	-4.4	1.180	2.153	3.6

(300) Geraldina
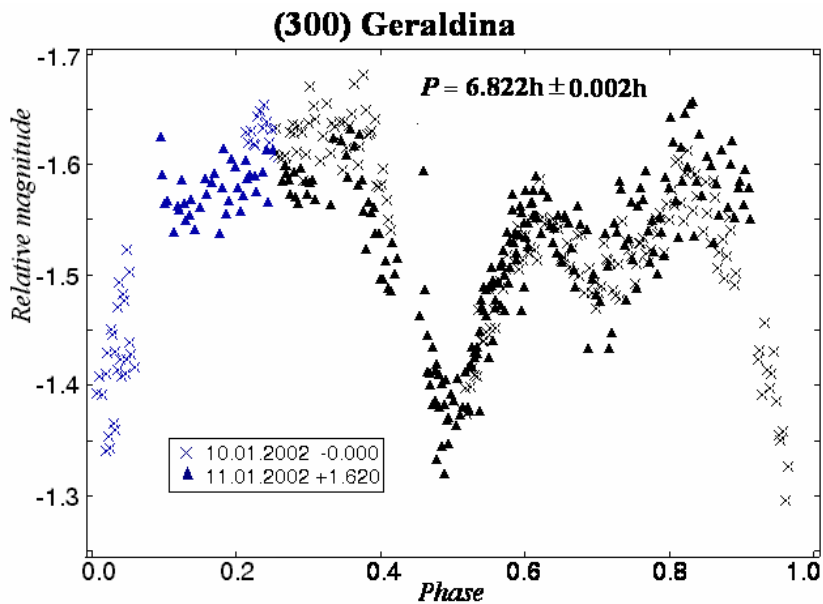
Fig 1.

This asteroid belongs to the outer part of the asteroid belt and according to the IPMS (IRAS Minor Planet Survey) Base Ground Data it has a diameter of 78 km. The observations of (300) Geraldina were carried out with the 2m RCC telescope. Two nights observations: 10 and 11 January 2001, were used for determination of the synodic period $P = 6.822h \pm 0.002h$ and the amplitude of the composite lightcurve $A = 0.303^m \pm 0.020^m$.

The reduction to the BVRI standard system of the asteroid magnitude was made by means of the observations of "dipper asterism" region from the open cluster M67 [5]. In this CCD standard-star field eight stars were used for calculation of the atmospheric extinction and transformation coefficients. On 25 March 2003, using a standard Johnson-Cousins set of filters, Geraldina was observed in B, V, R and I bands. The mean values of the color indices of the asteroid were measured as: $B\text{-}V = 0.784 \pm 0.152$, $V\text{-}R = 0.388 \pm 0.024$ and $R\text{-}I = 0.369 \pm 0.007$. The CLC has a rather complex form (Fig.1). The big scatter of observing points influenced the big error in the calculated values of the color indices.

(1011) Laodamia
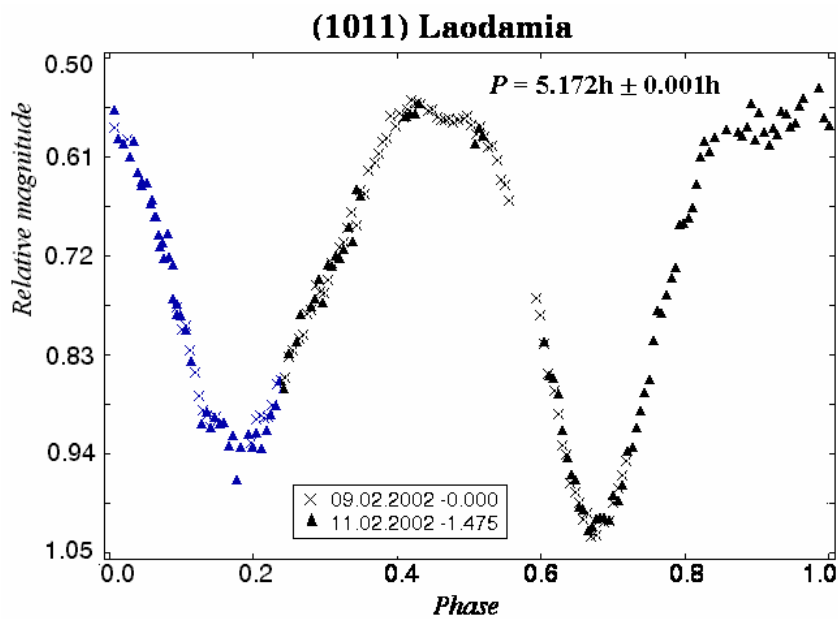
Fig 2.

(1011) Laodamia, is a Mars crosser asteroid. The CLC shown in Fig. 2 is constructed from observations from two nights in February 2002. It shows a non-symmetric form as to the depth of the minima and the humps of the maxima, which indicates an irregular shape. It needs more observations to determine it. The calculated period is $P = 5.172h \pm 0.001h$ and the amplitude of the CLC is $A = 0.470^m \pm 0.008^m$.

In order to transform observations to a standard magnitude scale standard field SA98 from the catalogue of Landolt [6] were observed on 9 February 2002. The mean values of the color indices are: $B\text{-}V = 0.819 \pm 0.135$, $V\text{-}R = 0.461 \pm 0.020$ and $R\text{-}I = 0.399 \pm 0.031$. The calculated value of $B\text{-}V$ confirms that Laodamia belongs to S-type as it was in Tholen taxonomy [7]. The stony asteroids or S-type have an albedo of 0,1 do 0,22 and are composed of silicates and approximately 10 percent of nickel and iron. This S-type accounts for some 15% of all known asteroids.

(3443) Leetsungdao
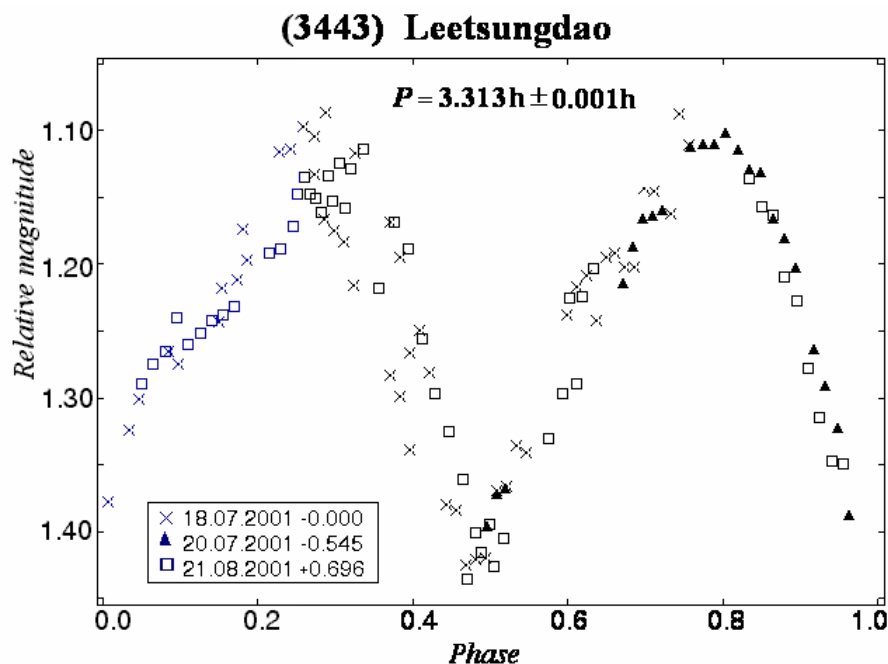
Fig. 3

The minor planet (3443) Leetsungdao is named after the Chinese theoretical physicist, Nobel prise winner - Tcung-dao-Lee. It's orbit comes close to the orbit of Mars and so some authors consider Leetsungdao as a Mars crosser asteroid. In order to construct a CLC presented in Fig. 3, we choose for the reference lightcurve the LC with the best quality and most observed points. All other LC are shifted along the ordinate axis according to the referent LC. Leetsungdao with the calculated period of $P = 3,313h \pm 0.001h$ may be referred to as a fast rotation asteroid. It is the asteroid with the shortest period we have observed. The amplitude of the composite lightcurve, Fourier fitted of order 6, is $A = 0.297^m \pm 0.015^m$.

Standards fields SA110 and SA114 from the catalogue of Landolt were observed on 16 July 2001. According to the determined values of the color indices: B-$V = 0.606 \pm 0.075$, V-$R = 0.625 \pm 0.034$ and R-$I = 0.625 \pm 0.034$ it could be concluded that the asteroid Leetsungdao is a member of the group of carbonate asteroids. This C-type accounts for some 75% of all known asteroids. They are similar to the carbonate hondrite meteorites. It is

assumed that they represent unprocessed material from the time of the formation of the solar system. Carbonate asteroids are very dark, with an albedo of approximately 0,05 and are hard to notice in observations in the visible part of the spectrum.

Conclusion

The study of small bodies in the Solar system has enormous significance due to the fact that they are composed from the same protomatter as that from which the solar system was formed. Studying physical and chemical processes of these objects and their dynamic behaviour, scientists hope to understand the conditions and make-up of matter during the creation of our solar system, the only one, so far, that we can study in detail. The significance of this research is increasing due to the fact that lately, planets have been found around number of other stars as well.

The results from the CCD photometric research in BNAO Rozhen during the period from 2001 to 2004 are more than 20 differential lightcurves of 11 asteroids. The constructed composite lightcurves were used to evaluate for the first time the synodic period of rotation for 10 asteroids. Out of the fitted composite lightcurves the amplitudes of the variation of the light were calculated. For five asteroids, the mean values of the color indexes were calculated.

The results gathered by photometric observations contribute to the enlargement of the database of known rotational and physical properties of asteroids and could be used in their taxonomically classification These, together with the CCD observations of the asteroids from their next oppositions are expected to contribute in the calculation of the pole position, and shape of asteroids.

References

1. Denchev, P., Z. Donchev, V. Ivanova, J. Mateeva. Seasonal and short-term variations of the atmospheric extinction at Rozhen National Observa-tory and AO Belogradchik, Bulgarian Journal of Physics 26, 1999, 250-265

2. Magnusson, P., C. I. Lagerkvist. Analyses of asteroid lightcurves. I. Data base and basic reduction, Astron. Astrophys. Suppl. Ser. 86, 1990, 45-51

3. Ivanova, V., G. Apostolovska, G. Borisov, B. Bilkina. Results from photometric studies of asteroids at Rozhen National Observatory, Bulgaria, Proc. ACM, ESA-SP-500, 2002, 505-508

4. Apostolovska, G., V. Ivanova, G. Borisov. Lightcurves and rotational periods of 1474 Beira, 1309 Hyperborea, and 2525 O'Steen, The Minor Planet Bulletin of the Minor Planets Section of the Assoc. of Lunar and Planetary Observers, Vol. 31, No. 2, 2004. 44-45

5. Chevalier, C., S. A. Ilovaiscy. Cousins BVRI CCD photometry of stars in the M67 ″dipper asterism″ Astron.Astrophys. Suppl.Ser. 90, 1991, 225-229

6. Landolt, A.U. *UBVRI* Photometric standard stars in the magnitude range 11.5<V<16.0 around the celestial equator. Astron. J. 104 **,** 1992, 340-491

7. Tholen, D.J..Asteroid Taxonomy from Cluster Analysis of Photometry, Ph.D. Thesis, Univ. of Arizona 1984

RADOSAV VASOVIC (1868-1913) ON THE BELGRADE OBSERVATORY

V. Trajkovska and S. Ninkovic

Astronomical Observatory, Volgina 7, 11160 Belgrade 74, Serbia and Montenegro

Abstract.

In the first half of the XIX century in Serbia the conditions for formation of institutions and development of science arose, whereas in its second half among Serbian intelectuals there was a decisive position to follow the achievements of the European progress, especially in natural sciences. R. Vasovic was one of such intelectuals. His educational and scientific activities took place in areas of geography and climatology. In one of his papers he presented his criticism towards the activity of the Belgrade Astronomical and Meteorological Observatory which had been founded somewhat earlier.

In the second half of the XIX century in Serbia, after the liberation in spite of the state of being undeveloped economically, there were efforts aimed at the founding of scientific and educational institutions following the example of well known institutions of such kind abroad. A rich publishing activity took place, especially that concerning textbooks [1]. For a number of intelectuals of that time a strong tendency existed to follow the progress of the European scientific thought. Radosav Vasovic (Ranc in the region of Novi Pazar, September 9, 1868 - Belgrade, July 18, 1913 - both dates are according to Julian calendar) was among them (Fig. 1). He finished the primary school and the real

Fig. 1. Photograph of R. Vasovic it belongs to the Archives of Serbia (A.S. P.O. 65:64)

gymnasium in Uzice and took degree at the Faculty of Philosophy (Division of Natural and Mathematical Sciences) of Grand School in Belgrade in 1893. From the existing data (Archives of Serbia) one can conclude that he was a successful student in spite of his bad material conditions. From 1893 to 1913 he was employed as a teacher at first in Sabac, Nis and Krusevac and later on in Belgrade, in the II and III Belgrade Gymnasiums (Figs. 2, 3).

Fig. 2. Building of III Belgrade Gymnasium (photograph is taken of Branko Vujovic's book "Beograd u proslosti i sadasnjosti", Belgrade, 1994)

Наставници школске 1909—10 године.

Fig. 3. R.Vasovic with his colleagues, teachers of III Belgrade Gymnasium from 1909/10
(taken of the book "Pedesetogodisnjica Trece beogradske gimnazije", Belgrade, 1910)

Vasovic wrote textbooks in geography to be used in secondary schools which had several editions. He also wrote some articles concerning the teaching of geography [2]. Among others he published a few scientific contributions in glaciology and climatology. He undertook many scientific travels so that he visited as distant parts of Europe as Scandinavia and Southeast Russia [3].

In 1904 Vasovic's critical position towards the activity of the Belgrade Observatory was published in Belgrade (Fig. 4) [4]. The Observatory had been founded in 1887 due to the endeavour of Milan Nedeljkovic, a teacher in the Grand School. It also belonged to the Grand School. In the period covered by Vasovic's analysis the Observatory was foreseen to comprise not only astronomical, but also meteorological, geomagnetic and seismological activities.

Fig. 4. Head page of Vasovic's critical review on Belgrade Observatory from 1904

      With regard that then many necessary instruments were still not available the meteorological activities were, practically, the only ones really performed. The meteorological data were regularly published as monthly reports (Bulletin Mensuel de l'observatoire central de Belgrade, in French). Besides, these data were also published in some papers and journals of that time

(late XIX century and early XX one). Vasovic's criticism mentioned above concerns the correctness of the data communicated there, as well as the control of the work of Meteorological Network activity. In his opinion a vast body of data published by the Observatory was not appropriate and such a meteorological service had to be abolished in order to keep the reputation of other cultural institutions in Serbia.

A characteristic property of newly founded institutions is that they meet many problems concerning their internal organisation. It is necessary to bear in mind that Nedeljkovic missed a qualitative meteorological staff and also one should be aware of numerous difficulties which at that time followed the activity of the Observatory. In spite of all the foundation of an institution like the Observatory was very important for the development of natural sciences in Serbia. The achievements of the scientific organisations having their origins in the Observatory are in favour of this.

References

1. Trajkovska, V., Astronomski sadrzaji u udzbenicima u Srbiji u drugoj polovini XIX veka, Flogiston, casopis za istoriju nauke, Beograd, 2000, 9, 19-48
2. Ninkovic, S., Trajkovska, V., Nastava geografije u Srbiji u drugoj polovini XIX veka, Zbornik radova naucnog skupa "Prirodne i matematicke nauke u Srba 1850-1918.", Novi Sad, 2001, 195-197
3. ***, Izv. o II Beogr. gim. za sk. 1913.14. god., Beograd, 1914, 41-42
4. Vasovic, R., Nasa Opservatorija (Prestampano iz "Stampe"), Beograd, 1904

ON A DOCUMENT CONCEERNING THE CALENDAR REFORM

Veselka Trajkovska

Astronomical Observatory, Volgina 7, 11160 Belgrade 74, Serbia and Montenegro, e-mail: vtrajkovska@aob.bg.ac.yu

Abstract*.*

One considers the contents of a document from 1927 which belongs to the archive material of the Serbian Orthodox Church and where the introducing of the calendar reform according to the project of Maksim Trpkovic (1864-1924) was proposed and its advantages over the modification done at the Panorthodox Congress in Constantinople in 1923 by Milutin Milankovic (1879-1958) were emphasized.

After the First World War the Gregorian Calendar was adopted by many states. At the Panorthodox Congress in Constantinople in 1923 a solution was adopted according to which the Julian Calendar should be improved, but it was not accepted, i. e. followed, by all Orthodox Churches. Since the Serbian Orthodox Church had not reformed its calendar, Jovan Zivkovic (1859-1929), professor at the Theological School in Sremski Karlovci (he taught church rule and elements of orthodox paschalia) [1], who was appointed by the Church for the matter of calendar reform, addressed the Holy Archiereic Council with intention to solve the question of calendar reform.

Two copies of this document (following the enclosed material) are kept in the Archives of Serbian Orthodox Church as No 91/40 dated on November 19, 1927, i. e. December 2 according to the Gregorian Calendar, as well as No 2456 dated on December 2/15, 1927, with regard that it was further sent for consideration to the Holy Archiereic Synod (see Appendix). In this document Zivkovic requires the calendar to be reformed according to the project of Maksim Trpkovic (1864-1924) and emphasizes the advantages of such a solution over the modification done during the Panorthodox Congress in Constantinople in 1923 by Milutin Milankovic (1879-1958). Zivkovic's greatest objections to the modified variant concern the fact that for such a way of reckoning the vernal equinox occurs on March 20. In Trpkovic's project the

vernal equinox occurs on March 21 according to the existing rules. In the document Zivkovic writes: "When the Pan-Orthodox Congress adopted badly modified Trpkovic's project, it is to expect our Holy Synod to accept the quite good original","our Church and our people can be proud of Trpkovic's project, instead of avoiding this and letting it to be damaged by others, and being proud of it as something belonging to them, would mean a treason to Serbian Culture".

He addressed several times the highest Church Authorities explaining the necessity of calendar reform and its adequate solving. Also, he published (in 1919, 1922, 1923, 1927, 1929) several articles concerning the calendar reform wherein he explains and favourises the project of Maksim Trpkovic [2]. The reform has not still been carried out by Serbian Orthodox Church for a number of reasons having essentially no scientific character.

References

1.   ***, Glasnik Srpske Pravoslavne Patrijarsije, 5, 1929
2.   Trajkovska, V., Reform of calendar: Maksim Trpkovic and Milutin Milankovic, Publ. Astron. Obs. Belgrade, 75, 2003, 301-306

Свети Архијерејски Саборе!

Свети Архијерејски Сабор Српске Православне Цркве у Краљевини Срба, Хрвата и Словенаца донео је, поводом одлуке Свеправославног Конгреса 1923. о календару, своју одлуку, којом се већином гласова (18 : 3) сагласио са одлуком истога конгреса донетом по том предмету, но под условом, да реформа ступи у живот једновремено са свима црквама у уверењу и оправданом очекивању, да ће и остале православне цркве тако поступити.

Међутим суседне православне цркве у Грчкој и Румунији, па и мало даље, у Пољској решиле су календарско питање не чекајући истовременог уважања, а што је још горе, и за осуду, решиле су га свака на свој начин и то сасвим погрешно: Грчка је црква усвојила григоријански календар а задржала православну пасхалију, која се с оним никако не може у склад довести, Румунска црква удесила је свој календар према одлуци Цариградског Свеправославног Конгреса 1923. који је добру српску реформу унаказио, а Пољска има — како се чује — два календара: један за вароши (поправљен!) а други за село (непоправљен!).

Таквим поступцима нарушено је молитвено јединство у Једној Светој Саборној и Апостолској Цркви, које ваља зарана васпоставити, да се дисхармонија календарска не претвори у раскол.

Могућност за то васпостављање поседује само Српска Православна Црква јер она једина има добар пројект за правилно решење календарског питања у духу наређења св. I. Васељенског Сабора, и штета је велика што га као таквог није у живот увела још 1919. г., кад је стао на снагу државни закон о изједначењу календара, па би се досад већ и заборавило да смо се негда служили нетачним календаром.

Поменуту могућност пружа светом Српском Архијерејском Сабору пројект за реформу календара, који је још пре 30 година израдио, сад већ покојни, проф. Максим Трпковић, јер тај пројект задовољава свима потребама и црквеним и државним и то у тавкој мери, да тако рећи за хиљаде векова неће настати потреба даљег поправљања календара.

Исти је пројект на Свеправославном Конгресу 1923. модификован, али тако неспретно и несретно, да ће се 2000. године равнодневница спустити заједно са григоријанском на 20. март, а то се противи наређењу св. I. Васељенског Сабора, који је утврдио равнодневницу на 21. март. Од григоријанске

Fig. 1

330

реформе има свеправославна модификација само ту предност, што ће јој равно-
дневница, кад се спусти на 20. март, на том датуму и остати, штавише по-
пеће се у 900 година двапут на 21. март али само за 1 час и 20 минута
односно за 4 часа. Много је правилнији управо једино правилан Трпковићев
пројект, по ком ће равнодневница остати вечито на 21. марту, а и кад се спусти
на 20. март, недостајаће јој само 1 час 20 минута, односно 4 часа до потпуног
навршења дана, што ће се догодити свега по једанпут у 900 година. Тај малени
недостатак се не да никојим начином избећи а да се не падне у већу погрешку,
у какву је н. пр. већ пао Свеправославни Конгрес а по њему и Румунска Црква.
Стога се око те незнатне и невине грешке не треба ни задржавати, још мање
због ње усвајање Трпковићева пројекта даље одлагати, да не би још која црква
залутала за свеправославном модификацијом или чак и григоријанским календа-
ром. Кад је Свеправославни Конгрес усвојио рђаво модификован Трпковићев про-
јект, тим пре може наш Свети Архијерејски Сабор усвојити сасвим добар
оригиналан.

Пошто за правилно решење календарског питања нема и не може бити
бољег пројекта од Трпковићевог, и пошто је тај пројект плод научнога рада
сина наше вере, крви и језика, то би нашем Светом Архијерејском Сабору у
национ лну и патриотску *дужност* спадало, да томе пројекту прибави ува-
жење, које он својом врсноћом потпуно заслужује, јер се наша Црква и наш
род може Трпковићевим пројектом само поносити, па би обилажење истога
и пуштање да га други кваре и њиме се као својим диче, значило издајство
српске културе, коју је и Српска Црква дужна помагати.

А што Трпковићеву пројекту даје још већу цену је то, да се њему може
прилагодити и садашња православна Пасхалија. Тако за ово столеће важе сви
датуми Ускрса почевши од 1. године столећа са 1. годином Индиктијона. За
идуће столеће требаће датуме Индиктијона повећати за 1 јединицу, тако н. пр.
2001. г., за коју у Индиктијону стоји ускршњи датум 8. априла, биће 9. априла,
2001. г. биће 1. април место 31. марта и т. д., а само ће се 2031. поправити
на 14. април (место 7. април), 1938. на 19. април (м. 26. априла на који Ускрс
не сме пасти) и 2051. на 3. април (место 27. март); сви остали ускршњи да-
туми се повећавају само за 1 јединицу. Таквим начином били бисмо мирни до
2100. године, кад ће наши потомци имати дужност, да у Индиктијону учине
даље исправке, ако буду хтели да се њиме служе.

Исправком календара на овај начин неће се ништа мењати у црквеној
години ни у црквеним књигама. Постови ће остати на своме месту и дужини
као и досад. Једном речи ући ћемо без икакве штете а са великом моралном
и материјалном добити у нов ваљан ред.

Сам прелаз на тачан календар може се најзгодније извршити или у
јануару, на појутарје Св. Саве — у години кад се месојеђе држе, или пред
Видов-дан — у години кад је петровски пост дужи, или на појутарје Крстова-
дне — ма које године.

Fig. 2

Потписани је у 38. броју „Весника", од 6. нов. о. г/ математички доказао надмоћност Трпковићеве реформе не само над григоријанском, него и над свеправославном модификацијом Трпковићева пројекта, и тиме јасно показао, да наша св. Црква може примити само Трпковићев пројект у оригиналу, а свако противљење истоме значило би неверовање својим рођеним очима, и св. ап. Јован би могао сваком скептику и противнику тога пројекта с пуним правом рећи: Како можеш тврдити да верујеш у Бога којег не видиш, кад не верујеш ни у оно што својим очима јасно видиш (1. посл. гл. 4. ст. 10.)

Ми смо навикли говорити о *старом*, јулијанском календару и о *новом* григоријанском, те и најновијем Трпковићевом, рецимо српском календару. У ствари је то све један те исти календар, само потоњи боље регулисан него претходни, као н. пр. од оца наслеђени сат што наследнику један сајџија регулише ал не сасвим добро, а други га удеси да показује време сасвим тачно. Онај први календарски сајџија био је папа Григорије XIII., а овај други је наш Трпковић. А који паметан наследник неће дати очев сат да се добро оправи и тачно удеси па да се с њим и поносити и служити може?

Изјављујем, да сам вољан у свако доба и на сваком месту дати потребна разјашњења на свако питање које у овај предмет засеца.

<div align="center">

Св. Арх. Сабора најоданији

Прот. ЈОВАН ЖИВКОВИЋ
умировљени професор богословије карловачке

</div>

27. XI. 1927. год.
Срем. Карловци.

<div align="center">

Fig. 3

</div>

Календарско питање

С В Е Т О М

АРХИЈЕРЕЈСКОМ САБОРУ
СРПСКЕ ПРАВОСЛАВНЕ ЦРКВЕ
у
Срем. Карловцима

Представка

прот. Јована Живковића унирова,
професора богословије карловачке

у предмету регулисања
православног календара

са 1 прилогом

Fig. 4

333

АСБр.91/Зап.40/1927.
20.XI.(3.XII).1927.г.
у СРЕМСКИМ КАРЛОВЦИМА

СВЕТОМ АРХИЈЕРЕЈСКОМ СИНОДУ

СРЕМСКИ КАРЛОВЦИ

У смислу одлуке Светог Архијерејског Сабора под горњим бројем и датумом част Нам је предмет уступити Светом Архијерејском Синоду на проучење и мишљење.

За Председника
Светог Архијерејског Сабора

Митрополит Скопљански

1/14.XII.1927.
СРЕМСКИ КАРЛОВЦИ

Fig. 5

ON THE FUNDAMENTAL CONTRIBUTION OF MAKSIM TRPKOVIC'S PROJECT TO THE PAN-ORTHODOX SOLUTION OF THE CALENDAR REFORM IN CONSTANTINOPLE IN 1923

Veselka Trajkovska

Astronomical Observatory, Volgina 7, 11160 Belgrade, Serbia and Montenegro
e-mail: vtrajkovska@aob.bg.ac.yu

Abstract.

In this paper Maksim Trpkovic's contribution to the calendar reform from the late XIX century and the first decades of the XX one is discussed. The importance and the contribution of his project in the solving of the calendar reform at the Pan-Orthodox Congress in Constantinople in 1923 is specially presented. In this context one also considers the controverse question whether the modification of Trpkovic's project done at the Congress by Milutin Milankovic is Trpkovic-Milankovic's calendar or Milankovic's calendar.

Because of some drawbacks of civil calendars used in the past, which is due to the difficulties of fitting them to the natural periodical phenomena, the question of calendar reform has been initiated from time to time during the history of human civilisation. In late 19th century, was actualised the question of the Reform of the Julian Calendar used in the Eastern Orthodox Church countries, not only because of inaccuracy with respect to the tropical year but also because of the difference with respect to the Gregorian Calendar used in a larger part of the world, which is also, but less, inaccurate. The difference between the two calendars produced difficulties in mutual communications in all spheres of public life. In the Kingdom of Serbia the question of calendar reform was also initiated. As a result of the work of some scientists and professors (Lj. Uzun-Mirkovic, M. Nedeljkovic, M. Trpkovic, Dj. Stanojevic, Petar A. Tipa) several projects of calendar reform were published. The proposal of professor Maksim Trpkovic (1864 - 1924), published in 1900 met a strong echo in the scientific community.

Maksim Trpkovic originates from Orlanci (village in the surroundings of Kicevo), then within the Ottoman Empire (now Republic of Macedonia). Already as a grown-up boy, he was brought (with his father) to the only

liberated Belgrade after the Serbo-Turkish wars 1876-1878 where he graduated at the Belgrade "Realka" (special gymnasium) and the Faculty of Philosophy (Division of Natural Sciences and Mathematics). He was especially interested in astronomy. He taught mathematics, physics, cosmography and mineralogy at the Belgrade "Realka" and afterwards at the I, II and IV Belgrade Gymnasiums and for a short time also at the gymnasiums in Pirot and Skopje. Maksim Trpkovic worked conscientiously on the question of calendar reform. His project of calendar reform was published in Belgrade in 1900 entitled "Reforma kalendara" ("Calendar Reform"). The new intercalation rule introduced by M. Trpkovic is: the secular years will be leap years if divided by 9 yield a rest of 0 or 4, otherwise a secular year is a simple one. Also he included in his project the epact calculation for the 20th century and new paschal limits. Trpkovic (1900, 1901, 1909, 1910, 1919-1921) extended his own ideas about calendar reform and presented them in the papers published in church-social journals and the journal of Professor Society, out of which three were printed as special editions. His book "Pravoslavna pashalija i proveravanje datuma" ("The Orthodox Paschalia and the Date Verification") according to a decision of the Presidency of the Academy of Social Sciences (II meeting on June 5, 1913; XI meeting on October 16, 1913) should have been printed as an Academy publication i. e. "awarded from the fund of Dr Ljubomir Radivojevic", however, during the First World War this manuscript, together with the printed material had perished. Only one copy containing printed the first eight sheets of this work was found in the Academy of Sciences [1]. In 1936. in this Academy an edition from Radivojevic's fund was prenumerated in an unusual way by omitting Book 14 in which Trpkovic's work should have been printed, but to arrange the issue number to correspond to the next editions from this fund an issue not belonging to Radivojevic's fund was inserted as Book 1. Later on, in 1986, the original numeration of editions of this fund was specified again.

The Serbian Church in 1903 adopted Trpkovic's proposal for the calendar reform as the most reasonable "both from the point of view of time reckoning and from the religious standpoint concerning the christian calendar". At the Pan-Orthodox Congress in Constantinople, in May 1923, at which the question of calendar reform was solved, the official proposal of the Serbian Orthodox Church was Maksim Trpkovic's project. One of the delegates Milutin Milankovic (1879-1958), as the only scientist present at the Congress, modified

Trpkovic's project and proposed this variant to the Congress which was finally adopted by the Congress after a long debate, due to Milankovic's authority. Milankovic adopts the basic idea of Trpkovic's project but changes the intercalation rule only to read: secular years will be leap years only if the number of their centuries divided by 9 yelds the rest 2 or 6. Depending on the assumed intercalation one can come closer or farther to some of the assumed criteria: Trpkovic wanted with his intercalation to put the vernal-equinox date on March 21 (in accordance with the natural equinox and also following one of the principal requirements of the Church), whereas Milankovic achieved an accordance with the Gregorian Calendar over a longer period (at the cost of allowing the vernal equinox to occur on March 20). As written by various authors (Zivkovic (1923, 1927, 1929), Vukicevic (1932), Miskovic (1966), Jankovic (1985), Keckic (2001)) Trpkovic's solution was better than Milankovic's [1 and references therein]. As a disadvantage of Milankovic's solution many of them mention Milankovic's effort to be in accordance with the Gregorian calendar as much as possible because this calendar is also incorrect and, consequently, in both calendars the vernal equinox occurs more frequently on March 20 thus being discordant with natural equinox and the Church requirements concerning the date for Easter. Keckic thinks that Milankovic's attitude towards Trpkovic was not correct. V. V. Miskovic (1892-1976), Director of the Astronomical Observatory in Belgrade, reproaches to Milankovic for introducing an intercalation rule aimed at approaching the Gregorian Calendar, which is also not quite correct and, consequently, its errors interfere also in Milankovic's calendar. He also reproaches due to the fact that this property is even emphasized by Milankovic. Jovan Zivkovic (1859-1929), Professor at the theological school in Sremski Karlovci, who was appointed by the Serbian Orthodox Church for the question of calendar reform, has also a critical view towards the changes introduced by Milankovic and adopted by the Congress taking into account the coincidence of dates with the Gregorian Calendar over a long period, but not an essential improvement of the Julian Calendar. He in a few his articles and addressing to the highest Church authorities justifies with arguments advantages of Trpkovic's solution over the modified variant adopted at the Pan-Orthodox Congress and requires the calendar to be reformed according to the project of Maksim Trpkovic [1][2]. Zivkovic's greatest objections to the modified variant concern the fact that for

such a way of reckoning the vernal equinox occurs on March 20. He also, considers that the determination of the paschal full moon on the basis of astronomical calculations of several observatories is a superfluous and improper novelty adopted by the Congress because in his opinion the new Paschalia (Epacta) formed by Trpkovic by using existing astronomical tables is more appropriate [3]. The Commission at the mentioned Congress adopted Trpkovic's Paschalia, but later following Milankovic's proposal it was accepted to use calculations which would have been performed at several observatories [4]. Such an alternative of paschal tables including time according to the Jerusalem Meridian was also proposed by Maksim Trpkovic in 1900 in his project. In Zivkovic's opinion, Trpkovic's Paschalia was not taken into account on occasion of the formation of the proposal of the Julian-Calendar reform at the Congress to avoid Trpkovic's mentioning. Vukicevic (1932) publishes a study concerning the calendar question. In a tabular form he presents the difference of the calendar dates of several calendars covering a given period compared to the natural dates where it is possible to see that Trpkovic's solution is the closest to the natural sequence.

In the formation of his calendar-reform project Trpkovic tried to include astronomical achievements, as well as the rules according to which Christian holidays are determined, and because of that his project is acceptable both from the scientific aspect and from that of the canonic rules and it was ready for practical use. It also possesses for the Church necessities completely correct Paschalia. There are interpretations of several authors according to which Trpkovic's project satisfied the calendar-reform requirements, both from the accuracy aspect and that of simplicity in the practical use, a very important property of any calendar. In the case of Milankovic's solution there is the problem of vernal equinox which occurs on March 20 disagreeing with the initial reform requirements.

The fundamental characteristics of Trpkovic's and Milankovic's proposals are similar (for instance, year duration) simply because Milankovic preserved the base of Trpkovic's project and changed the intercalation rule only. Due to this fact, as well as that the official proposal of the Serbian Orthodox Church at the Pan-Orthodox Congress in Constantinople in 1923 had been Trpkovic's project, the modification of this project done then by Milankovic and accepted at this Congress has been referred to by some authors

as Trpkovic-Milankovic's calendar, i. e. as Milankovic's calendar by other ones. In the literature this modification (calendar) has been also referred to as: Pan-Orthodox modification (calendar), Reformed Julian Calendar. Both Trpkovic's proposal and its modification by Milankovic had advantages with respect to both Julian and Gregorian Calendars. In 1923, the Holy Archiereus Council of the Serbian Church adopted in principle the proposal of the Pan-Orthodox Congress, but the reform has never taken effect for reasons having essentially no scientific character.

Although the question of calendar reform, as a delicate one, requires a solution to the benefit of both church and public life, the way of its solving and putting into effect has encountered difficulties. In spite of an intensive campaign and interest expressed in the reform by both specialists and publicity initiated in the second half of the XIX century, which also extended into the first decades of the XX century, it has not been brought to a close yet. In this action Maksim Trpkovic's proposal, certainly, occupied an important place. Milankovic joined the calendar-reform activity at one month date before the Pan-Orthodox Congress (April 1923) and he published a few papers dealing with the calendar question. Some authors seized by the "cult of a great scientist" with regard to Milutin Milankovic's person glorify his work also in the calendar reform omitting or erroneously interpreting Maksim Trpkovic's fundamental contribution [1]. In a talk by M.S. Dimitrijevic at the Meeting on History of Astronomy held in Belgrade between April 25 and 28, 2004 there was an attempt to diminish the contribution of Maksim Trpkovic by mentioning that also Oriani Barnaba in 1785 had formulated the basic idea of Trpkovic's calendar-reform project, namely that over nine centuries the difference between the tropic and julian years is exactly seven days and that these secular years should be made common. However, in his project "Reforma kalendara" from 1900 Trpkovic communicates how he reached his idea and this is his own reasoning. After all, history of science knows many cases when two or more authors discovered the same thing quite independently of each other. In the textbook of astronomy for IV form of gymnasium written by M. S. Dimitrijevic and A. Tomic (1995), in the part concerning the calendar, Milankovic is the only person to be mentioned, whereas Trpkovic's fundamental contribution to the calendar reform in Serbia is not mentioned at all, but following the insisting of Dr Mijat Mijatovic (1950-2000), Professor at the Faculty of Natural and

Mathematical Sciences in Skopje, in the Macedonian translation, about the contribution of Maksim Trpkovic to the calendar reform is inserted. Furthermore, in the media Dimitrijevic and the group following him, with respect to the calendar only Milankovic mentioned and repeat constantly that the most exact calendar in the world has been given by Milankovic which, in fact, is not true with regard that Trpkovic's solution, as emphasized by many authors, is better. Those authors who have omitted or tried to diminish the basic Trpkovic's contribution to the calendar have been unjust towards his work and, at the same time, attributing these merits to Milankovic they have violated Milankovic's reputation acquired by him through a work on the theory of the Earth's insolation, climate variations and on the one of ice periods.

In the science every contribution should be evaluated and in this way appreciated, but not to diminish its importance without arguments. Sometimes in history of science (also in general history) attempts of some political and cultural groups aimed at influencing the objectivity of events have appeared, something which could change the real picture in the final outcome. Science should not be a contest, but a field in which a research is to be done aimed at a better approaching the truth where every contribution will be evaluated in a proper way. Finally, Milankovic's merits in his theory of Earth insolation and ice periods are, certainly, important, and also, Trpkovic's fundamental contribution to the calendar reform should be duly appreciated.

References
1. Trajkovska, V., Reform of calendar: Maksim Trpkovic and Milutin Milankovic, Publ. Astron. Obs. Belgrade, 75, 2003, 301-306.
2. Trajkovska, V., On a Document Concerning the Calendar Reform (in this publication)
3. Zivkovic, J., S. P. Crkva i Manifest Nj. V. Kralja, Glasnik Srpske Pravoslavne Patrijarsije, 3, 1929, 39-41
4. Skrobonja, B., O racunanju vremena i pravoslavnom kalendaru, Prizren, 2000

A WOODEN CALENDAR FROM SOUTHEASTERN BULGARIA

Vesselina Koleva[1], Iliya Georgiev[2]

[1]*Institute of Astronomy, BAS, P.O.Box 136, 4700 Smolyan, Bulgaria,*
e-mail: ves_koleva@abv.bg
[2]*University "Prof. Dr. Asen Zlatarov", 8010 Burgas, Bulgaria*

Introduction

Wooden calendars are a specific tool for preserving the church calendar in medieval Europe. The Christian symbols are skillfully interwoven with traditional signs, which mark the days of importance for the economic and ritual life in a year. The archaic method of time reckoning has turned into a tool for disseminating and establishing the Christian festival system, and is one of the proofs of the syncretism between the pagan tradition and the new religious ritualism.

Bulgarian Christians used such objects until the beginning of the 20th century. The earliest date fixed on a wooden calendar is 1783 [1]. These calendars are also called *rabosh* in Bulgaria. The calendar presented here is based on the Julian (solar) calendar containing the major fixed feasts of the Orthodox Church. It has not been published so far and is kept in a private collection.

The wooden calendar from Lyulyakovo

The calendar's owners were Bulgarians who moved to the village of Lyulyakovo, Burgas region, from the village of Chatal Tepe, Lampsak region, in Asia Minor in 1913. Legends tell that Chatal Tepe was set up in the 17th - 18th century by Bulgarians who left their villages in the Ivaylovgrad region in order to make charcoal and breed stock for a living. In 1913, their descendants were forced to migrate to the newly liberated Bulgaria together with a large number of other Christian Bulgarians from Asia Minor and eastern Trace, whose homes remained within Turkey under the peace treaty of Bucharest. It is noteworthy that all known rabosh calendars from southeastern Bulgaria were property of Bulgarian migrants from these territories [2], [3].

The calendar, like the rest of the Bulgarian rabosh calendars, is carved on a four-sided stick. The stick is 713 mm long and the width of its sides varies between 17 and 25 mm (Fig. 1). It weighs only 140 grams. The color of the stick is dark brown to black. There are peeled off spots on the surface, which suggest that the calendar has a kind of varnish coating. Probably later incised notches reveal wood of light brown color.

The structure of the "record" is as simple as possible. On the four edges, at intervals of 5 to 9 mm, short 5 to 7 mm long notches are carved. The total number of notches is 366. Nine wider and 20 to 50 mm long notches varying in shape separate the 12 months from one another. The months are distributed in seasons, in groups of three on each of the four edges. The number of days in each month corresponds to the Julian calendar. February contains 29 notches. A sign between the last two notches shows the two possible ways of reckoning: 28 days in a normal year and 29 days in a leap year. There are no special signs marking the day distribution in weeks.

Figure 1. Pictures of each of the four sides of the calendar from Lyulyakovo

The beginning of the reckoning could be the beginning of the church year, September 1, which is marked by a cross-shaped sign at one end of the stick. The schedule of fixed feasts in the Menaion (a set of twelve books, one for each month, containing the liturgical services for the fixed feasts) begins on September 1 - the New Year's and Indiction Day of the Byzantine Empire. It always includes the feasts of Christ, Virgin Mary and other Christian saints, as well as the feasts of many Old Testament saints.

March is located on the opposite edge after a wider, long notch at the very beginning of the stick. There is no festive sign on March 1. March contains the day of the vernal equinox, in relation to which the date of the most significant Orthodox festival, Easter (Christ's Resurrection, Pascha), is determined. A large number of ancient luni-solar calendars, including the Slav ones, had their beginning in March.

The beginning of the reckoning could also be the beginning of the civil year, January 1, which is located in the middle of the stick. Right in front of this date, in the middle of the long notch separating December from January, there is a (probably later) little round groove. Close to the date January 1, placed on opposite edges we find April 23 (St. George's Day) and October 26 (St. Dimiter's Day). These two dates mark the beginnings of the summer and the winter half-year periods of the economic year.

The dates June 24 (Birth of St. John the Baptist) and December 25 (Christmas, Christ' birth), which are connected to the summer and winter solstices, are on the left end of the stick. The dates March 25 (the Annunciation, Conception of the Blessed Virgin Mary) and September 23 (Conception of John the Baptist), related to the vernal and autumn equinoxes, are to be found on the right end of the stick.
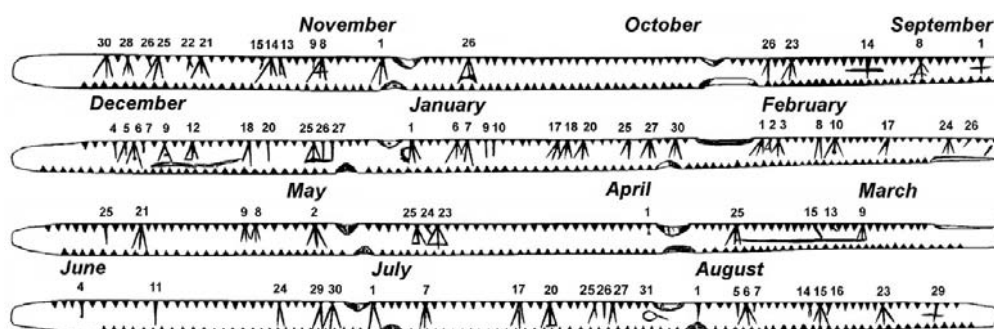
Figure 2. Scheme of the signs on the four sides of the wooden calendar from Lyulyakovo

Date	Feast in the orthodox calendar	Date	Feast in the orthodox calendar
September	A-side	3	St. Simeon & Anna the Prophet
1	New Year; New Indiction; St. Simeon	8	St. Theodore Stratelates the Great Martyr;
8	Nativity of the Blessed Virgin Mary		St. Zachariah the Prophet
14	Exaltation of the Holy Cross	10	St. Haralambos Hieromartyr
23	Conception of St. John the Baptist	17	St. Theodore of Tyre the Great Martyr
26	The Falling Asleep of St. John the Theologian (the Apostle and Evangelist)	24	1st and 2nd Finding the Head of St. John the Baptist

October	
26	St. Dimiter the Myrrhstreamer
November	
1	Sts. Unmercenaries Cosmas & Damian
8	St. Michael the Archangel
9	*(short notch)*
13	St. John Chrysostom
14	St. Philip the Apostle
15	*(short notch)*
21	The Entrance of the Blessed Virgin Mary into the Temple
22	*(short notch)*
25	St. Katherine the Great Martyr
26	*(short notch)*
28	St. Stephen the New
30	Apostle Andrew the first Called
December	**B-side**
4	St. Barbara the Great Martyr
5	St. Sava the Sanctified
6	St. Nicholas the Wonderworker
7	*(short notch)*
9	Conception of the Blessed Virgin Mary
12	St. Spiridon the Wonderworker
18	St. Modest the Patriarch of Jerusalem
20	St. Ignatius the God-Bearer
25	Holy Nativity of Jesus Christ
26	Synaxis of the Blessed Virgin Mary
27	St. Stephen the Protomartyr
January	
1	Circumcision of Jesus Christ; St. Basil the Great; New Year
6	Holy Epiphany
7	Synaxis of St. John the Baptist

25/26	*(newer short notch)*
Mart	**C-side**
9	Sts. 40 Martyrs of Sebaste
12/13	*(newer short notch)*
14/15	*(newer short notch)*
25	Annunciation of the Blessed Virgin Mary
April	
1	*(short notch)*
23	St. George the Great Martyr
24	*(short notch)*
25	St. Mark the Apostle and Evangelist
May	
2	Relics of St. Atanasius the Great
8	St. John the Theologian
9	St. Isaiah the Prophet; Relics of St. Nicholas
21	Sts. Constantine and Elena
25	3rd Finding of the Head of the Baptist John
June	**D- side**
4	St. Metrophanes the Patriarch of Constantinople
11	Sts. Bartholomew & Barnabas the Apostles
24	Nativity of St. John the Baptist
29	Sts. Peter & Paul the Apostles
30	Synaxis of the 12 Apostles
July	
1	Sts. Unmercenaries Cosmas & Damian
7	St. Nedelya – Kiriakiya the Great Martyr
17	St. Marina the Great Martyr
20	St. Elias the Prophet
25	The Falling Asleep of St. Anna
26	St. Hermolaus the Hieromartyr
27	St. Panteleimon the Great Martyr

9	St. Polyeuctus the Martyr	31	Sanctify of the church in Vlaherna,
10	St. Gregory of Nyssa	**August**	
17	St Anthony the Great	1	St. 7 Maccabean Youts
18	St. Athanasios the Patriarch of Alexandria	5	Forefeast of the Transfiguration
20	St. Euthymios the Great; St. Evtimy the Patriarch of Tyrnovo	6	Holy Transfiguration
25	St. Gregory the Theologian	7	Afterfeast of the Transfiguratin
27	Relics of St. John Chrysostom	14	Forefeast of the Falling Asleep
30	Three Saints	15	The Falling Asleep of the Blessed Virgin Mary
February		16	Icon "Not Made by Hands" of Jesus Christ
1	St. Trifon the Martyr	23	Conclusion of the Falling Asleep; St. Lup
2	Meeting of Christ in the Temple	29	Beheading of the Baptist John

Table 1. Identification of the signs on the wooden calendar with some Christian festivals

The dates from March 9 to 25 and from December 9 to 18 are especially underlined by parallel to the edges notches. One of the reasons for this might be to mark the days around the dates of the vernal equinox and the winter solstice which reaches 12 days in the 19th century and 13 days in the 20th century due to the inaccuracy of the Julian calendar. (The Council of Nicaea in AD 325 fixed March 21 as the date of the vernal equinox.)

The direction of reckoning of the days is from right to left on the first edge, then continuing from left to right on the next edge, i.e. the reckoning takes place without a break (the so-called boustrophedon style). Interrupted day reckoning, i.e. which takes place in one direction only, is found very rarely.

Reading of the festive signs

The festive signs are incised on the sides of the stick and are related to precise day notches. The signs including straight line, two-edged pitchfork, trident and their combinations are typical markers of the fixed Orthodox festivals on all rabosh calendars from western, southern and southeastern Bulgaria. In our case, there are several letter-signs, which are noteworthy because they are very rare. Along with the festive sign for January 1, the letter "С" is added (from *Сурва*, Surva - the Bulgarian folk name for the feast of Christ's Circumcision). The letter-signs "Д" for October 26

(*Димитровден*, St. Dimiter's Day in Bulgarian) and "A" for December 9 (*Анино зачатие*, Conception of St. Anna) are also used. Cross-shaped signs mark the dates September 1, September 14, August 29 (Fig. 2).

A specific peculiarity in our case are the broad shallow grooves around some major feasts which bear traces of older short notches in the days before or after the feast.

The identification of the signs on the wooden calendar with some Christian festivals is given in Table 1.

It is presumed that the one who used such a calendar knew well the number of days, weeks and months between the different fixed feasts. For example, people knew the major feasts, which fell on one and the same day of the week. A prerequisite is also to remember the day of the week when the year starts or the date of the first Sunday in a year. Then one will be able to calculate the date of the Resurrection and Easter Day and to determine the dates of the rest of the movable feasts during the year.

Conclusions

The rabosh calendar from Lyulyakovo confirms the fact that people paid special attention to and were very careful when making such "eternal calendars". A proof that the calendar was highly appreciated and necessary for its owners is the fact that after almost 200 years of usage by different generations and in different social and historical circumstances the calendar has reached us safe and sound. We can assume that when making a wooden calendar the craftsman consciously tries to achieve a good mnemonic structure, which in turn speaks for thorough knowledge of the official and the traditional calendars.

The wooden rabosh calendar could be considered as one of the archaic "tools" to pass on the calendar knowledge to next generations in a multilingual and multicultural environment in order to strengthen the position of Christianity in the cult practice and ritualism of the people.

References

1. K o l e v a E. Naroden kalendar – rabosh ot 1783 godina. Muzei i pametnici na kulturata, 1, 1967, 20-23

2. V a k a r e l s k i Hr. Bit i ezik na trakijskite i maloazijski bylgari. Chast I. Bit. Sofia, 1936, 269-273

3. G o r o v G. Strandzhanskiyat vechen naroden kalendar – "pop". More, 9-10, 1997, 9-11

LIFE STANDARD, SCIENCE AND ASTRONOMY

Tsvetan B. Georgiev
Institute of Astronomy, Bulgarian Academy of Sciences
tsgeorg@astro.bas. bg

Abstract.

The bibliometrc data published by Sanches & Benn (2004, arXiv:astro-ph/0401228) are analized. The proprotionality in log-log coordinates between the population and annual gross domestic product (GDP) with coefficient equal to unit is used for selection of "developed" countries and for futher reveal of dependances through them. The proportionality coefficients between the GDP and the citation of all-science or only of the 1000 astronomy top-articles in 1991-98 occur 0.75 and 0.93, respectivelly. The fact that coefficients are less then 1 gives evidence that when the wealth of the community grows up the citation (i.e. the quality) of the articles increases with a less speed. Correlations between the "cost" of 1% citation as part of the GDP or as a part of the GDP per person for all-science and for the 1000 astronomy top-articles only are found. They show that the scientific papers are relatively more "cheap" for the big scientific communities (USA, EU), but in the same time the most cited astronomical articles are relatively more "expensive", up to 2 times. Generally, the astronomy seems to be more interesting, but also more expensive than the science on average.
Key words: *scienciometric, bibliometric, productivity in science*
PACS No.

Till July 1, 2004, the ADS archive (Abstract Service of the Harvard-Smithsonian Center for Astrophysics; http://adswww.harvard.edu/ads_-abstracts.html) already contains more than 1 000 000 records for papers in Astronomy & Astrophysics and more than 1 770 000 in Physics and Geophysics. It is considered, that the astronomical papers sample published after 1970 is well enough complete. It comprises of the most representative journals with a small exception of the hardly accessible ones. Another usual source of information to date used for bibliometric studies is the Institute of Scientific Information (ISI, see for instance Abt (2003) for details). Different

investigations could be made based on the information from ADS and ISI. Here we reanalyze the data of one such recent article.

The impact of astronomical research carried out by different countries has been compared in the paper of Sanches & Benn (2004) based on analysis of the 1000 most cited astronomy papers published 1991-98 (125 such per year). The data about 22 countries and 2 comunities (EU, presented by 9 countries – BE, DK, FR, DE, IT, NL, ES, SE, UK, and ESO, presented by 8 countries – BE, DK, FR, DE, IT, NL, SE, CH), prodused at least 2 such top papers, are collected in Table 1. The Table 1 columns contain the following data: 1 – 2 – name of the country and ISI code used in Fig.1-3; 3 – 4 – the number of the top-cited 1000 articles N_A with first author hosted by the given country or community and the respective citation fraction C_A; 5 – the *all-science* citation fraction C_S (from ISI, 1995); 6 – total population N_P (1999); 7 - annual gross domestic product (GDP) per head of population $\$/N_P$; 8 – 9 – GDP per percent of astronomy (top 1000) citation $\$/C_A$ or per all-science citation $\$/C_S$; 10 – 11 – GDP per head of population per percent astronomical $\$/N_P/C_A$ or all-sceince $\$/N_P/C_S$ citation.

Language bias against both publication and citation need to be considered when comparing citation counts for different countries, because of: (i) the favorization of the english-speaking scientists, which write naturally in english and tend not to read papers in other languages; (ii) citation databases provide uneven coverage of foreign-language journals; (iii) the big comunities (f. i. USA, UK) tend to over-cite their own results, e.g. through preferentially reading and citing national journals (Sanches & Benn, 2004). We can add that many scientists are leaving their countries and work mainly in the USA, thus the results of the statistics is more favorable for the smaller countries. Another source of biases is the insufficient statistics and by this reason we exclude 4 countries (Austria, Estonia, Finland and S. Korea), these are presented in the current investigation with only one astronomical top-cited paper.

Table 1. The data about the countries and the citations

Country	Code	N_A	C_A [%]	C_S [%]	N_P [10^6]	$/N_P$ [$\$10^6$]	$/C_A$ [$\$10^9$]	$/C_S$ [$\$10^9$]	$/N_P/C_A$ [$\$10^3$]	$/N_P/C_S$ [$\$10^3$]
1	2	3	4	5	6	7	8	9	10	11
Australia	AU	18	1.6	2.2	18.8	20.9	246	179	13.1	9.5
Belgium	BE	2	0.2	1.1	10.2	23.1	1180	214	115.7	21.0
Canada	CA	40	3.8	4.3	31.0	22.2	181	160	5.8	5.2
Denmark	DK	6	0.7	1.0	5.4	23.0	177	124	32.8	23.0
France	FR	35	2.9	5.7	59.0	22.4	455	232	7.7	3.9
Germany	DE	56	4.9	7.2	82.1	22.1	370	252	4.5	3.1
Israel	IL	3	0.3	1.1	5.8	17.4	337	92	58.0	15.8
Italy	IT	31	3.2	3.4	56.7	20.8	369	347	6.5	
6.1 Japan	JP	23	2.4	8.2	126.2	23.0	1210	354	9.6	2.8
Netherlands	NL	23	2.1	2.3	15.8	22.0	166	151	10.5	9.6
Spain	ES	7	0.8	2.0	39.2	16.5	806	322	20.6	8.2
Sweden	SE	4	0.6	1.8	8.9	19.7	292	97	32.8	10.9
Switzerland	CH	14	1.9	1.6	7.3	26.2	100	119	13.8	16.4
UK	UK	101	10.7	7.9	59.1	21.2	117	158	2.0	2.7
USA	US	599	60.6	30.8	272.6	31.2	140	276	0.5	1.0
ESO	ESO	171	16.5	14.1	245.4	22.0	326	382	1.3	1.6
Europe	EU	265	17.1	32.5	336.4	21.1	415	218	1.2	0.6
Brazil	BR	2	0.1	0.6	171.1	6.0	10350	1725	60.5	10.1
Chile	CL	5	0.4	0.2	15.0	12.3	460	920	30.7	61.3
Poland	Pl	4	0.4	0.9	38.6	6.8	658	292	17.0	7.6
Russia	RU	2	0.1	4.1	146.4	4.1	5930	145	40.5	1.0
S.Africa	ZA	3	0.4	0.4	43.4	6.7	725	725	16.7	16.7
Ukraine	UA	2	0.2	0.6	49.8	2.2	540	180	10.8	3.6
Venezuella	VE	2	0.3	0.1	23.2	8.4	647	1940	27.9	83.6

In spite of the disadvantages of such kind of data, Sanches & Benn (2004) show in log-log coordinates the proportionalities between the citation fraction of the 1000 top-papers and the population, GDP per head of population, IAU numbers and percent of all-science citation for considered
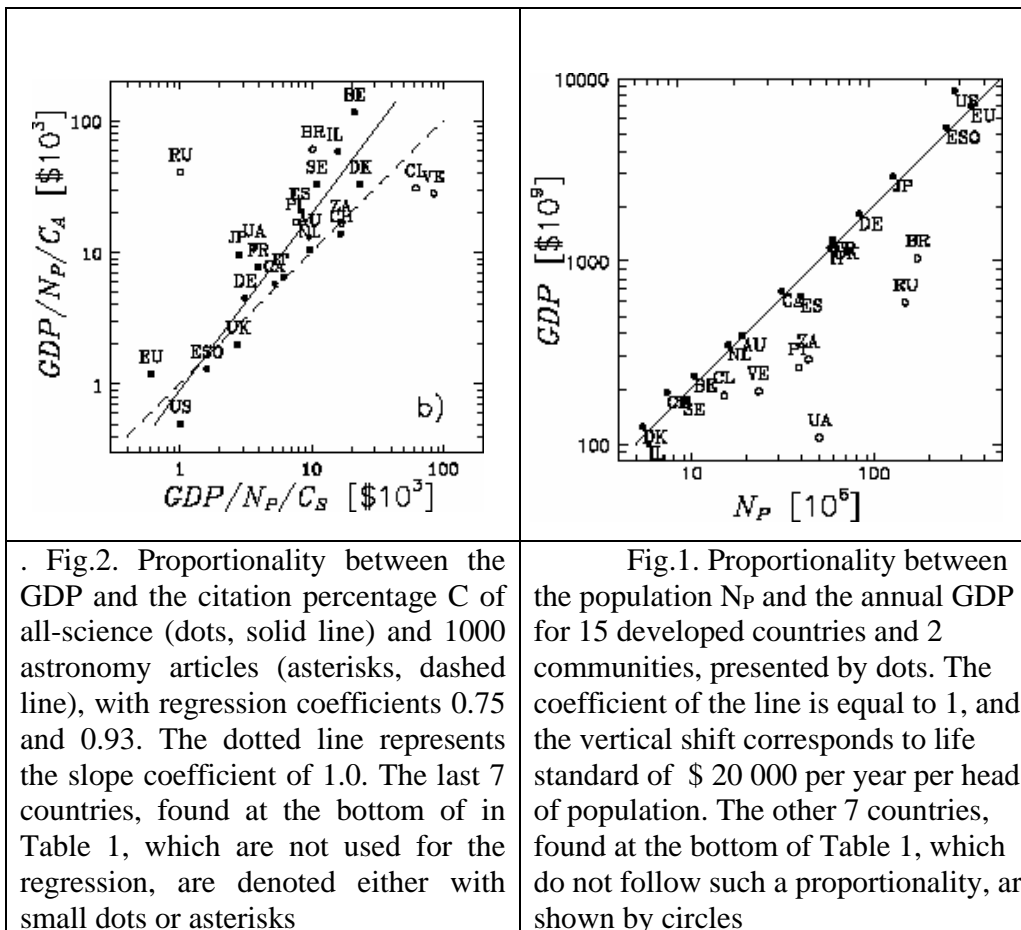
countries and communities. Generally, the phenomenon seems to have fractal nature. The most cited astronomical authors are hosted in USA, EU, ESO and UK, but in all-science case the USA and EU changes their positions. One special case is Russia, having significant all-science impact but low contribution to the 1000 astronomical top-cited articles. Further we emphasizes on the citation "cost" in comparison with the GDP and GDP per head of population.

The narrow dependence between the population and the annual GDP of 15 well developed countries and communities, which are involved in deriving the dependence in the next figures in Fig. 1 is conspicuous. These countries well contribute the coefficient equal to 1. This means that they are approximately equally developed in sense of life standard, corresponding to $ 20 000 per year per person (in 1999). The other 7 countries which do not support this proportionality are collected in the bottom of Table 1.

Figure 2 shows the approximate proportionality between the annual GDP and the citation of the all-science and the 1000 top-cited astronomy articles. Having in mind the dependence presented in Fig.1, one can expect regression coefficients close to 1. However, the phenomenon is more interesting – the coefficients are less than 1 and are different. The dependence of all-science citation on the GDP (build on other, large and may be full "observing material") is characterized by coefficient 0.75. Therefore, the richer the scientific community, the more scientific quality, but not so fast with respect to Fig. 1. Obviously, we find some decreasing of the interest in the all-science investigations in the rich communities and we claim for the existence of the "3/4 law" in this field. However, the dependence of the astronomical citation on the richness of the community (build on a limited "observing material") is stepper – 0.93. This fact shows in general that the interest in the astronomy is more strong and resistant against the wealth then in the all-science case.

Figure 3 compires the relative "costs" of the all-science and the 1000 top-citated astronomy articles, expressed as parts of the GDP and as parts of GDP per person.The correlation in Fig.3a is poor prominent, but it gives evidence that in comparison with the high quality astronomical articles the all-science citation is "cheaper" up to 2 times. The correlation in Fig. 3b is more prominent and it shows that the efficiency (i.e. low cost in comparison with the life standard) of all-science or astronomy investigations is most efficient in the

large and rich communities (USA,EU,ESO,UK), decreasing when the community population decreases. This tendency is more strong for the astronomy, where the citation of the top articles seem to be up to 1.5 times more expensive.

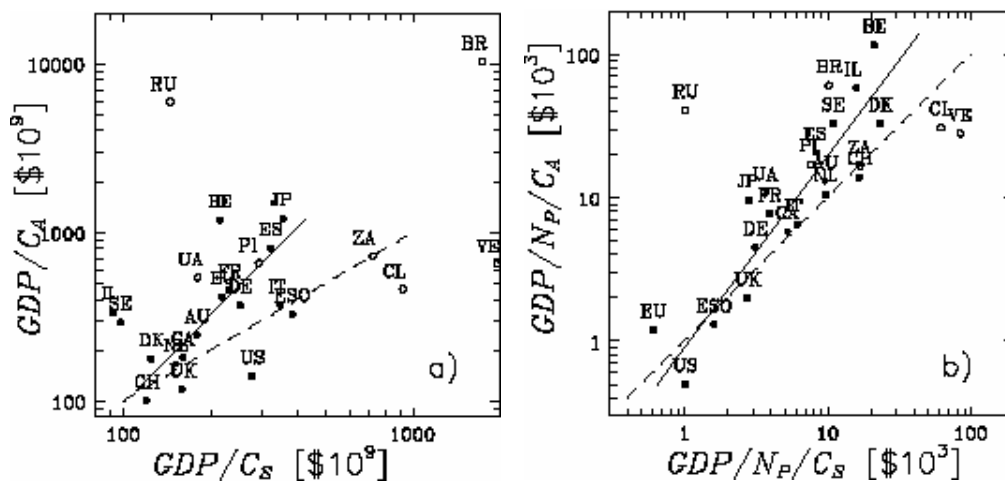|	
. Fig.2. Proportionality between the GDP and the citation percentage C of all-science (dots, solid line) and 1000 astronomy articles (asterisks, dashed line), with regression coefficients 0.75 and 0.93. The dotted line represents the slope coefficient of 1.0. The last 7 countries, found at the bottom of in Table 1, which are not used for the regression, are denoted either with small dots or asterisks	Fig.1. Proportionality between the population N_P and the annual GDP for 15 developed countries and 2 communities, presented by dots. The coefficient of the line is equal to 1, and the vertical shift corresponds to life standard of $ 20 000 per year per head of population. The other 7 countries, found at the bottom of Table 1, which do not follow such a proportionality, are shown by circles

.

Fig. 3. Correlation between the "cost" of the citations of the all-science papers (C_S) and the 1000 astronomical top-articles (C_A) with respect to the GDP (a) and GDP/N_P (b). The solid lines represent the orthogonal regressions and the dashed lines represent the dependences with coefficients equal to 1. The last 7 countries, found at the bottom in Table 1, which are not used for the regressions, are presented by circles.

Generally, the astronomy seems to be more interesting (Fig.2) and more expensive (Fig.3) than the science on average.

The author is gratefull to R. Kurtev, V. Golev and P. Nedialkov for the valuable discussions.

R e f e r e n c e

A b t H., in Organizations and Strategies in Astronomy, Vol. 4, 197, 2004
S a n c h e z S. F., C. R. B e n n, 2004, arXiv:astro-ph/0401228;
        Astr. Nachr. (in print)

A THRACIAN LUNISOLAR CALENDAR

Nikolai Sivkov

Historical Museum, 2300 Pernik, Bulgaria, e-mail: nsivkov@abv.bg

Introduction

In antiquity, astronomy was closely related to the measuring of time. The first calendars based on the movement of the Moon and the Sun date back to the Paleolithic and Neolithic ages [1]. In the course of the centuries the lunar calendars developed into lunisolar and, in order to measure more precisely long periods of time, information about other astronomical objects such as planets and stars was used as well [2]. Except for the everyday practical needs of a society, calendars serve also other social needs – religious, ideological, and philosophical. By establishing a specific bond between Man and Nature, between Man and Cosmos, they become practically involved in building up of the people's worldview – a notion, which in ancient times was mainly mythological in character [3].
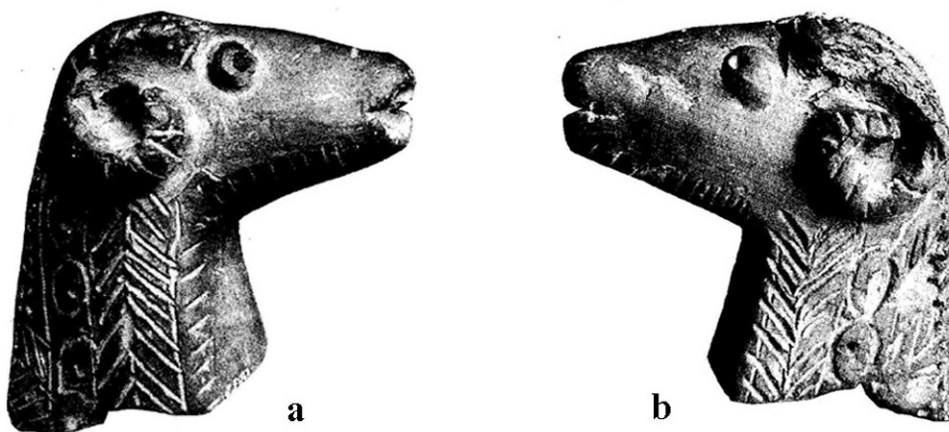

Figure 1.

On the outskirts of the village of Bosnek, Pernik Region, Western Bulgaria, a clay ram head (*prothome*) has been found, dated to the late antiquity (I-III cc) [4]. Its height is 19 cm, and the length at the base is 13 cm. The origin of this artifact is questionable. The ram- and horse-shaped figures made of clay and stone, and found in southern Bulgaria along the

Struma River (defined as the westernmost area where they are to be found) are usually considered monuments of the Celtic culture [5]. According to some authors, however, similar figures are also found in places where there are no traces of Celts, and for that reason they associate them with the culture of Thracians [6].

Interpretation

As a whole, the object is well preserved, except for some minor damages, and represents a completed statuette (Fig. 1 – a, b). The artifact's structure allows for its interpretation as a zoomorphic model of the world (World Tree) reflecting the Thracians' worldview. The image of the ram (a hoof animal) is the basis of this model which is complemented with therio- and ornithomorphic images. We suppose that the pragmatic function of the object is to serve as a time-measuring device, and the calendar information could be presented through the groups of notches and dents on the body of the prothome. As a calendar this object could be used in two aspects: for practical purposes – for time-reckoning in everyday and agricultural life (civic calendar), and in the cult practice – for religious rite purposes (cultic calendar). Some typologically similar objects confirm such multifunctionality, for example the Dacian sanctuary in Muncelulu, Romania [7]. In the first case (in the everyday time-reckoning), the "parapegma" (indents for movable pegs serving as markers) could be used (Fig.2). In the second case (for cultic purposes), the notches on the prothome body could be the main bearer of information.

The total number of sings on the head of the ram is 265 and is equal to the number of days in 9 lunar months (29.53 x 9 =265.77 days) or the so-called "Apollo" part of the year according to Plutarch [8].

The signs are grouped into 4 clusters.

354

CLUSTER A

This could be the working part of the calendar – the main device for calendar calculations. It consists of three independent groups of signs on the back of the prothome (Fig. 2 b):
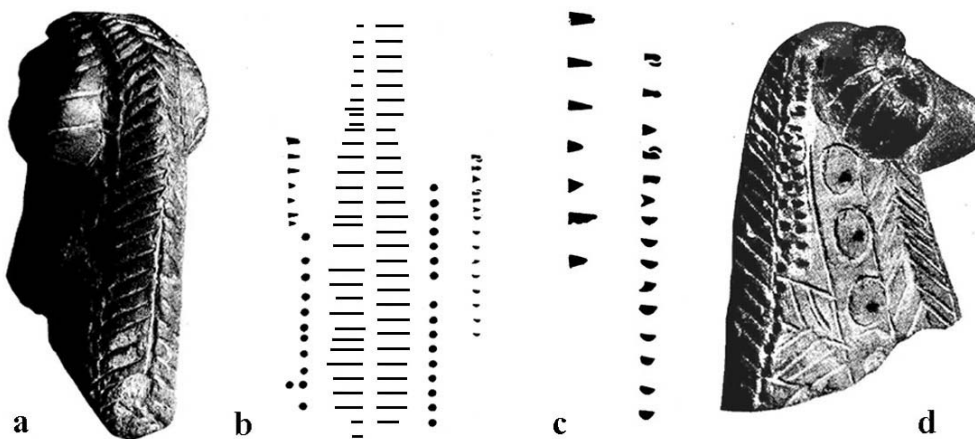

Figure 2.

Fishbone-Notches. In the combination $31 + 28 = 59$ signs they could represent two synodic months ($29.53 \times 2 = 59.06$ days) or 1/6 of the lunar year (354 days) (Fig. 2 – a, b);

Big Parapegma. The parapegmatic signs on both sides of the central axis, in the combination $(11 + 1) + 16 = 28$ signs, represent, for example, one sidereal month (27.32 days) (Fig. 2 – b, d).

Lunar Phases. The parapegmatic signs on both sides of the prothome's back in the combination $7(8) + 15 = 22(23)$ signs are equal to the number of days in a lunar month from new moon to the third phase of the moon, when it starts to wane (Fig. 2 – c, d).

CLUSTER B

There are three independent groups of signs on both sides of the prothome's body:

Small Parapegma. It includes $5 = 3 + 2$ indents - three on the right and two on the left side of the prothome (Fig. 3 – a, b), complemented by $4 = 2 + 2$ indents at the front – the two eyes and the two nostrils of the ram (Fig. 1). The various combinations of the Small and the Big Parapegma give the number of days in months in a lunar calendar similar to the Roman ones

from VIII-VII cc. BC (28, 30, 31 days) [9]. In the case of a solar calendar, when the year is of the "Egyptian" type (12 months x 30 days = 360 days), which is similar to the year used by the ancient Greeks, these five indents could complete the five missing days in the solar year of 365 days.

Figure 3.
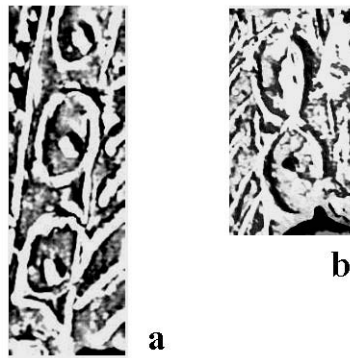
Plant Ornament includes notches on the left and the right side of the ram head, which are grouped as follows: (16+6) + (17+3+3) = 45. The sum is equal to 1.5 synodic months (Fig. 4 – a, b). Since antiquity this number has been related to the measurement of the periods of solar and lunar eclipses [10]. A solar or lunar eclipse can occur only when the Sun and the New respectively the Full Moon are at or near the nodes of the Moon's orbit. In the first case the Sun passes the zone of eclipse for 36 days, and in the second case for 22 days. The number 45 allows precise defining of the instant of the solar eclipses, for example, since it indicates the day of New Moon, if the count of this interval starts at Full Moon.

The numbers 22 and 23 from the Plant Ornament separately correspond to the additional month of 22 (23) days in the lunisolar calendar with a two-year cycle of Numa Pompilius, VII c. BC [11]. They also correspond to the number of signs in the Lunar Phase parapegma.
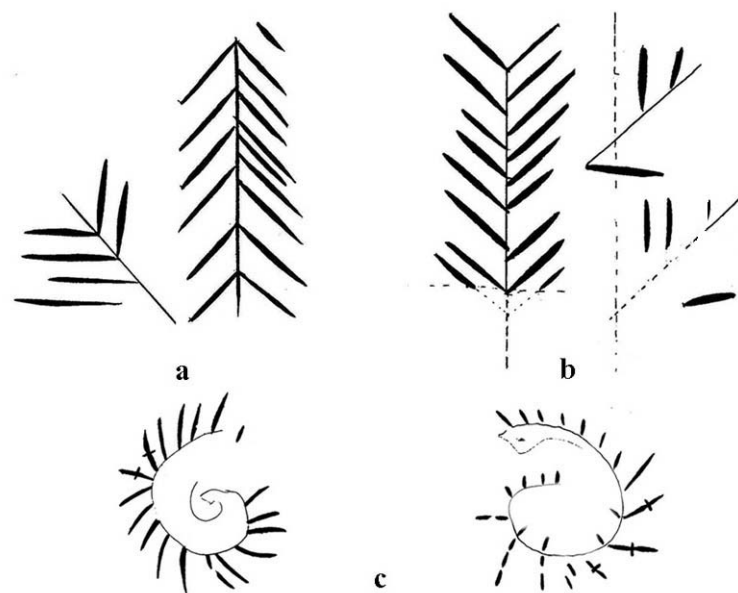

Figure 4.

Notches on the Ram Horns. The notches represent a complex pattern consisting of short lines (Fig. 4 - c). Their sum is 20 + 18 = 38 and the following sums of signs are also possible: 28 + 19 = 47 and 31 + 21 = 52. Together with the Plant Ornament notches the notches on the horns give number values that can be regarded as "seasons" or "cycles" depending on the context of the particular analysis. For example, the combination of the signs: (38 + 22) x 6 = 60 x 6 = 360 can correspond to the Egyptian year of 360 days, while (38 + 23) x 6 = 61 x 6 =366 – to the leap year in the Julian calendar. The combination of the signs (47 + 23) x 4 = 70 x 4 = 280 can correspond to the cycle of a woman's pregnancy (280 days).

CLUSTER C

At the front part of the prothome there are two groups of notches which largely differ in shape from those in cluster B. On the right side, along the brim of the prothome's body there are 18(19) notches, and on the left – 12 notches (Fig. 5 – a, b).

The notches could correspond to the number of years in the Metonic cycle (19), where there are 235 synodic months and to the number of months in a lunar year (12), respectively.

The signs on the right side of this block could mark the number of years in one saros (18 years + 10/11 days), the period through which lunar and solar eclipses repeat regularly [12]. The number of these signs could correspond as well to the period of the movement of the lunar nodes – 18.61 tropical years (18 years + 222 days). The interval of 222 days can be measured by using the Big and the Small parapegmas: 37 x 6 = 222 signs.
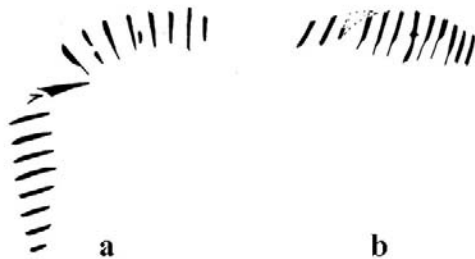

Figure 5.   Figure 6.

CLUSTER D

On the pate of the ram 17 signs are situated like carnivorous bird head (Fig. 6). In aspect of composition they are related to the central group of notches (the body of a dragon?), in aspect of number – to the draconian (eclipse) year (346.62 days). As a separate time interval they could mark the passing of the Sun through the "eclipse zones". For a period of 17 days before it reaches the lunar node, and 17 days after that there is a possibility for solar eclipses. The Sun makes its way from one lunar node to the other for 173.31 days. The sum of the rest of notches on the body of the prothome of the ram, without counting the parapegmas, is 173 in total.

Conclusions

The calendar and astronomical information coded in the system of signs of the ram prothome from the village of Bosnek testify to thorough astronomical knowledge that people in antiquity (the priests, for example) possessed and used in their ritual practices, in agricultural and everyday life. Synodic and siderial month, draconian and tropical year, seasonal and calendar cycles could be represented by specific means and in original ways in this interesting and yet not completely studied artifact.

The different calendar periods are complemented and emphasized by the semantics of the mythological characters, interlaced in the semiotic structure of the prothome. Being a time-measurement device, this lunisolar calendar most probably served mainly the cultic and ritual practices of the Thracian tribes that inhabited these lands.

References:

1. S t o j c h e v T., 1998, Archeoastronomia: Praistoricheski svidetelstva za izmervane na vremeto ot Bulgaria. Sofia [in Bulgarian]
2. B i k e r m a n E., 1975, Hronologia drevnego mira. Blizhnij Vostok i antichnost. Moskva [in Russian]
3. E l i a d e M., 1987, Kosmos i istoria. Moskva [in Russian]
4. R a d o n o v Z., 1965, Kultovi pametnici v Okryzhnija muzej v Pernik. Arheologia, VII, № 4, 47 – 53 [in Bulgarian]
5. G e r a s i m o v T., 1960, Keltski kultovi figuri ot Bulgaria. Izvestia na arheologicheskia institut, XXIII, Sofia, 165 – 203 [in Bulgarian]
6. L y u b e n o v a V., 1985, Antichna zoomorfna plastika ot Okryzhnija muzej – Pernik. V: Terra Antiqua Balcanica 2, 260-261,273 [in Bulgarian]
7. O p p e r m a n n M.,1984, Thraker. Zwischen Karpatenbogen und Ägäis. Leipzig, 182-184
8. P l u t a r c h, 1978, Moralii. Ob "E" v Delfah. IX-X. Vestnik drevnej istorii № 1, 245 [in Russian]
9. S e l e s h n i k o v S. I., 1985, Istoria na kalendara i hronologija. Sofia, 55-56, tablici 3, 4 [in Bulgarian]
10. L a r i c h e v V. E., 1989, Mudrost zmei: Pervobitnij chelovek, Luna i Solnce. Novosibirsk, 112-115 [in Russian]
11. S e l e s h n i k o v S. I., 1985, 54 – 57
12. V u d D., 1981, Solnce, luna i drevnie kamni. Moskva, 97 [in Russian]

CLASS OF INHOMOGENEOUSLY DRIVEN DYNAMICAL SYSTEMS: GENERAL THEORY, REGULAR AND CHAOTIC PROPERTIES

*Vladimir Damgov, Nikolay Erokhin * and Plamen Trenchev*

Space Research Institute at the Bulgarian Academy of Sciences, Sofia, Bulgaria
* Space Research Institute at the Russian Academy of Sciences, Moscow, Russia

Abstract:

A generalized model of an oscillator, subjected to the influence of an external wave is considered. It is shown that the systems of diverse physical background which this model encompasses by their nature should belong to the broader class of "kick-excited self-adaptive dynamical systems".

INTRODUCTION

The main goal of this report is to present a phenomenon of highly general nature manifested in various dynamical systems. We present the occurrence of peculiar "quantization" by the parameter of intensity of the excited oscillations (See the References below [1-9]). Quantization (the idea of quantums, photons, phonons, gravitons) is postulated in Quantum Mechanics, while Theory of Relativity does not derive quantization from geometric considerations. In the case of the established phenomenon the "quantized nature" of portioned energy transfer stems directly from the mechanisms of the process and has a precise mathematical description.

Here we also consider the generalized "oscillator-wave" model [10] and show that, in this case, the inhomogeneous external influence is realized naturally and does not require any specific conditions.

1. **A NUMERIC DEMONSTRATION** OF THE EXCITATION OF "QUANTIZED" PENDULUM OSCILLATIONS

The inhomogeneously AC driven, damped pendulum system can be described by the following equation:

$$\frac{d^2 x}{dt^2} + 2\delta \frac{dx}{dt} + \sin x = \varepsilon(x) F_o \sin vt , \qquad (1)$$

where the function $\varepsilon(x)$ can be analytically expressed in various ways, such as:

$$\varepsilon(x) = \begin{cases} 1 & for \quad |x| \le d' \\ 0 & for \quad |x| > d' \end{cases} \tag{2}$$

or $\varepsilon(x) = e^{-\frac{x^2}{2d'^2}}$, $\varepsilon(x) = \begin{cases} \dfrac{1}{2}\left[1 + \cos(\dfrac{\pi}{d'}x)\right] & for \quad |x| \le d' \\ 0 & for \quad |x| > d' \end{cases}$ and so on; $d' << 1$

is a parameter limiting the external action on a small part of the trajectory of motion in the system (in the particular case(2) the parameter d' thereby determines a symmetric zone of action in the area of the lower equilibrium position).

Results from the computer experiment are presented in [1,2].

2. ANALYTICAL PROOF OF EXISTENCE OF KICK-PENDULUM "QUANTIZED" OSCILLATIONS

The analytic approach for the cases of small and large amplitudes of pendulum oscillation is given in [1,2,3,4,5,6,7,8,9].

The spectrum of the symmetrical solution amplitudes can be expressed

as [2,7]: $2vK(k_o) = 2\pi\left(l + \dfrac{1}{2}\right)$, l= 0, 1, 2, 3…, which yields the spectrum

of amplitudes k_o, $K(k_o) = \left(l + \dfrac{1}{2}\right)\dfrac{\pi}{v}$, l= 0, 1, 2, 3… and an odd ratio of

frequency division $N = 2l + 1$, l= 0, 1, 2, 3…, $K(k_o) = \left(l + \dfrac{1}{2}\right)\dfrac{\pi}{v}$ is

complete normal elliptic integral of first kind.

A phenomenon of rotation excitation with strictly determined discrete set of possible rates is presented. The model considered is that of a pendulum rotator under inhomogeneous action [1,2].

General conditions for pendulum oscillation excitation under the action of external nonlinear force has been derived [1,2,9].An analytical approach for large amplitudes of pendulum oscillation (strong nonlinearity) has been also demonstrated [1,2,5,6,7].

3. MODEL OF THE INTERACTION OF AN OSCILLATOR WITH AN FALLING WAVE

Analytical approaches applicable for small and large amplitudes (for weak and strong nonlinearity) of the oscillations in a nonlinear dynamic system subjected to the influence of a wave has been developed [1,10].

The performed analysis shows that the continuous wave having a frequency much larger than the frequency of a given oscillator can excite in it oscillations with a frequency close to its natural frequency and an amplitude belonging to a discrete set of possible stable amplitudes.

4. "QUANTIZED" CYCLOTRON MOTION

An electric charge, moving on a circular orbit in a homogeneous permanent magnetic field has been considered. When the charge was irradiated by a flat electromagnetic wave having a length commensurable with the orbit's radius, an effect of discretization ("quantization") of the possible stable orbital radii (or motion velocities) was observed (See [1,10]).

5. THE WAVE NATURE AND DYNAMICAL QUANTIZATION OF THE SOLAR SYSTEM

The Solar system planets mean distances are presented (See [1,10]). For comparison reasons, the direct astronomic measurements data is given parallel to the result, computed by the classical Titius-Bode law (11) and an Equation according to the "oscillator-wave" model, described above. A good correspondence is observed between the computed and astronomically measured radii. Especially significant is the correspondence between the computed and measured radii of Neptune and Pluto. The Titius-Bode law determines the mean distances of those two planets with an error of 23% and 49%, respectively.

The computed data of the mean satellite distances from Saturn, Uranus and Jupiter, as well as the mean ring system distances from Saturn, are also presented (See [1,10]). The calculations are made on the basis of the "oscillator-wave" model. Again, a good correspondence is seen between the calculated and measured mean distances [1,10].

Assumption that the Solar system is e a wave dynamic system and hence, the micro-mega-analogy (MM-analogy) is valid [11], is the essence and grounds for the presented consideration.]

6. GENERAL CONDITIONS FOR TRANSITION TO IRREGULAR BEHAVIOUR IN AN OSCILLATOR UNDER WAVE ACTION

General conditions for transition to irregular and chaotic behaviour in an oscillator under wave action have been derived using the notion about the Melnikov distance [1,10].

7. GENERAL CHARACTERISTIC FEATURES OF THE CLASS OF KICK-EXCITED SELF-ADAPTIVE DYNAMICAL SYSTEMS. CONCLUSIONS

The main characteristics and regularities, characterizing the considered class of kick-excited self-adaptive dynamical systems are as follows:

1. The excitation of oscillations with a quasi-natural system frequency and numerous discrete stationary amplitudes, depending only on the initial conditions.

2. Adaptive self-control of the energy contribution in the oscillating process.

Regardless of its simplicity, the "oscillator-wave" model obviously reflects a number of processes in the micro- and macro-world.

On the basis of the presented oscillator-wave model it is also possible to create heuristic models of the interaction of electromagnetic waves with plasma particles in the Earth's ionosphere and magnetosphere, heuristic models of the generation of powerful low-frequency waves in the space around the Earth when a cosmic electromagnetic background is present etc. High-efficient sub-millimeter emitter, built on this basis, could be suitable for radio-physical heating of plasma, e.g. in the experiments aimed the achievement of controllable thermonuclear reaction [1].

The method developed of entering energy in oscillation processes and the excitation of "quantized" oscillations in dynamic macro-systems finds and will find in the future applications which could be grouped in the following way:

1. Transformation of signals and oscillations of different nature by frequency with a high efficiency at single division of the frequency by ratio of tens, hundreds and thousands.

2. Energy transformation of one kind into another, for example of electric into mechanical and vice-versa.

3. Stabilization of different parameters with their change in a wide range (e.g. 50-100-300%).

4. The development of new base elements for specialized calculating devices possessing a large number of stable discrete states.

5. Intensification of different processes through a special organization of interaction of different oscillation or development of different wave technologies.

6. The modelling of micro- and macro- processes with the methods of classic oscillation theory.

REFERENCES

1. D a m g o v, V.N. Nonlinear and Parametric Phenomena: Theory and Applications in Radiophysical and Mechanical Systems. Monograph. Series A: Monographs (Series of Nonlinear Sciences), Series Edition: University of California, Berkeley, New York, London, World Scientific, 2004, 650 p**.,** Chapter 10

2. D a m g o v, V. and Pl. T r e n c h e v. Class of Kick-Excited Self-Adaptive Dynamical Systems: "Quantized" Oscillation Excitation. Chaos, Solitons and Fractals, Oxford, vol. 17, 2003, No 1, pp. 11-40

3. D a m g o v, V.N. "Quantized" Oscillations and Irregular Behaviour of a Class of Kick-Excited Self-Adaptive Dynamical Systems, Progress of Theoretical Physics Suppl, Kyoto, Japan, №139, 2000, pp. 344-352

4. D a m g o v, V. and Pl. T r e n c h e v. Phenomenon of "Quantized" Oscillation Excitation, in: Nonlinearity and Disorder: Theory and Applications, F.Abdulaev et al. (Eds), Kluwer Academic Publishers, Netherlends, 2001, pp. 397 – 409

5. D a m g o v, V.N. and I. P o p o v. "Discrete" Oscillations and Multiple Attractors in Kick-Excited Systems. Discrete Dynamics, in Nature and Society (International Multidisciplinary Research and Review Journal), vol. 4, 2000, pp. 99-124

6. D a m g o v, V.N. "Quantized" Oscillations and Irregular Behaviour of Inhomogeneously Driven, Damped Pendulum, in: Dynamical Systems and Chaos, vol.2, World Scientific, London, pp. 558-561

7. D a m g o v, V. and P. G e o r g i e v. Amplitude Spectrum of the Possible Pendulum Motions in the Field of an External, Nonlinear to the Coordinate Periodic Force, in: Dynamical Systems and Chaos, vol.2, World Scientific, London, pp. 304-307

8. D a m g o v V. and I. P o p o v. Multiple Attractors in a Class of Dynamical Systems, Comptes Rendus de la Academy Bulgare des Science, 52, 1999, No.5-6, 31-34

9. D a m g o v V. and P. G e o r g i e v. General Conditions for Resonance Oscillations Excitation Under the Action of External Nonlinear Force, Comptes Rendus de la Academy Bulgare des Science, 52, 1999, No.9-10, 22-25

10. D a m g o v, V., Pl. T r e n c h e v and K. S h e i r e t s k y. "Oscillator-Wave" Model: Properties and Heuristic Instances, "Chaos, Solitons and Fractals", Oxford, vol. 17, 2003, No 1, pp. 41-60

11. C h e c h e l n i t s k y, A.M. Wave Structure of the Solar System. Publishing House Geo, Dubna, 2000, 132 p.

12. M o i s e e v, S., V. P u n g i n and V. O r a e v s k y. Nonlinear Instabilities in Plasmas and Hydrodynamics, Institute of Physics Publishing, Bristol and Philadelphia, 2000, 162 p.

THE ROZHEN NATIONAL ASTRONOMICAL OBSERVATORY:
OBSERVATIONAL FACILITIES, RESEARCH ACTIVITIES AND POSSIBILITIES FOR COLLABORATION BETWEEN COUNTRIES FROM SEE

Kiril Panov

Institute of Astronomy, BAS

Summary.

The observing facilities of the National Astronomical Observatory are presented: 2-m Ritchey-Chretien-Coude telescope, equipped with a 1024x1024 CCD (Photometrics, USA), 60-cm Cassegrain telescope for photometric observations, equipped with a single channel, photon counting, UBV-filters, computer controlled photometer, and the 50/70 cm Schmidt telescope, equipped with a SBIG ST8 CCD.
The research departments (Sectors) of the Institute of Astronomy are presented which are: Sun, Solar System, Nonstationary Stars, Chemically Peculiar Stars, Stellar Atmospheres and Envelopes, Stellar Clusters and Galaxies.

Brief description is given of a number of research projects, including projects of international collaboration. The important role of the Rozhen NAO in the on-going international collaboration has been pointed out. During the past 23 years since the official inauguration of Rozhen NAO, research projects have been carried out with a number of European countries, including Germany, France, Italy, Norway, Finland, UK, Greece, Russia, and all of the East-European countries.
New projects have been recently started with Serbia and MN, Romania, Turkey and Macedonia. Results have been presented demonstrating the atmospheric and seeing conditions in the Rozhen NAO. In addition, results from several photometric programs were shown as a demonstration of the capabilities of the observing facilities.

Special attention is dedicated to the recent activities of UNESCO-ROSTE in the region of SEE. The decision of ROSTE to grant and to supply a new, high-performance CCD camera to Rozhen NAO is a strong boost of the regional collaboration in Astronomy, including Bulgaria, Romania, Serbia and MN, and Turkey. Perspectives of future joint research are outlined.